UNIVERSITY OF CALIFORNIA,
IRVINE

Characterization of Trace Gases During the Front Range Air Pollution and Photochemistry Experiment (FRAPPÉ) Field Campaign

DISSERTATION

submitted in partial satisfaction of the requirements
for the degree of

DOCTOR OF PHILOSOPHY

in Chemistry

by

Stacey Cristina Hughes

Dissertation Committee:
Professor Donald R. Blake, Chair
Professor Barbara J. Finlayson-Pitts
Professor Sergey X. Nizkorodov

2018

DEDICATION

To my family,

old and new,

for being a constant source

of

love and support.

TABLE OF CONTENTS

Page

LIST OF FIGURES v

LIST OF TABLES xiii

LIST OF ABREVIATIONS xvii

ACKNOWLEDGMENTS xviii

CURRICULUM VITAE xvix

ABSTRACT OF THE DISSERTATION xxiii

1. INTRODUCTION…… 1
- 1.1 Atmospheric Trace Gases 1
  - 1.1.1 Methane 2
  - 1.1.2 Carbon Monoxide 5
  - 1.1.3 Non-Methane Hydrocarbons 8
    - a. Biogenic Non-Methane Hydrocarbons 8
    - b. Anthropogenic Non-Methane Hydrocarbons 10
    - c. Chemistry of Non-Methane Hydrocarbons 11
  - 1.1.4 Tropospheric Ozone 14
    - a. Air Quality Legislation 15
- 1.2 Oil and Natural Gas 16
  - 1.2.1 Formation, Composition, and Location of Oil and Natural Gas in Colorado 16
  - 1.2.2 Oil and Natural Gas Processing and Infrastructure 18
    - a. Fugitive Emissions 19
  - 1.2.3 Previous Work Regarding Oil and Natural Gas Emissions 19
    - a. United States Oil and Natural Gas Emissions 20
    - b. Colorado Oil and Natural Gas Emissions 22
- 1.3 Objectives and Motivation for this Work 24
  - 1.3.1 Front Range Air Pollution and Photochemistry Experiment 25
- 1.4 References 26

2. METHODS……..… 35
- 2.1 Study Design 35
- 2.2 Campaign Measurements 37
  - 2.2.1 FRAPPÉ Airborne Measurements 37
  - 2.2.2 FRAPPÉ Surface Measurements 40
  - 2.2.3 DISCOVER-AQ Measurements 41
- 2.3 VOC Measurements 42

2.3.1 Canister Preparation 42
a. AWAS Canisters 42
b. WAS Canisters 43
2.3.2 Analysis 44
a. Methane 44
b. Carbon Monoxide 44
c. Non-Methane Hydrocarbons 45
2.4 References 51

3. QUANTIFYING GASEOUS EMISSIONS IN THE COLORADO NORTHERN FRONT RANGE METROPOLITAN AREA…… 54
3.1 NFRMA Emissions 54
3.1.1 Oil and Natural Gas Source Signature 61
a. Methane 61
b. Non-Methane Hydrocarbons 65
3.1.2 Mass Balance Approach 69
3.2 Conclusion 80
3.3 References 81

4. EMISSION CHARACTERIZATION OF THE COLORADO WESTERN SLOPE…. 85
4.1 Previous Studies of the Piceance and Surrounding Basins 87
4.2 Results 89
4.2.1 Potential Ozone Formation from the Piceance and Uintah Basins 111
4.3 Conclusion 115
4.4 References 116

5. CHARACTERIZATION OF MOUNTAIN-VALLEY CIRCULATION EVENTS… 121
5.1 Ozone in the NFRMA 121
5.1.1 Surface Observations 121
5.1.2 Aircraft Observations 125
a. NASA P3-B 125
b. NSF/NCAR C-130 1-Hz Measurements 134
c. NSF/NCAR C-130 AWAS Measurements 143
5.2 Conclusion 155
5.3 References 156

APPENDIX…… 159

LIST OF FIGURES

		Page
Figure 1.1	Topographical map of Colorado. Overlaid is the NFRMA non-attainment area for O_3 (orange) and active oil and gas wells (red). Adapted from Pétron et al., 2012.	17
Figure 1.2	(top) Map of the known oil and natural gas reserves in the United States as of February 2014. (bottom) Map of the concentration of oil and natural gas wells per county in the United States, with the highest concentration in Kern County, CA with 122,512 wells, followed by Weld County, CO with 28,475 wells	21
Figure 1.3	Colorado energy production estimates for 2015. Adapted from EIA, 2017. https://www.eia.gov/state/?sid=CO#tabs-3	22
Figure 1.4	Diagram of mountain-valley circulation. Red arrows are incoming upslope events that bring air from the Denver-Julesburg Basin to the foothills of the Rocky Mountains. Red arrows show the air mass rising up the eastern side of the mountains. The purple arrows indicate prevailing westerly winds. The cyan arrow shows the recirculation pattern. Adapted from Sullivan et al., 2016.	23
Figure 2.1	(Top) Map of generalized flight plans and areas of research focus during the campaign. (Bottom) Actual flight paths for all 15 research flights during the FRAPPÉ campaign.	36
Figure 2.2	Left) Components of the *AWAS*. (Right) *AWAS* modules and pump in rack. (Atlas & UCAR/NCAR - Earth Observing Laboratory, 2009)	38
Figure 2.3	Location of AWAS samples collected onboard the C-130. Sample locations are colorized by research flight (RF) number and the number of samples collected (n) per flight is shown in the legend.	39
Figure 2.4	Map of the location of ground samples collected during FRAPPÉ.	41
Figure 2.5	DISCOVER-AQ flight pattern shown in red. The NASA P3-B performed spirals over surface sites while the NSF/NCAR C-130 flight paths covered the entire study area. Image courtesy of NASA https://www.nasa.gov/larc/2014-discoveraq-campaign/.	42
Figure 2.6	Schematic of GC system used for NMHC analysis.	46

Figure 3.1	Map of research flights 1, 2, and 3 colorized by methane (a, c, d) and ethane (b, d, f) concentration. Points are sized by altitude. Figures a, c, and d include a wind rose constructed using continuous 1-min averaged wind data collected by NOAA at the Platteville ground station (pink).	56
Figure 3.2	Wind roses from the C-130 flight 2 (a) and flight 3 (b) measured within the boundary layer and north of the Denver Metropolitan area. The size of the petal represents frequency (%) and are colorized by wind speed.	60
Figure 3.3	Flight tracks for flights 1 (a), 2 (b), and 3 (c), colorized by carbon monoxide concentration. Points are sized by altitude with smaller points indicating higher altitude.	60
Figure 3.4	Correlation plots of ethane to methane emission ratios from 1-Hz measurements collected during flights 1, 2, and 3 (top), and separated by upwind and downwind flight segments (bottom). Emission ratios (ER) are in units of ppbv/ppbv.	62
Figure 3.5	Correlation plot of propane to ethyne for all measurements from flights 1, 2, 3 (top) and separated by upwind and downwind transects (bottom).	67
Figure 3.6	Correlation plots of *i*-pentane versus *n*-pentane for all AWAS measurements collected onboard the C-130 during flights (top) and of the upwind (blue) versus downwind (red) transects (bottom). Also shown is the emission ratio for GWA unprocessed (green) and processed (cyan) natural gas. The black dotted line in both Figures is the 1:1 line.	68
Figure 3.7	A map of AWAS measurement locations, colorized by n-pentane concentration and sized by altitude, with smaller markers at higher altitude.	69
Figure 3.8	Map of flight path of P3-B flight (top) and vertical profiles over Fort Collins and Platteville (bottom). Flight paths are colorized by methane where dark blue is low methane concentrations and green to red is higher concentrations to highlight PBL height.	72
Figure 3.9	Wind roses displaying wind speed and direction frequencies from the NOAA Platteville ground station. Figures a, c, and e show average wind data from 8:00 pm to 6:00am local the evening prior to flights. Figures b, d, and f show average wind data during the research flights.	73

Figure3.10	Measured methane upwind (blue) and downwind (red) as a function of the distance perpendicular to wind direction for flight for flights 1 (a), 2 (b), and 3 (c). The dashed line is the average upwind CH_4 concentration.	74
Figure 3.11	Vertical profiles of methane (a), isoprene (b), water (c) and potential temperature (d) collected onboard the P3-B over Platteville at 12:00 local time on July 27th, 2014 used in determining boundary layer heights.	75
Figure 3.12	Vertical profile measured onboard the C-130 during research flight 1 (left), and 1-Hz sondes released from the Platteville ground site at 13:20:39 local, reduced to < 3km (initial release elevation: 1534 m ASL).	75
Figure 4.1	Oil and natural gas production in the Denver-Julesburg Basin (DJB) and the Piceance Basin with more than 85% of total natural gas production is concentrated in either Weld County in the DJB and Garfield County in the Piceance basin. Information courtesy of COGCC.	85
Figure 4.2	Map of Colorado counties colorized by natural gas production (top) and oil production (bottom) in 2014.The Piceance basin is highlighted in red, the DJB basin is highlighted in blue.	86
Figure 4.3	Map of the Denver-Julesburg, Piceance, Uintah, and Green River oil and natural gas basins. Adapted from Jaffe, 2012, courtesy of USGS and NOAA.	87
Figure 4.4	Map of research flights 8, 13, and 15 colorized by 1-Hz measurements of methane (a, c, e) and ethane (b, d, f), and AWAS ethane measurements (g). All points are sized by pressure altitude, with smaller symbols for higher altitudes.	90
Figure 4.5	Wind rose plots for flight 8 (left), 13 (middle), and 15 (right). Measurements of wind speed and direction were filtered to only include measurements collected west of -106 °W and below a pressure altitude of 4 km.	93
Figure 4.6	Time series plots of pressure altitude (black), methane (red), and ethane (blue) of research flights 08 (a), 13 (b), and 15 (c).	94
Figure 4.7	Time series plot of CH_4 (black), CO (blue), NO (purple), NO_2 (green), and SO_2 (orange) during flight 8 (a) and flight 13 (b) over the Uintah basin.	98

Figure 4.8	Correlation plot of methane to ethane for all measurements during flight 8 (fuchsia), flight 13 (cyan), and flight 15 (green).	101
Figure 4.9	Correlation plots of CH_4 and C_2H_6 over the Uintah (red) and Piceance (black) basins and the local background (blue) for research flights 8 (a), 13 (b), and 15 (c), with all data points shown in d.	102
Figure 4.10	Correlation plot of *i*-butane to *n*-butane over the Piceance (black) and Uintah (red) basins. The iC_4/nC_4 ratio of background measurements is shown in blue.	110
Figure 4.11	Correlation plot of *i*-pentane to *n*-pentane over the Piceance (black) and Uintah (red) basins. The iC_5/nC_5 ratio of background measurements is shown in blue.	110
Figure 4.12	Time series plot of NO (black) and O_3 (colorized by CH_4 concentration) during flight 08 over the Piceance and Uintah basins.	114
Figure 4.13	Total OH reactivity of NMHCs measured over the Piceance and Uintah basins, compared to local background, shown as percent of total reactivity (left) and total reactivity (right). Methane and biogenic reactivity is removed in c and d.	114
Figure 5.1	Time series plot of daily measured 8-hour ozone during the FRAPPÉ campaign. The top Figure shows data from all monitoring areas in Colorado. The bottom Figure shows only data collected in the NFRMA (Denver and Fort Collins). Open data points indicate non-flight days. Data courtesy of the CDPHE, available at https://www.colorado.gov/airquality/report.aspx.	123
Figure 5.2	48-hour time series plot, starting with Julian Day 214 (08/02/2014), of 1-min O_3 (a), 1-hour averages of O_3 (b), 1-min NO_2 in blue and 1-min $j(NO_2)$ in black (c), 1-min CH_4 (d), and 5-min averages of wind direction colorized by wind speed (e) from the ground site in Platteville, CO.	123
Figure 5.3	Vertical profiles of O_3 measured aboard the NASA P3-B on August 2nd, 2014 with a center bearing over Fort Collins starting at approximately 8:00 am (a), 10:30 am (b), and 1:40 pm (c), local time (UTC -6:00:00).	126

Figure 5.4	Vertical profiles of NO_2 measured aboard the NASA P3-B August 2nd, 2014 with a center bearing over Fort Collins starting at approximately 8:00 am (a), 10:30 am (b), and 1:40 pm (c), local time (UTC -6:00:00).	126
Figure 5.5	Vertical profiles of CH_4 measured aboard the NASA P3-B August 2nd, 2014 with a center bearing over Fort Collins starting at approximately 8:00 am (a), 10:30 am (b), and 1:40 pm (c), local time (UTC -6:00:00).	126
Figure 5.6	Vertical profiles of O_3 measured aboard the NASA P3-B August 3rd, 2014 with a center bearing over Fort Collins starting at approximately 8:00 am (a), 10:30 am (b), and 4:30 pm (c), local time (UTC -6:00:00).	127
Figure 5.7	Vertical profiles of NO_2 measured aboard the NASA P3-B August 3rd, 2014 with a center bearing over Fort Collins starting at approximately 8:00 am (a), 10:30 am (b), and 4:30 pm (c), local time (UTC -6:00:00).	127
Figure 5.8	Vertical profiles of CH_4 measured aboard the NASA P3-B August 3rd, 2014 with a center bearing over Fort Collins starting at approximately 8:00 am (a), 10:30 am (b), and 4:30 pm (c), local time (UTC -6:00:00).	127
Figure 5.9	Vertical profiles of H_2O measured in the afternoon aboard the NASA P3-B on August 2nd (a), and 3rd (b), 2014 with a center bearing over Fort Collins.	129
Figure 5.10	Vertical profiles of CO measured in the afternoon aboard the NASA P3-B on August 2nd (a), and 3rd (b), 2014 with a center bearing over Fort Collins.	129
Figure 5.11	72-hour 3-D kinematic back trajectory computed over Fort Collins spiral location starting at 08/02/2014 13:42:05 local time (top) and 08/03/2014 16:26:11 local time (bottom).	131
Figure 5.12	72-hour 3-D kinematic back trajectory computed over Denver spiral location starting at 08/03/2014 09:39:47 local time (top) and 08/03/2014 15:38:02 local time (bottom).	132
Figure 5.13	Map of research flights 6 (top) and 7 (bottom). Flight tracks are colorized by ozone concentration and sized by altitude above ground level, with smaller markers at higher altitude.	136

Figure 5.14	Map of research flights 6 (top) and 7 (bottom). Flight tracks are colorized by ozone concentration.	137
Figure 5.15	Map of research flights 6 (top) and 7 (bottom). Flight tracks are colorized by methane concentration and sized by altitude above ground level with smaller markers at higher altitude.	138
Figure 5.16	Correlation plot of C_2H_6 to CH_4 measured during research flights 6 (top) and 7 (bottom). Points are colorized by longitude and sized by altitude.	139
Figure 5.17	Averaged longitudinal and altitudinal flight legs from research flights 6 (top) and 7 (bottom) colorized by average wind direction and sized by average O_3 concentration. Overlaid is the latitudinal cross-section of the Rocky Mountains and eastern slope.	142
Figure 5.18	A map of AWAS measurement locations during research flights 6 (top) and 7 (bottom), colorized by averaged 1-Hz O_3 measurements and sized by altitude, with smaller markers at higher altitude.	147
Figure 5.19	Correlation plot of *i*-pentane to *n*-pentane showing all data points (top) and low concentration points (bottom). Solid data points are low altitude measurements, open data points indicate middle altitude measurements, and open data points with a dot indicate highest altitude measurements. The black dotted line is the 1:1 ratio line.	149
Figure 5.20	Correlation plot of ethyne to propane. Solid data points are low altitude measurements, open data points indicate middle altitude measurements, and open data points with a dot indicate highest altitude measurements.	152
Figure 5.21	Reaction pathway denoting the formation of alky nitrates, $RONO_2$.	153
Figure A.1	Vertical profiles of O_3 (a, b, c), CH_4 (d, e, f), and H_2O (g, h, i) measured aboard the NASA P3-B August 2nd, 2014 with a center bearing over Denver starting at 9:40 am (a, d, g), 12:00 pm (b, e, h), and 3:15 pm (c, f, i), local time (UTC -6:00:00).	158
Figure A.2	Vertical profiles of O_3 (a, b, c), CH_4 (d, e, f), and H_2O (g, h, i) measured aboard the NASA P3-B August 3rd, 2014 with a center bearing over Denver starting at 9:40 am (a, d, g), 12:00 pm (b, e, h), and 3:40 pm (c, f, i), local time (UTC -6:00:00).	159

Figure A.3	72-hour 3-D kinematic back trajectory computed over Fort Collins spiral location starting at 08/02/2014 08:03:44 local time as a function of latitude and longitude (top), and altitude and longitude (bottom).	160
Figure A.4	72-hour 3-D kinematic back trajectory computed over Fort Collins spiral location starting at 08/02/2014 10:30:01 local time as a function of latitude and longitude (top), and altitude and longitude (bottom).	161
Figure A.5	72-hour 3-D kinematic back trajectory computed over Fort Collins spiral location starting at 08/02/2014 13:42:05 local time as a function of latitude and longitude (top), and altitude and longitude (bottom).	162
Figure A.6	72-hour 3-D kinematic back trajectory computed over Fort Collins spiral location starting at 08/03/2014 08:07:35 local time as a function of latitude and longitude (top), and altitude and longitude (bottom).	163
Figure A.7	72-hour 3-D kinematic back trajectory computed over Fort Collins spiral location starting at 08/03/2014 10:25:16 local time as a function of latitude and longitude (top), and altitude and longitude (bottom).	164
Figure A.8	72-hour 3-D kinematic back trajectory computed over Fort Collins spiral location starting at 08/03/2014 14:05:39 local time as a function of latitude and longitude (top), and altitude and longitude (bottom).	165
Figure A.9	72-hour 3-D kinematic back trajectory computed over Fort Collins spiral location starting at 08/03/2014 16:26:11 local time as a function of latitude and longitude (top), and altitude and longitude (bottom).	166
Figure A.10	72-hour 3-D kinematic back trajectory computed over Denver spiral location starting at 08/02/2014 9:39:2 local time as a function of latitude and longitude (top), and altitude and longitude (bottom).	167
Figure A.11	72-hour 3-D kinematic back trajectory computed over Fort Collins spiral location starting at 08/02/2014 12:05:07 local time as a function of latitude and longitude (top), and altitude and longitude (bottom).	168

Figure A.12	72-hour 3-D kinematic back trajectory computed over Denver spiral location starting at 08/02/2014 15:15:10 local time as a function of latitude and longitude (top), and altitude and longitude (bottom).	169
Figure A.13	72-hour 3-D kinematic back trajectory computed over Denver spiral location starting at 08/03/2014 09:39:47 local time as a function of latitude and longitude (top), and altitude and longitude (bottom).	170
Figure A.14	72-hour 3-D kinematic back trajectory computed over Denver spiral location starting at 08/03/2014 11:58:13 local time as a function of latitude and longitude (top), and altitude and longitude (bottom).	171
Figure A.15	72-hour 3-D kinematic back trajectory computed over Denver spiral location starting at 08/03/2014 15:38:02 local time as a function of latitude and longitude (top), and altitude and longitude (bottom).	172
Figure A.16	Wind data (top panel) for each respective flight leg from research flight 6 and corresponding flight leg location (bottom panel).	173
Figure A.17	Wind data (top panel) for each respective flight leg from research flight 7 and corresponding flight leg location (bottom panel).	174

LIST OF TABLES

		Page
Table 1.1	Average global estimate of methane sources and sinks from 2000-2009. Adapted from Kirschke et al., 2013.	3
Table 1.2	Global tropospheric CO emission estimates in Tg(CO) yr^{-1}.	6
Table 1.3	2016 Emissions of US CO by source category (EPA, 2016b).	6
Table 1.4	Sources of global biogenic NMHC emissions. Adapted from Singh & Zimmerman, 1992; Guenther et al., 1995; Brasseur, Orlando, & Tyndall, 1999)	9
Table 1.5	Sources of global anthropogenic NMHC emissions. Adapted from Singh & Zimmerman, 1992; Guenther et al., 1995; Brasseur, Orlando, & Tyndall, 1999.	10
Table 1.6	Global sources of select NMHC species Adapted from Singh & Zimmerman, 1992; Guenther et al., 1995; Brasseur, Orlando, & Tyndall, 1999.	10
Table 1.7	2016 emissions of US NMHCs by source category (EPA, 2016b).	11
Table 1.8	Select NMHCs measured and their corresponding formulas, ▪OH reaction rate constant and estimated lifetime.	13
Table 1.9	Current NAAQS for gaseous criteria pollutants. Adapted from EPA, 2016c.	15
Table 2.1	Flight information for all research flights flown by the C-130 during FRAPPÉ.	37
Table 2.2	List of instruments onboard the NSF/NCAR C-130 and species analyzed for use in this dissertation.	40
Table 2.3	List of instruments onboard the NASA P3-B and species analyzed for use in this dissertation.	42
Table 2.4	Column information and GC parameters and temperature program information used during NMHC analysis.	47
Table 2.5	NMHCs measured during FRAPPÉ. Included is the limit of detection (LOD) and the precision and accuracy of each compound measured. Lifetimes were calculated assuming 295 K and 1 atm (Colman et al., 2001; Atkinson et al., 2006; Simpson et al., 2010).	48

Table 3.1	Statistics of trace gases measured during upwind and downwind transects during flights 1, 2, and 3. CO, CH_4, and C_2H_6 data were collected using 1-Hz measurements and are in units of ppbv. C_3 – C_6 hydrocarbons are from AWAS samples and in units of pptv, upwind n=13 (n_1=5, n_2=5, n_3=3) and downwind n=12 (n_1=4, n_2=5, n_3=3).	59
Table 3.2	Methane emission ratios measured upwind and downwind of the NFRMA. Also shown is the emission ratio from air free gas composition of unprocessed natural gas from the GWA and known emission ratios. The reported emission ratios for processed natural gas (Xcel Energy) is also shown. Units are ppbv/ppbv, written as percent.	63
Table 3.3	Summary of variables used in emission estimates during research flights 1, 2, and 3.	76
Table 3.4	Trace gas flux rates determined during flights 1, 2, and 3, and the total mean flux over all three flights. Also shown is is the averaged trace gas flux during just flights 1 and 3 and the 2012 VOC flux determined by Pétron et al., 2014. Units are $\times 10^3$ kg VOC hr^{-1}.	76
Table 4.1	Minimum (Min), maximum (Max), average (Avg), and standard deviation (StD) of 1-Hz measurements of CH_4, C_2H_6, CO, CO_2, NO, NO_2, SO_2 and O_3 measured over the Piceance (PB) and Uintah (UB) basins. Local background values are also included as well as maximum enhancements (Max Enh.: basin max/BKG) and average enhancements (Avg. Enh.: basin avg./BKG) of measurements collected over basins over background. Units of CH_4, C_6H_6, CO, CO_2, and O_3 are ppbv. Units of NO, NO_2, and SO_2 are pptv. <LOD=below limit of detection. Maximum and average enhancements greater than 10.00 over background averages are highlighted in bold.	95
Table 4.2	Statistics of AWAS measurements of select NMHCs measured over the Piceance (n=16) and Uintah (n=9) basins compared to local background (n=42) measurements. Units are in pptv, unless otherwise stated. Maximum (basin max/background) and average enhancements (basin avg/background) over background values greater than 10.00 are highlighted in bold.	96
Table 4.3	Comparison of select VOC to CH_4 emission ratios (ER) in the Piceance and Uintah basins, compared to background. Units are ppbv/ppbv, written as percent.	104

Table 4.4	Comparison of CH_4 emission ratios from the produced natural gas composition (Xcel Energy, WRAP) and VOC emissions measured from various ONG operations (Hilliard, 2016) in the Piceance Basin. Units are mol/mol, written as percent.	104
Table 4.5	Comparison of CH_4 emission ratios from the produced natural gas composition (WRAP) and surface VOC measurements (Helmig et al., 2014) in the Uintah Basin. All units are mol/mol, written as percent.	104
Table 4.6	Correlation matrix of select trace gases measured over the Piceance and Uintah basins. Correlations with R2 ≥0.70 are in bold. For the VOCs CO, CO_2, NO, NO_2, SO_2, O_3, methane, and ethane, 1 Hz measurements were used. For all other compounds, AWAS measurements were used. (C_2H_2=Ethyne; C_3=Propane; *n*C_4=*n*-Butane; *n*C_7=*n*-Heptane).	106
Table 4.7	Comparison with previous studies of *i*C_5/*n*C_5 emission ratios (ER) measured over the Piceance and Uintah basins.	111
Table 5.1	Correlations of C_2H_6 to CH_4 (C_2/C_1), written as percent, measured at each flight leg and compared to NFRMA and western slope emission ratios. Emission ratios statistically similar to NFRMA downwind ratios are highlighted in bold; R^2 values less than 0.70 are highlighted in italics.	140
Table 5.2	Average concentration of select trace gases measured during research flight 6 for each respective flight leg, arranged by longitude and altitude. Maximum values for each compound are highlighted in bold. Units are pptv unless otherwise specified.	145
Table 5.3	Average concentration of select trace gases measured during research flight 7 for each respective flight leg, arranged by longitude and altitude. Maximum values for each compound are highlighted in bold. Units are pptv unless otherwise specified.	146
Table 5.4	Correlations of *i*-pentane to *n*-pentane measured at each flight leg and compared to NFRMA and western slope emission ratios. Emission ratios statistically similar to NFRMA downwind ratios are highlighted in bold; R^2 values less than 0.70 are highlighted in italics.	150
Table 5.5	Average, minimum, and maximum air mass age calculated in hours for each flight leg during research flight 6. Flight leg ID corresponds to Figure A.17.	154

Table 5.6 Average, minimum, and maximum air mass age calculated in hours for each flight leg during research flight 7. Flight leg ID corresponds to Figure A.18. 154

LIST OF ABREVIATIONS

ACOM	Atmospheric Chemistry Observations and Modeling
AGL	Above Ground Level
ASL	Above Sea Level
AWAS	Advanced Whole Air Sampler
BAO	Boulder Atmospheric Observatory
CAMS	Compact Atmospheric Multispecies Spectrometer
CDPHE	Colorado Department of Public Health and Environment
CIMS	Chemical Ionization Mass Spectrometer
COGCC	Colorado Oil and Gas Conservation Commission
DACOM	Differential Absorption Carbon Monoxide Measurement
DISCOVER-AQ	Deriving Information on Surface Conditions from Column and Vertically Resolved Observations Relevant to Air Quality
DJB	Denver-Julesburg Basin
DLH	Diode Laser Hygrometer
ECD	Electron Capture Detector
ER	Emission Ratio
FID	Flame Ionization Detector
FRAPPÉ	Front Range Air Pollution and Photochemistry Experiment
GC	Gas Chromatograph
GHG	Greenhouse Gas
GWA	Greater Wattenberg Area
HAPs	Hazardous Air Pollutants
HySPLIT	Hybrid Single Particle Lagrangian Integrated Trajectory
INSTAAR	Institute of Arctic and Alpine Research
LOD	Limit of Detection
MSD	Mass Selective Detector
MVC	Mountain-Valley Circulation
NAAQS	National Ambient Air Quality Study
NCAR	National Center for Atmospheric Research
NFRMA	Northern Front Range Metropolitan Area
NMHC	Non-Methane Hydrocarbon
ONG	Oil and Natural Gas
PBL	Planetary Boundary Layer
PLOT	Porous Layer Open Tubular
PTR-Tof-MS	Proton Transfer Reaction Time of flight Mass Spectrometer
TCD	Thermal Conductivity Detector
VOC	Volatile Organic Compound
WMRS	White Mountain Research Station
WRAP	Western Regional Air Partnership

ACKNOWLEDGMENTS

First, I would like to thank my committee chair, Professor Donald Blake, for not only being a wonderful boss, but a great friend. I consider myself incredibly lucky to have had the opportunity to travel the world with someone like you, and sitting in your office with a PBR venting about teaching and research, and talking about life are some of my favorite memories of UCI.

I would also like to thank my committee members, Professor Barbara Finlyason-Pitts, whose success as a female scientist has been an inspiration to me, and reading about her work initially encouraged me to apply to UCI. And to Professor Sergey Nizkorodov, whose enthusiasm, sense of humor, and encouragement has made my time at UCI truly enjoyable.

In addition, a thank you to Professor Steven Wofsy and soon to be Professor Róisín Commane at Harvard University, for providing me with a space to write my thesis. Without them, I would surely have gone crazy.

I would like to express my gratitude to Professor Carol Babyak, for being an absolutely amazing mentor and guide throughout my academic carrier. And to Dr. Barkley Sive for motivating me to apply to grad school and his support throughout my time at Appalachian and UCI.

I would also like to thank the entire FRAPPÉ and DISCOVER-AQ teams for not only a successful campaign, but for providing an incredibly thorough data set.

A special thank you to everyone in the Rowland-Blake lab: Simone, my one and only lobster who taught me how to correctly spell all the countries of the world. Gloria, for being a beacon of positivity and joy in the lab, and an amazing friend. There is no one I would rather organize with! Brent, for his dedication to producing HQD, introducing everyone in the lab to GOT, and endless Seinfeld quotes. Barb, without you the lab would cease to function, but I am also eternally grateful for your ability to get things done! Without you, I would not have been able to complete my thesis. Nicola, for not only editing my thesis as I plugged along, but for being the main member of my "field family." I will always cherish our travels together. Jason, for not only collecting the data in this thesis, but for teaching me that thunder only happens when it's raining. Charlie, who taught me the joy of crosswords! Josette, my original office/dancing/hotel snuggles mate. Barbara, for putting up with Simone. And everyone else, thank you for making each day in lab a unique treat!

To my family, thank you for being supportive of me from the very beginning. A special thank you goes to my Mom, the best metiche I could ask for, and to my Dad, who always encouraged me to do what makes me happy. Thank you to my sisters, Steph, for helping me find chemistry, and Susan, my biggest cheerleader.

To the Oldenhuis clan, I couldn't have asked for better in-laws!

And finally, to my husband, best friend, and pod pea, Nathan, who pushed me, literally and figuratively, to work hard and accomplish my goals, and who provided the much-needed stress relief. Your hugs at the end of each day made the struggle doable.

CURRICULUM VITAE

Stacey C. Hughes
schughes@uci.edu

Education

University of California — Irvine, CA
Ph. D., Analytical Chemistry — 2012 - 2018
Advisor: Dr. Donald R. Blake

Appalachian State University — Boone, NC
B.Sc., Chemistry (ACS certified) and Environmental Chemistry — 2008 - 2012
Minor: Mathematics
Advisors: Dr. Carol Babyak, Dr. Barkley Sive

Awards

C.W. Ackerman Endowed Fellowship (Fund #7325)	2015 - 2017
NASA Group Achievement Award	2013, 2017
NASA Langley Peer Award	2013
NSF-REU Summer Fellowship	2011
Lake Junaluska Women Leadership Award	2011

Research Experience

Graduate Research Assistant – University of California, Irvine
Chemistry Department
Dr. Donald Blake, 2012 – 2018
Quantitative analysis of atmospheric trace gases during field campaigns.

- Investigating emissions in the Colorado Front range and their impact on local and regional air quality during the Front Range Air Pollution and Photochemistry Experiment (FRAPPÉ)
- Explored the effects of the North American Monsoon and deep convection on ozone production in the upper troposphere during the Studies of Emissions and Atmospheric Composition, Clouds, and Climate Coupling by Regional Surveys (SEAC^{4}RS).

Visiting Fellow – Harvard University
School of Engineering and Applied Sciences
Earth and Planetary Sciences
Dr. Steven Wofsy, 2017 – 2018

Undergraduate Research Assistant – Appalachian State University
Department of Chemistry
Environmental Science
Dr. Barkley Sive, 2011 – 2012

- Measurement of greenhouse gases (CO_2, CH_4, N_2O, SF_6) and the criteria pollutant CO in Boone, NC using gas chromatography.

Department of Chemistry
Dr. Carol Babyak, 2009 - 2012

- Developed a method relating trace metal concentration to magnetic susceptibility in river sediment samples impacted by a coal fly ash spill at the Kingston Fossil Plant.
- Studied the effect of bio-retention and pervious pavement on urban storm-water runoff analyzing phosphates, sulfates, metals, nitrates, and total dissolved solids.
- Investigated the impact of the papermill industry on the Pigeon River in Canton, NC by analyzing heavy metal concentrations in sediment and water samples.

Department of Biology
Dr. Chishimba Mowa, 2008 –2009

- Investigated the up regulation or down regulation of cervix proteins involved in cervical remodeling in mice using DNA microarray analysis.

Teaching Experience

Graduate Student Mentor
NASA Student Airborne Research Program (SARP) — JJA 2016, 2017

- Assisted under graduate student interns in Earth Science develop research projects analyzing data collected on board the NASA DC-8 in 2016 and the NASA C-23 Sherpa in 2017.

Graduate Teaching Assistant
University of California, Irvine

- Head TA General Chemistry A — Fall 2013, Fall 2016
- Head TA Prep General Chemistry — Fall 2015
- Head TA General Chemistry B — Winter 2015
- General Chemistry Lab 1LC Instructor — Spring 2013
- Honors General Chemistry TA — Winter 2013
- General Chemistry Lab 1LD Instructor — Fall 2012

Undergraduate Teaching Experience
Appalachian State University

- Quantitative Analysis Chemistry Lab TA — Fall 2011
- AppalSEED Academy Instructor, an enrichment program for minority high school students in North Carolina. — 2008-2010

Publications and Presentations

Kim, S., D. Jeong, D. Sanchez, M. Wang, R. Seco, **S. Hughes**, B. Barletta, D. Blake, J. Jung, D. Kim, G. Lee, M. Lee, J. Ahn, S. Lee, G. Cho, M. Sung, Y. Lee, D. Kim, Y. Kim, J. Woo, D. Jo, R. Park, J. Park, Y. Hong, J. Hong, *In review.* "The controlling factors of photochemical ozone production in Seoul, South Korea."

Kim, S., D. Sanchez, M. Wang, R. Seco, D. Jeong, **S. Hughes**, B. Barletta, D. Blake, J. Jung, D. Kim, G. Lee, M. Lee, J. Ahn, S. Lee, G. Cho, M. Sung, Y. Lee, D. Kim, Y. Kim, J. Woo, D. Jo, R. Park, J. Park, Y. Hong, J. Hong *(2016)*. "OH reactivity in urban and suburban regions in Seoul, South Korea – an East Asian megacity in a rapid transition." *Faraday Discussions.* **189**. 231-251.

Huber, D., **S. Hughes**, D. Blake. "Examining Dimethyl Sulfide Emissions in California's San Joaquin Valley." Abstract **B11E-1717** presented at 2017 Fall Meeting, AGU, New Orleans, LA, 11-15 Dec 2017.

Rund, P., **S. Hughes**, D. Blake. "Investigating elevated concentrations of hydrogen in the LAX Region." Abstract **A43G-2557** presented at 2017 Fall Meeting, AGU, New Orleans, LA, 11-15 Dec 2017.

Sive, B., A. Prenni, J. Cheatham, B. Schictel, J. Vimont, Y. Zhou, K. Benedict, A. Evanoski-Cole, E. Fischer, D. Day, S. Callahan, A. Sullivan, J. Collett, E. Apel, R. Hornbrook, **S. Hughes**, Y. Zhou, H. Mao. "Impacts of Oil & Natural Gas Operations and Urban Emissions on Air Quality in Rocky Mountain National Park during FRAPPÉ." National Environmental Monitoring Conference, August 9, 2017, Washington, D.C.

Sive, B., A. Prenni, J. Cheatham, B. Schictel, J. Vimont, Y. Zhou, K. Benedict, A. Evanoski-Cole, E. Fischer, D. Day, S. Callahan, A. Sullivan, J. Collett, E. Apel, R. Hornbrook, **S. Hughes**, Y. Zhou and H. Mao. "Impacts of Oil & Natural Gas Operations and Urban Emissions on Air Quality in Rocky Mountain National Park during FRAPPÉ." RMSS-AWMA, May 9, 2017, Lakewood, CO.

Sive, B. C., A. Prenni, J. Cheatham, B. Schictel, J. Vimont, Y. Zhou, K. Benedict, A. Evanoski-Cole, E. Fischer, D. Day, S. Callahan, A. Sullivan, J. Collett, E. Apel, R. Hornbrook, **S. Hughes**, Y. Zhou and H. Mao. "Ozone and VOC Distributions in Rocky Mountain National Park during FRAPPÉ: Key Insight into Factors Affecting Park Air Quality." FRAPPÉ/DISCOVER-AQ Science Team Meeting, May 2-3, 2017, Boulder, CO.

Hughes, S., S. Townsend-Small, J. Schroeder, N. Blake, T. Campos, A. Fried, D. Blake. "Quantifying methane emissions and sources in the Colorado Front Range." Abstract **H33I-1671** presented at 2016 Fall Meeting, AGU, San Francisco, CA, 12-16 Dec 2016.

Vann, K., **S. Hughes**, D. Blake. "Investigating methane emission sources in the San Joaquin Valley." Abstract **A31I-0169** presented at 2016 Fall Meeting, AGU, San Francisco, CA, 12-16 Dec 2016.

Black, J., **S. Hughes**, D.Blake. “Quantifying sulfur-containing compounds over the Santa Barbara Channel.” Abstract **A51F-0129** presented at 2016 Fall Meeting, AGU, San Francisco, CA, 12-16 Dec 2016.

Schaefer, C., **S. Hughes**, D. Blake. “Emissions from the Bena landfill.” Abstract **A21C-0065** presented at 2016 Fall Meeting, AGU, San Francisco, CA, 12-16 Dec 2016.

Jarnot, A., **S. Hughes**, D. Blake. “The atmosphere of Crystal Cave: Understanding sources and sinks of trace gases.” Abstract **A31C-0049** presented at 2016 Fall Meeting, AGU, San Francisco, CA, 12-16 Dec 2016.

Blake, N., I. Simpson, S. Meinardi, B. Barletta, J. Schroeder, **S.Hughes**, D. Blake, D. Apel, R. Hornbrook, T. Campos, L. Emmons, A. Townsend-Small, G. Diskin. “Atmospheric organic gases from fossil fuel extraction activities: analysis and modeling.” Abstract **A21A-0017** presented at 2015 Fall Meeting, AGU, San Francisco, CA, 14-18 Dec 2015.

Hughes, S., C. Babyak, E. Cowan, K. Seramur. “Investigation of Trace Metals and Magnetic Susceptibility in River Sediments Impacted by a Coal Fly Ash Spill." 2012 National Council on Undergraduate Research Meeting, Ogden, UT. 30 Mar 2012.

Hughes, S., C. Babyak, E. Cowan, K. Seramur. "Short and Long-Term Analysis of River Sediments Impacted by a Coal Fly Ash Spill." State of North Carolina Undergraduate Research and Creativity Symposium, SS Meeting, East Carolina University, Greenville, NC. 19 Nov 2011.

Hughes, S., **S. Hughes**, C. Mowa "VEGF Regulates Gene Expression of Matrix Factors During Cervical Remodeling in Rodents," Experimental Biology Conference, The American Physiological Society, New Orleans, LA. 18-22 Apr 2009.

Affiliations Member, American Geophysical Union (AGU)

Language Fluent in English and Spanish

ABSTRACT OF THE DISSERTATION

Characterization of Trace Gases During the Front Range Air Pollution and Photochemistry Experiment (FRAPPÉ) Field Campaign

By

Stacey Cristina Hughes

Doctor of Philosophy in Chemistry

University of California, Irvine, 2018

Professor Donald Blake, Chair

In recent years, hydrocarbon emissions from oil and natural gas (ONG) industries has been an area of extensive research in an effort to reduce air quality impacts from ONG fugitive emissions. In particular, the Northern Front Range Metropolitan Area (NFRMA) in Colorado, an area with extensive ONG infrastructure, has been designated as an area of ozone National Ambient Air Quality Standard (NAAQS) non-attainment area. There are various factors, from multiple pollution sources to the local meteorology, which exacerbate ozone pollution events in the NFRMA.

The Front Range Air Pollution and Photochemistry Experiment (FRAPPÉ) field campaign was designed to answer the scientific question: "*What are the factors controlling NFRMA surface ozone and are current emission controls sufficient to reduce ozone levels below the NAAQS?*" This campaign took place from 26 July – 17 August, 2014, and consisted of a network of ground and aircraft measurements. Flight plans and sampling were designed to

measure background conditions, source specific emissions, and meteorological effects by assessing local and regional photochemistry. The project aimed to create a comprehensive data set that will be used to elucidate the complex mechanisms that lead to enhanced ozone production.

Specifically, this work characterized emissions from the NFRMA and the Colorado western slope, and determined emissions from the ONG industry are the dominant source of hydrocarbons throughout the study area. Furthermore, from the examination of local meteorology events and spatial hydrocarbon distribution, it was determined that ozone pollution events in the NFRMA are a result of both local emissions and long-range transport.

In response to the posed question, despite strict emission controls in Colorado, emissions from the ONG industry are still pervasive throughout the research study area. To improve local air quality and achieve NAAQS ozone attainment, the effect of local meteorology needs to be strongly considered in future emission standards.

1. INTRODUCTION

1.1 Atmospheric Trace Gases

The chemistry of the earth's atmosphere has been studied over the years and has been found to contain nitrogen (78%), oxygen (21%), argon and carbon dioxide (less than 1%), varying amounts of water vapor, and trace gases (0.002%) (Hodgman, 1961). Within the last century, as air pollution began affecting cities and public health, atmospheric chemists began identifying trace gas species associated with poor air quality and their properties in order to understand their effects within the natural and polluted environment. At such a small percentage of the atmosphere, these trace gas species have a disproportionate effect on local and regional air quality and global climate change: they disturb the balance of terrestrial radiation in the atmosphere, play a major role in biogeochemical cycles, and are key in defining the oxidative capacity of the atmosphere (Finlayson-Pitts & Pitts, 2000; Seinfeld & Pandis, 2006; Brasseur, Orlando, & Tyndall, 1999). Therefore, it is imperative to characterize emission sources of these gases and their influence on atmospheric chemistry.

In recent years, climate change has been at the forefront of discussion in not only the sciences, but political discussions as well, focusing on the human contribution to climate change primarily through the increased emissions of radiatively active gases, including CO_2 and methane, into the atmosphere (Kiehl & Rasmussen, 1983; Ramanathan, 1985; Seinfeld & Pandis, 2006). Radiatively active gases are those which absorb or emit radiation at discrete wavelengths and can influence the radiation budget of the atmosphere (Ramanathan, 1985). Outgoing terrestrial infrared radiation is absorbed by radiatively active gases, more commonly referred to as greenhouse gases (GHGs), which inhibit thermal energy from escaping the atmosphere

(Finlayson-Pitts & Pitts, 2000; Forster et al., 2008). This phenomenon, termed the "greenhouse effect," has become a major concern because of the correlation between increasing global temperatures and increases in anthropogenic emissions of GHGs into the atmosphere.

As energy demands have increased, fossil fuel consumption has increased, and subsequently the emission of volatile organic compounds (VOCs) which have altered the atmospheres radiative balance. These trace gases can also photochemically oxidize in the presence of sunlight and nitrogen oxides ($NO_X = NO + NO_2$) to form tropospheric ozone (O_3) (Finlayson-Pitts & Pitts, 2000). Ozone, a constituent of smog, at high concentrations has been associated with adverse health effects and, therefore, emissions of ozone precursors have been heavily controlled. Federal laws such as the Clean Air Act (1970) were put into place to reduce emissions and National Ambient Air Quality Standards (NAAQS) were established to protect the public (EPA, 2017a).

Despite efforts to reduce emissions, NAAQS non-attainment areas are pervasive in the United States. This work aims to define the cause of poor air quality in the Colorado Front Range by examining emissions of trace gases within the state and the role the unique meteorology of the area plays in compounding trace gas concentrations. Discussed below are the species analyzed by this work and their contribution to atmospheric chemistry.

1.1.1 Methane

Methane, CH_4, is 34 times more effective as a greenhouse gas when compared to carbon dioxide on a 100-year timescale (Hartmann et al., 2013). It is also the second most abundant carbon containing compound in the atmosphere, after carbon dioxide, and the second largest contributor to positive radiative forcing (Forster et al., 2008; EPA, 2016a). A large fraction of CH_4 is produced from natural processes such as anaerobic decomposition in wetland

environments, and microbial activity in cattle and termites (Brasseur, Orlando, & Tyndall, 1999; Kirschke et al., 2013). Global methane concentrations have increased from 700 ppbv in pre-industrial times to 1842 ppbv in 2017, primarily as the result of increased fossil fuel use (Dlugokencky, 2017). Currently, it is estimated that human activities account for 49% of global methane emissions, with 29% of anthropogenic emissions attributed to fossil fuels (Kirschke et al., 2013), as shown in Table 1.1.

Table 1.1 Average global estimate of methane sources and sinks from 2000-2009. Adapted from Kirschke et al., 2013.

	Tg CH_4 yr^{-1}	**Range**
Natural sources	**347**	**238 - 484**
wetlands	217	177 - 284
fresh water (lakes and rivers)	40	8 - 73
wild animals	15	15
wildfires	3	1 - 5
termites	11	2 - 22
geological (includes oceans)	54	33 - 75
hydrates	6	2 - 9
permafrost	1	0 - 1
Anthropogenic Sources	**331**	**304 - 368**
agriculture and waste	200	187 - 224
biomass burning	35	32 - 39
fossil fuels	96	85 - 105
Sinks	**632**	**592 - 785**
soils	28	9 - 47
tropospheric OH	528	454 - 617
stratospheric loss	51	16 - 84
tropospheric Cl	25	13 - 37

With a relatively long lifetime of 9 to 12 years, compared to other hydrocarbons (hours to days (Table 1.8), CH_4 is prevalent in the atmosphere at high concentrations and exhibits a more uniform vertical distribution (Vaghjiani & Ravishankara, 1991). Methane's long lifetime is dependent on the reaction with the hydroxyl radical, ·OH, informally referred to as the "detergent of the atmosphere" (Graedel & Crutzen, 1989). The hydroxyl radical is formed when ozone

photolyzes to produce molecular oxygen and an excited oxygen, O(^{1}D). The excited oxygen then reacts with water to form OH, reactions 1.1 and 1.2 (DeMore & Raper, 1966; Parasevopoulos & Cvetanovic, 1971; Vaghjiani & Ravishankara, 1991; Finlayson-Pitts & Pitts, 2000).

$$O_3 + h\nu\ (\lambda < 310\ nm) \rightarrow O_2 + O(^1D) \quad (1.1)$$

$$O(^1D) + H_2O \rightarrow 2 \cdot OH \quad (1.2)$$

The reaction for the oxidation of CH_4 by ·OH is shown in reaction 1.3 is the major sink for methane (Levy II, 1971; Atkinson, 2000; Finlayson-Pitts & Pitts, 2000).

$$CH_4 + \cdot OH \rightarrow \cdot CH_3 + H_2O \quad (1.3)$$

The methyl radical formed in reaction 1.3 can react with an oxygen molecule to form a methyl peroxy radical (Heicklen, 1968; Finlayson-Pitts & Pitts, 2000).

$$\cdot CH_3 + O_2 + M \rightarrow CH_3OO \cdot + M \quad (1.4)$$

Combustion in motor vehicles is the main source of NO_X in the atmosphere (Haagen-Smit, 1952; Calvert, 1976). In a polluted environment, such as an urban center, the peroxy radical, CH_3O_2, can react with NO_X to form ozone (Blacet, 1952; Heicklen, 1968; Nicolet, 1970; Atkinson, 2000; Finlayson-Pitts & Pitts, 2000).

$$CH_3OO \cdot + NO \rightarrow CH_3O \cdot + NO_2 \quad (1.5)$$

$$CH_3O \cdot + O_2 \rightarrow HCHO + HO_2 \quad (1.6)$$

$$HO_2 + NO \rightarrow OH + NO_2 \quad (1.7a)$$

$$NO_2 + h\upsilon \rightarrow NO + O(^3P) \quad (1.7b)$$

$$O_2 + O(^3P) + M \rightarrow O_3 + M \quad (1.8)$$

In non-polluted environments, in the absence of NO_X, the peroxy radical, $CH_3OO\cdot$ can react via three different pathways to form a hydroperoxide, an alkoxy radical, or formaldehyde

and methanol, shown below in reactions 1.9-1.11 (Heicklen, 1968; Atkinson et al., 1995; Finlayson-Pitts & Pitts, 2000).

$$CH_3OO\cdot + HO_2 \rightarrow CH_3OOH + O_2 \quad (1.9)$$

$$2\ CH_3OO\cdot \rightarrow 2\ CH_3O\cdot + O_2 \quad (1.10)$$

$$2\ CH_3OO\cdot \rightarrow HCHO + CH_3OH + O_2 \quad (1.11)$$

Formaldehyde, HCHO, an oxidation product formed in reaction 1.6 and 1.11 can either photolyze or react with OH via three possible reaction mechanisms shown in reaction 1.12 (Calvert & Pitts, 1966; Finlayson-Pitts & Pitts, 2000).

$$HCHO + h\nu \rightarrow H + HCO\cdot \quad (1.12a)$$

$$HCHO + h\nu \rightarrow H_2 + CO \quad (1.12b)$$

$$HCHO + OH \rightarrow HCO\cdot + H_2O \quad (1.12c)$$

The formyl radical, HCO, can then react with O_2 to form carbon monoxide, CO, and the hydroperoxyl radical, HO_2 (McMillan & Calvert, 1965; Finlayson-Pitts & Pitts, 2000).

$$HCO\cdot + O_2 \rightarrow CO + HO_2 \quad (1.13)$$

In conclusion, the oxidation of methane leads to the formation of carbon monoxide and ozone. A net reaction is shown in reaction 1.14 (Seinfeld & Pandis, 2006).

$$CH_4 + 8O_2 + h\nu \rightarrow 2\cdot OH + H_2O + CO + 4O_3 \quad (1.14)$$

1.1.2 Carbon Monoxide

Carbon monoxide, CO, has a shorter lifetime than CH_4 (1-2 months) and is spatially variable (Fishman & Seiler, 1983). As shown above, methane and other hydrocarbon oxidation is a major source of CO in the atmosphere, and accounts for roughly 44% of total global CO budget (Finlayson-Pitts & Pitts, 2000; Holloway & Kasibhatla, 2000; Seinfeld & Pandis, 2006). Nearly half of total global CO emissions, 42%, can be attributed to anthropogenic sources such as

incomplete combustion of fossil fuels and biomass burning (Holloway & Kasibhatla, 2000). Natural sources of CO include biological processes in soils, and the ocean (Finlayson-Pitts & Pitts, 2000; Holloway & Kasibhatla, 2000). Table 1.2 shows estimated global CO emissions. Table 1.3 shows estimated anthropogenic emissions of CO by source category in the U.S.

Table 1.2 Global tropospheric CO emission estimates in Tg(CO) yr^{-1}.

	Holloway and Kasibhatla, 2000	IPCC, 1996	IPCC, 2001
Oxidation Sources (indirect)			
methane	760	400-1000	800
isoprene		200-600	270
industrial NMHC			110
biomass NMHC	683[a]		30
acetone			20
Direct Emissions			
vegetation		60-160	150
oceans		20-200	50
biomass burning	748	300-700	700
fossil & domestic fuel	300	300-550	650
Total Sources	2491	1800-2700	2780

[a] Includes all biogenic NMHC oxidation sources (isoprene, monoterpenes, etc.)

Table 1.3 2016 Emissions of US CO by source category (EPA, 2016b).

	Emissions, *Tg(CO)*
Fuel combustion	
Electric, Utility	0.65
Industrial	0.87
Other	2.22
Chemical & Allied Product MFG	0.12
Metals Processing	0.55
Petroleum and related industries	0.78
Other industrial processes	0.55
Solvent utilization	0.001
Storage and Transport	0.01
Waste disposal & recycling	1.96
Highway vehicles	16.21
Off-highway vehicles	11.78
Wildfires	9.37
Miscellaneous	8.43
Total	**53.51**

The primary sink of CO is the reaction with OH (reaction 1.15) and accounts for a loss of 1920 Tg(CO) yr^{-1}, with surface deposition, the secondary sink, at a loss rate of 190 Tg(CO) yr^{-1} (Hauglustaine et al., 1998; Holloway & Kasibhatla, 2000). Carbon monoxide is a key criteria pollutant and indirectly influences the lifetimes of other gases by reacting with OH. Because of this reaction, if CO concentrations increase, OH concentrations may decrease (IPCC, 2001). For example, it was estimated that CO emissions from wildfires in Indonesia in 1997 reduced global OH concentrations by 6% (Duncan et al., 2003).

$$CO + \cdot OH \rightarrow CO_2 + H \tag{1.15}$$

The reaction of CO with ·OH produces a hydrogen atom which can combine with molecular oxygen to form a hydroperoxyl radical, reaction 1.16. This radical can then self-react to form hydrogen peroxide, reaction 1.17 (Kaufman, 1969; Seinfeld & Pandis, 2006)

$$H + O_2 + M \rightarrow HO_2 + M \tag{1.16}$$

$$2HO_2 \rightarrow H_2O_2 + O_2 \tag{1.17}$$

Hydrogen peroxide can then either photolyze or oxidize to form HO_X (·OH + HO_2) (Schumb, Satterfield, & Wentworth, 1955; Seinfeld & Pandis, 2006).

$$H_2O_2 + h\nu \rightarrow 2 \cdot OH \tag{1.18}$$

$$H_2O_2 + \cdot OH \rightarrow HO_2 + H_2O \tag{1.19}$$

As mentioned above, in a polluted environment, when NO_X is present, the peroxyl radical formed in reaction 1.16 can react with NO to form NO_2 and ·OH, reaction 1.7a. NO_2 can then photolyze to form O_3, reactions 1.7b and 1.7c (Seinfeld & Pandis, 2006). This leads to a net reaction of:

$$CO + 2O_2 + h\nu \rightarrow CO_2 + O_3 \tag{1.20}$$

This reaction can only occur when elevated NO_X levels impede the hydroperoxyl radical from self-reacting (reaction 1.17). However, if NO_X levels are elevated, this leads to a termination of the NO_X cycle, reactions 1.7, to form nitric acid, HNO_3, reaction 1.21, thus removing NO_X and HO_X. Therefore, reaction 1.20 is mostly a theoretical limit (Johnston, 1970; Seinfeld & Pandis, 2006).

$$NO_2 + \cdot OH + M \rightarrow HNO_3 + M \quad (1.21)$$

1.1.3 Non-Methane Hydrocarbons

Non-methane hydrocarbons (NMHCs) are VOCs that contain both hydrogen and carbon; methane is not included here as the concentration of CH_4 in the atmosphere is significantly greater than that of NMHCs and is much less reactive. If included, CH_4 would misrepresent this diverse category of trace gases (Finlayson-Pitts & Pitts, 2000; Seinfeld & Pandis, 2006). NMHCs can be categorized into either anthropogenic or biogenic sourced compounds. While biogenic sources of NMHCS have remained relatively constant, as energy demands and populations increase, anthropogenic NMHC emissions have increased (Finlayson-Pitts & Pitts, 2000). Many of these compounds are highly reactive and can form tropospheric ozone via the same mechanisms described above, and thus impact the oxidative capacity of the troposphere (Calvert J. G., 1976; Brasseur, Orlando, & Tyndall, 1999). Their unique characteristics and varied spatial and temporal distribution can be used to define emission sources in a mixed air mass and are a definitive tool used in pollution mitigation strategies.

a. Biogenic Non-Methane Hydrocarbons

More than 50% of total U.S., and roughly 90% of total global NMHC emissions are biogenic (Seinfeld & Pandis, 2016). The most common biogenic sources are plant respiration processes (photosynthesis and photorespiration), microbial production, and marine sources, with

emissions from vegetation accounting for 99% of total biogenic NMHC emissions (Guenther et al., 1995; Seinfeld & Pandis, 2006). Terpenoids such as isoprene and α/β-pinene are common terrestrial sourced compounds that are emitted by deciduous trees, plants, and shrubs, with isoprene dominating global emissions. Terpenoids are the most common biogenic trace gas even though sulfur containing and nitrogen containing compounds, and several alkanes and alkenes, are known to be emitted by vegetation, but are generally emitted at much lower rates compared to terpenoids (Guenther et al., 2000). It is important to note that all terrestrial emission rates are highly variable and are greatly dependent on temperature, water availability, nitrogen levels, insects/disease and various other stresses as shown by Guenther (2002). Because of these not fully understood drivers of vegetation emissions, most global emission rates rely heavily on models. It is estimated that the average flux of NMHCs is 7 g C m^{-2}, with a great deal of uncertainty, ranging from less than 0.1 to greater than 100 g C m^{-2} (Guenther, 2002). Table 1.4 shows average global biogenic trace gas emission sources

Table 1.4 Sources of global biogenic NMHC emissions. Adapted from Singh & Zimmerman, 1992; Guenther et al., 1995; Brasseur, Orlando, & Tyndall, 1999)

	Emissions, TgC yr^{-1}
Oceanic	
Light hydrocarbons	5-10
C_9-C_{28} *n*-alkanes	1-26
Terrestrial	
Microbial production	6
Emissions from vegetation	
Isoprene	500
Monoterpenes	125
Other	520*
Total emissions	**1170**

*Uncertain

b. Anthropogenic Non-Methane Hydrocarbons

Anthropogenic point sources of NMHCs are based in energy consumption and transportation (Watson, Chow, & Fujita, 2001). Several NMHCs have been identified by the United States Environmental Protection Agency (EPA) as hazardous air pollutants (HAPs) as they are known or expected carcinogens, such as benzene, toluene, hexane, and tetrachloroethylene, to name a few (EPA, 2017b). This and their potential to form ground level ozone make it essential to define and quantify emissions of these gases. Emission estimates of global anthropogenic NMHCs are shown in Table 1.5 and for individual species in Table 1.6.

Table 1.5 Sources of global anthropogenic NMHC emissions. Adapted from Singh & Zimmerman, 1992; Guenther et al., 1995; Brasseur, Orlando, & Tyndall, 1999.

	Emissions, *TgC yr^{-1}*
Transportation	22
Stationary source fuel combustion	4
Industrial (Including oil and natural gas production)	17
Biomass burning	45
Organic Solvents	15
Total	**103**

Table 1.6 Global sources of select NMHC species. Adapted from Singh & Zimmerman, 1992; Guenther et al., 1995; Brasseur, Orlando, & Tyndall, 1999.

Compound	**Emission, *TgC yr^{-1}***	**Major Source**
ethane	10 – 15	ONG, biomass burning, oceans, vegetation emissions
ethene	20 – 45	fuel combustion, biomass burning, terrestrial ecosystems
ethyne	3 – 6	fuel combustion, biomass burning
propane	15 – 20	ONG, biomass burning, oceans, vegetation emissions
propene	7 – 12	fuel combustion, biomass burning, oceans
butanes	2 – 4	fuel combustion, ONG, biomass burning, oceans
butenes	2 – 3	fuel combustion, biomass burning, oceans
pentanes	3 – 5	fuel combustion, ONG, biomass burning
benzene	4 – 5	fuel combustion, biomass burning
toluene	4 – 5	fuel combustion, biomass burning, solvents
xylenes	2 – 3	fuel combustion, biomass burning, solvents
isoprene	500	forest/plant emissions
monoterpenes	125	forest/plant emissions

In 2010, it was estimated that anthropogenic emissions of C_2-C_5 alkanes and higher alkanes add 46 Tg yr^{-1} and 47 Tg yr^{-1}, respectively, to the global NMHC budget (Pozzer et al., 2010). Unlike biogenic emissions, anthropogenic emissions are not as susceptible to seasonal change as there is a constant release from fossil fuel combustion and production (Leuchner et al., 2015). In the United States, petroleum and related industries, including storage and transport, accounted for 25% of total anthropogenic NMHC emissions, with fossil fuel combustion in vehicles and industry accounting for an additional 25% (EPA, 2016b), with an average annual increase of 1.2 (± 0.8) Tg yr^{-1} (Helmig et al., 2016). Table 1.7 shows all of US anthropogenic NMHC emissions for 2016.

Table 1.7 2016 emissions of US NMHCs by source category **(EPA, 2016b)**

	Emissions, *Tg*
Fuel combustion	
Electric, Utility	0.03
Industrial	0.10
Other	0.35
Chemical & Allied Product MFG	0.07
Metals Processing	0.03
Petroleum and related industries	2.92
Other industrial processes	0.32
Solvent utilization	2.67
Storage and Transport	0.62
Waste disposal & recycling	0.18
Highway vehicles	1.60
Off-highway vehicles	1.43
Wildfires	2.20
Miscellaneous	1.87
Total	**14.39**

c. Chemistry of Non-Methane Hydrocarbons

Like methane, NMHC chemistry is often initiated by the reaction with ·OH, forming an alkyl radical, R· and water, reaction 1.22 (Finlayson-Pitts & Pitts, 2000).

$$RH + \cdot OH \rightarrow \cdot R + H_2O \quad (1.22)$$

This radical can then react with molecular oxygen to form an alkyl peroxy radical, RO_2, just as in reaction 1.4. In the presence of NO_X, the alkyl peroxy radical can react via 3 mechanisms (Seinfeld & Pandis, 2006).

$$ROO\cdot + NO \rightarrow RO\cdot + NO_2 \quad (1.23a)$$

$$\rightarrow RONO_2 \quad (1.23b)$$

$$ROO\cdot + NO_2 + M \rightleftharpoons ROONO_2 + M \quad (1.24)$$

Here, the formation of the alkoxy radical, RO·, is the dominant reaction and can add to the NO_X cycle described above and form ozone (Finlayson-Pitts & Pitts, 2000; Seinfeld & Pandis, 2006). Reaction 1.23b shows the formation of alkyl nitrates, $RONO_2$. The relationship between the initial hydrocarbon and the resulting alkyl nitrate has been used extensively to study polluted air masses as the reaction rate at which the alkyl nitrate forms can be used to determine the photochemical age of an air mass (Bertman et al., 1995; Simpson et al., 2006; Perring et al., 2010). The only known natural source of alkyl nitrates is in the aqueous phase in oceans from the reaction of $ROO\cdot$ and NO (Dahl et al., 2003; Chuck et al., 2002). It is important to note that the formation of alkyl nitrates will terminate the NO_X cycle by removing NO from the system. Alkyl nitrates have relatively long atmospheric lifetimes (1-4 weeks) and when formed can be transported long distances. Acting as a reservoir for NO_X, long range transport can bring NO_X to rural environments and alter regional chemistry through the following reactions (Schultz et al., 1999; Talukdar et al., 1997; Turberg et al., 1990).

$$RONO_2 + h\nu\ (\lambda < 340nm) \rightarrow RHO + HONO \quad (1.25a)$$

$$\rightarrow RO\cdot + NO_2 \quad (1.25b)$$

$$\rightarrow RHO + NO + \cdot OH \quad (1.25c)$$

Reaction with ·OH is the dominant sink for most hydrocarbons. The reaction rate constant, k_{OH}, determines their atmospheric lifetime and can be used as a proxy to estimate ozone formation potential (Carter & Atkinson, 1989), shown in Table 1.8.

Table 1.8 Select NMHCs measured and their corresponding formulas, ·OH reaction rate constant and estimated lifetime.

Compound	**Formula**	**k_{OH}, $\times 10^{-12}$ cm^3 $molecule^{-1}$ s^{-1}**	**Lifetime***
Ethane	C_2H_6	0.2	47 days
Ethene	C_2H_4	8.5	1.4 days
Ethyne	C_2H_2	0.9	12-17 days
Propane	C_3H_8	1.1	11 days
Propene	C_3H_6	26.3	11 hrs
n-butane	C_4H_{10}	2.4	4.9 days
i-butane	C_4H_{10}	2.2	5.5 days
n-pentane	C_5H_{12}	4.0	5 days
i-pentane	C_5H_{12}	3.6	5 days
Isoprene	C_5H_8	100.0	2.8 hrs
Benzene	C_6H_6	1.2	9.5 days
2,2-Dimethylbutane	C_6H_{14}	2.2	2 days
2,3-Dimethylbutane	C_6H_{14}	5.8	2 days
Cyclohexane	C_6H_{12}	7.2	1.7 days
n-Hexane	C_6H_{14}	5.2	2.2 days
2-Methylpentane	C_6H_{14}	5.2	2.2 days
3-Methylpentane	C_6H_{14}	5.2	2.2 days
Toluene	C_7H_8	5.6	1.9 days
Methylcylohexane	C_7H_{14}	10.0	1.3 days
n-Heptane	C_7H_{16}	6.8	1.7 days
n-Octane	C_8H_{18}	8.7	1.3 days
Ethylbenzene	C_8H_{10}	7.1	1.7 days
m+*p*-Xylene	C_8H_{10}	23.6, 14.3	12-20 hrs
o-Xylene	C_8H_{10}	13.7	20 hrs
2-Ethyltoluene	C_9H_{12}	11.9	1 day
3-Ethyltoluene	C_9H_{12}	19.2	15 hrs
4-Ethyltoluene	C_9H_{12}	12.1	1 day
1,3,5-Trimethylbenzene	C_9H_{12}	56.7	4.9 hrs
1,2,4-Trimethylbenzene	C_9H_{12}	32.5	8.5 hrs
1,2,3-Trimethylbenzene	C_9H_{12}	32.7	8.5 hrs
α-Pinene	$C_{10}H_{16}$	52.3	5.3 hrs
β-Pinene	$C_{10}H_{16}$	74.3	3.7 hrs

* Estimated lifetimes calculated assuming a 12-hour daytime average ·OH concentration of 2×10^6 molecules cm^{-3} at 298 K. Kinetic data is from Atkinson et al., 2006.

1.1.4 Tropospheric Ozone

The formation of tropospheric O_3 has a profound impact on the oxidative capacity of the troposphere while substantially influencing chemistry and contributing to the global greenhouse effect (Fishman & Seiler, 1983; Wang et al., 1988). The fact that photochemically produced O_3 from urban sources could impact tropospheric concentrations was not documented until the 70's as it was originally thought that the primary source of O_3 in the troposphere was from stratospheric injections (Crutzen, 1973; Chameides & Walker, 1973). Today we know that approximately 10% of tropospheric O_3 is from stratospheric injections, and the remainder is a product of photochemistry (IPCC, 2013). This production of tropospheric O_3 is driven by the photochemical oxidation of CO, CH_4 and NMHCs by $\cdot OH$ in the presence of NO_X (Finlayson-Pitts & Pitts, 2000). The net reaction for O_3 formation is shown in reaction 1.26. It is important to note that the resulting carbonyl can oxidize to form additional O_3. Despite the importance and impact that these O_3 precursors have on atmospheric chemistry, the O_3 budget and global O_3 distribution are not well established in part due to uncertainties in modeling and transport of O_3 precursors (National Resource Council, 2010).

$$RH + 4O_2 + h\nu \rightarrow R'CHO + H_2O + 2O_3 \qquad (1.26)$$

Tropospheric O_3 is a strong oxidant and can be especially harmful to humans and vegetation (Forster et al., 2008). It has been shown that increased ozone exposure leads to increased mortality rates. Even short-term exposure has been shown to increase hospital admissions. In a study by Bell et al., 2004, an average increase of 10 ppbv O_3 from the week prior increased daily mortality rates by 0.52% in urban communities within the United States. This study indicated that even small changes in O_3 concentrations can impact public health. These statistics are especially true for the elderly and those with cardiovascular and/or

respiratory conditions. Though O_3 is generally concentrated in urban areas, it has been shown that long range transport can affect rural areas, damage vegetation, and decrease crop yields (Benton et al., 2000; Simpson et al., 2007; Sharma et al., 2017).

a. Air Quality Legislation

In 1955, the very first piece of legislation that addressed air pollution and its effect on public health was established, the Air Pollution Control Act (EPA, 2017c). This act was established to investigate the prevention of air pollution but did little to ameliorate it. The Clean Air Act of 1963 and its subsequent amendments led to the formation of the Environmental Protection Agency (EPA) which developed national ambient air quality standards, NAAQS, and the classification of primary and secondary standards were established (EPA, 2017a). Primary standards were made to first protect public health, with emphasis on protecting populations sensitive to poor air quality such as the elderly and people with respiratory ailments, by creating a margin of safety to reduce risks to public health. Secondary standards were established to protect the public from criteria pollutants, (EPA, 2017a). Several compounds were listed as criteria pollutants such as CO, NO_2, O_3, particulate matter, sulfur dioxide, and lead. These criteria pollutants were singled out as they are directly associated with adverse health effects. This led to regulations regarding these pollutants and specifically for short (hours to days) and long-term exposure (months to years) (EPA, 2016c).

Table 1.9 Current NAAQS for gaseous criteria pollutants. Adapted from EPA, 2016c.

CO	**NO_2**	**O_3**	**SO_2**
8 hour: 9 ppm	1 hour: 100 ppb	8 hour: 70 ppb	1 hour: 75 ppb
1 hour: 35 ppm	1 year: 53 ppb		3 hour: 500 ppb

In Colorado, the Northern Front Range Metropolitan Area (NFRMA) was first designated as a non-attainment area in 2004 (EPA, 2017d; CDPHE, 2017). Throughout the years there has

been a great number of polices enacted to reach attainment status. In 2013, the NFRMA was still not in attainment and therefore adopted regulations to reduce emissions from oil and natural gas production, aiming to reduce VOC and NO_X emissions by 93,000 tons per year and 35,000 tons per year, respectively, by 2018. Currently, Colorado classifies attainment using the 2008 8-hour standard of 75 ppb ozone. For this reason, the air quality in the NFRMA is designated as "moderate." However, in 2018 when the standard is officially reduced in Colorado to 70 ppb, it is expected to be designated "serious" (CDPHE, 2017). With the oil and natural gas industry pervasive in this area, defining the influence this source of ozone precursors has on the NFRMA is vital in assessing and improving the air quality.

1.2 Oil and Natural Gas

As mentioned above, oil and natural gas emissions have a profound impact on local and regional air quality. Here we will discuss the formation, composition, and infrastructure of the oil and natural gas sector that leads to VOC emissions.

1.2.1 Formation, Composition, and Location of Oil and Natural Gas in Colorado

Oil and natural gas are formed when organic matter is exposed to high temperatures and pressures deep beneath the earth's surface (Berger & Anderson, 1992). In the NFRMA, this process began roughly 70 million years ago. The ONG that formed migrated towards the surface via fissures to reservoir rocks such as sandstone (Weimer, Sonnenberg, & Young, 1986; Matuszczak, 1976). An impermeable cap rock above the reservoir allows ONG to accumulate over time and form large basins such as the Denver-Julesburg Basin (COGCC, 2007). Oil is more dense than natural gas and is a mix of NMHCs. Natural gas, which consists of mostly methane and $C_2 – C_5$ alkanes, separates from the oil during upward movement into reservoir rocks and pools into gas fields such as the Greater Wattenberg Area (GWA), a natural gas pool

within the Denver-Julesburg Basin designated by the Colorado Oil and Gas Conservation Commission (COGCC) for regulation purposes (Berger & Anderson, 1992; COGCC, 2007). Unprocessed natural gas in the GWA is approximately 78% methane, 12% ethane, 5% propane, 2% butanes, 0.6% pentanes, and 0.3% C_{6+} alkanes/alkenes (COGCC, 2007).

The Denver-Julesburg Basin extends from the Wyoming border in Colorado to just north of the New Mexico border and contains the GWA (Nelson & Santus, 2011). During the 1970s, fossil fuel exploration and drilling in Colorado was concentrated in the GWA. There are nearly 46,000 active wells in Colorado with more than half located in the GWA (EIA, 2017). Figure 1.1 is a map of Colorado and shows the oil and gas wells within the state and the density of active wells in the GWA.

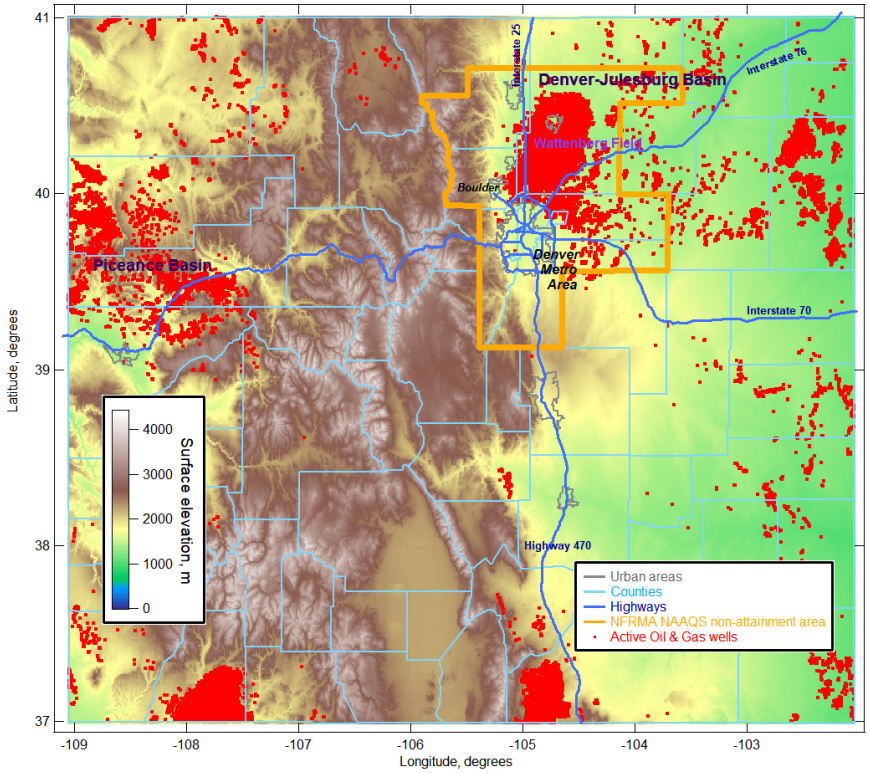

Figure 1.1 Topographical map of Colorado. Overlaid is the NFRMA non-attainment area for O_3 (orange) and active oil and gas wells (red). Adapted from Pétron et al., 2012.

1.2.2 Oil and Natural Gas Processing and Infrastructure

Oil and natural gas production begins at extraction, which occurs by one of three mechanisms. The first mechanism is solution gas drive and is used when the temperature and pressure inside the reservoir is high enough to prevent separation between oil and natural gas. Once the bore hole reaches the reservoir, the pressure differential causes bubbles to form and expand and forces the mixture to the surface (Berger & Anderson, 1992). The second mechanism is gas cap drive and is used when bypassing the gas pool at the top of the reservoir to extract only the oil. In this case, as the oil is extracted the natural gas can expand, forcing the oil to the surface (Berger & Anderson, 1992). The third mechanism is bottom water drive, used when reservoirs contain water and the pressure release from the bore hole forces oil to the surface. However, water must be continuously injected and the pressure monitored to ensure oil extraction (Berger & Anderson, 1992)

Extracted crude oil and unprocessed natural gas from oil wells undergoes processing before use. Crude oil is a mixture of hydrocarbons that must be separated out into its desired products, which occurs via fractional distillation. This process separates the hydrocarbons in the oil by their boiling point, which corresponds to the number of carbons, with light alkanes distilling first and higher chained alkanes remaining (Berger & Anderson, 1992). Most refineries use a continuous distillation column, a process where oil continuously enters the column and is separated into various fractions that are removed in a continuous stream. The distilled fractions go on to make products such as gasoline and diesel. The remaining heavier products can be used to make lubricants, wax, and tar (Berger & Anderson, 1992)

Natural gas in a reservoir is either separate or dissolved in the oil in an overlying gas cap, or a combination of natural gas and hydrocarbons, more commonly referred to as condensate

(Berger & Anderson, 1992; EPA, 2016d). Production begins on site with the separation of oil, hydrocarbons, and other gases from the natural gas. Field processing equipment varies greatly as the composition of gas from well to well can change as drilling conditions change (Berger & Anderson, 1992). Once separated from the oil and other liquids, natural gas is taken through a dehydrator to remove excess water before being transported by a pipeline (Berger & Anderson, 1992). Natural gas transmission also includes storage facilities used for load balancing. Storage can be either above ground stored in tanks or underground in depleted reservoirs (EPA, 2016d).

a. Fugitive Emissions

Fugitive emissions of VOCs can happen in several ways throughout the extraction, production, and transportation process. Perhaps one of the most significant sources of VOC emissions are storage vessels containing either crude oil or condensate. These vessels can potentially emit 6 tons of VOCs per year (EPA, 2016d). It is common for flashing to occur when transferring to a storage vessel, the sudden vaporization of natural gas caused by the pressure change during transfer, or breathing losses are that caused by temperature changes (EPA, 2016d). Pneumatic devices, such as controllers or pumps, are used along pipeline systems and powered by the pressurized natural gas and can bleed natural gas to the atmosphere. During pipeline maintenance, natural gas is vented to the atmosphere to relieve pressure in the line for safe working conditions (F. Oldenhuis, personal communication, Oct. 17, 2017). The vapors that are emitted are a mix of hydrocarbons, comprised of mostly methane, but also contain various amounts of HAPS (EPA, 2016d) .

1.2.3 Previous Work Regarding Oil and Natural Gas Emissions

Thirty four percent of US electricity generation is from natural gas, producing 4 trillion kilowatt-hours of electricity in 2016 (EIA, 2017). The impacts of emissions from this sector and

the toll it has on air quality has been a topic of great interest in recent years. Here we will discuss the effect of oil and natural gas emissions within the United States and Colorado.

a. United States Oil and Natural Gas Emissions

There have been several studies that have examined the effects of ONG on air quality in the United States. A recent study by Helmig et al. (2016) examining trends of light alkanes in North America found that ethane concentrations have been increasing at an average of 0.42 ± 0.19 Tg yr^{-1} from 2009 to 2014, and NMHCs have been increasing by 1.2 ± 0.8 Tg yr^{-1}. The greatest increases in ethane and propane were in areas of ONG development, central and eastern US (Helmig et al., 2016). Katzenstein and colleagues (2003) analyzed the surface composition in the Southwestern US and determined that elevated concentrations of CH_4 and $C_2 - C_4$ alkanes in the area were likely from ONG wells and storage tanks. It was also estimated that an average of 4-6 TgCH_4 yr^{-1} is released in this area, double what was being reported by the EPA.

Multiple studies measuring emissions from refineries and petrochemical plants in Houston, TX have concluded that emissions from these point sources are a major source for ozone formation (Ryerson et al., 2003; Washenfelder et al., 2010; Gilman et al., 2009). In 2009, a study examined the source of winter ozone events in the Upper Green River Basin in Wyoming. It was determined that the local meteorology led to an accumulation of NMHCs and NO_X resulting in high levels of ozone, up to 117 ppb (Schnell et al., 2009). Each of these studies, and many more (Mellqvist et al., 2010; Simpson et al., 2010; Townsend-Small et al., 2012; Karion et al., 2013; Marrero et al., 2013) conclude that to improve local and regional air quality in areas where ONG production is a major industry, fugitive emissions from wells and infrastructure need to be quantified and regulated. A map of the distribution of oil and gas wells in the continental United States is shown in Figure 1.2.

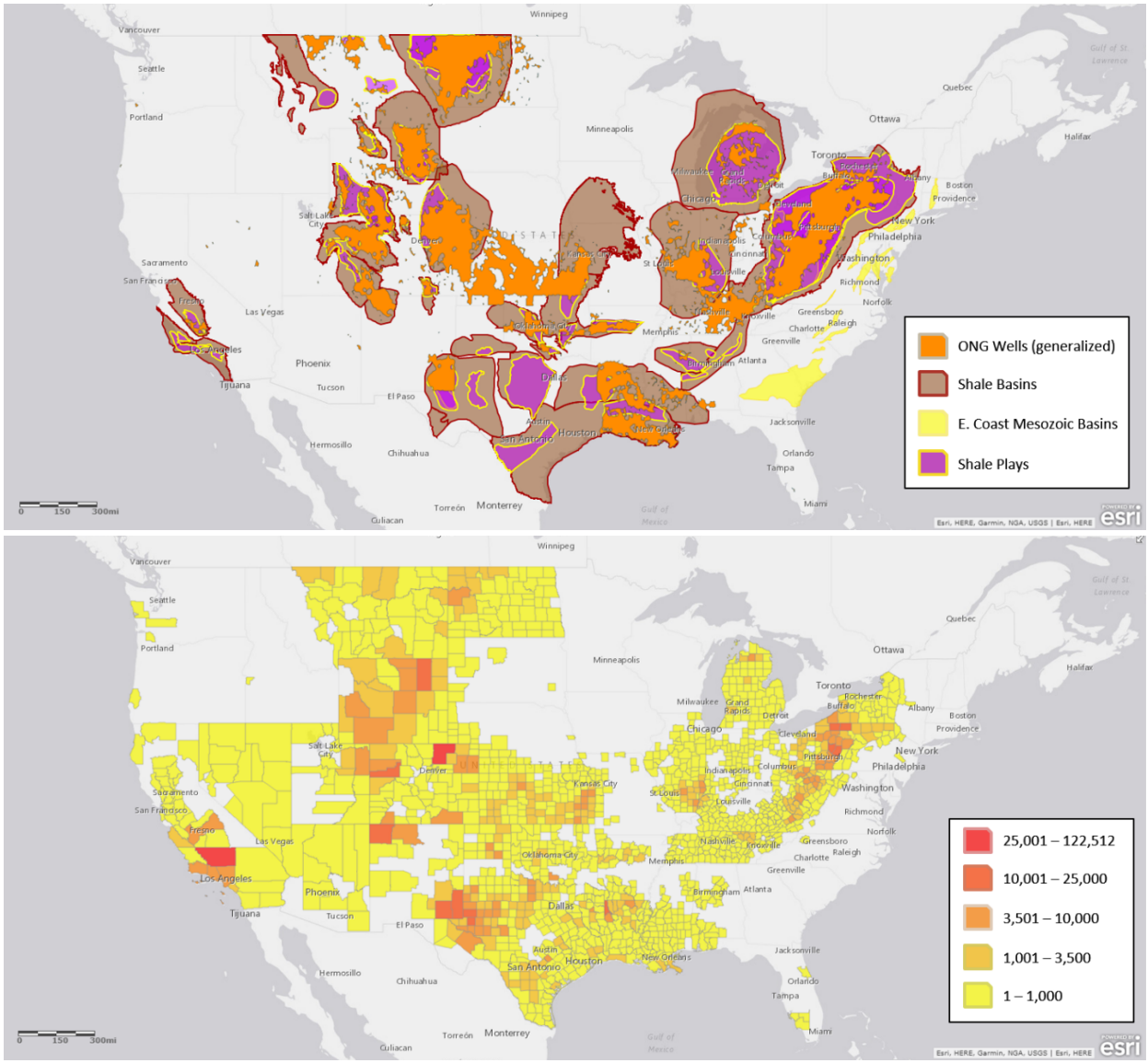

Figure 2.2 (top) Map of the known oil and natural gas reserves in the United States as of February 2014. (bottom) Map of the concentration of oil and natural gas wells per county in the United States, with the highest concentration in Kern County, CA with 122,512 wells, followed by Weld County, CO with 28,475 wells. These maps were created using ArcGIS® software by Esri. ArcGIS® and ArcMap™ are the intellectual property of Esri and are used herein under license. Copyright © Esri. All rights reserved. For more information about Esri® software, please visit www.esri.com. Data courtesy of Fractracker Alliance, https://www.fractracker.org/2014/03/active-gas-and-oil-wells-in-us/; USGS, https://catalog.data.gov/dataset/national-assessment-of-oil-and-gas-project-east-coast-mesozoic-basins-of-the-piedmont-blue-rid; US Energy Information Administration, https://www.eia.gov/pub/oil_gas/natural_gas/analysis_publications/maps/maps.htm

b. Colorado Oil and Natural Gas Emissions

Oil and natural gas production in Colorado has been an area of extensive research in recent years as the state ranks 5th in the nation for natural gas production and 7th for oil. Combined, these two sectors represent 84% of Colorado's total energy production as shown in Figure 1.3 (EIA, 2017). A study in 2012 found that this industry is the largest anthropogenic CH_4 emission source in the state at approximately 19 t CH_4 h^{-1}, roughly 74% of total CH_4 emissions (Pétron et al., 2014). The large difference between these two sectors is due to natural gas condensate storage tanks which operate at high pressures resulting in higher leak rates. It is estimated that emissions from these storage tanks are responsible for 68% of total VOC emissions from fossil fuel production (Bar-Ilan et al., 2008). The Colorado Department of Public Health and Environment (CDPHE) estimated that in 2006, roughly 40% of anthropogenic emissions in the NFRMA non-attainment area for ozone were from ONG production (CDPHE, 2008). These studies led to the series of policies enacted to reduce emissions from the ONG sector in the NFRMA mentioned above.

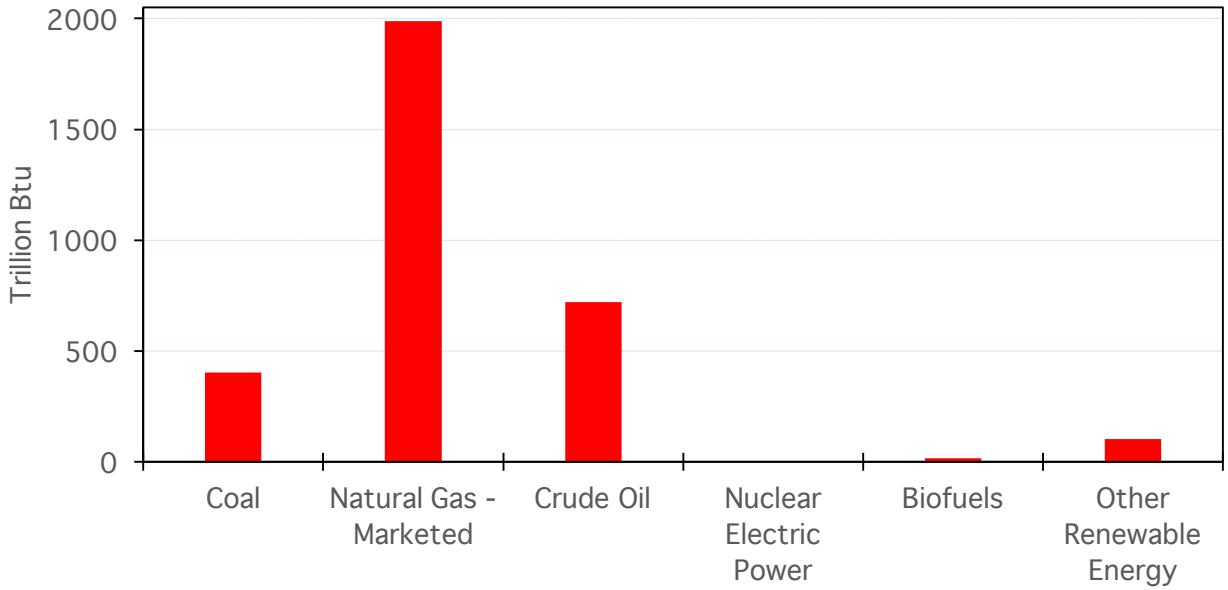

Figure 1.3 Colorado energy production estimates for 2015. Adapted from EIA, 2017. https://www.eia.gov/state/?sid=CO#tabs-3

More recently, a study from the NOAA Boulder Atmospheric Observatory (BAO), a 300 m tower located in the southwest corner of the GWA, found that measurements taken daily over three years measured elevated concentrations of $C_3 - C_5$ alkanes that were ten times greater than background concentrations (Pétron et al., 2012). A separate study from BAO found that contributions from ONG accounted for 72%, 90%, 95%, and 96% of emissions of ethane, propane, n-butane, and n-pentane, respectively, with these ozone precursors representing 60% of total OH reactivity (Gilman et al., 2013).

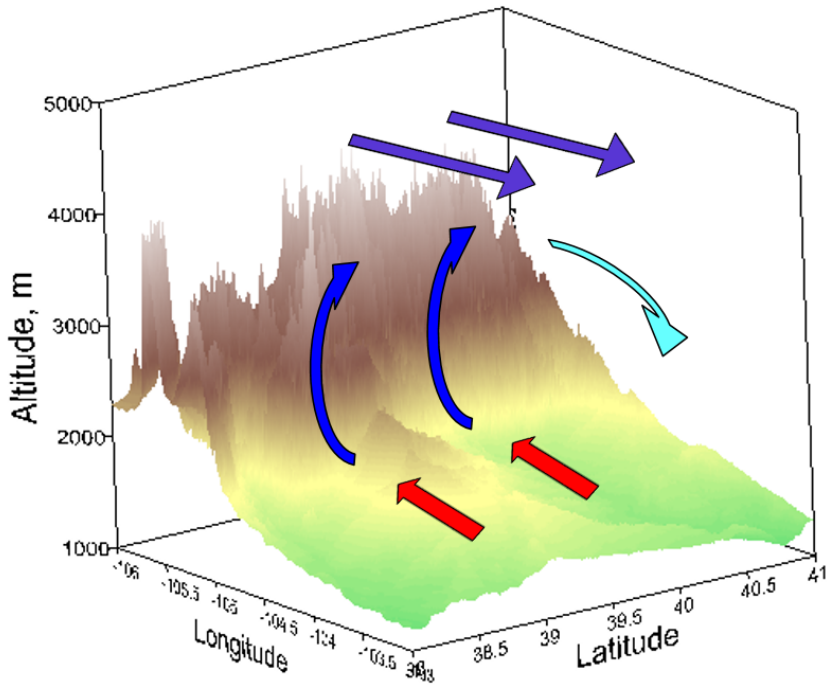

Figure 1.4 Diagram of mountain-valley circulation. Red arrows are incoming upslope events that bring air from the Denver-Julesburg Basin to the foothills of the Rocky Mountains. Red arrows show the air mass rising up the eastern side of the mountains. The purple arrows indicate prevailing westerly winds. The cyan arrow shows the recirculation pattern. Adapted from Sullivan et al., 2016.

The topography of Colorado drives the local meteorology and resulting wind patterns have led to a buildup of ozone precursors in the NFRMA. The Rocky Mountains peak at 4400 m above sea level and divide the state in half. Thermal gradients during the day and this barrier

leads to a recirculation pattern, commonly referred to as mountain-valley circulation effects, that is characterized by easterly winds rising into the foothills of the eastern Rocky Mountains. As the air mass travels up the mountains, westerly winds create a convergence, circulating the air mass back into the NFRMA where O_3 and O_3 precursors can accumulate. In the evening as the air mass cools, it drains to the east, leading to long range transport of VOCs (Toth & Johnson, 1985; Reddy & Pfister, 2016; Sullivan et al., 2016). A schematic of mountain valley circulation is shown in Figure 1.4.

The oil and natural gas industry is not the only emission source of VOCs in this area. The Denver Metropolitan Area is located within the NFRMA and is a large urban emission source as shown by elevated CO and benzene emissions from combustion sources such as engines and automobiles (Pétron et al., 2012). There are more than 100 dairies and cattle feedlots throughout the GWA, as well as landfills, waste water treatment plants, and other microbial sources (Pétron et al., 2014). A recent isotopic analysis of this area has shown that about 50% of CH_4 emissions in the NFRMA are from biogenic sources and could account for discrepancies seen in emission inventories and estimates (Townsend-Small et al., 2016).

1.3 Objectives and Motivation for this Work

The Denver Metropolitan Area is home to more than 2.6 million people and is the 18th largest metropolitan area in the United States (U.S. Census Bureau, 2012). The policies enacted to reduce ozone precursors in this area have yet to be successful as this area has been in non-attainment since 2007 with an average of 30 exceedances per year (EPA, 2017d). The magnitude of the ONG industry in this area, the complex meteorology, and the diverse point sources such as urban and industrial emissions and agricultural and biogenic emissions sources, create a unique environment that is conducive to ozone formation. This work aims to address what factors are

contributing to ozone formation in this area, how transportation impacts ozone formation, and how much the ONG industry contributes to the air quality of this region.

1.3.1 Front Range Air Pollution and Photochemistry Experiment

The Front Range Air Pollution and Photochemistry Experiment (FRAPPÉ) was designed to characterize air quality in the NFRMA. This campaign conducted 15 research flights from July 26th to August 17th, 2014 onboard the NSF/NCAR C-130 aircraft and complementing surface measurements to address "*what are the factors controlling NFRMA surface ozone and are current emission controls sufficient to reduce ozone levels below the NAAQS?"* (Flocke & Pfister, 2013). Flight plans and sampling were designed to measure background conditions, source specific emissions, mountain valley circulation effects, and pollution in/outflow by assessing local and regional photochemistry. The project aimed to create a comprehensive data set that will be used to elucidate the complex mechanisms that lead to enhanced ozone production.

This campaign coordinated with the NASA Deriving Information on Surface Conditions from Column and Vertically Resolved Observations Relevant to Air Quality (DISCOVER-AQ 2014) campaign. This project was devised to improve satellite measurements of surface air quality from onboard the NASA P3-B aircraft and surface based measurements (Crawford, 2014).

1.4 References

Atkinson, R. (2000). Atmospheric chemistry of VOCs and NOX. *Atmospheric Environment*, 34, 2063-2101.

Atkinson, R., Baulch, D., Cox, R., Crowley, J., Hampson, R., Hynes, R., . . . Troe, J. (2006). Evaluated kinetic and photochemical data for atmospheric chemistry: Volume II - gas phase reactions of organic species. *Atmospheric Chemistry and Physics*, 6(11), 3625-4055.

Atkinson, R., Kwok, E., Arey, J., & Aschmann, S. (1995). Reactions of alkoxy radicals in the atmosphere. *Faraday Discussions*, 100, 23-27.

Bar-Ilan, E. (2008). Development of baseline 2006 emissions from oil and gas activity in the Denver-Julesburg Basin, WRAP Phase III report. Fort Collins, CO: Western Regional Air Partnership.

Bell, M., McDermott, A., Zeger, S., Samet, J., & Dominici, F. (2004). Ozone and short-term mortality in 98 US urban communities, 1987-2000. J*ournal of American Medical Association*, 292(19).

Benton, J., Fuhrer, J., Gimeno, B., Skarby, L., Palmer-Brown, D., Ball, G., . . . Mills, G. (2000). An international cooperative programme indicates the widespread occurrence of ozone injury on crops. *Agriculture Ecosystems and Environment*, 78, 19-30.

Berger, B., & Anderson, K. (1992). Modern Petroleum: A basic primer of the industry, third edition. Tulsa, OK: PennWell Publising Company.

Bertman, S., Roberts, J., Parrish, D., Buhr, M., Goldan, P., Kuster, W., & Fehsenfeld, F. (1995). Evolution of alkyl nitrates with air mass age. *Journal of Geophysical Research*, 100(D11), 22805-22813.

Blacet, F. (1952). Photochemistry in the Lower Atmosphere. *Industrial and Engineering Chemistry*, 44(6), 1339-1342.

Brasseur, G. P., Orlando, J. J., & Tyndall, G. S. (1999). Atmospheric Chemistry and Global Change. New York, NY: Oxford University Press.

Calvert, J. G. (1976). Test of the theory of ozone generation in Los Angeles atmosphere. *Environmental Science and Technology,* 10, 248-256.

Calvert, J., & Pitts, J. (1966). Photochemistry. New York: John Wiley and Sons.

Carter, W., & Atkinson, R. (1989). An experimental study of incremental hydrocarbon reactivity. *Environmental Science and Technology*, 23, 864-880.

CDPHE. (2008). Denver metron area and North Front Range Ozone Action Plan. Denver, CO. Retrieved from https://www.colorado.gov/pacific/sites/default/files/AP_PO_Denver-Ozone-Action-Plan-2008.pdf

CDPHE. (2017). History of Ozone in Colorado. Retrieved October 17, 2017, from Colorado department of Public Health and Environment: https://www.colorado.gov/pacific/cdphe/ozone-planning-chronology

Chameides, W., & Walker, J. (1973). A photochemical theory of tropospheric ozone. *Journal of Geophysical Research*, 78(36), 8751-8760.

Chuck, A., Turner, S., & Liss, P. (2002). Direct evidence for a marine source of C1 and C2 alkyl nitrates. Science, 297, 1151-1154.

COGCC. (2007). GREATER WATTENBERG AREA. Denver, CO: LT ENVIRONMENTAL, INC.

Crawford, J. (2014, July 15). 2014 DISCOVER-AQ Campaign. Retrieved October 20, 2017, from https://www.nasa.gov/larc/2014-discoveraq-campaign/

Crutzen, P. (1973). A discussion of the chemistry of some minor constituents in the stratosphere and troposphere. *Pure and Applied Geophysics*, 106-108, 1385-1399.

Dahl, E., Saltzman, E., & de Bruyn, W. (2003). The aqueous phase yield of alkyl nitrates from ROO + NO: Implications for photochemical production in seawater. *Geophysical Research Letters*, 30(6), 1271.

DeMore, W., & Raper, O. (1966). Primary processes in ozone photolysis. *Journal of Chemical Physics*, 44(5), 1780-1783.

Dlugokencky, E. J. (2017). Recent Global CH4. (NOAA/ESRL) Retrieved October 5, 2017, from Global Greenhouse Gas Reference Network: www.esrl.noaa.gov/gmd/ccgg/trends_ch4/

Duncan, B., Bey, I., Chin, M., Mickley, L., Fairlie, T., Martin, R., & Matsueda, H. (2003). Indonesian wildfires of 1997: Impact on tropospheric chemistry. *Journal of Geophysical Research*, 1088888(D15), 2156-2202.

EIA. (2017, May 10). Electricity in the United States. Retrieved October 17, 2017, from Electricity Explained: https://www.eia.gov/energyexplained/index.cfm?page=electricity_in_the_united_states

EIA. (2017, September 29). Number of producing gas wells. Retrieved October 19, 2017, from Natural Gas: https://www.eia.gov/dnav/ng/ng_prod_wells_s1_a.htm

EIA. (2017). State Profile and Energy Estimates: Colorado. Retrieved October 20, 2017, from U.S. Energy Information Administration Independent Statistics and Analysis: U.S. Energy Information Administration Independent Statistics and Analysis

EPA. (2016a, April). Inventory of U.S. Greenhouse Gas Emissions and Sinks: 1990-2014. Retrieved September 27, 2017, from GreenHouse Gas Emissions: https://www.epa.gov/ghgemissions/inventory-us-greenhouse-gas-emissions-and-sinks-1990-2014

EPA. (2016b). Air pollutant emissions trends data. Retrieved October 7, 2017, from Air Emissions Inventories: https://www.epa.gov/air-emissions-inventories/air-pollutant-emissions-trends-data

EPA. (2016c). NAAQS Table. Retrieved October 11, 2017, from Criteria Pollutants: https://www.epa.gov/criteria-air-pollutants/naaqs-table

EPA. (2016d). Control Techniques Guidelines for the Oil and Natural Gas. Research Triangle Park, NC: EPA-453/B-16-001.

EPA. (2017a, January 10). Clean Air Act Overview. Retrieved September 25, 2017, from Clean Air Act Requirements and History: https://www.epa.gov/clean-air-act-overview/clean-air-act-requirements-and-history

EPA. (2017b). Health effects notebook for hazardous air pollutants. Retrieved October 9, 2017, from https://www.epa.gov/haps/health-effects-notebook-hazardous-air-pollutants

EPA. (2017c). Evolution of the Clean Air Act. Retrieved October 13, 2017, from Clean Air Act Overview: https://www.epa.gov/clean-air-act-overview/evolution-clean-air-act

EPA. (2017d, September 9). Colorado Nonattainment/Maintenance Status for Each County by Year for All Criteria Pollutants. Retrieved October 17, 2017, from Greenbook: https://www3.epa.gov/airquality/greenbook/anayo_co.html

Finlayson-Pitts, B. J., & Pitts, J. N. (2000). Chemistry of the Upper and Lower Atmosphere: Theory, experiments, and Applications. San Diego, California: Academic Press.

Fishman, J., & Seiler, W. (1983). Correlative nature of ozone and carbon monoxide in the troposphere: Implications for the tropospheric ozonebudget. *Journal of Geophysical Research: Oceans*, 88(C6), 3662-3670.

Flocke, F., & Pfister, G. (2013). Front Range Air Pollution and Photochemistry Experiment FRAPPÉ: A proposed field experiment in Colorado for summer 2014. Retrieved from http://www2.acd.ucar.edu/frappe

Forster, P., Ramaswamy, V., Artaxo, P., Berntsen, T., Betts, R., Fahey, D., . . . Van Dorland, R. (2008). Changes in Atmospheric Constituents and in Radiative Forcing. In S. S. al. (Ed.), Climate Change 2007: The Physical Science Basis. Contribution of Working Group I to the Fourth Assessment Report of the IPCC. Cambrige, UK: Cambridge University Press. Retrieved from http://www.cambridge.org/catalogue/catalogue.asp?isbn=9780521705967

Fujita , E., Croes, B., Bennett, C., Lawson, D., Lurman, F., & Main, H. (1992). Comparison of emission inventory and ambient mixing ratios of CO, NMOG, and NOX in Californias Southcoast Basin. *Journal of Air Waste Management Associeation*, 42(3), 264-276.

Gilman, J., Kuster, W., Goldan, P., Herndon, S., Zahniser, M., Tucker, S., . . . de Gouw, J. (2009). Measurements of volatile organic compounds during the 2006 TexAQS/GoMACCS campaign: Industrial influences, regional characteristics, and diurnal dependencies of the OH reactivity. *Journal of Geophysical Research: Atmospheres*, 114(D7).

Gilman, J., Lerner, B., Kuster, W., & de Gouw, J. (2013). Source signature of volatile organic compounds from oil and natural gas operations in Northeastern Colorado. *Environmental Science and Technology*, 47, 1297-1305.

Graedel, T., & Crutzen, P. (1989). The Changing Atmosphere. Scientific American, 261(3), 58-69.

Guenther, A. (2002). The contribution of reactive carbon emissions from vegetation to the carbon balance of terrestrial ecosystems. *Chemosphere*, 49, 837-844.

Guenther, A., Geron, C., Pierce, T., Lamb, B., Harley, P., & Fall, R. (2000). Natural emissions of non-methane volatile organic compounds, carbon monoxide, and oxides of nitrogen from North America. *Atmospheric Environment*, 34, 2205-2230.

Guenther, A., Hewitt, C., Erickson, D., Fall, R., Geron, C., Graedel, T., . . . Zimmerman, P. (1995). A global model of natural volatile organic compound emissions. *Journal of Geophysical Research*, 100(D5), 8873-8892.

Haagen-Smit, A. (1952). Chemistry and Physiology of Los Angeles Smog. *Industrial and Engineering Chemistry*, 44(6), 1342-1346.

Hartmann, D. L., Tank, A. M., Rusticucci, G. K., Alexander, L. V., Bronnimann, S. Y., Charabi, F. J., . . . Zhai, P. M. (2013). Observations: Atmosphere and surface. In G.K. Stocker et al. (Ed.), Climate Change 2013 the Physical Science Basis: Working Group I Contribution to the Fifth Assessment Report of the Intergovernmental Panel on Climate Change (Vol. 9781107057999, pp. 159-254). Cambridge, UK: Cambridge University Press.

Hauglustaine, D., Brasseur, G., Walters, S., Rasch, P., Muller, J., Emmons, L., & Carroll, M. (1998). MOZART, a global chemical transport model for ozone and related chemical tracers: 2. Model results and evaluation. *Journal of Geophysical Research*, 103, 28291-28335.

Heicklen, J. (1968). Gas-phase reactions of alkylperoxy and alkoxy radicals. In R. Mayo (Ed.), Oxidation of Organic Compounds, Volume II. Gas-Phase Oxidations, Homogeneous and Heterogeneous Catalysis, Applied Oxidations and Synthetic Processess. *American Chemical Society*, 76, 23-39.

Helmig, D., Rossabi, S., Hueber, J., Tans, P., Montzka, S., Masarie, K., . . . Pozzer, A. (2016). Reversal of global atmospheric ethane and propane trends largely due to US oil and natural gas production. *Nature*, 9.

Hodgman, C. (1961). Handbook of Chemistry and Physics. Cleveland, Ohio: Chemical Rubber Publishing Co.

Holloway, T., & Kasibhatla, P. (2000). Global distribution of carbon monoxide. Journal of Geophysical Research, 105(D10), 12123-12147.

Intergovernmental Panel on Climate Change (IPCC). (1996). Climate Change 1995: The science of climate change. Cambridge, UK: Cambridge University Press.

Intergovernmental Panel on Climate Change (IPCC). (2001). Climate Change 2001: The scientific basis. Cambridge, UK: Cambridge University Press.

Intergovernmental Panel on Climate Change. (2013). Fifth Assessment Report: Climate Change 2013. Cambridege, UK: Cambridge University Press.

Johnston, H. (1970). Reactions in the Atmosphere. Project Clean Air Task Force Assessments, 4, 3.

Karion, A., Sweeney, C., Pétron, G., Frost, G., Hardesty, R., Kofler, J., . . . Conley, S. (2013). Methane emissions estimate from airborne measurements over a western United States natural gas field. *Geophysical Research Letters*, 40, 4393-4397.

Katzenstein, A., Doezema, L., Simpson, I., Blake, D., & Rowland, F. (2003). Extensive regional atmospheric hydrocarbon pollution in the southwestern United States. *Proceedings of the National Academy of Science*, 100(21), 11975-1979.

Kaufman, F. (1969). Neutral reactions involving hydrogen and other minor constituents. *Canadian Journal of Chemistry*, 47, 1917-1924.

Kiehl, M., & Rasmussen, R. (1983). CO2 radiative parameterization used in climate models: Comparison with narrow-band models and laboratory data. *Journal of Geophysical Research*, 88, 5191-5202.

Kirschke, S., Bousquet, P., Ciais, P., Saunois, M., Canadell, J., Dlugokencky, E. J., . . . Zeng, G. (2013). Three decades of global methane sourcs and sinks. *Nature Geoscience*, 6, 813-823.

Leuchner, M., Gubo, S., Schunk, C., Wastl, C., Kirchner, M., Menzel, A., & Plass-Dulmer, C. (2015). Can positive matrix factorization help to understand patterns of organic trace gases at the continental Global Atmosphere Watch site Hohenpeissenberg? *Atmospheric Chemistry and Physics*, 15, 1221-1236.

Levy II, H. (1971). Normal Atmosphere: Large Radical and Formaldehyde Concentrations Predicted. *Science*, 173(3992), 141-143.

Marrero, J., Townsend-Small, A., Lyon, D., Tsai, T., Meinardi, S., & Blake, D. (2013). Estimating emissions of toxic hydrocarbons from natural gas production sites in the Barnett Shale region of Northern Texas. *Environmental Science and Technology*, 50, 10756-10764.

Matuszczak, R. (1976). Wattenberg Field, Denver Basin, Colorado. In J. Braunstein (Ed.), North American Oil and Gas Fields (Vol. 24). *American Association of Petroleum Geologists*.

McMillan, G., & Calvert, J. (1965). Gas phase photooxidation. Oxidation and Combustion Reviews, 1, 83-136.

Mellqvist, J., Samuelsson, J., Johansson, J., Rivera, C., Lefer, B., & Alvarez, S. (2010). Measurements of industrial emissions of alkened in Texas using the Solar Occultation Flux method. *Journal of Geophysical Research*, 115(D00F17).

National Resource Council. (2010). Global Sources of Local Pollution: An Assessment of Long-Range Transport of Key Air Pollutants to and from the United States. Washington, DC: The National Academies Press.

Nelson, P., & Santus, S. (2011). Gas, water, and oil production from Wattenberg field in the Denver Basin, Colorado: U.S. Geolgical Survey Open-File Report 2011-1175.

Nicolet, M. (1970). Ozone and hydrogen reactions. *Annales de Geophysique*, 26, 531-546.

Parasevopoulos, G., & Cvetanovic, R. (1971). Relative rate of reaction of O(1D2) with H2O. *Chemical Physics Letters*, 9(6), 603-605.

Perring, A., Bertram, T., Farmer, D., Wooldridge, P., Dibb, J., Blake, N., Blake, D., Singh, H., Fuelberg, H., Diskin, G., Sachse, G., & Cohen, R. (2010). The production and persistence of ΣRONO2 in the Mexico City plume. *Atmospheric Chemistry and Physics*, 10, 7215-7229.

Pétron, G., Grost, G., Miller, B., Hirsch, A., Montzka, S., Karion, A., . . . Tans, P. (2012). Hydrocarbon emissions characterization in the Colorado Front Range: A pilot study. *Journal of Geophysical Research*, 117(D04304).

Pétron, G., Karion, A., Sweeney, C., Miller, B., Montzka, S., Frost, G., . . . Schnell, R. (2014). A new look at methane and nonmethane hydrocarbon emissions from oil and natural gas operations in the Colorado Denver-Julesburg Basin. Jou*rnal of Geophysical Research: Atmospheres*, 119, 6836-6852.

Pozzer, A., Pollmann, J., Taraborrelli, D., Jockel, P., Helmig, D., Tans, P., . . . Lelieveld, J. (2010). Observed and simulated global distribution and budget of atmospheric C2-C5 alkanes. *Atmospheric Chemistry and Physics*, 10, 4403-4422.

Ramanathan, V. (1985). Trace gas trends and their potential role in climate chane *Journal of Geophysical Research: Atmospheres*, 90, 5547-5566.

Reddy, P., & Pfister, G. (2016). Meteorological factos contributing to the interannua variability of mid-summer ozone in Colorado, Utah, and other western US States. *Journal of Geophysical Research: Atmospheres*, 121, 2434-2456.

Ryerson, T., Trainer, M., Angevine, W., Brock, C., Dissly, R., Fehsenfeld, F., . . . Sueper, D. (2003). Effect of petrochemical industrial emissions of reactive alkenes and NOX on tropospheric ozone formation in Houston, Texas. *Journal of Geophysicl Research*, 108(D8), 4249.

Schnell, R., Oltmans, S., Neely, R., Endres, M., Molenar, J., & White, A. (2009). Rapid photochemical production of ozone at high concentrations in a rural site during winter. *Nature Geoscience*, 2, 120-122.

Schultz, M., Jacob, D., Wang, Y., Logan, J., Atlas, E., Blake, D., . . . Talbot, R. (1999). On the origin of tropospheric ozone and NOX over the tropical South Pacific. *Journal of Geophysical Research*, 104(D5), 5829-5843.

Schumb, W., Satterfield, C., & Wentworth, R. (1955). Hydrogen Peroxide. New York: Reinhold Publishing Corporation.

Seinfeld, J. H., & Pandis, S. N. (2006). Atmospheric Chemistry and Physics: From Air Pollution to Climate Change, 2nd ed,. Hoboken, NJ: John Wiley & Sons, Inc.

Seinfeld, J., & Pandis, S. (2016). Atmospheric Chemistry and Physics: From Air Pollution to Climate Change, Third edition. John Wiley & Sons.

Sharma, S., Sharma, P., & Khare, M. (2017). Photo-chemical transport modelling of tropospheric ozone: A review. *Atmospheric Environment*, 159, 34-54.

Simpson, D., Ashmore, M., Emberson, L., & Tuovinen, J. (2007). A comparison of two different approaches for mapping potential ozone damage to vegetation: A model study. *Environmental Pollution*, 146, 715-725.

Simpson, I., Blake, N., Barletta, B., Diskin, G., Fuelberg, H., Gorham, K., . . . Blake, D. (2010). Characterization of trace gases measured over alberta oil sands mining operations :76 speciated C2-C10 volatle orgainc coumpounds (VOCs), CO, CH4, CO, NO, NO2, NOy, O3 and SO2. *Atmospheric Chemistry and Physic*s, 10, 11931-11954.

Simpson, I., Wang, T., Guo, H., Kwok, Y., Flocke, F., Atlas, E., . . . Blake, D. (2006). Long-term atmospheric measurements of C1-C5 alkyl nitratesin the Pearl River Delta region of southeast China. *Atmospheric Environment*, 40, 1619-1632.

Singh, H., & Zimmerman, P. (1992). Atmospheric distribution and sources of nonmethane hydrocarbons. In J. Nriagu (Ed.), Gaseous Pollutants: Characterization and Cycling. New York, NY: John Wiley and Sons.

Sullivan, J., McGee, T., Langford, A., Alvarez II, R., Senff, C., Reddy, P., . . . Hoff, R. (2016). Quantifying the contribution of thermally driven recircultion to a high-ozone event along the Colorado Front Range using lidar. *Journal of Geophysical Research: Atmospheres*, 121, 10377-10390.

Talukdar, R., Burkholder, J., Hunter, M., Gilles, M., Roberts, J., Ravishankara, A. (1997). Atmospheric fate of several alkyl nitrates Part 2 UV absorption cross-sections and photodissociation quantum yields. *Journal of the Chemical Society, Faraday Transactions,* 93(16), 2797-2805.

Toth, J., & Johnson, R. (1985). Summer surface flow characteristics over northeast Colorodo. *Monthly Weather Review*, 113(9), 1458-1469.

Townsend-Small, A., Botner, E., Jimenez, K., Schroeder, J., Blake, N., Meinardi, S., . . . Flocke, F. (2016). Using stable isotopes of hydrogen to quantify biogenic and thermogenic atmospheric methane sources: A case study from the Colorado Front Range. *Geophysical Research Letters*, 43, 11462-11471.

Townsend-Small, A., Tyler, S., Pataki, D., Xu, X., & Christensen, L. (2012). Isotopic measurements of atmospheric methane in Los Angeles, California, USA: Influence of "fugitive" fossil fuel emissions. *Journal of Geophysical Research*, 117(D07308).

Turberg, M., Giolando, D., Tilt, C., Soper, T., Mason, S., Davies, M., Klingensmith, P., Takacs, G. (1990). Atmospheric photochemistry of alkyl nitrates. *Journal of Photochemistry and Photobiology A: Chemistry*. 51(3), 281-292.

U.S. Census Bureau. (2012, November 15). Largest urbanized areas with selected cities and metro areas. Retrieved October 20, 2017, from https://www.census.gov/dataviz/visualizations/026/508.php

Vaghjiani, G. L., & Ravishankara, A. R. (1991, April 4). New measurement of the rate coefficient for the reaction of OH with methane. *Nature*, 406-409.

Wang, W., Sze, N., Molnar, G., Ko, M., & Goldenberg, S. (1988). Ozone-climate interactions with increasing atmospheric trace gases. In I. Isaksen, Tropospheric Ozone (pp. 147-159). Hingham, MA: D. Reidel.

Washenfelder, R., Trainer, M., Frost, G., Ryerson, T., Atlas, E., de Gouw, J., . . . Zheng, W. (2010). Characterization ofNOx, SO2, and propene from industrial emission sources in Houston, Texas. *Journal of Geophysical Research*, 115(D16311).

Watson, J., Chow, J., & Fujita, E. (2001). Review of volatile organic compounds source apportionment by chemical mass balance. *Atmospheric Environment*, 35, 1567-1584.

Weimer, R., Sonnenberg, S., & Young, G. (1986). Wattenberg Field, Denver Basin, Colorado. In C. Spencer, & R. Mast (Eds.), Geology of tight gas reservoirs (pp. 143-165). American Association of Pertroleum Geologist.

2. METHODS

Data presented here were collected during the FRAPPÉ field campaign onboard the NSF/NCAR C-130, which took place from July 26th through August 17th, 2014 in Colorado. The UCAR/NCAR Advanced Whole Air Sampler (AWAS) was used to collect air samples and they were analyzed at UC Irvine for VOCs. One-second measurements of CH_4, CO, CO_2, water vapor, C_2H_6, HCHO, and other compounds were made by collaborators onboard the C-130. A detailed description of this is provided below. An overview of the campaign can be found at https://www2.acom.ucar.edu/frappe.

The NASA DISCOVER-AQ 2014 campaign is a separate campaign that occurred in Colorado from July 8th through August 12th, 2014. Samples for this campaign were collected onboard the NASA P3-B and used throughout this work to complement the FRAPPÉ data set. The NASA B-200 aircraft also contributed to this campaign but was not used in this work. An overview of the campaign can be found at https://www.nasa.gov/larc/2014-discoveraq-campaign/.

2.1 Study Design

During FRAPPÉ, the C-130 flew 15 research flights over Colorado and was based at the UCAR/NCAR Research Aviation Facility in Broomfield, CO (UTC – 6:00 hours). Flight plans that focused on NFRMA emissions were a north – south "lawnmower" pattern at a constant altitude of approximately 1 km above ground level (AGL). Flights analyzing the mountain-valley circulation effect were a larger scale north – south lawnmower pattern going east to west up the mountains. Flights also focused on NFRMA outflow and westerly inflow from western ONG fields. Maps of the flight plans and actual flights are shown in Figure 2.1 and a more detailed description of each flight is shown in Table 2.1.

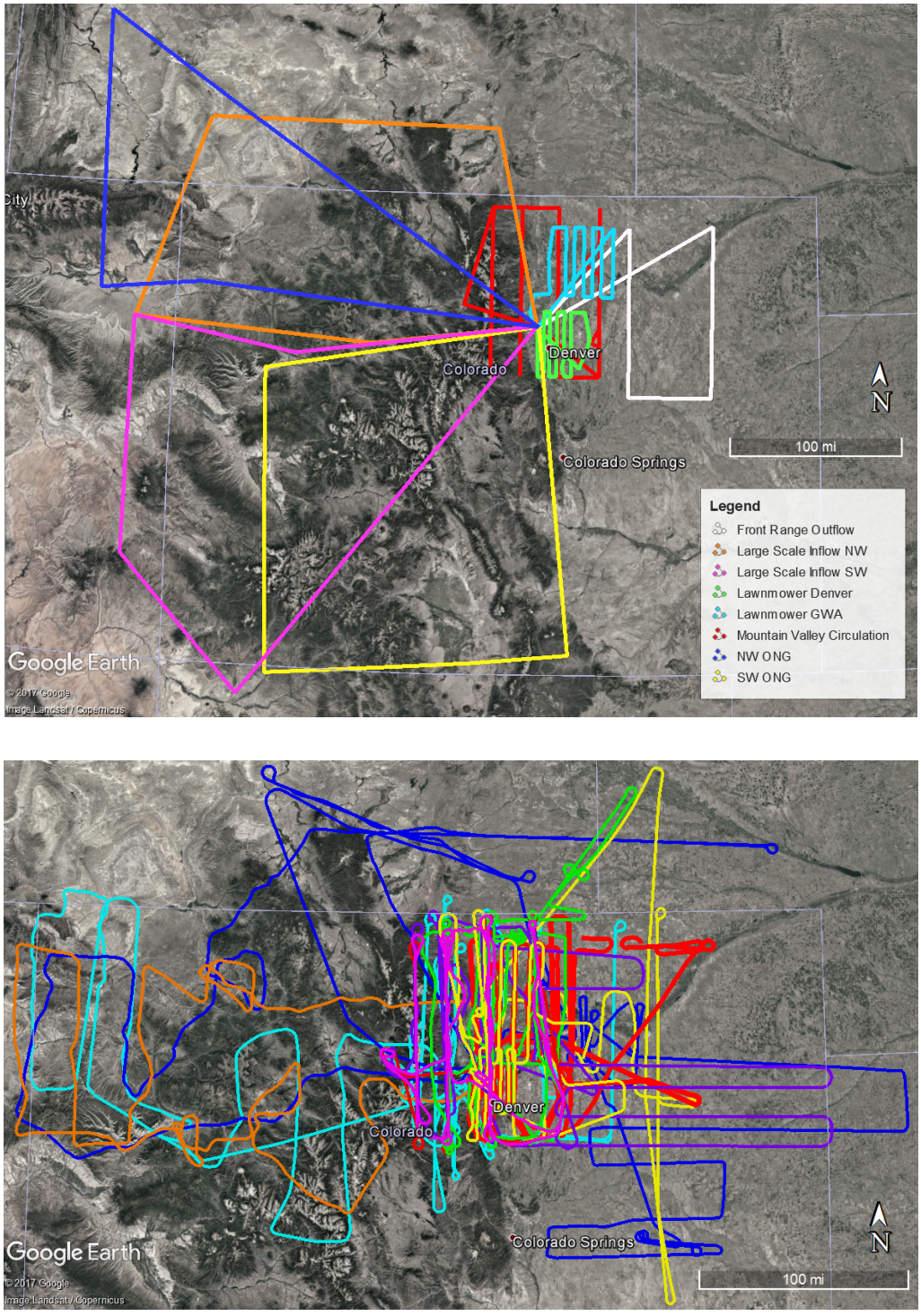

Figure 2.1 (Top) Map of generalized flight plans and areas of research focus during the campaign. (Bottom) Actual flight paths for all 15 research flights during the FRAPPÉ campaign.

Table 2.1 Flight information for all research flights flown by the C-130 during FRAPPÉ.

Flight	Date, 2014	Takeoff, UTC	Duration, Hours	Primary objective
1	07/26	15:40	4:06	NFRMA emissions
2	07/27	17:14	4:30	NFRMA emissions
3	07/28	16:32	4:20	NFRMA emissions
4	07/29	14:57	3:40	Large scale inflow NW
5	07/31	19:55	5:15	Mountain-valley circulation
6	08/02	21:00	4:49	Mountain-valley circulation
7	08/03	20:27	4:32	Mountain-valley circulation
8	08/06	16:00	4:30	Large scale inflow NW and SW
9	08/07	16:35	4:45	NFRMA emissions, NE emission pattern
10	08/08	14:54	3:30	Large scale inflow E
11	08/11	18:24	4:58	Mountain-valley circulation
12	08/12	18:04	8:22*	Mountain-valley circulation
13	08/15	15:20	9:04*	Large scale inflow NW, Front range outflow
14	08/16	17:12	4:32	Front range outflow
15	08/17	16:00	10:41*	Mountain-valley circulation, Large scale inflow NW/ SW

* Includes a ~1-hour refuel stop.

2.2 Campaign Measurements

Onboard the NSF/NCAR C-130, there was a suite of instruments used to measure meteorological conditions, aerosols and their microphysical properties, and gas-phase chemistry. Here we will discuss the measurements made throughout the campaign used in this work.

2.2.1 FRAPPÉ Airborne Measurements

During this campaign, 775 AWAS samples were collected onboard the C-130. *In-situ* samples are collected through a forward-facing inlet on the exterior of the plane and plumbed to a metal bellows dual-stage pump into a manifold of evacuated 1.3 L stainless steel whole air canisters. Canisters were arranged in modules of 12 canisters and 5 modules were collected per flight allowing for up to 60 samples. The canisters are separated from the manifold via an air-actuated valve. When a sample is collected, a command from a computer controller closes the exhaust valve and pressurizes the manifold to a limit that is preset by a pressure relief valve. Once the manifold is pressurized, the computer opens the canister, pressurizes it to a preset limit,

and closes the canister. A schematic of the manifold is shown in Figure 2.2. A schematic of the module and pump of the rack the manifold is contained in on the plane is also shown (Atlas & UCAR/NCAR - Earth Observing Laboratory, 2009). For more information regarding the AWAS system, readers are referred to Andrews et al., 2016.

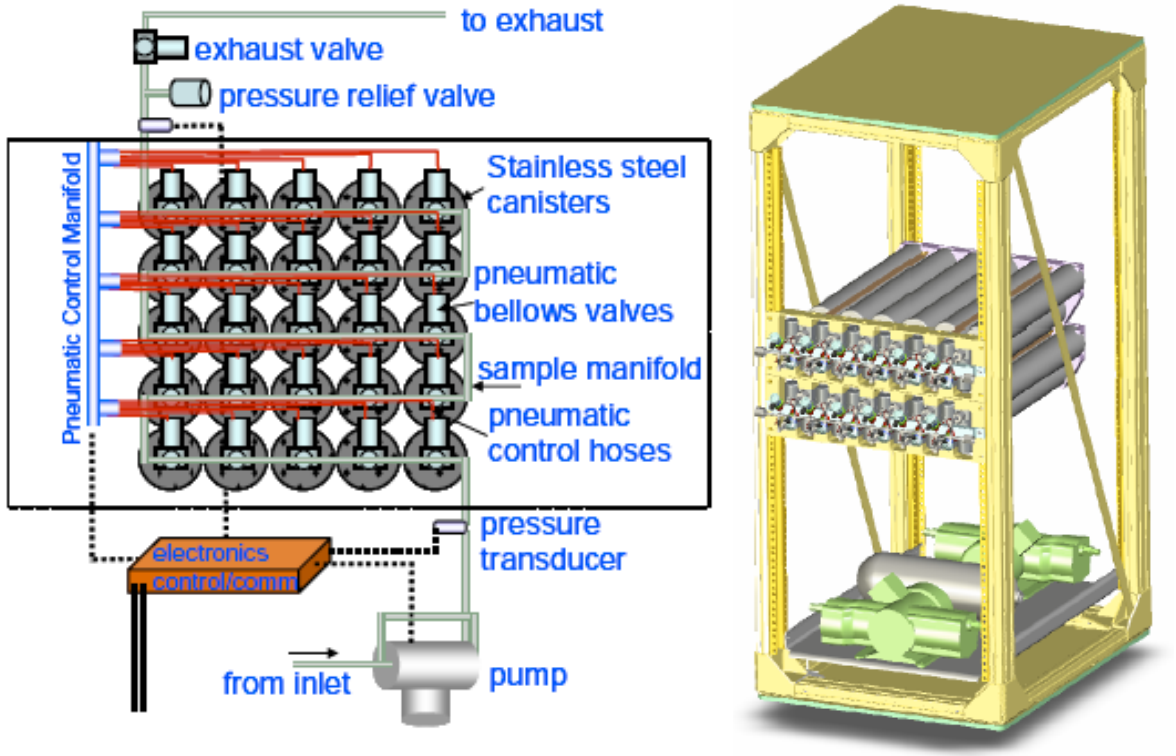

Figure 2.2 (Left) Components of the *AWAS*. (Right) *AWAS* modules and pump in rack. (Atlas & UCAR/NCAR - Earth Observing Laboratory, 2009)

AWAS samples were pressurized to 50 psig over the course of ~10 seconds. Sampling frequency depended on the location, altitude, and objective of the flight and ranged from 30 seconds to 10 minutes. Once filled, modules were shipped to UC Irvine to be analyzed by gas chromatography, described in section 2.3. After analysis, select samples were transferred to glass vials for CH_4 isotope analysis at the University of Cincinnati via isotope ratio mass spectrometry (IRMS) (Yarnes, 2013; Townsend-Small et al., 2016). Figure 2.3 shows the location of all AWAS samples collected during this campaign.

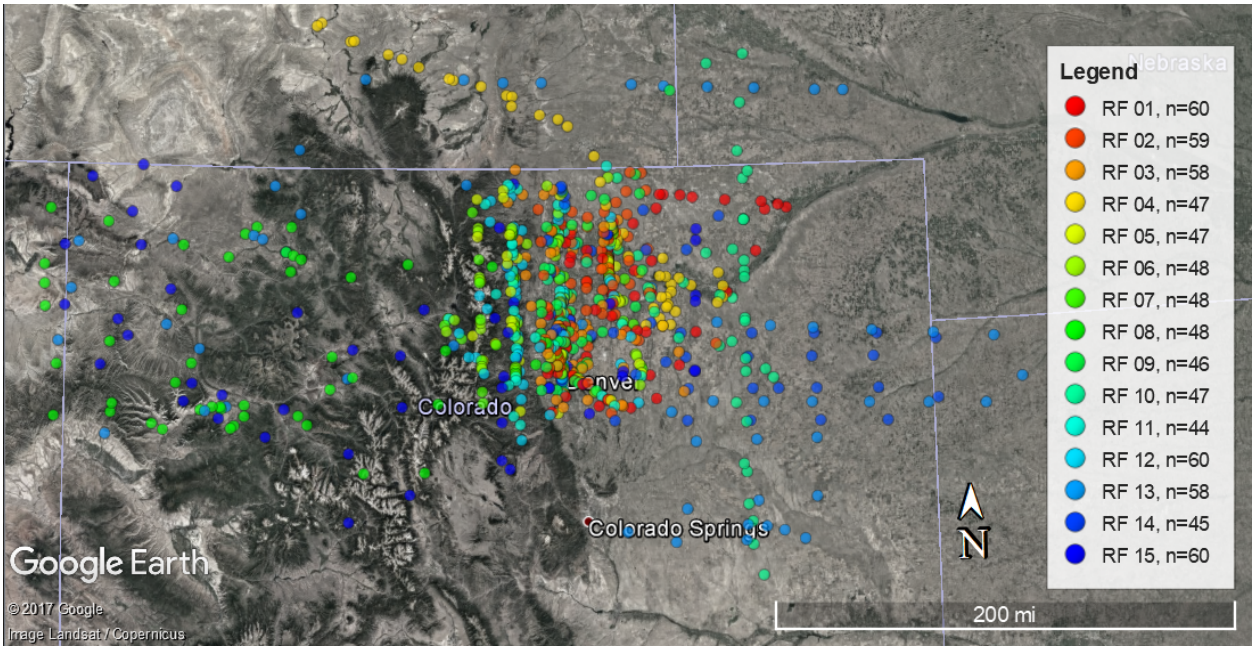

Figure 2.3 Location of AWAS samples collected onboard the C-130. Sample locations are colorized by research flight (RF) number and the number of samples collected (n) per flight is shown in the legend.

One second measurements of various trace gas species were also collected onboard the C-130. Methane, carbon dioxide, and water vapor 1Hz measurements were obtained via wavelength-scanned cavity ring down spectroscopy using a Picarro G2311-f operated by the NCAR Atmospheric Chemistry Observations and Modeling (ACOM) laboratory (Campos & Flocke, 2015). Carbon monoxide measurements were obtained via the Aero-Laser AL-4002 Vacuum UV Resonance Fluorescence instrument operated by NCAR ACOM (Campos & Flocke, 2015). Ethane and formaldehyde measurements were made using the Compact Atmospheric Multispecies Spectrometer (CAMS) instrument which uses absorption spectroscopy with an advanced fiber optically pumped difference-frequency generation laser source, operated by the University of Colorado, Boulder Institute of Arctic and Alpine Research (INSTAAR) (Weibring et al., 2007). Ozone and NO_x measurements were made using chemiluminescence operated by NCAR ACOM (Ridley et al., 2004). Sulfur dioxide, SO_2 measurements were made using a chemical ionization mass spectromenter (CIMS) (Huey, 2007). For a more detailed list of

instruments and species measured during the FRAPPÉ campaign, readers are referred to https://www2.acom.ucar.edu/frappe/participants.

Table 2.2 List of instruments onboard the NSF/NCAR C-130 and species analyzed for use in this dissertation.

Instrument	Species Measured	PI, Institution	Reference
AWAS	VOCs	Blake, UC Irvine	Colman et al., 2001
AWAS	CH_4 Isotopes	Townsend-Small, U Cin.	Yarnes, 2013
Picarro G2311-f	CH_4, CO_2, H_2O vapor	Campos, NCAR ACOM	Campos et al., 2015
Aero-Laser AL 5002	CO	Campos, NCAR ACOM	Campos et al., 2015
CAMS	C_2H_6, HCHO	Fried, CU INSTAAR	Weibring et al., 2007
Chemiluminescence	O_3, NO, NO_2	Weinheimer, NCAR ACOM	Ridley et al., 2004
CIMS	SO_2	Huey, Georgia Tech	Huey, 2007

2.2.2 FRAPPÉ Surface Measurements

Surface whole air samples were collected throughout Colorado during the campaign with sample locations chosen based on the flight path. Sample locations were also chosen to provide a more detailed analysis of emission sources within and outside of the NFRMA. A total of 248 ground samples were collected during FRAPPÉ from July 17th through August 13th, 2014 upwind and downwind of point sources such as ONG fields, landfills, feedlots, and throughout the GWA gas field. Samples were also collected at fixed ground sites in Rocky Mountain National Park (n=30) and at various altitudes to correspond to mountain-valley circulation flights. Samples collected at Golden (n= 73), Platteville (n=35), and Chatfield (n=6) were collected to correlate with the DISCOVER-AQ campaign, discussed in section 2.2.3. Samples were collected in 2 L electropolished evacuated stainless-steel canisters with a Nupro/Swagelock SS-4BG bellows-sealed valve. A map of the location of ground samples collected is shown in Figure 2.4.

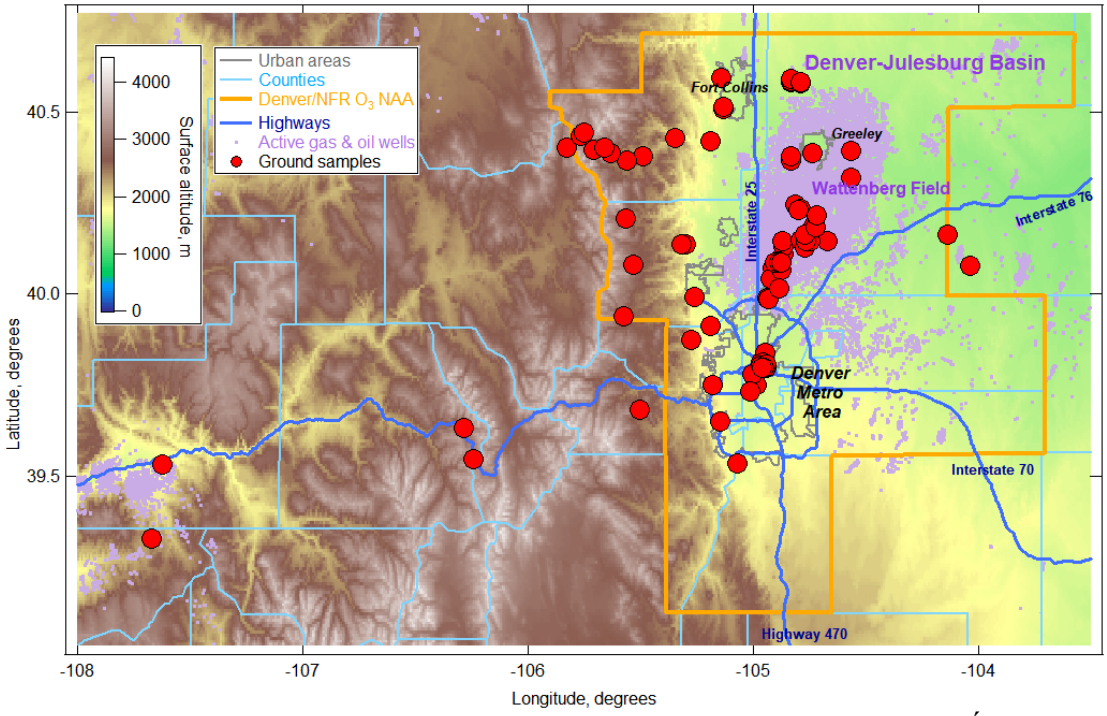

Figure 2.4 Map of the location of ground samples collected during FRAPPÉ.

2.2.3 DISCOVER-AQ Measurements

The DISCOVER-AQ campaign conducted a series of spirals from the NASA P3-B throughout the NFRMA to create column measurements to improve satellite measurements of surface pollution. The spiral sites chosen were air quality monitoring sites maintained by the CDPHE or NOAA. Data from this campaign were used to supplement the FRAPPÉ data set, such as detailed information of boundary layer conditions throughout the NFRMA.

One second measurements of CH_4, CO, and N_2O were collected via a diode laser spectrometer, the Differential Absorption Carbon Monoxide Measurement (DACOM) instrument, operated by NASA Langley (Warner et al., 2010). Water vapor 1Hz measurements were made via a Diode Laser Hygrometer (DLH), operated by NASA Langley (Diskin et al., 2002). Non-methane hydrocarbons were measured using a proton transfer reaction time of flight mass spectrometer (PTR-ToF-MS) at frequences varying from 1 Hz to 20 Hz, operated by the University of Innsbruck (Muller et al., 2014). A table of the measurements used from the

DISCOVER-AQ campaign are shown in Table 2.3 and a schematic of the flight flight plan is shown in Figure 2.5.

Table 2.3 List of instruments onboard the NASA P3-B and species analyzed for use in this dissertation.

Instrument	Species Measured	PI, Institution	Reference
DACOM	CH_4, CO, N_2O	Diskin, NASA Langley	Warner et al., 2010
DLH	H_2O vapor	Diskin, NASA Langley	Diskin et al., 2002
PTR-ToF-MS	NMHCs	Wisthaler, U. Innsbruck	Muller et al., 2014

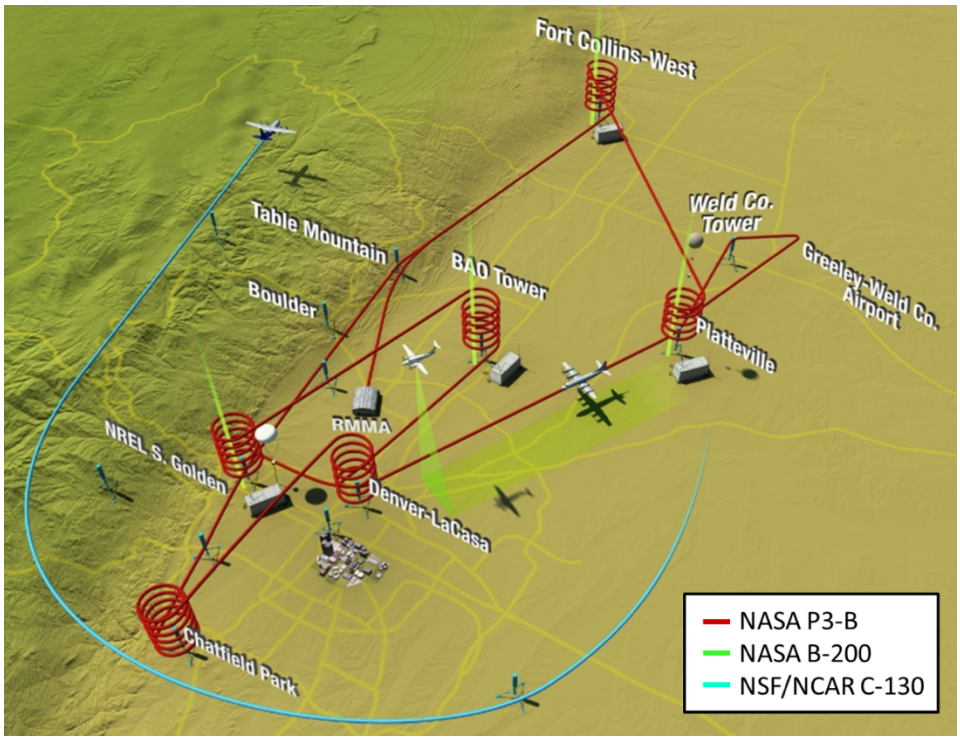

Figure 2.5 DISCOVER-AQ flight pattern shown in red. The NASA P3-B performed spirals over surface sites while the NSF/NCAR C-130 flight paths covered the entire study area. Image courtesy of NASA https://www.nasa.gov/larc/2014-discoveraq-campaign/.

2.3 VOC Measurements

2.3.1 Canister Preparation

a. AWAS Canisters

The AWAS canisters used on the C-130 were electropolished stainless-steel canisters sealed with pneumatic Swagelok bellows valves. Before use, each module is placed in an oven and connected to a pump system. The modules were then evacuated, and leak checked using a

helium leak detector. Once leak checked, the canisters were opened and evacuated to 30 mTorr and the oven is heated to 80 ºC. While in the oven, the canisters were pumped and flushed 10 times with nitrogen gas to 760 Torr. Canisters were then evacuated to 30 mTorr and the oven cooled to room temperature. Once at room temperature, 5 Torr of water vapor was added to the modules and the cans are closed (Andrews et al., 2016).

b. WAS Canisters

The WAS canisters used for ground sampling were also electropolished stainless steel and were preconditioned before sample collection. The canisters are subject to 20 rounds of pumping and flushing using ambient air pressurized to 40 psig. The canisters are then opened and placed in a humidified oven to bake at 150 ºC for approximately 20 hours. This process creates an oxidized surface on the interior of the canister to prevent surface adsorption (Sive, 1998). Once baked and cooled to room temperature, the canisters are again pumped and flushed a minimum of 10 times with air collected in a cylinder at the White Mountain Research Station (WMRS) in Bishop, CA. The WMRS is an isolated facility located at 10,200 ft above sea level in the Western Sierra Mountains, far from pollution sources. After pumping and flushing, canisters were left pressurized with WMRS air for a minimum of 24 hours to test for leaks. The canisters are then evacuated, pressurized to 200 Torr with ultra-high purity helium, and then evacuated to 10^{-2} Torr and closed and set aside for a minimum of one week. The canisters are then rechecked for leaks and then sent to the field (Sive, 1998; Colman et al., 2001; Baker, 2007; Simpson et al., 2010).

All airborne and ground samples were analyzed using a NMHC gas chromatography system. Additionally, ground samples were also analyzed for CH_4, CO, and CO_2. Here all three systems used during analysis are discussed.

2.3.2 Analysis

a. Methane

Methane analysis is performed using an HP 5890 gas chromatograph (GC). The sample is loaded into an evacuated manifold and sample loop and pressurized to 400 Torr. Once isolated in the sample loop, the sample is injected and a nitrogen carrier gas is used to carry the sample to the column at a rate of 30 mL min^{-1}. The sample is then injected into a 0.9 m stainless steel column with a diameter of 1/8 in and packed with 80/100 mesh molecular sieve Spherocarb. The GC is kept at a constant temperature of 85 ºC and after being separated in the column, CH_4 is detected using a Flame Ionization Detector (FID). The signal is recorded using a Spectra-Physics Chromjet Integrator.

Throughout analysis, a working standard of 1.771 ppmv CH_4 is analyzed after every eight injections and used to determine a response factor. The recorded peak heights of the samples are compared to the standard to determine the concentration of methane within each sample. For a more thorough description of this system, readers are referred to Blake (1984).

b. Carbon Monoxide and Carbon Dioxide

Carbon monoxide analysis is performed using an HP 5890 GC equipped with an FID. The sample is loaded onto the evacuated manifold to a pressure of 500 Torr. Once isolated in the sample loop, the sample is injected and a helium carrier gas is used to carry the sample to the column, a 3 m long, 1/4 in diameter stainless steel 80/100 mesh molecular sieve 5A column. During the 7.6 min analysis time, the GC temperature is increased from 60 ºC to 110 ºC.

FIDs are sensitive only to carbon-carbon or carbon-hydrogen bonds, and therefore the FID was equipped with a methanizer to catalytically hydrogenate CO using a nickel catalyst. Once eluted from the column, the sample is mixed with a hydrogen carrier gas and directed to

the catalyst which is held at a constant temperature of 365 ºC. This process converts CO to CH_4, reaction 2.1, which can then be detected by the FID (Habazakia et al., 1998). For a more thorough description of this system, readers are referred to Lopez (2002).

$$CO + 3H_2 \xrightarrow{N_2} CH_4 + H_2O \quad (2.1)$$

For CO_2 analysis, an HP 5890 GC equipped with a thermal conductivity detector (TCD) is used. Utilizing the same manifold for CO analysis, samples are injected into 80/100 Carbosphere packed 2 m long column with a diameter of 1/8 in. The GC temperature increases from 150 ºC to 220 ºC during analysis time. Using a helium carrier gas, the sample is directed to the TCD that compares the conductivity of the carrier gas to the sample to produce a signal.

During the analysis of CO and CO_2, a standard is analyzed after every eight samples are injected. The standard is used to determine the concentration of CO and CO_2 within the sample and contains 192 ppbv CO and 364 ppmv CO_2. The signals from the FID and the TCD are both quantified using Chromeleon chromatography software.

c. Non-Methane Hydrocarbons

NMHC analysis was performed using three separate Hewlett-Packard 6890 GCs, each equipped with two columns and two detectors. Samples were loaded onto an evacuated manifold to a pressure of 900.0 Torr. Once isolated on the manifold, a 2033 cm^3 aliquot of sample enters a 5 cm^3 preconcentration loop packed with glass beads and immersed in liquid nitrogen. This was used to remove the most volatile components (N_2, O_2, Ar), and cryogenically condense analytes of interest on the glass beads. Once the volatile components have been removed, the preconcentration loop is immersed in a bath of near boiling water to revolatilize the sample. The GCs are cryogenically cooled to an initial temperature and the sample is injected with a helium carrier gas into a splitter box which reproducibly partitions the sample before it is directed to the

six separate columns. For the analysis of C_2-C_{10} hydrocarbons, a DB-1 column was used connected to an FID. Separation of C_2-C_7 hydrocarbons was accomplished using a GS-alumina porous layer open tubular (PLOT) column in series with a DB-1 column connected to an FID. For halocarbons and alkyl nitrates, a Restek-1701 column connected to an electron capture detector (ECD) was used. Halocarbons and alkyl nitrates were also analyzed using a DB-5 column in series with a Restek-1701 column connected to an ECD. Aromatic compounds were analyzed via a Cyclodex column connected to an FID. Unambiguous detection of all compounds was accomplished via a DB-5MS column connected to a HP 5973 quadrupole mass selective detector (MSD). Figure 2.6 shows the NMHC analysis system and Table 2.4 shows detailed information for each column and GC used in this analysis (Sive, 1998). Compounds analyzed by this system and used in this dissertation are shown in Table 2.5.

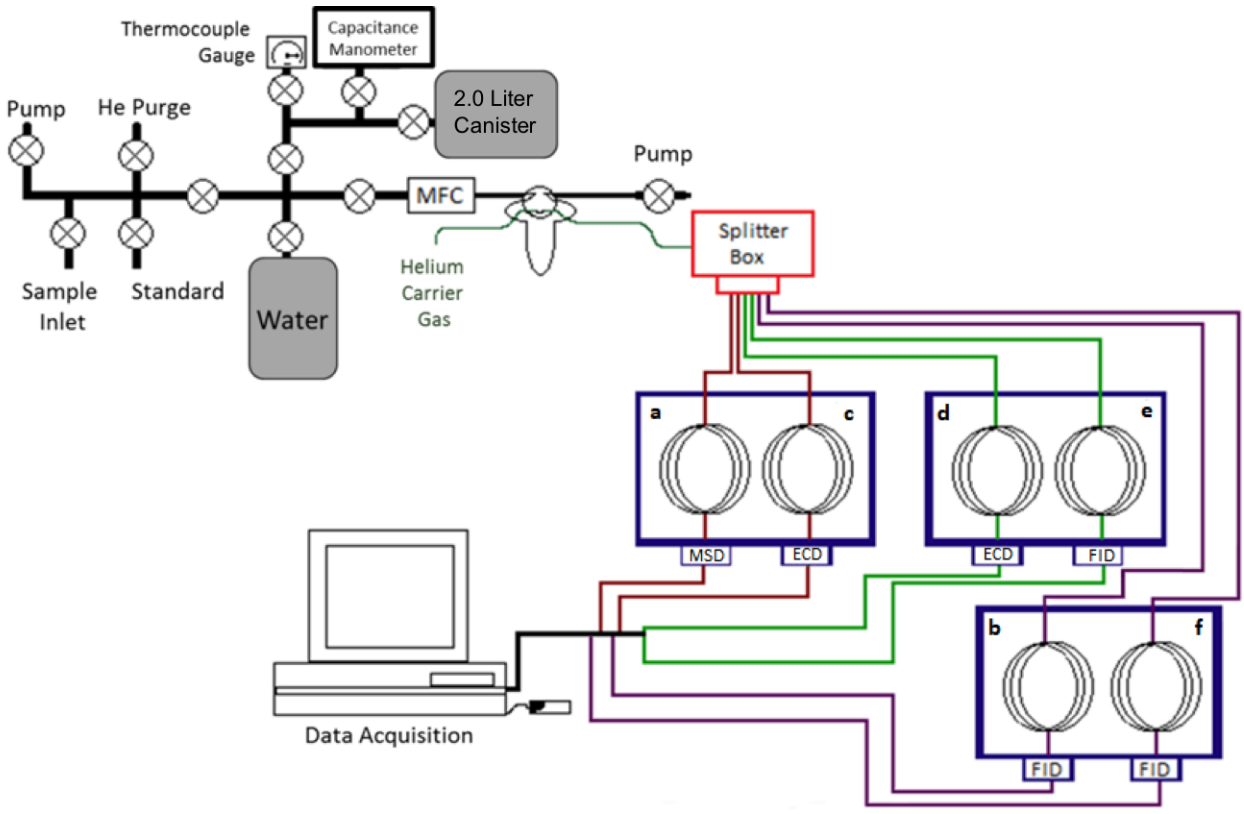

Figure 2.6 Schematic of GC system used for NMHC analysis.

Table 2.4 Column information and GC parameters and temperature program information used during NMHC analysis.

GC	1		2		3	
Column ID	A	C	D	E	B	F
Detector	MSD	ECD	ECD	FID	FID	FID
Column Section 1	DB-5ms	DB-5	Restek-1701	GS-AluminaPLOT	DB-1	Cyclodex
Column Section 1 length, *m*	60	30	60	30	60	30
Column Section 1 width, *mm*	0.25	0.25	0.25	0.53	0.32	0.25
Column Section 2	-	Restek-1701	-	DB-1	-	-
Column Section 2 width, *mm*	-	0.25	-	5	-	-
Column Section 2 length, *m*	-	5	-	0.53	-	-
Target Analytes	· Unambiguous	· Halocarbons · Alkyl nitrates	· Halocarbons · Alkyl nitrates	· C_2-C_7 hydrocarbons	· C_2-C_{10} hydrocarbons	· Aromatics
Initial Temp, *°C*	-60	-60	-20	-20	-60	-60
Wait Time 1, *min*	1.5	1.5	1.5	1.5	1.5	1.5
Rate 1, *°C* min^{-1}	15	15	30	30	10	10
Temp 2, *°C*	110	110	60	60	0	0
Wait Time 2, *min*	0	0	0	0	0	0
Rate 2, *°C* min^{-1}	29	29	14	14	17	17
Temp 3, *°C*	220	220	200	200	145	145
Wait Time 3, *min*	1.88	1.88	4.34	4.34	0	0
Rate 3, *°C* min^{-1}	-	-	-	-	65	65
Temp 4, *°C*	-	-	-	-	200	200
Wait time 4, *min*	-	-	-	-	1.2	1.2
Received flow, *%*	10.1	11.4	9.4	47.5	12.2	9.4
Total Run Time, *min*	18.5	17.5	17.5	17.5	18.5	18.5

Table 2.5 NMHCs measured during FRAPPÉ. Included is the limit of detection (LOD) and the precision and accuracy of each compound measured. Lifetimes were calculated assuming 295 K and 1 atm (Colman et al., 2001; Atkinson et al., 2006; Simpson et al., 2010).

	Formula	Lifetime	LOD *pptv*	Precision *%*	Accuracy *%*
Hydrocarbons					
Ethane	C_2H_6	47 d	3	1	5
Ethene	C_2H_5	1.4 d	3	3	5
Ethyne	C_2H_2	12-17 d	3	3	5
Propane	C_3H_8	11 d	3	2	5
Propene	C_3H_6	11 hr	3	3	5
Propyne	C_3H_4	2 d	3	30	20
n-Butane	C_4H_{10}	4.9 d	3	3	5
i-Butane	C_4H_{10}	5.5 d	3	3	5
1-Butene	C_4H_8	8.8 hr	3	3	5
i-Butene	C_4H_8	5.4 hr	3	3	5
cis-2-Butene	C_4H_8	4.9 hr	3	3	5
trans-2-Butene	C_4H_8	4.3 hr	3	3	5
1,3-Butadiene	C_4H_6	4.2 hr	3	3	5
n-Pentane	C_5H_{12}	5 d	3	3	5
i-Pentane	C_5H_{12}	5 d	3	3	5
Isoprene	C_5H_8	2.8 hr	3	3	5
2-Methypentane	C_6H_{14}	2-3 d	3	3	5
3-Methylpentane	C_6H_{14}	2-3 d	3	3	5
Benzene	C_6H_6	9.5 d	3	3	5
Toluene	C_7H_8	2.1 d	3	3	5
m+p-Xylene	C_8H_{10}	12-19 hr	3	3	5
o-Xylene	C_8H_{10}	20 hr	3	3	5
Ethylbenzene	C_8H_{10}	1.7 d	3	3	5
2-Ethyltoluene	C_9H_{12}	23 hr	3	3	5
3-Ethyltoluene	C_9H_{12}	15 hr	3	3	5
4-Ethyltoluene	C_9H_{12}	24 hr	3	3	5
1,2,3-Trimethylbenzene	C_9H_{12}	8.5 hr	3	3	5
1,2,4-Trimethylbenzene	C_9H_{12}	8.5 hr	3	3	5
1,3,5-Trimethylbenzene	C_9H_{12}	4.9 hr	3	3	5
α-Pinene	$C_{10}H_{16}$	5.3 hr	3	3	5
β-Pinene	$C_{10}H_{16}$	3.7 hr	3	3	5
Alkyl Nitrates					
Methyl nitrate	CH_3ONO_2	1 mo	0.02	5	10
Ethyl nitrate	$C_2H_5ONO_2$	2-4 wk	0.02	5	10
1-Propyl nitrate	$C_3H_7ONO_2$	1-2 wk	0.02	5	10
2-Propyl nitrate	$C_3H_7ONO_2$	1-3 wk	0.02	5	10
2-Butyl nitrate	$C_4H_9ONO_2$	1-2 wk	0.02	5	10
2-Pentyl nitrate	$C_5H_{11}ONO_2$	4-5 d	0.02	5	10
3-Pentyl nitrate	$C_5H_{11}ONO_2$	4-5 d	0.02	5	10

Table 2.5 (Cont.) NMHCs measured during FRAPPÉ. Included is the limit of detection (LOD) and the precision and accuracy of each compound measured. Lifetimes were calculated assuming 295 K and 1 atm (Colman et al., 2001; Atkinson et al., 2006; Simpson et al., 2010).

	Formula	Lifetime	LOD *pptv*	Precision *%*	Accuracy *%*
Halocarbons					
CFC-11	$CFCl_3$	45 yr	10	1	3
CFC-12	CF_2Cl_2	100 yr	10	1	3
CFC-113	CCl_2FCClF_2	85 yr	5	1	3
CFC-114	$CClF_2CClF_2$	300 yr	1	1	10
Methyl chloroform	CH_3CCl_3	5 yr	0.1	1	5
Carbon tetrachloride	CCl_4	26 yr	1	1	5
Halon-1211	$CBrClF_2$	16 yr	0.1	1	5
Halon-2402	$CBrF_2CBrF_2$	20 yr	0.01	1	5
HCFC-22	CHF_2Cl	12 yr	2	2	5
HCFC-134a	CH_2FCF_3	14 yr	1	3	10
HCFC-141b	CH_3CCl_2F	9.3 yr	0.5	3	10
HCFC-142b	CH_2CClF_2	18 yr	0.5	3	10
Methyl bromide	CH_3Br	0.7 yr	0.5	5	10
Methyl chloride	CH_3Cl	1 yr	50	5	10
Methyl iodide	CH_3I	4 d	0.005	5	20
Dibromomethane	CH_2Br_2	3-4 mo	0.01	5	20
Dichloromethane	CH_2Cl_2	3-5 mo	1	5	10
Chloroform	$CHCl_3$	3-5 mo	0.1	5	10
Trichloroethene	C_2HCl_3	5 d	0.01	5	10
Tetrachloroethene	C_2Cl_4	2-3 mo	0.01	5	10
1,2-Dichloroethane	$C_2H_4Cl_2$	1-2 mo	0.1	5	10
Bromoform	$CHBr_3$	11 mo	0.01	10	20
Bromodichloromethane	$CHBrCl_2$	2-3 mo	0.01	10	50
Dibromochloromethane	$CHBr_2Cl$	2-3 mo	0.01	10	20
Bromochloromethane	CH_2BrCl	5 mo	0.01	10	20
Sulfur Compounds					
Carbonyl sulfide	OCS	2.5 yr	10	2	10
Dimethyl sulfide	CH_3SCH_3	1-2 d	1	10	20
Dimethyl disulfide	CH_3SSCH_3	1 hr	10	2	10
Carbon disulfide	CS_2	2-3 d	10	2	10

After eight injections, a working standard with known concentrations of NMHCs were used to quantify the concentration of trace gases in samples. Samples detected by the ECDs and FIDs were quantified using Chromeleon software, and samples detected by the MSD were quantified using Enhanced ChemStation software by Agilent technologies. All peaks detected by this system were manually inspected to insure accurate analysis.

2.4 References

Andrews, S., Carpenter, L., Apel, E., Atlas, E., Donets, V., Hopkins, J., . . . Schauffler, S. (2016). A comparison of very short lived halocarbons (VSLS) and DMS aircraft measurements in the tropical west Pacific from CAST, ATTREX and CONTRAST. *Atmospheric Measurement Techniques, 9*, 521-5225.

Atkinson, R., Baulch, D., Cox, R., Crowley, J., Hampson, R., Hynes, R., . . . Troe, J. (2006). Evaluated kinetic and photochemical data for atmospheric chemistry: Volume II - gas phase reactions of organic species. *Atmospheric Chemistry and Physics, 6*(11), 3625-4055.

Atlas, E., & UCAR/NCAR - Earth Observing Laboratory. (2009). *Advanced Whole Air Smpler (AWAS) for HIAPER.* Retrieved October 24, 2017, from UCAR/NCAR - Earth Observing Laboratory: https://doi.org/10.5065/D65X270F

Baker, A. (2007). *Ground-based an Aircrafft Measurements of Volatile Organic Compounds in United States and Mexico City Urban Atmospheres.* University of California, Irvine.

Blake, D. (1984). *Increasing concentrations of atmospheric methane: 1979-1983.* University of California, Irvine: Ph.D. Thesis.

Campos, T., & Flocke, F. (2015). National Center for Atmospheric Research (NCAR), 2015: Aircraft Instrumentation - Gas Concentrations: CH4, CO2, H2O. Retrieved October 24, 2017, from https://www.eol.ucar.edu/node/208

Campos, T., & Flocke, F. (2015). *National Center for Atmospheric Research (NCAR), Aircraft Instrumentation - Gas Concentrations: CO*. Retrieved October 24, 2017, from https://www.eol.ucar.edu/node/219

Colman, J., Swanson, A., Meinardi, S., Sive, B., Blake, D., & Rowland, F. (2001). Description of the analysi of a wide range of volatile organic compounds in whole air samples collected during PEM-Tropics A and B. *Analytical Chemistry, 73*, 3723-3731.

Diskin, G., Podolske, J., Sachse, G., & Slate, T. (2002). Open-path airborne tunable diode laser hygrometer. (A. Fried, Ed.) *Proceedings of the Society for Photo-Optical Instrumentation Engineers, 4817*, 196-204.

Habazakia, H., Yamasakia, M., Zhanga, B., Kawashimaa, A., Kohnob, S., Takaic, T., & Hashimotoa, K. (1998). Co-methanation of carbon monoxide and carbon dioxide on supported nickel and cobalt catalysts prepared from amorphous alloys. *Applied Catalysts A: General, 172*(1), 131-140.

Huey, L. G. (2007), Measurement of trace atmospheric species by chemical ionization mass spectrometry: Speciation of reactive nitrogen and future directions, Mass Spectrom. Rev., 26(2), 166-184.

Lopez, J. (2002). *Seasonality and global growth trends of carbon monoxide 1995-2001.* University of California, Irvine: Ph.D. Thesis.

Muller, M., Mikoviny, T., Feil, S., Haidacher, S., Hanel, G., Hartungen, E., . . . Wisthaler, A. (2014). A compact PRT-ToF-MS instrument for airborne measurements of volatile organic compounds at high spatiotemporal resolution. *Atmospheric Measurement Techniques, 7*, 3763-3772.

Ridley, B., Ott, L., Pickering, K., Emmons, L., Montzka, D., Weinheimer, A., . . . Brasseur, G. (2004). Florida Thunderstorms: A faucet of reactive nitrogen to the upper troposphere. *Journal of Geophysical Research, 109*(D17305).

Simpson, I., Blake, N., Barletta, B., Diskin, G., Fuelberg, H., Gorham, K., . . . Blake, D. (2010). Characterization of trace gases measured over Alberta oil sands mining operations: 76 speciated C2-C10 volatile organic compounds (VOCs), CO, CO2, CH4, CO, NO, NO2, NOy, O3 and SO2. *Atmospheric Chemistry and Physics, 10*, 11931-11954.

Sive, B. (1998). *Atmospheric Nonmethane Hydrocarbons: Analytical Methods and Estimated Hydroxyl Radical Concentrations.* University of California, Irvine.

Townsend-Small, A., Tyler, S., Pataki, D., Xu, X., & Christensen, L. (2012). Isotopic measurements of atmospheric methane in Los Angeles, California, USA: Influence of "fugitive" fossil fuel emissions. *Journal of Geophysical Research, 117*(D07308).

Warner, J., Wei, Z., Strow, L., Barnet, C., Sparling, L., Diskin, G., & Sachse, G. (2010). Improved agreement of AIRS tropospheric carbon monoxide products with other EOS sensors using optimal estimation retrievals. *Atmospheric Chemistry and Physics, 10*, 9521-9533.

Weibring, P., Richter, D., Walega, J., & Fried, A. (2007). First Demonstration of a High Performance Difference Frequency Spectrometer on Airborne Platforms. *Optics Express, 15*, 13476-13495.

Yarnes, C. (2013). δ13C and δ2H measurement of methane from ecological and geological sources by gas chromatography/combustion/ pyrolysis isotope-ratio mass spectrometry. *Rapid Comminicatoins Mass Spectrometry, 27*, 1036-1044.

3. QUANTIFYING GASEOUS EMISSIONS IN THE COLORADO NORTHERN FRONT RANGE METROPOLITAN AREA

There have been several studies regarding inventory emission estimates from the oil and natural gas industry that have determined that bottom-up methane emissions from this sector have been underestimated (Pétron et al., 2012; Gilman et al., 2013; Karion et al., 2013; Peischl et al., 2015). In 2014, the Colorado Department of Public Health and Environment estimated that natural gas and oil systems represented 7.7% of Colorado's total greenhouse gas emissions and 39% of total CH_4 emissions. It is projected that emissions from the ONG sector will increase to 47% by 2020 and 51% by 2030 of total CH_4 in the state (Arnold, Dileo, & Takushi, 2014). A study from the Boulder Atmospheric Observatory (BAO) tower in 2013 estimated that 72% of ethane, 94% of butanes, 96% of pentanes, and 32% of benzene in Northeastern Colorado are a result of ONG fugitive emissions (Gilman et al., 2013). The ONG industry is a non-trivial source of VOC emissions in the NFRMA and source characterization and emission estimates are vital in reducing the impact oil and natural gas systems have on regional air quality.

This chapter will focus on data collected in the NFRMA on the eastern side of the Rocky Mountains and characterize methane and other trace gas sources in this region. Here we present atmospheric methane emission estimates measured during FRAPPÉ in the Colorado Front Range on the NCAR C-130. Also presented is information from other hydrocarbons measured from whole air samples to attribute methane emissions to urban, agricultural, and/or oil and natural gas (ONG) sources. This work expands on previous studies in this area (Pétron et al., 2012; Gilman et al., 2013; Townsend-Small et al., 2016) by providing a detailed analysis of VOCs on a regional scale.

3.1 NFRMA Emissions

During FRAPPÉ, emissions over the GWA were observed and were found to contain enhanced mixing ratios of several VOCs. Research flights 1, 2, 3, and 9 on July 26th, 27th, 28th, and August 7th, respectively, consisted of the lawnmower pattern over the NFRMA designed to assess emission sources in this area. Flight 9, however, was excluded from this analysis as a passing storm system created a stratified atmosphere with a very shallow boundary layer. As a result, the majority of measurements during this flight were collected above the boundary layer and thus are excluded from this analysis. Flights 5, 6, 7, 11, 12 and 15 consisted of a similar north – south pattern throughout the NFRMA but were not used in this analysis as these flights characterized the mountain-valley circulation effect and samples collected would misrepresent emissions directly from the NFRMA.

A study of the analysis of the air free gas composition of unprocessed natural gas in the GWA determined that the major components of natural gas in this area are methane, at 77.6 ± 5.3%, and ethane at 11.8 ± 2.8% (COGCC, 2007), while residential and commercial delivery natural gas in Denver reported by Xcel Energy, a utility company with holdings in Colorado, contained 83.1% methane and 8.0% ethane (personal communication D. Bon Dec. 30, 2017). We can therefore use this relationship to examine ONG influence in the NFRMA. Figure 3.1 shows flight paths in the NFRMA colorized by 1-Hz methane and ethane measurements. The variability in CH_4 and other trace gas measurements collected within the boundary layer is due to the distribution of emission sources in the GWA. As shown in Figure 3.1, methane and ethane emissions are concentrated downwind of the GWA to the western side of the NFRMA due to prevailing easterly winds across the basin, as shown in a corresponding wind rose constructed using 1-minute wind speed and direction averages collected at the NOAA Platteville ground

station (Figure 3.1a, 3.2, and 3.9). Downwind enhancements of hydrocarbons associated with ONG emissions measured during this campaign, such as the C_1-C_5 alkanes, were significantly elevated over the GWA compared to background concentrations, indicative of fugitive emissions from local ONG infrastructure. Oxygenates, such as methanol and ethanol, commonly emitted from dairies, were only slightly enhanced. A summary of measurements of select trace gases from flights 1, 2, and 3 and downwind enhancements are shown in Table 3.1.

During flights 2 and 3, the Denver Cyclone, a gyre that forms near the city center, was present (Wilczak & Glendening, 1988). During these flights, the gyre can clearly be seen when examining the distribution of trace gases over the NFRMA. The Denver cyclone was strongest during flight 2 and corresponding downwind enhancements were decreased. These flights were still used to assess NFRMA emission sources as easterly winds dominated both at the surface and aloft. Figure 3.2 shows wind roses constructed using 1 Hz data from the aircraft, filtered to represent measurements collected within the boundary layer and north of 40.0º latitude. As downwind emission enhancements were statistically greater than measurements made upwind of the basin, and easterly winds dominated during both research flights, we can conclude that emission estimates using downwind enhancements from flights 2 and 3 are valid in this assessment.

From the analysis of CO, a trace gas most commonly associated with vehicular combustion (Fujita et al., 1992; Harley et al., 2001; Parrish et al., 2006; Baker et al., 2008), we can determine the extent of urban emissions within the GWA. As shown in Figure 3.3, CO was most enhanced over the Denver metropolitan area, and only slightly enhanced over downwind transects (Table 3.1). Ethyne, another combustion tracer (Sachsse, 1954; Blake et al., 2003; Guo et al., 2007; Warneke et al., 2007), was only slightly elevated in downwind transects at 240 ± 90

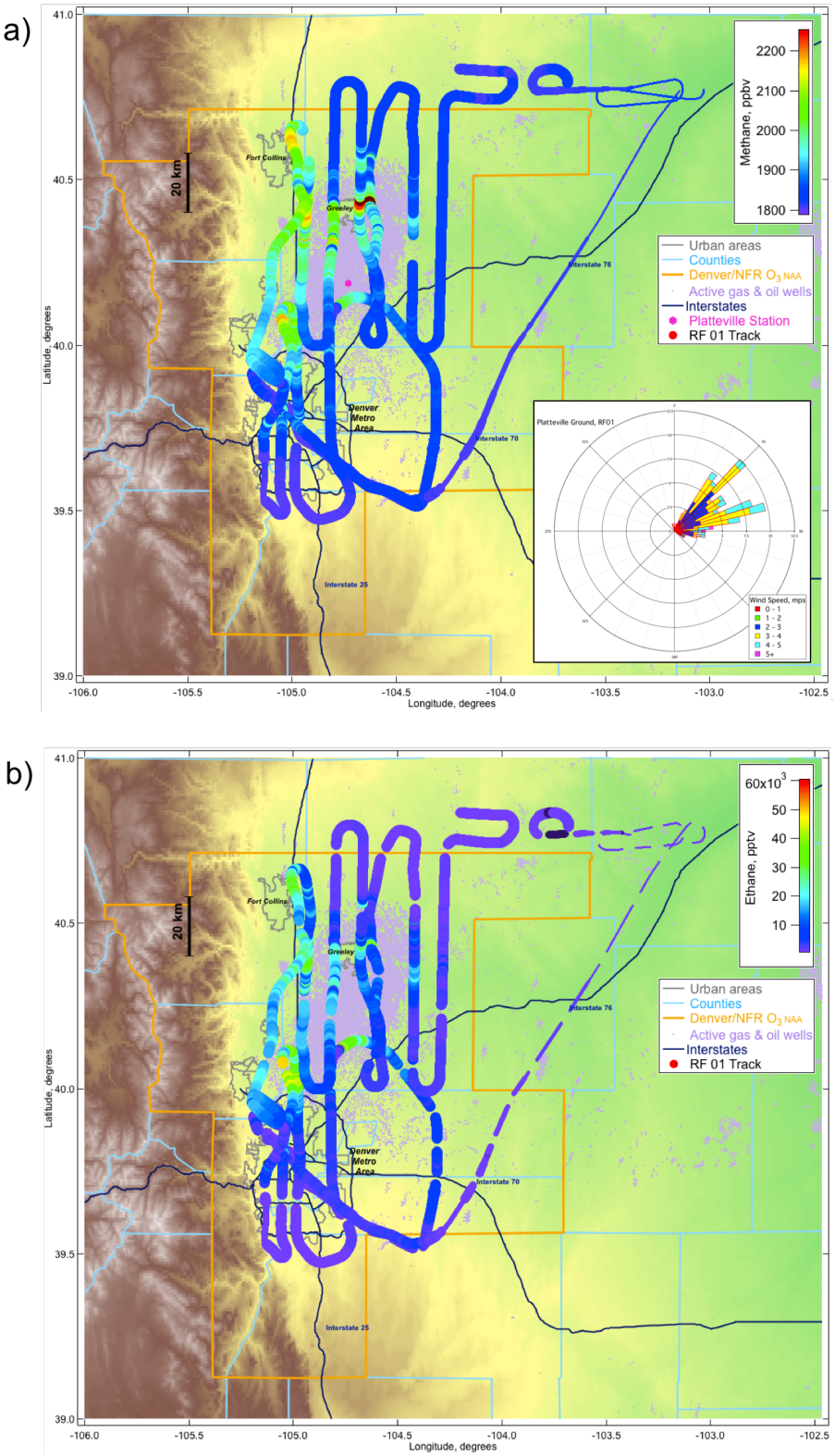

Figure 3.1 Map of research flights 1, 2, and 3 colorized by methane (a, c, d) and ethane (b, d, f) concentration. Points are sized by altitude. Figures a, c, and d include a wind rose constructed using continuous 1-min averaged wind data collected by NOAA at the Platteville ground station (pink).

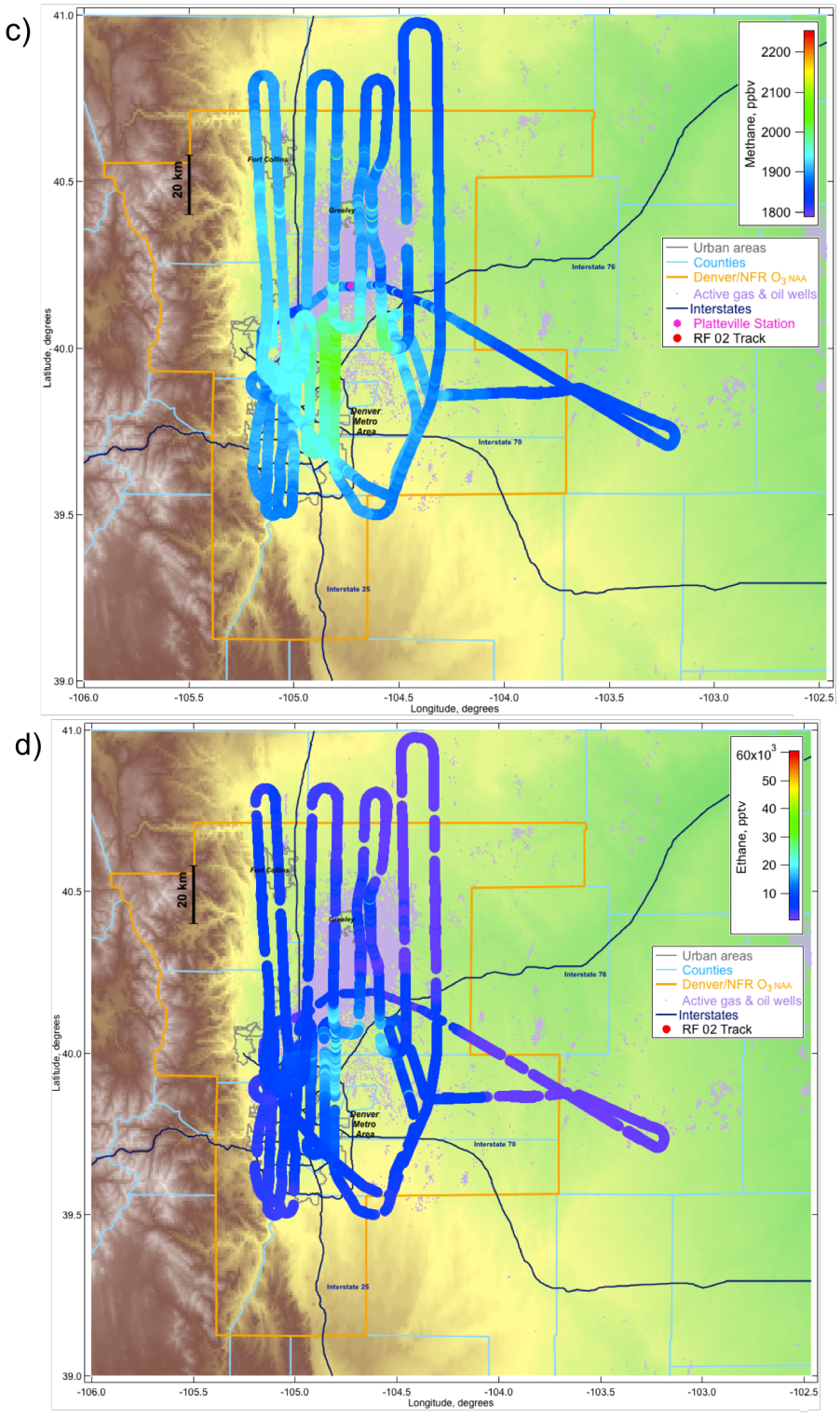

Figure 3.1 (Cont.) Map of research flights 1, 2, and 3 colorized by methane (a, c, d) and ethane (b, d, f) concentration. Points are sized by altitude. Figures a, c, and d include a wind rose constructed using continuous 1-min averaged wind data collected by NOAA at the Platteville ground station (pink).

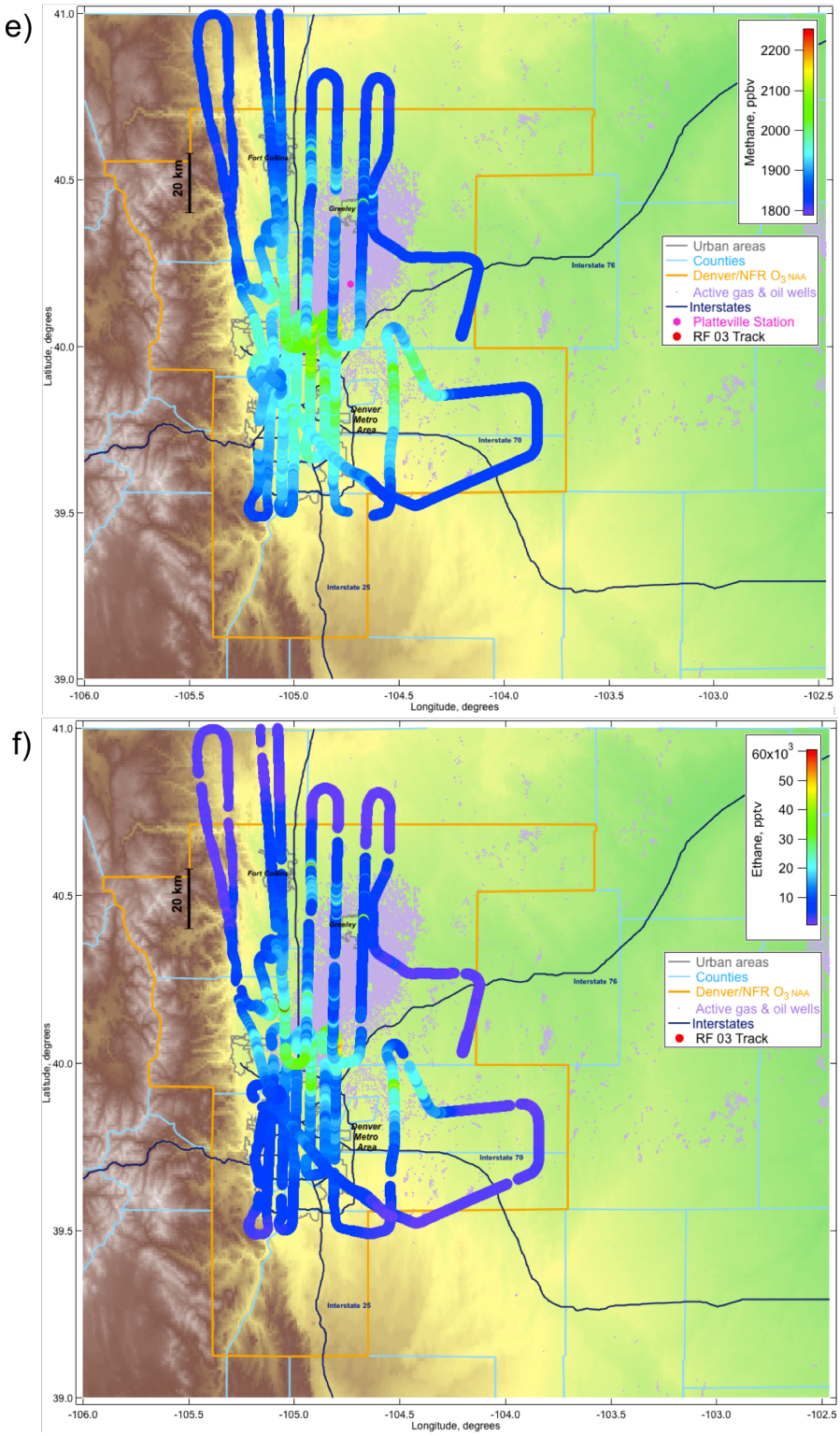

Figure 3.1 (Cont.) Map of research flights 1, 2, and 3 colorized by methane (a, c, d) and ethane (b, d, f) concentration. Points are sized by altitude. Figures a, c, and d include a wind rose constructed using continuous 1-min averaged wind data collected by NOAA at the Platteville ground station (pink).

Table 3.1 Statistics of trace gases measured during upwind and downwind transects during flights 1, 2, and 3. CO, CH_4, and C_2H_6 data were collected using 1-Hz measurements and are in units of ppbv. $C_3 - C_6$ hydrocarbons are from AWAS samples and in units of pptv, upwind n=13 (n_1=5, n_2=5, n_3=3) and downwind n=12 (n_1=4, n_2=5, n_3=3).

		Upwind				Downwind			
		Min	Median	Max	**Mean**	Min	Median	Max	**Mean**
Flight 1	CO	98	103	112	**103±2**	110	127	171	**132±13**
	CH_4	1821	1844	1856	**1843±6**	1897	2014	2180	**2013±69**
	C_2H_6	1.0	1.8	6.1	**2.0±0.8**	11.2	19.3	33.6	**20.4±5.0**
	C_3H_8	459	1436	1883	**1180±640**	13.2*	16.5*	20.6*	**16.7±3.4***
	nC_4H_{10}	116	601	775	**490±320**	6129	8368	10117	**8245±1825**
	iC_4H_{10}	55	187	240	**160±90**	2205	2969	3501	**2910±650**
	nC_5H_{12}	37	183	261	**150±100**	1972	2823	3501	**2780±702**
	iC_5H_{12}	46	162	212	**140±80**	1770	2491	3221	**2493±658**
	$C_6H_{6\,t}$	31	35	44	**40±10**	214	249	305	**254±43**
	CH_3OH	3130	4224	4698	**4020±650**	3887	5239	6433	**5200±1074**
	C_2H_5OH	325	373	587	**420±100**	667	989	1269	**978±256**
	DMS	<LOD	1.3	3.6	**1 ±2**	6.5	17.25	24.8	**16.5±7.5**
Flight 2	CO	109	115	129	**116±5**	123	133	145	**133±5**
	CH_4	1853	1873	1893	**1873±12.3**	1887	1920	1936	**1917±11**
	C_2H_6	1.40	1.70	5.92	**2.35±1.40**	3.77	5.89	9.06	**6.0±1.2**
	C_3H_8	673	812	2054	**1012±587**	3158	4173	6239	**4395±1157**
	nC_4H_{10}	149	231	772	**312±260**	1297	1795	3121	**1993±698**
	iC_4H_{10}	57	81	261	**110±85**	463	617	1159	**716±269**
	nC_5H_{12}	35	62	251	**92±90**	361	574	955	**611±225**
	iC_5H_{12}	34	55	216	**83±75**	347	574	924	**602±220**
	C_6H_6	32	34	48	**37±6**	69	95	120	**97±19**
	CH_3OH	3509	4638	5305	**4400±744**	3239	4363	4536	**4015±530**
	C_2H_5OH	272	363	442	**352±67**	341	399	540	**434±90**
	DMS	1.7	2.3	3.4	**2.4±0.7**	3.3	4	5.8	**4.3±1.1**
Flight 3	CO	95	99	102	**99±2**	99	115	135	**115±8**
	CH_4	1821	1824	1862	**1824±4**	1849	1911	2044	**1920±48**
	C_2H_6	1.84	1.96	2.12	**1.96±0.67**	5.55	13.19	65.63	**15.3±7.5**
	C_3H_8	744	745	933	**807±109**	8.23*	13.26*	18.29*	**13.3±7.1***
	nC_4H_{10}	144	148	217	**170±41**	3925	6037	8149	**6037±2986**
	iC_4H_{10}	59	64	89	**71±16**	1342	2320	3297	**2320±1382**
	nC_5H_{12}	28	37	60	**42±17**	1340	2110	2880	**2110±1090**
	iC_5H_{12}	30	33	59	**41±16**	1198	1889	2580	**1890±980**
	C_6H_6	29	31	32	**31±2**	120	244	367	**240±170**
	CH_3OH	2374	2763	3410	**2849±523**	3679	3855	4031	**3850±250**
	C_2H_5OH	237	261	349	**282±59**	553	597	640	**600±60**
	DMS	1.4	1.7	3.2	**2.1±1.0**	5.4	6.5	7.5	**6.5±1.5**

*Units for these AWAS samples are ppbv.

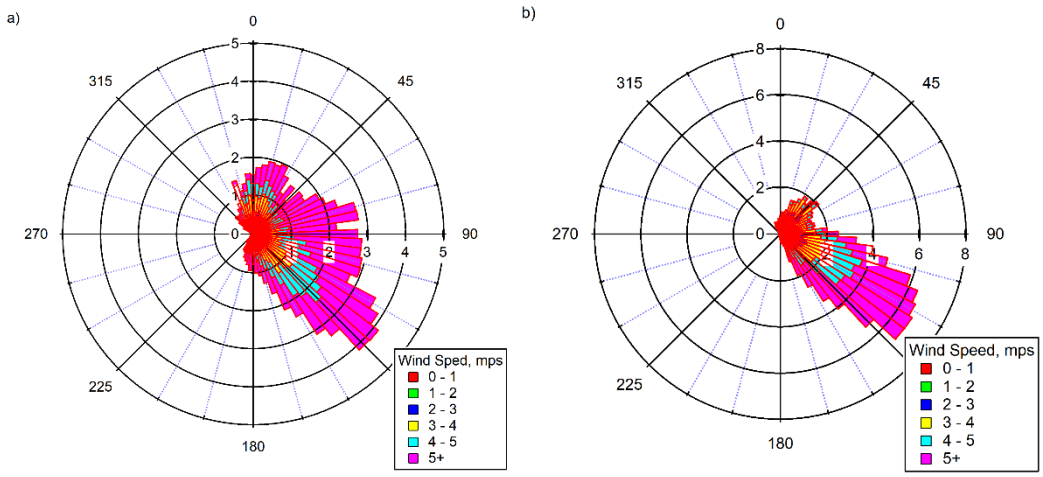

Figure 3.2 Wind roses from the C-130 flight 2 (a) and flight 3 (b) measured within the boundary layer and north of the Denver Metropolitan area. The size of the petal represents frequency (%) and are colorized by wind speed.

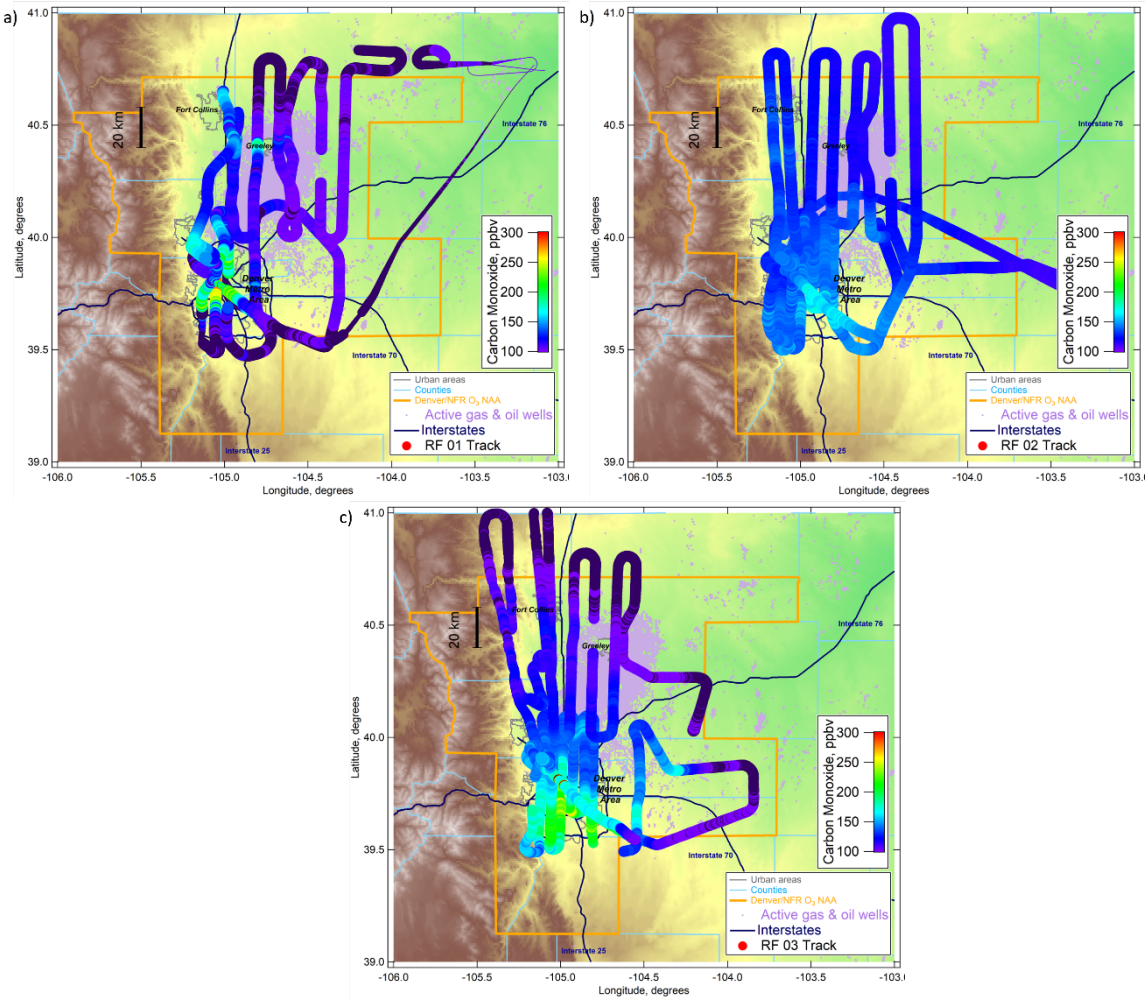

Figure 3.3 Flight tracks for flights 1 (a), 2 (b), and 3 (c), colorized by carbon monoxide concentration. Points are sized by altitude with smaller points indicating higher altitude.

pptv, compared to upwind measurements of 90 ± 16 pptv, with an overall maximum value of 2734 pptv over Denver. Weak to no correlations of the ONG tracers methane, ethane, and benzene to CO of R^2=0.30, R^2=0.002, and R^2=0.20, respectively, effectively eliminate combustion as a major source of hydrocarbons in the NFRMA. We can conclude that there are minimal urban emissions in downwind transects used in this analysis.

3.1.1 Oil and Natural Gas Source Signature

Measurements downwind of the GWA showed elevated concentrations of hydrocarbons consistent with oil and natural gas operations. Correlations between light alkanes have been used to characterize ONG emissions (Gilman et al., 2013). Here we examine hydrocarbons associated with ONG emissions and other emission sources in the NFRMA.

a. Methane

As mentioned above, methane and ethane have been used historically to measure ONG influence. From the analysis of unprocessed natural gas from the GWA, the ratio of C_2H_6 to CH_4 in this area is 15.2 ± 3.7% (COGCC, 2007), and 9.7% in processed delivery natural gas from Xcel Energy. We can use this relationship to examine ONG influence in the NFRMA. The average C_2H_6/CH_4 emission ratio measured over all three research flights downwind of the NFRMA was determined to be 9.9 ± 0.2%, Figure 3.4. The measured C_2H_6/CH_4 ratio and the ratio measured in unprocessed and processed natural gas are statistically different, indicative of multiple CH_4 sources in the NFRMA, as can be seen by the two lobes visible in Figure 3.4. This is viable as the emission inventory from the CDPHE estimates that 36.4% of methane emissions in Colorado are from biogenic sources (CDPHE, 2014), and a bottom-up analysis of non-ONG methane sources in the NFRMA estimated this fraction to be 25% of total methane emissions (Pétron et al., 2014). The measured downwind emission ratio was most similar to the emission

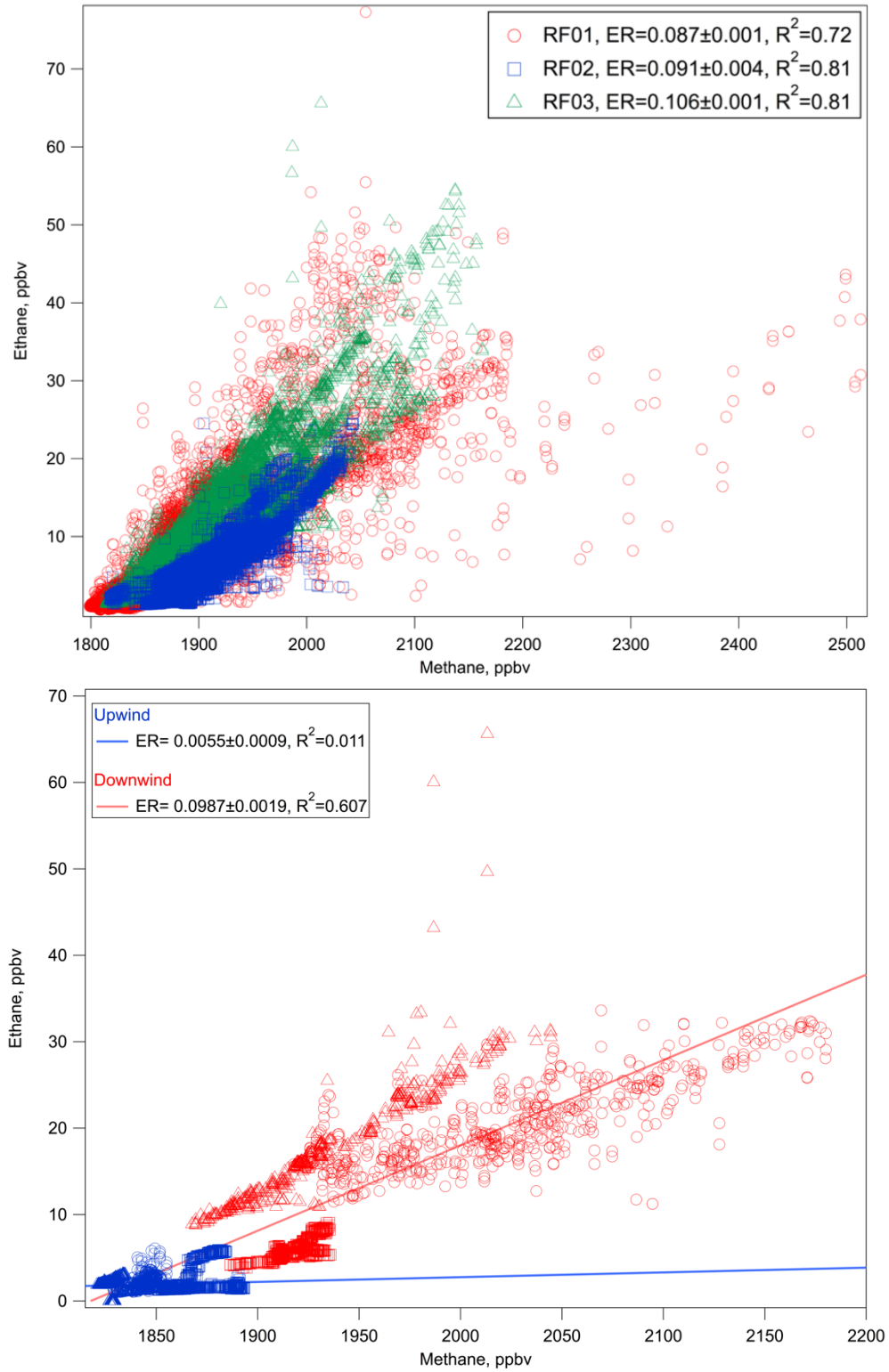

Figure 3.4 Correlation plots of ethane to methane emission ratios from 1-Hz measurements collected during flights 1, 2, and 3 (top), and separated by upwind and downwind flight segments (bottom). Emission ratios (ER) are in units of ppbv/ppbv.

ratio reported for processed natural gas, this implies processed natural gas has a higher leak rate than unprocessed natural gas in the NFRMA. To further investigate CH_4 sources in the NFRMA, we examine $C_3 - C_6$ hydrocarbons. Table 3.2 shows the hydrocarbon to CH_4 emission ratios determined in the upwind and downwind transects and the corresponding correlation.

Table 3.2 Methane emission ratios measured upwind and downwind of the NFRMA. Also shown is the emission ratio from air free gas composition of unprocessed natural gas from the GWA and known emission ratios. The reported emission ratios for processed natural gas (Xcel Energy) is also shown. Units are ppbv/ppbv, written as percent.

	Upwind	R^2	Downwind	R^2	GWA	Xcel Energy
C_2H_6/CH_4	0.55±0.09	0.01	9.87±0.19	0.61	15.16±3.74[a]	9.65
C_3H_8/CH_4	0.76±0.74	0.09	8.27±1.55	0.76	6.15±3.14[a]	1.50
nC_4H_{10}/CH_4	0.33±0.39	0.06	4.19±0.71	0.79	1.63±1.09[a]	0.19
iC_4H_{10}/CH_4	0.09±0.11	0.06	1.52±0.27	0.77	0.88±0.52[a]	0.10
nC_5H_{12}/CH_4	0.10±0.13	0.05	1.48±0.25	0.79	0.39±0.36[a]	0.02
iC_5H_{12}/CH_4	0.07±0.11	0.05	1.30±0.22	0.79	0.42±0.31[a]	0.03
C_6H_6/CH_4	0.01±0.01	0.17	0.11±0.03	0.62	0.14[b]	-
CH_3OH/CH_4	2.36±1.08	0.30	1.08±0.26	0.66	2.7[c1], 5.7[c2]	-
C_2H_5OH/CH_4	0.06±0.14	0.02	0.38±0.06	0.80	4.1[c1], 10.3[c2]	-
DMS/CH_4	0.003±0.001	0.36	0.009±0.001	0.83	0.07[d]	-

[a] COGCC, 2007
[b] Gilman et al., 2013
[c] Sun et al., 2007. [1]dry cows. [2]manure.
[d] Shaw et al., 2007

By comparing CH_4 to other trace gases measured in the NFRMA, we can conclude that sources of CH_4 in this area are varied. By examining biogenic tracers such as methanol, ethanol, and dimethyl sulfide (DMS), known dairy/feedlot emissions (Sun et al., 2007; Shaw et al., 2007), it was determined that biogenic emissions of methane in the NFRMA are substantial, with relatively high correlations, $0.66 \leq R^2 \leq 0.83$. This finding agrees with that of Townsend-Small, et al. (2016), who examined methane isotopes from ground and aircraft measurements during FRAPPÉ and estimated that roughly 50% of CH_4 emissions in the NFRMA were from a biogenic source. However, this isotopic method differentiates CH_4 emissions by biogenic and thermogenic sources and CH_4 emission ratios did not match known correlations from dairies (Shaw et al.,

2007; Sun et al., 2007) in measurements collected downwind. To further examine methane sources in the NFRMA, we turn to higher alkanes.

Landfills are a substantial methane source produced from anaerobic microbial degradation of organic materials (Rettenberger & Stegmann, 1996; Allen, Braithwaite, & Hills, 1997). By comparing CH_4 to other compounds known to be emitted from landfills we can assess the influence of this source in measurements collected downwind of the NFRMA. Benzene is emitted from both landfills and ONG infrastructure. An emission ratio of $\sim 1\times10^{-6}$ ppb/ppb is typical in landfill emissions (Kim et al., 2006). In the NFRMA, upwind and downwind aircraft enhancements were 1.2×10^{-4} (R^2=0.17) and 1.1×10^{-3} ppb/ppb (R^2=0.62), respectively, compared to WAS ground samples (n=14) collected near local landfills, $1.4\times10^{-5} \pm 0.3\times10^{-6}$ ppb/ppb (R^2=0.66), indicating that there was little influence of CH_4 landfill emissions during FRAPPÉ. This corresponds to a previous study in the NFRMA of 1.4×10^{-3} ppb/ppb (Pétron et al., 2012), and other studies of C_6H_6/CH_4 emission ratios from ONG, ranging from 6×10^{-4} ppb/ppb in the Uintah Basin (Helmig et al., 2014), to 4×10^{-3} ppb/ppb in the Upper Green River Basin (Field et al., 2015), and an average urban signature of 0.1 ppb/ppb (Kirchstetter et al., 1996). Weak correlations to CO and C_2H_2, at R^2= 0.02 and R^2=0.43, respectively (Table 3.3), eliminate combustion as a source of benzene. Although benzene is only a small component of natural gas, a strong downwind correlation of C_6H_6/C_2H_6 at R^2=0.89 (ER=1.22 ±0.14%) suggests that the main source of benzene in downwind measurements is from ONG systems.

Comparison of C_3-C_5 alkanes to methane emission ratios in measurements collected downwind in the NFRMA correlated extremely well, with R^2 values greater than 0.60, and with C_3H_8 and iC_4H_{10} statistically similar to ratios measured in unprocessed natural gas. We can conclude that a major source of methane in this area is from ONG sources.

b. Non-methane Hydrocarbons

Higher chained alkanes are commonly used to assess ONG influence as emission ratios are more precise because sources are less varied. Here we will discuss emissions of C_3-C_5 alkanes measured during FRAPPÉ.

As mentioned previously, CO and C_2H_2 emissions correspond to urban vehicular combustion (Sachsse, 1954; Blake et al., 2003; Guo et al., 2007; Warneke et al., 2007). These compounds were only slightly enhanced in the downwind aircraft samples, however, using these trace gases and their correlation to known ONG hydrocarbons, we define urban sources of hydrocarbons. Industrial sources of propane, C_3H_8, include raw and processed natural gas that contain little to no C_2H_2. The mean mixing ratio of propane in samples collected downwind was 10.5 ± 6.7 ppbv, much greater than the average reported for other U.S. cities, 1.4 ± 4.4 ppbv (Baker et al., 2008), and indicates a large propane source in the NFRMA. By examining the C_3H_8/C_2H_2 emission ratio, we can assess the extent of urban emission influence in the area downwind of the GWA. In samples collected downwind, the emission ratio was 69 ± 16 ppbv/ppbv compared to an upwind ratio of 20 ± 9 ppbv/ppbv (Figure 3.5). This is significantly larger than a typical urban signature of 0.10 to 2.5 ppb/ppb and closer to an ONG signature ratio of 97 (Gilman et al., 2013), indicating a non-combustion/non-urban source of propane.

The *i*-pentane to *n*-pentane emission ratio as an indicator of ONG influence is used here as pentanes are known to be co-emitted from ONG sources and have similar OH radical reaction rates, and similar boiling points (Atkinson, 1990, Gilman et al., 2013). Therefore, this ratio would remain unaffected by changing boundary layer conditions, photochemistry, or dilution. Figure 3.6 compares the emission ratio of *i*-pentane to *n*-pentane for all three NFRMA emission

flights and compares upwind and downwind transects. Figure 3.7 is a map of AWAS sample locations, colorized by *n*-pentane.

In Figure 3.6, the downwind emission ratio of 0.88 ± 0.01 (R^2=0.99) is statistically the same as the iC_5/nC_5 ratio for raw natural gas in the GWA basin, 0.86 ± 0.02 (R^2=0.95) (COGCC, 2007). This suggests that observations downwind of the GWA were strongly influenced by the ONG operations in the area. The ratio measured in processed natural gas was 1.11, much greater than both upwind and downwind measurement, and implies the primary source of pentanes in the NFRMA are not from pipelines, but active drilling and storage. Upwind emission ratios were the lowest observed at 0.81 ±0.01 (R^2=0.99). As shown in the literature, iC_5/nC_5 emission ratios greater than 1 are generally associated with urban areas and gasoline vapors. For example, a study in a Los Angeles, CA tunnel measured a iC_5/nC_5 ratio of 2.45 (Fraser et al., 1998). Another study in Riverside, CA examined the seasonal variation of iC_5/nC_5 based on gasoline composition and measured a range from 2.30 to 3.80 (Gentner et al., 2009). Houston, TX is a well-known area of ONG production. During the Texas Air Quality study in 2006, a iC_5/nC_5 emission ratio of 1.39 was measured, compared to 3.80 in a Houston tunnel (McGaughey et al., 2004; Gilman et al., 2009).

Values of iC_5/nC_5 are known to vary by not only type of source, but location. Studies of ONG reservoirs have shown iC_5/nC_5 emission ratios ranging from 0.82 measured in the Gulf of Mexico after the Deepwater Horizon oil spill in 2010 (Ryerson et al., 2011), to 0.99 over ONG fields in Kern County, CA (Hartt, 2013). The iC_5/nC_5 ratio (0.81 ± 0.01) measured upwind for this work was statistically different from both downwind measurements and processed/unprocessed natural gas measurements of the area, and was only moderately correlated, R^2=0.30, indicating pentanes in measurements upwind were from a different source.

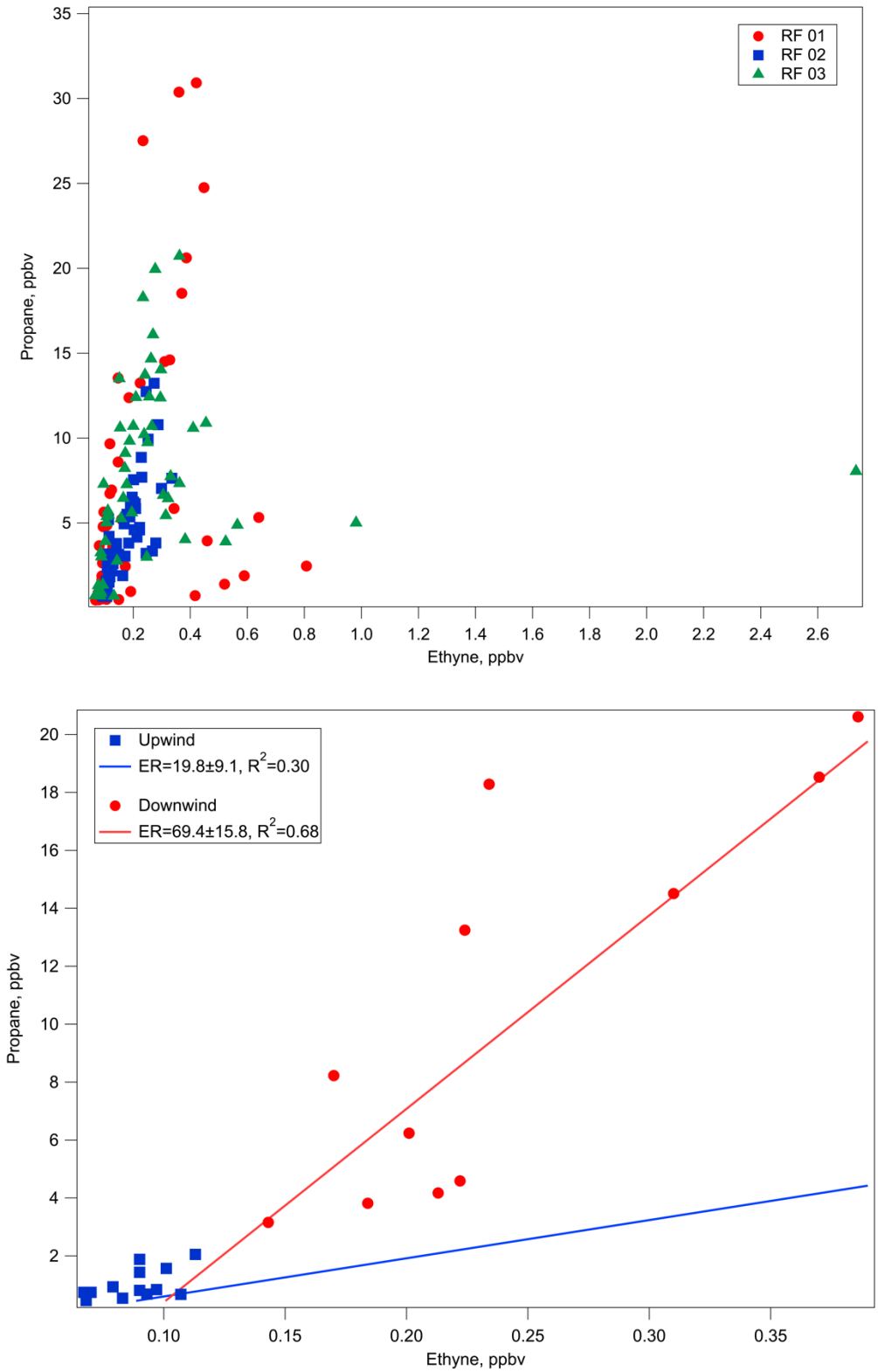

Figure 3.5 Correlation plot of propane to ethyne for all measurements from flights 1, 2, 3 (top) and separated by upwind and downwind transects (bottom).

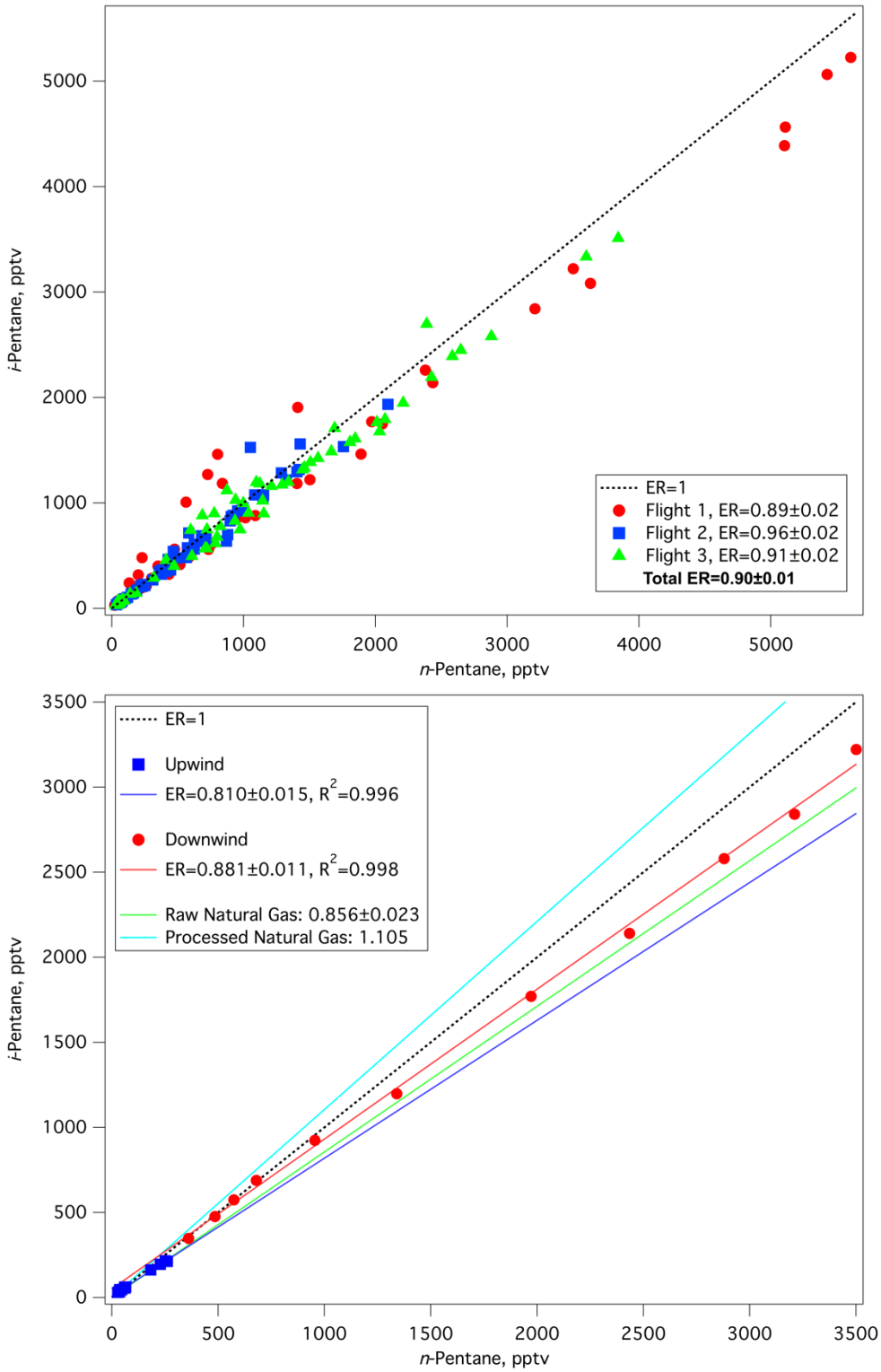

Figure 3.6 Correlation plots of *i*-pentane versus *n*-pentane for all AWAS measurements collected onboard the C-130 during flights (top) and of the upwind (blue) versus downwind (red) transects (bottom). Also shown is the emission ratio for GWA unprocessed (green) and processed (cyan) natural gas. The black dotted line in both Figures is the 1:1 line.

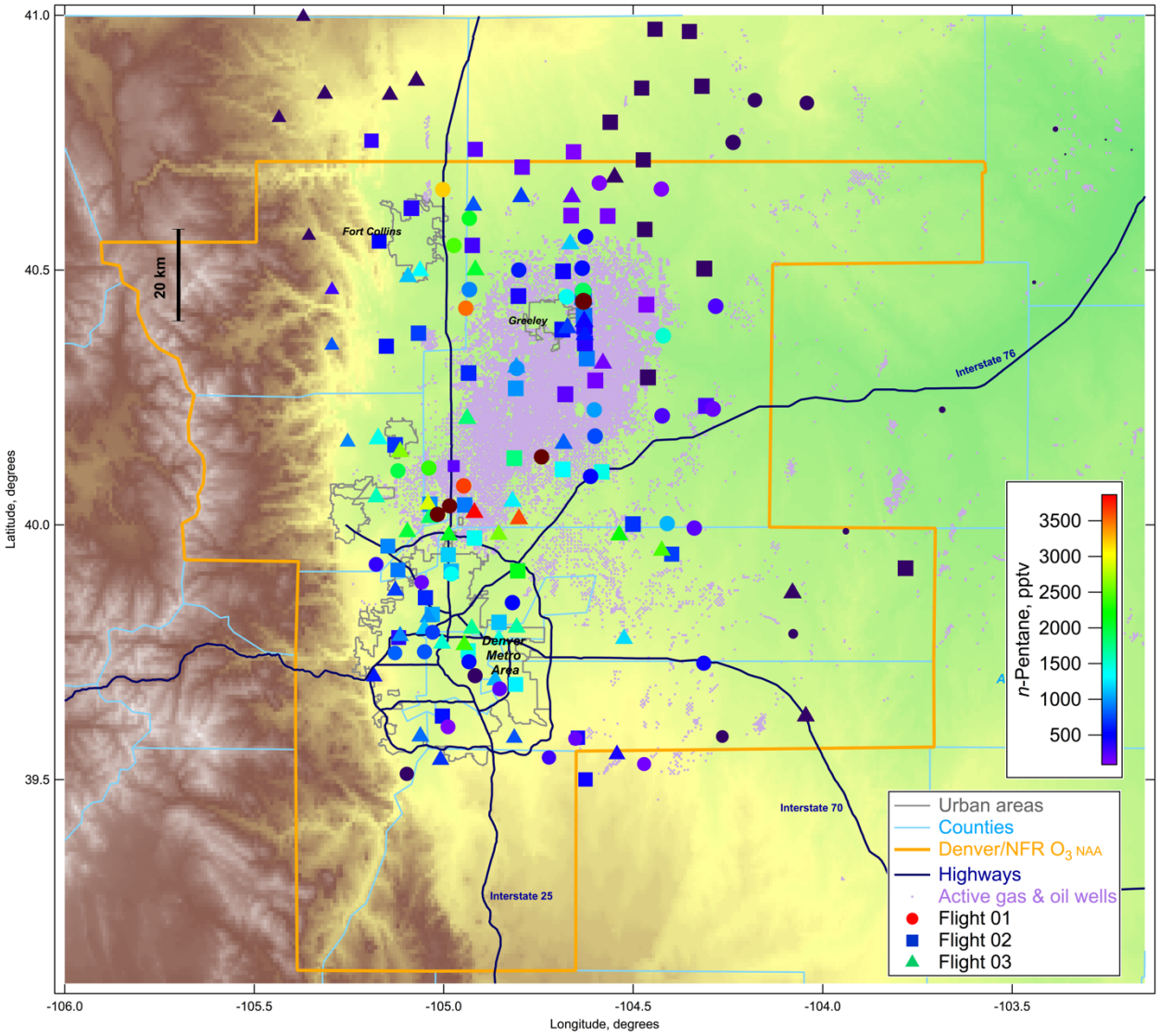

Figure 3.7 A map of AWAS measurement locations, colorized by n-pentane concentration and sized by altitude, with smaller markers at higher altitude.

3.1.2 Mass Balance Approach

To determine emission estimates of trace gases in the NFRMA, the mass balance approach was used. This method has been used to estimate emissions from point sources and area sources and directly assess uncertainties in measurements (White et al., 1976; Ryerson et al., 2001; Mays et al., 2009; Turnbull et al., 2011; Karion et al., 2013; Peischl et al., 2015). To use this method, several conditions must be met. Steady horizontal winds are necessary to define

locations upwind/downwind of source area and to determine emission ratios. A well-developed planetary boundary layer (PBL) height is needed to determine the vertical distribution of source emissions, and sufficient measurements collected downwind of the emission source.

The GWA provides a study area that is applicable to this approach using aircraft measurements as 43% of the oil and natural gas wells in Colorado are concentrated in this area. During FRAPPÉ, the C-130 was able to make multiple transects of this area while the P3-B performed vertical profiles, providing ample information on local emissions and boundary layer conditions, Figure 3.8. Surface and aircraft measurements of wind speed and direction showed strong easterly winds across the basin during the time of the flight. Continuous surface winds measured at the NOAA Platteville ground station at night prior to flights from 8pm to 6am showed strong westerly winds that would thoroughly "clean out" the basin. Wind data collected at the NOAA Platteville site were used to construct wind roses to represent wind speed and direction before and during research flights, Figure 3.9.

The mass balance approach uses the enhancement of trace gases collected downwind of a source and is integrated over the height and width of the plume. Steady winds are then transected at a perpendicular angle by the plane and the wind speed is used to determine a flux estimate shown in equation 3.1.

$$flux_{CH_4} = V \int_{-b}^{b} \Delta x_{CH_4} \left(\int_{z_{ground}}^{z_{PBL}} n_{air} dz \right) cos\theta dx \qquad \text{Equation 3.1}$$

Where V is the horizontal wind speed over the area of interest and averaged from the ground to the top of the PBL and over the air mass transit time. The molar enhancement of methane above background concentrations, Δx_{CH_4}, is integrated over the air mass width, -*b* to *b*. This value is then multiplied by the integral of the molar density of air, n_{air}, determined from pressure and temperature measurements collected on board the aircraft from the ground to the top of the

boundary layer (z_{ground} to z_{PBL}). The angle between the flight path and the wind direction is Θ, so that $cos\Theta dx$ gives the desired flight path perpendicular to the mean horizontal wind direction, Figure 3.10.

To use this approach, several assumptions were made. First, a constant emission rate of hydrocarbons from the GWA was assumed. Second, that the plume was thoroughly mixed within the boundary layer downwind of the source. The wind speed was determined using measurements collected on board the C-130 and averaged from the surface to the top of the PBL and again over the transit time of the plume across the GWA, ~4 hours. Aircraft heading and wind direction used in determining Θ were measured by the data system on board the C-130 with an estimated error of 1σ. Wind speed was also measured onboard the C-130 and averaged over the individual transects used in this method. Error in the wind speed and direction were determined using both data collected on board the C-130 and at the NOAA Platteville ground station to include temporal, horizontal, and spatial variance. The average relative difference between aircraft measurements and ground measurements was 17.6% in the wind speed and 33.2% in the wind direction. This method was used in determining the uncertainty in the flux.

Boundary layer heights varied throughout each day, from 500 m AGL to 1500 m AGL. Therefore, profiles collected on board the P3-B at the time of the upwind and downwind transects were used. Onboard measurements of CH_4, water, isoprene, and potential temperature were used to determine boundary layer heights (Figures 3.8 and 3.11). Spirals were typically 5 km in diameter and ascent/descent rates were approximately 5 ± 4 m s^{-1}. Trace gas enhancements were determined by comparing *in-situ* measurements collected upwind and downwind of the GWA, Table 3.1. The P3-B was not flying during research flight 1. To determine the boundary layer height during flight 1, both vertical profiles of CH_4, O_3, and potential temperature collected

onboard the C-130 and sondes released at Platteville, CO at 13:00 local were used (Figure 3.12). During NFRMA emission characterization C-130 flights, the plane remained in the boundary layer at 350 ± 140 m AGL. Table 3.3 summarizes data used in determining flux rates. Emission estimates for CH_4 and other trace gases measured are shown in Table 3.4

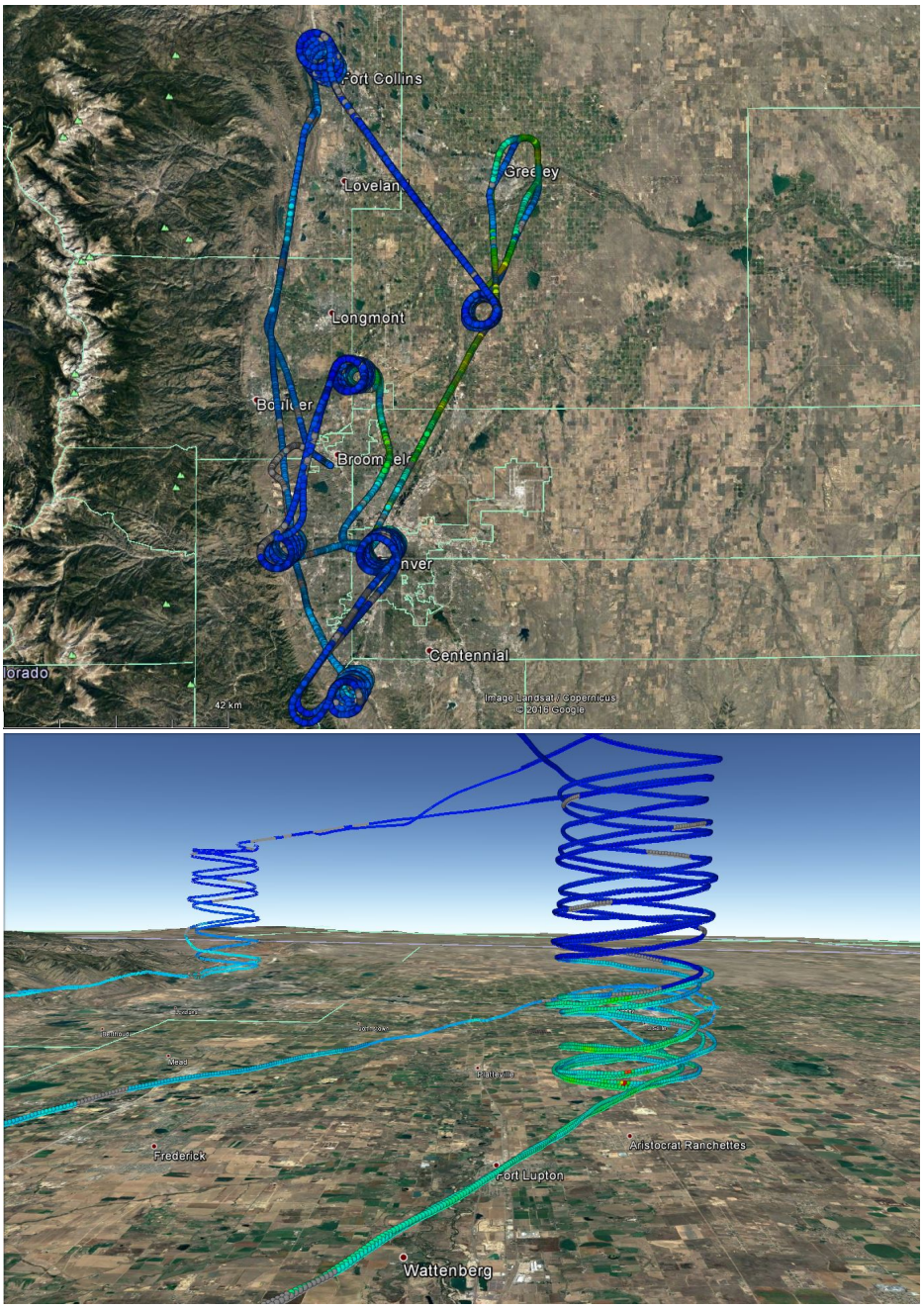

Figure 3.8 Map of flight path of P3-B flight (top) and vertical profiles over Fort Collins and Platteville (bottom). Flight paths are colorized by methane where dark blue is low methane concentrations and green to red is higher concentrations to highlight PBL height.

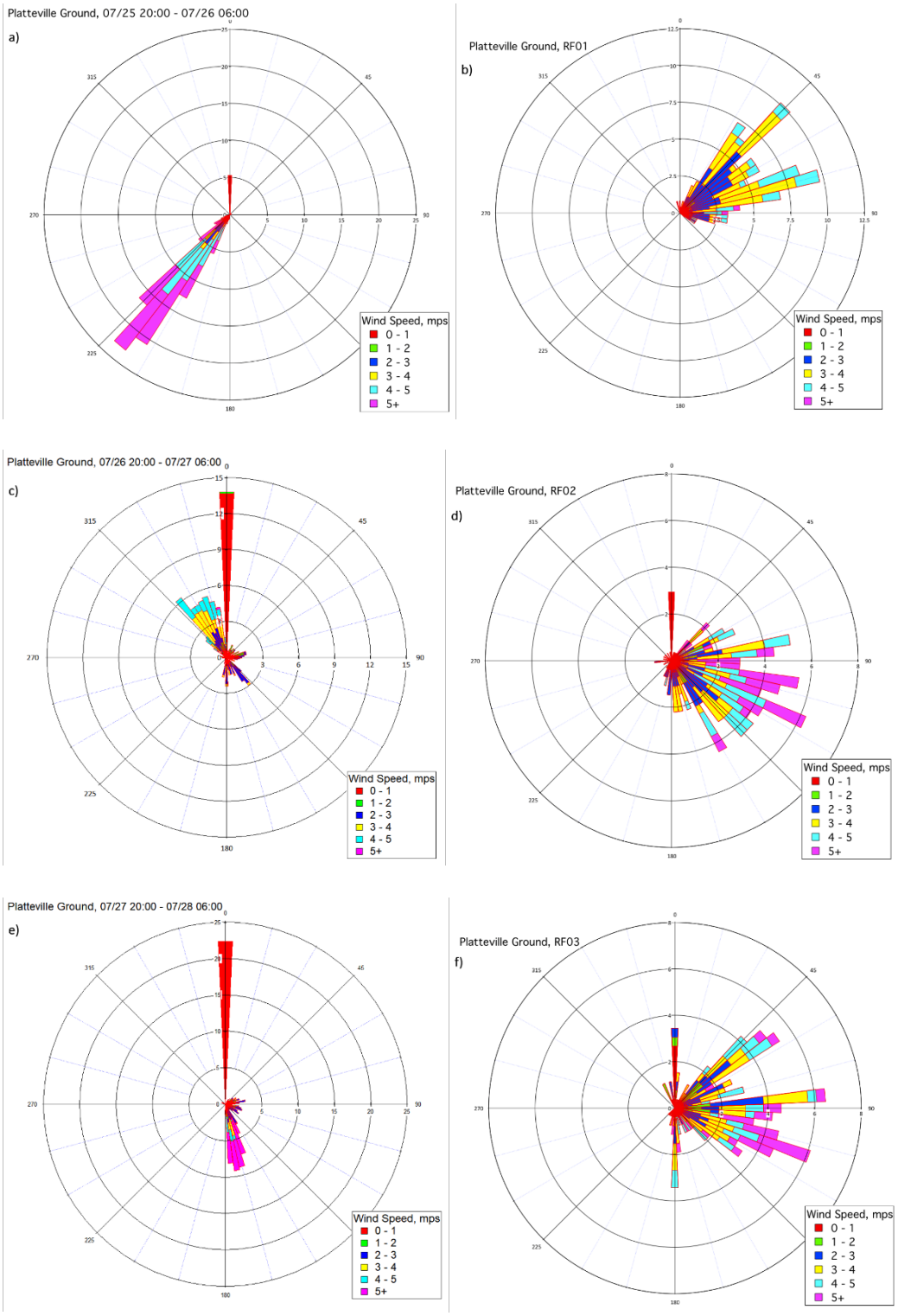

Figure 3.9 Wind roses displaying wind speed and direction frequencies from the NOAA Platteville ground station. Figures a, c, and e show average wind data from 8:00 pm to 6:00am local the evening prior to flights. Figures b, d, and f show average wind data during the research flights.

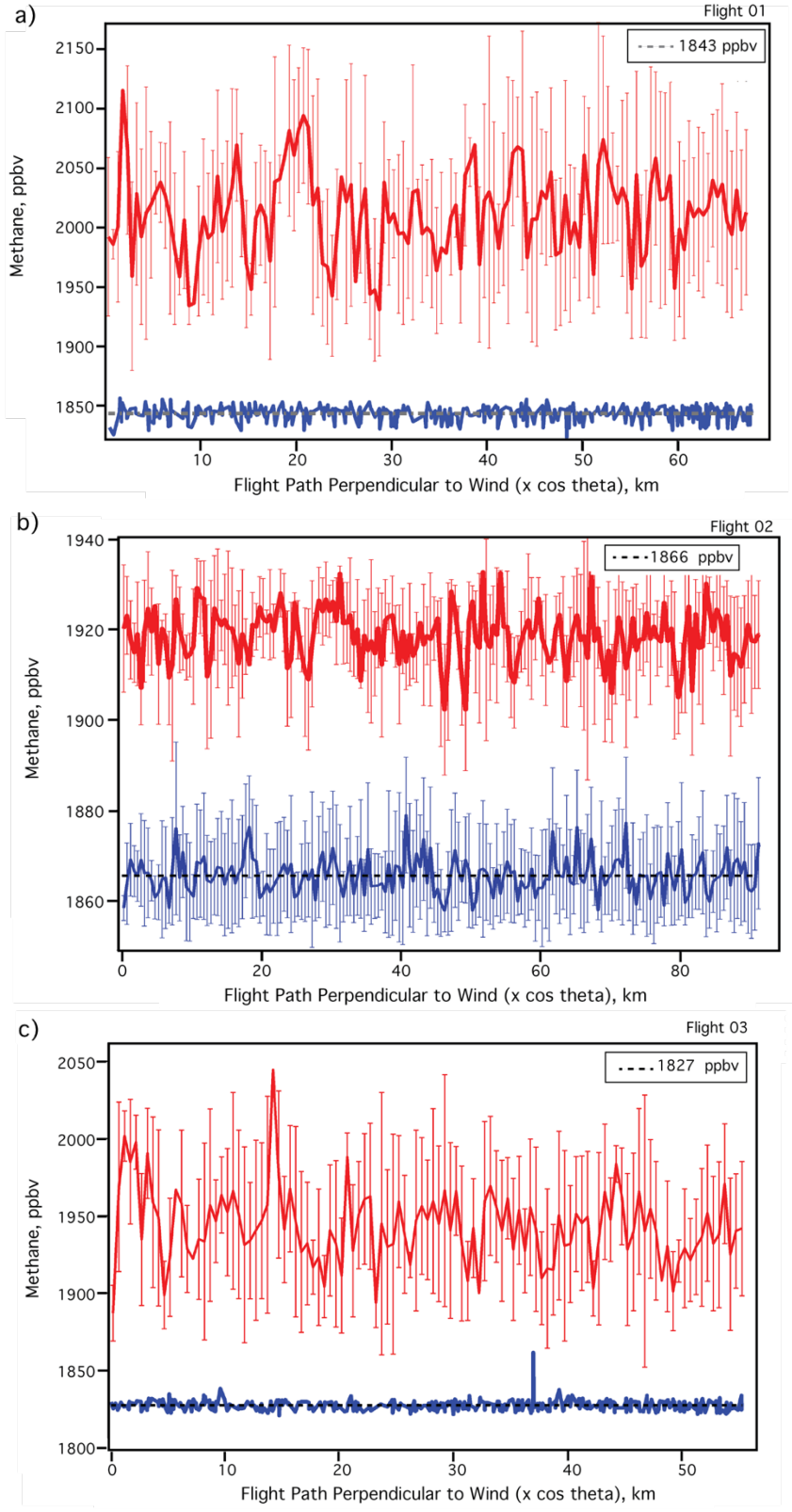

Figure 3.10 Measured methane upwind (blue) and downwind (red) as a function of the distance perpendicular to wind direction for flight for flights 1 (a), 2 (b), and 3 (c). The dashed line is the average upwind CH_4 concentration.

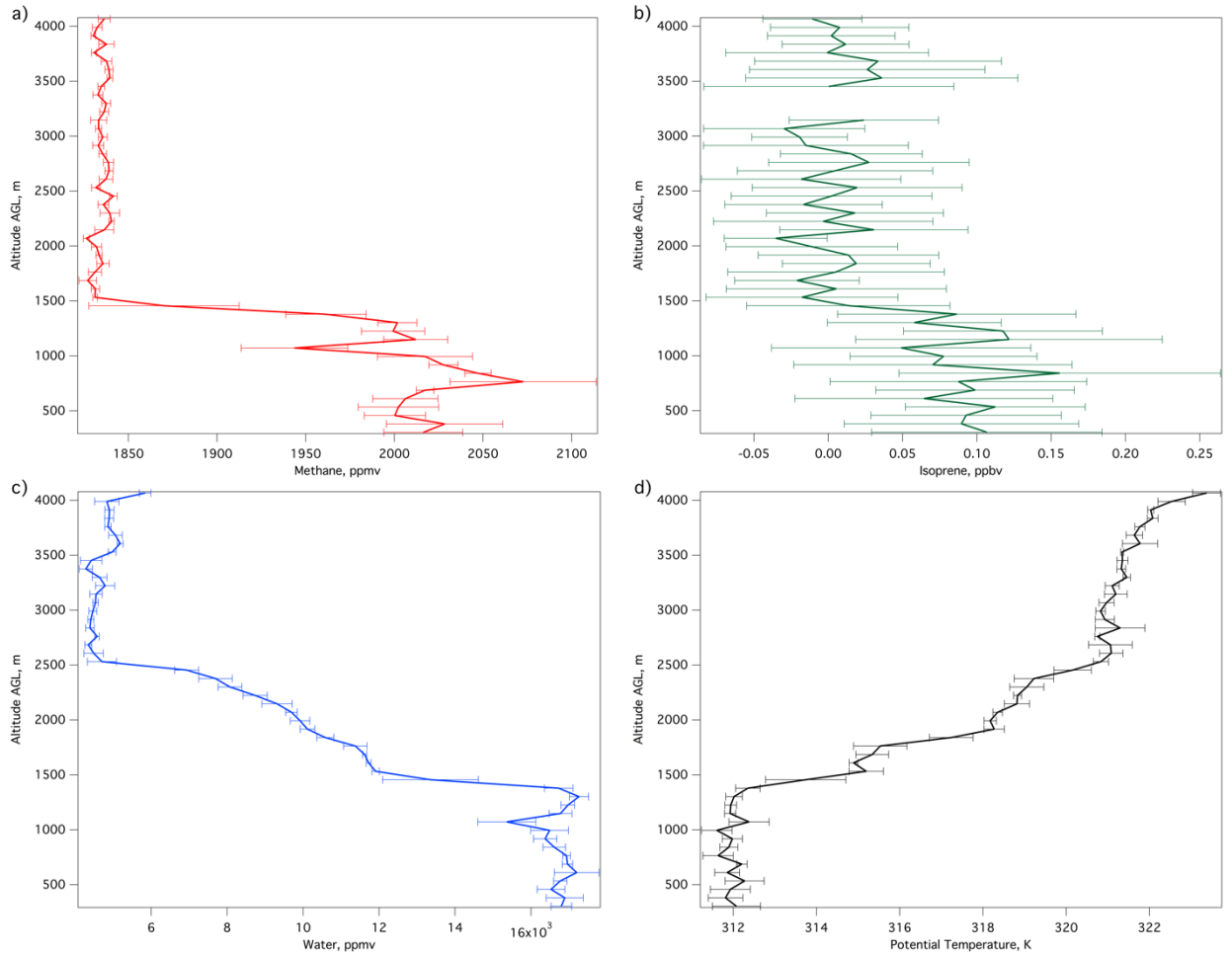

Figure 3.11 Vertical profiles of methane (a), isoprene (b), water (c) and potential temperature (d) collected onboard the P3-B over Platteville at 12:00 local time on July 27th, 2014 used in determining boundary layer heights.

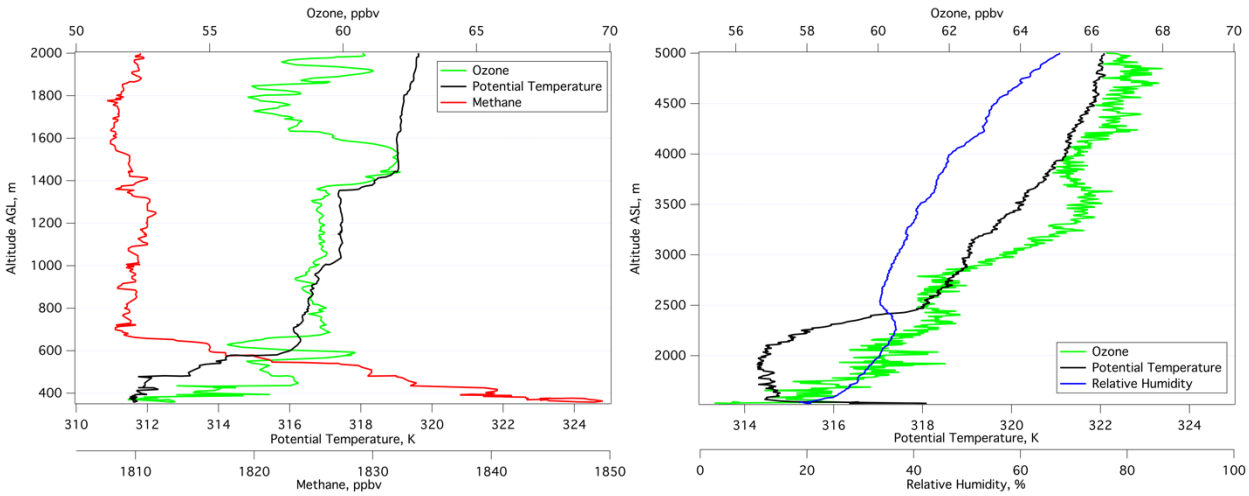

Figure 3.12 Vertical profile measured onboard the C-130 during research flight 1 (left), and 1-Hz sondes released from the Platteville ground site at 13:20:39 local, reduced to < 3km (initial release elevation: 1534 m ASL).

Table 3.3 Summary of variables used in emission estimates during research flights 1, 2, and 3.

	Wind Speed *m s^{-1}*	Wind Direction	Plane Heading	n_{air} *$\times 10^{25}$ m^{-3}*	PBL Height *m*	Plume Width *km*
Flight 1	2.7 ± 1.3	149 ± 65 º	190 ± 24 º	1.99 ± 0.03	678 ± 120	67.1
Flight 2	2.3 ± 1.4	71 ± 79 º	177 ± 6 º	2.01 ± 0.02	1152 ± 88	91.7
Flight 3	3.1 ± 1.0	78 ± 43 º	-1 ± 4 º	1.99 ± 0.05	934 ± 122	55.1

Table 3.4 Trace gas flux rates determined during flights 1, 2, and 3, and the total mean flux over all three flights. Also shown is is the averaged trace gas flux during just flights 1 and 3 and the 2012 VOC flux determined by Pétron et al., 2014. Units are $\times 10^3$ kg VOC hr^{-1}.

	Flight 1	Flight 2	Flight 3	Total Mean Flux	Flights 1 & 3 Flux	2012 Flux
CO	7.5 ± 2.9	9.3 ± 5.7	6.5 ± 2.1	7.7 ± 6.2	7.00 ± 3.6	-
CH_4	25.6 ± 9.7	15.5 ± 9.5	21.6 ± 7.0	20.9 ± 16.5	23.6 ± 11.4	26.0 ± 6.8
C_2H_6	5.2 ± 3.0	2.3 ± 2.1	5.6 ± 2.9	4.4 ± 5.2	5.4 ± 4.3	-
C_3H_8	6.4 ± 4.3	2.7 ± 2.4	6.4 ± 4.1	5.2 ± 6.7	6.5 ±6.1	11.8 ± 3.8
nC_4H_{10}	4.2 ± 0.2	1.8 ± 2.0	4.0 ± 2.6	3.3 ± 5.0	4.1 ± 4.2	7.7 ± 2.6
iC_4H_{10}	1.5 ± 1.0	0.65 ± 0.68	1.5 ± 1.1	1.2 ± 1.8	1.5 ± 1.5	-
nC_5H_{12}	1.8 ± 1.3	0.69 ± 0.83	1.8 ± 1.3	1.4 ± 2.3	1.8 ± 1.9	3.0 ± 1.0
iC_5H_{12}	1.6 ± 1.1	0.69 ± 0.80	1.6 ± 1.1	1.3 ± 2.0	1.6 ± 1.6	2.7 ± 0.9
C_6H_6	0.16 ± 0.07	0.03 ± 0.06	0.19 ± 0.15	0.15 ± 0.17	0.18 ± 0.16	0.17 ± 0.06
CH_3OH	0.35 ± 0.16	-0.23 ± 0.15	0.38 ± 0.14	0.17 ± 0.15	0.37 ±0.22	-
C_2H_5OH	0.24 ± 0.12	0.07 ± 0.05	0.17 ± 0.07	0.16 ± 0.15	0.21 ±0.14	-
DMS	0.009 ± 0.010	0.002 ± 0.002	0.003 ± 0.002	0.005 ± 0.007	0.006 ± 0.008	-

An average CH_4 flux of 21 ± 17 $\times 10^3$ kg hr^{-1} was determined for flights 1, 2, and 3. The CH_4 flux estimate during flight 2 was the lowest compared to the other flights. To our knowledge there is no publicly available data indicating reduced natural gas production in this area on July 27th, 2014, and it is estimated that production rates were relatively constant over the three research flight days. Therefore, we attribute this difference to different meteorological conditions, namely the Denver Cyclone. Though downwind measurements of CH_4, C_2H_6, and C_3 – C_5 alkanes were statistically greater than upwind measurements, it is apparent that the gyre pooled emissions away from the GWA despite prevalent easterly winds. It is important to note that this decreases our emission estimate, and had the cyclone not been present, the overall flux

would be comparable to rates measured from flights 1 and 3. If we remove the results from research flight 2 from our analysis, the average CH_4 flux changes to $24 \pm 11 \times 10^3$ kg hr^{-1}. The average trace gas flux rates measured from research flights 1 and 3 are also shown in Table 3.4.

In 2014, Pétron and colleagues reported a top-down flux rate of $26.0 \pm 6.8 \times 10^3$ kg CH_4 hr^{-1} from aircraft samples over the Denver Basin in May 2012. This is statistically the same to the estimate produced from this data (Table 3.4), indicating there was no statistically observable change in CH_4 emissions in this area from 2012 to 2014. From the comparison of 2012 and 2014 NMHC flux estimates, the flux averages are nearly 50% lower in 2014 than in 2012 for most compounds. However, there is significant overlap in the variability of these flux estimates and thus there is no statistical difference between this study and Pétron et al. (2014).

Townsend-Small et al. (2016) estimated that 50% of CH_4 emissions measured during FRAPPÉ were biogenic. Using the average flux rate for research flights 1 and 3, we estimate a CH_4 flux of $11.8 \pm 5.7 \times 10^3$ kg hr^{-1} from ONG fugitive emissions. Bottom-up estimates of non-ONG emissions in the NFRMA estimate 25% of total CH_4 emissions in this area are from non-ONG sources, with an emission estimate of ONG sources of $19.3 \pm 6.9 \times 10^3$ kg hr^{-1} (Pétron et al., 2014). Using this estimate, the average ONG fraction of CH_4 emission estimates from research flights 1 and 3 was determined to be $17.7 \pm 8.5 \times 10^3$ kg hr^{-1}.

From Table 3.4, it is apparent the highest flux measurements are in the $C_1 - C_5$ hydrocarbons. Biogenic trace gases, the oxygenates and DMS, flux rates were substantial. Assuming dairies are the primary source of ethanol in the region, and an average emission estimate of 1.27 g C_2H_5OH cow^{-1} hr^{-1} for lactating cows and manure from a chamber study (Sun et al., 2007), our flux rate corresponds to ~126,000 cows in the NFRMA. This estimate does not represent the NFRMA as there are more than 500,000 dry and lactating cattle at beef and dairy

farms in Weld County alone (USDA, 2012). Therefore, this method can only be used as a lower limit estimate of emissions from cattle.

The EPA Greenhouse Gas Reporting Program is charged with collecting emission estimates from large GHG sources in the US. Unfortunately, this reporting system only applies to ONG facilities that emit more than 25,000 $\times 10^3$ kg CO_2 equivalent per year (EPA, 2017). In 2014, only 10 of the ~260 ONG facilities in the Denver Basin reported a combined CH_4 emission estimate of $7.7 \pm 1.1 \times 10^3$ kg CH_4 hr^{-1}, or 62% of their total GHG emissions, extrapolated over the year, only reporting the GHGs CO_2, CH_4, and N_2O (from https://www.epa.gov/ghgreporting/ghg-reporting-program-data-sets). This estimate is appreciably lower than the mean total flux estimated in this study, by roughly a factor of 3. If we assume 50% of CH_4 measured during FRAPPÉ were from a biogenic source does the reported EPA ONG CH_4 emission rate compare to a rate determined by this study, $11.8 \pm 5.7 \times 10^3$ kg hr^{-1}. Given that emissions reported by the EPA represent only a small sample size from a very large region, we can use this emission rate to estimate an absolute lower limit of ONG emissions in this area.

The flux estimate determined for this study, $23.6 \pm 11.4 \times 10^3$ kg CH_4 hr^{-1}, is relatively low compared to previous studies of CH_4 from ONG basins such as the Uintah Basin in Utah, $54.6 \pm 15.5 \times 10^3$ kg CH_4 hr^{-1} (Karion et al, 2014), the Barnett Shale near Dallas, TX , $76 \pm 13 \times 10^3$ kg CH_4 hr^{-1} (Karion et al., 2015), the Haynesville Shale on the Louisiana/Texas border, $80 \pm 27 \times 10^3$ kg CH_4 hr^{-1}, and the Fayetteville Shale in northern Arkansas, $39 \pm 18 \times 10^3$ kg CH_4 hr^{-1} (Peischl et al., 2015). This value is also significantly lower than the emission estimate from the Aliso Canyon blowout in Los Angeles, CA, $53 \pm 3 \times 10^3$ kg CH_4 hr^{-1} (Conley et al., 2016). Our estimate is greater than fluxes measured in Kern County, CA 3.7×10^3 kg CH_4 hr^{-1} (Hartt, 2013), and the Marcellus Shale in Pennsylvania, $15 \pm 6 \times 10^3$ kg CH_4 hr^{-1} (Pieschl et al., 2015).

Using the CH_4 emission estimate from this work and the hourly natural gas and oil production rate, we can calculate an average natural gas fugitive emissions from the GWA. The total volume of natural gas produced in Colorado in July, 2014 was 3.89×10^9 m^3, and 1.11×10^8 m^3 from the Niobrara Region (from the U.S. Energy Information Administration at https://www.eia.gov/dnav/ng/hist/n9010co2m.htm), or 1.50×10^6 m^3 h^{-1} on average from the GWA. Using the fraction of CH_4 in unprocessed natural gas in the GWA (77.6 ± 5.3%), and the industry standard conditions for pressure and temperature, 1 atm and 288.7 K, respectively, the hourly emission rate during flights 1, 2, and 3 corresponds to a leak rate of 0.7 ± 0.1% per hour ONG production in the GWA. Assuming 50% (Townsend-Small et al., 2016) or 25% (Pétron et al., 2014) of CH_4 emissions measured were from non-ONG sources, we can reduce this to 0.3 ± 0.1% or 0.5 ± 0.1%, respectively. The U.S. Government Accountability Office, using 2006 inventory and production figures, estimated a CH_4 leak rate of 2.1% from the Denver-Julesburg Basin from natural gas flaring or venting (Rusco, 2010). Our estimated leak rate is much smaller than this estimate, especially when non-ONG estimates are considered, indicating that legislation enacted to reduce emissions from the ONG sector in the GWA has been effective. It is important to note however, that the CH_4 emission rate measured here does not include CO_2 measurements from CH_4 that has been flared. This emission leak rate also includes several assumptions, therefore there is a great deal of error associated with this estimate, for example, assuming that all samples collected during FRAPPÉ contained a 50% biogenic source adds a great deal of uncertainty to our estimate. There are many point sources of CH_4 emissions in the NFRMA and we can only infer that natural gas systems are the major source.

3.2 Conclusion

From the analysis of emissions from the NFRMA, it is evident that the oil and natural gas industry is a substantial source of methane and NMHCs. A methane emission rate of 10.4 ± 8.3 $\times 10^3$ kg hr^{-1} from oil and natural gas systems is estimated for this area with a resulting leak rate of 0.3% from local natural gas production. These estimates are considered lower limits as generalizations about emissions from this area were made to reach this conclusion. Measurements conducted over several months could provide insight into seasonal variability of emissions from the GWA as this estimate spans only 3 days. Increased sampling frequency over upwind and downwind flight transects would provide a higher resolution analysis of $C_3 - C_{6+}$ hydrocarbons. Our results are consistent with emission estimates from other basins (Hartt, 2013; Peischl et al., 2015; Pétron et al., 2014), however, this study is unique in that the top-down leak rate underestimated previous bottom-up measurements. To reduce the error associated with the top-down estimate determined here, more thorough emission inventories that are measurement-based are necessary. Assuming the generalizations made here were accurate, the GWA would provide an excellent case for how legislation and regulations can lead to emission reductions and pilot an industry standard for reducing environmental impact from fossil fuel production.

3.3 References

Allen, M., Braithwaite, A., & Hills, C. (1997). Trace organic compounds in landfill gas at seven U.K. waste disposal sites. *Environmental Science and Technology, 31*(4), 1054-1061.

Arnold, S., Dileo, J., & Takushi, T. (2014, October 2). *Colorado Greenhouse Gas Inventory - 2014 Update including projections to 2020 & 2030.* Retrieved from Colorado Department of Public Health & Environment: https://www.colorado.gov/pacific/sites/default/files/AP-COGHGInventory2014Update.pdf

Atkinson, R. (1990). Gas phase tropospheric chemistry of organic compounds: A review. *Atmospheric Environment, 24a*, 1-41.

Baker, A., Beyersdorf, A., Doezema, L., Katzenstein, A., Meinardi, S., Simpson, I., . . . Rowland, F. (2008). Measurement of nonmethane hydrocarbons in 28 United States cities. *Atmospheric Environment, 42*(1), 170-182.

Blake, N., Blake, D., Simpson, I., Meinardi, S., Swanson, A., Lopez, J., . . . Rowland, F. (2003). NMHCs and halocarbons in Asian continental outflow during the Transport and Chemical Evolution over the Pacific (TRACE-P) field campaign: Comparison with PEM-West B. *Journal of Geophysical Research, 108*(D20), 8806.

CDPHE. (2008). *Denver metron area and North Front Range Ozone Action Plan.* Denver, CO. Retrieved from https://www.colorado.gov/pacific/sites/default/files/AP_PO_Denver-Ozone-Action-Plan-2008.pdf

COGCC. (2007). *GREATER WATTENBERG AREA.* Denver, CO: LT ENVIRONMENTAL, INC.

Conley, S., Franco, G., Faloona, L., Blake, D., Peischl, J., & Ryerson, T. (2016). Methane emissions from the 2015 Aliso Canyon blowout in Los Angeles, CA. *Science, 351*(6279), 1317-1320.

EIA. (2017). *State Profile and Energy Estimates: Colorado*. Retrieved October 20, 2017, from U.S. Energy Information Administration Independent Statistics and Analysis: U.S. Energy Information Administration Independent Statistics and Analysis

Field, R., Soltis, J., McCarthy, M., Murphy, S., & Montague, D. (2015). Influence of oil and gas field operations on spatial and temporal distributions of atmospheric non-methane hydrocarbons and their effect on ozne formation in winter. *Atmospheric Chemistry and Physics, 15*(6), 3527-3542.

Fraser, M., Cass, G., & Simoneit, B. (1998). Gas-phase and particle-phase organic compounds emitted from motor vehicle traffic in a Los Angeles roadway tunnel. *Environmental Science Technology, 32*(14), 2051-2060.

Fujita , E., Croes, B., Bennett, C., Lawson, D., Lurman, F., & Main, H. (1992). Comparison of emission inventory and ambient mixing ratios of CO, NMOG, and NOX in Californias Southcoast Basin. *Journal of Air Waste Management Associeation, 42*(3), 264-276.

Gentner, D., Harley, R., Miller, A., & Goldstein, A. (2009). Diurnal and seasonal variability of gasoline-related volatile orgainc compound emissions in Riverside, California. *Environmental Science Technology, 43*(12), 4247-4252.

Gilman, J., Kuster, W., Goldan, P., Herndon, S., Zahniser, M., Tucker, S., . . . de Gouw, J. (2009). Measurements of volatile organic compounds during the 2006 TexAQS/GoMACCS campaign: Industrial influences, regional characteristics, and diurnal dependencies of the OH reactivity. *Journal of Geophysical Research: Atmospheres, 114*(D7).

Gilman, J., Lerner, B., Kuster, W., & de Gouw, J. (2013). Source signature of volatile organic compounds from oil and natural gas operations in Northeastern Colorado. *Environmental Science and Technology, 47*, 1297-1305.

Guo, H., So, K., Simpson, I., Barletta, B., Meinardi, S., & Blake, D. (2007). C1-C8 volatile organic compounds in the atmosphere of Hong Kong: Overview of atmospheric processing ans source apportionment. *Atmospheric Environment, 41*(7), 1456-1472.

Harley, R., McKeen, S., Pearson, J., Rodgers, M., & Lonneman, W. (2001). Analysis of motor vehicle emissions during the Nashville/Middle Tennessee ozone study. *Journal of Geophysical Research, 106*, 3559-3567.

Hartt, G. (2013). *Oil and gas emissions in the Gulf of Mexico and the San Joaquin Valley of Calfornia.* Ph. D. Thesis, University of California - Irvine.

Helmig, D., Thompson, C., Evans, C., Boylan, P., Hueber, J., & Park, J. (2014). Highly elevated atmosheric levels of volatile organic compounds in the Uintah Basin, Utah. *Environmental Science and Technology, 48*(9), 4707-4715.

Karion, A., Sweeney, C., Kort, E., Shepson, P., Brewer, A., Cambaliza, M., . . . Tans, P. (2015). Aircraft-baseeeee estimate of total methane emissions from the Barnett shale region. *Environmental Science Technology, 49*, 8124-8131.

Karion, A., Sweeney, C., Pétron, G., Frost, G., Hardesty, R., Kofler, J., . . . Conley, S. (2013). Methane emissions estimate from airborne measurements over a western United States natural gas field. *Geophysical Research Letters, 40*, 4393-4397.

Kim, K., Baek, S., Choi, Y., Sunwoo, Y., Jeon, E., & Hong, J. (2006). The emissions of major aromatic VOC as landfill gas from urban landfill sites in Korea. *Environmental Monitoring and Assessment, 118*, 407-422.

Kirchstetter, T., SInger, B., Harley, R., Kendall, G., & Chan, W. (1996). Impact of oxygenated gasoline ue on California light-duty vehicle emissions. *Environmental Science and Technology, 30*(2), 661-670.

Mays, K., Shepson, P., Stimm, B., Karion, A., Sweeney, C., & Gurney, K. (2009). Aircraft-based measuements of the carbon footprint of Indianapolis. *Environmental Science Technology, 43*(20), 7816-7823.

McGaughey, G., Desai, N., Allen, D., Seila, R., Lonneman, W., Fraser, M., . . . Price, J. (2004). Analysis of mtor vehicle emissions in a Houston tunnel during the Texas Air Quaity Study. *Atmopheric Environment, 38*(20), 3363-3372.

Parrish, D. (2006). Critical evaluatoin of US on-road vehicle emissoin inventories. *Atmospheric Environment, 40*, 2288-2300.

Peischl, J., Ryerson, T., Aiken, K., de Gouw, J., Gilman, J., Holloway, J., . . . Parrish, D. (2015). Quantifying atmospheric methane emissions from the Haynesville, Fayetteville, and northeasern Marcellus shale gas production regions. *Journal of Geophysical Research: Atmospheres, 120*, 2119-2139.

Pétron, G., Grost, G., Miller, B., Hirsch, A., Montzka, S., Karion, A., . . . Tans, P. (2012). Hydrocarbon emissions characterization in the Colorado Front Range: A pilot study. *Journal of Geophysical Research, 117*(D04304).

Pétron, G., Karion, A., Sweeney, C., Miller, B., Montzka, S., Frost, G., . . . Schnell, R. (2014). A new look at methane and nonmethane hydrocarbon emissions from oil and natural gas operations in the Colorado Denver-Julesburg Basin. *Journal of Geophysical Research: Atmospheres, 119*, 6836-6852.

Rettenberger, G., & Stegmann, R. (1996). Landfill gas components. In T. Christensen, R. Cossu, & R. Stegmann (Eds.), *Landfilling of Waste: Biogas* (pp. 51-58). London: E & FN Spoon.

Rusco, F. (2010). *Federal oil and gas leases: Opportunities exist to capture vented and flared natural gas, which would inrease royalty payments and reduce greenhouse gases.* Washington, D.C.: GAO.

Ryerson, T., Aikin, K., Angevine, W., Atlas, E., Blake, D., Brock, C., . . . Watts, L. (2011). Atmospheric emissions from the Deepwater Horizon Spill constrain air-water partitioning, hydrocarbon fate, and leak rate. *Geophysical Research Letters, 38*(L07803).

Ryerson, T., Trainer, M., Holloway, J., Parrish, D., Huey, L., Sueper, D., . . . Fehsenfeld, F. (2001). Observations of ozone formation in power plant plumes and implications for ozone control strategies. *Science, 292*(5517), 719-723.

Shaw, S., Mitloehner, F., Depeters, E., Fadel, J., Robinson, P., Holzinger, R., & Goldstein, A. (2007). Volatile organic compound emissions from dairy cows and their waste as measured by proton-transfer-reaction mass spectrometry. *Environmental Science and Technology, 41*, 1310-1316.

Sun, H., Trabue, S., Scoggin, K., Jackson, W., Pan, Y., Zhao, Y., . . . Mitleoehner, F. (2007). Alcohol, volatile fatty acid, phenol, and methane emissions from dairy cows and fresh manure. *Journal of Environmental Quality, 37*(2), 615-622.

Townsend-Small, A., Botner, E., Jimenez, K., Schroeder, J., Blake, N., Meinardi, S., . . . Flocke, F. (2016). Using stable isotopes of hydrogen to quantify biogenic and thermogenic atmospheric methane sources: A case study from the Colorado Front Range. *Geophysical Research Letters, 43*, 11462-11471.

Turnbull, J., Karion, A., Fischer, M., Faloona, I., Guilderson, T., Lehman, J., . . . Tans, P. (2011). Assessment of fossl fuel carbon dioxide and other anthropogenic trace gas emissions from airborne measurements over Sacramento, California in spring 2009. *Atmospheric Chemistry and Physics, 11*, 705-721.

USDA. (2012). *2007 Census of agriculture, county level data accessible via the USDA national agricultural statistical services quick stat.* Retrieved from http://quickstats.nass.usda.gov/

White, W., Anderson, J., Blumenthal, D., Husar, R., Gillani, N., Husar, J., & Wilson, W. (1976). Formation and transport of secondary air-pollutants: Ozone and aerosols in St. Louis urban plume. *Science, 194*(4261), 187-189.

Wilczak, J., & Glendening, J. (1988). Observations and mixed-layer modeling of a terrain-induced mesoscale gyre: The Denver Cyclone. *Monthly Weather Review, 116*, 2688-2711.

4. EMISSION CHARACTERIZATION OF THE COLORADO WESTERN SLOPE

The Northern Front Range of Colorado has been the site of extensive research over the years due to the high concentration of oil and natural gas activity in the area and its potential effect on local air quality. In particular, there have been numerous studies on emission characterization of the Denver-Julesburg basin, from ground samples (Klusman & Jakel, 1998; Pétron et al., 2012), tall towers (Gilman et al., 2013; LaFranchi et al., 2013; Swarthout, et al, 2013), and aircraft (Pétron et al., 2014). However, to our knowledge there has been much less work targeted on the characterization of emissions from the Piceance basin on the western slope of Colorado.

In 2014, there were 52,906 active wells in Colorado, 12,942 of which were located in the Piceance Basin (EIA, 2017). In the Denver-Julesburg Basin there were 24,209 active wells in 2014, but this basin produced 50% less natural gas than the smaller Piceance Basin, Figure 4.1 and 4.2 (COGCC, 2014). Natural gas is mainly comprised of light alkanes, $C_1 - C_5$, with higher chained alkanes, $C_6 - C_{10+}$, more commonly associated with oil production (Pedersen et al., 1989). This makes the Piceance a non-trivial source of ozone precursors that can reach the NFRMA. This chapter seeks to answer a part of the scientific question "*To what degree does*

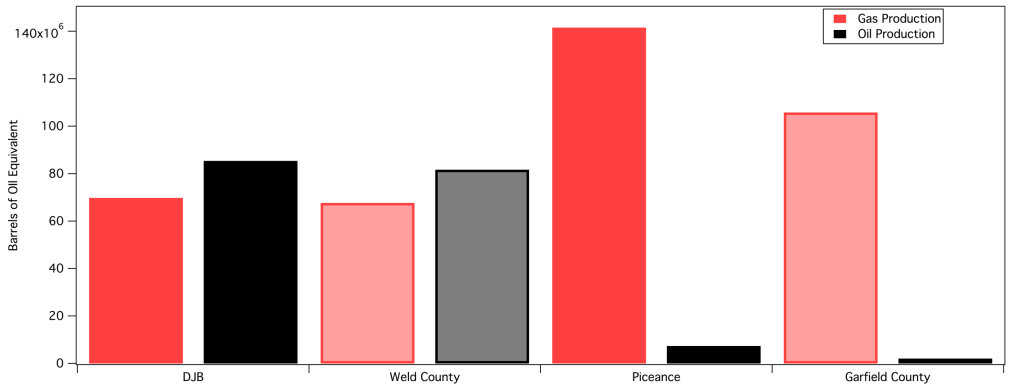

Figure 4.1 Oil and natural gas production in the Denver-Julesburg Basin (DJB) and the Piceance Basin with more than 85% of total natural gas production is concentrated in either Weld County in the DJB and Garfield County in the Piceance basin. Information courtesy of COGCC.

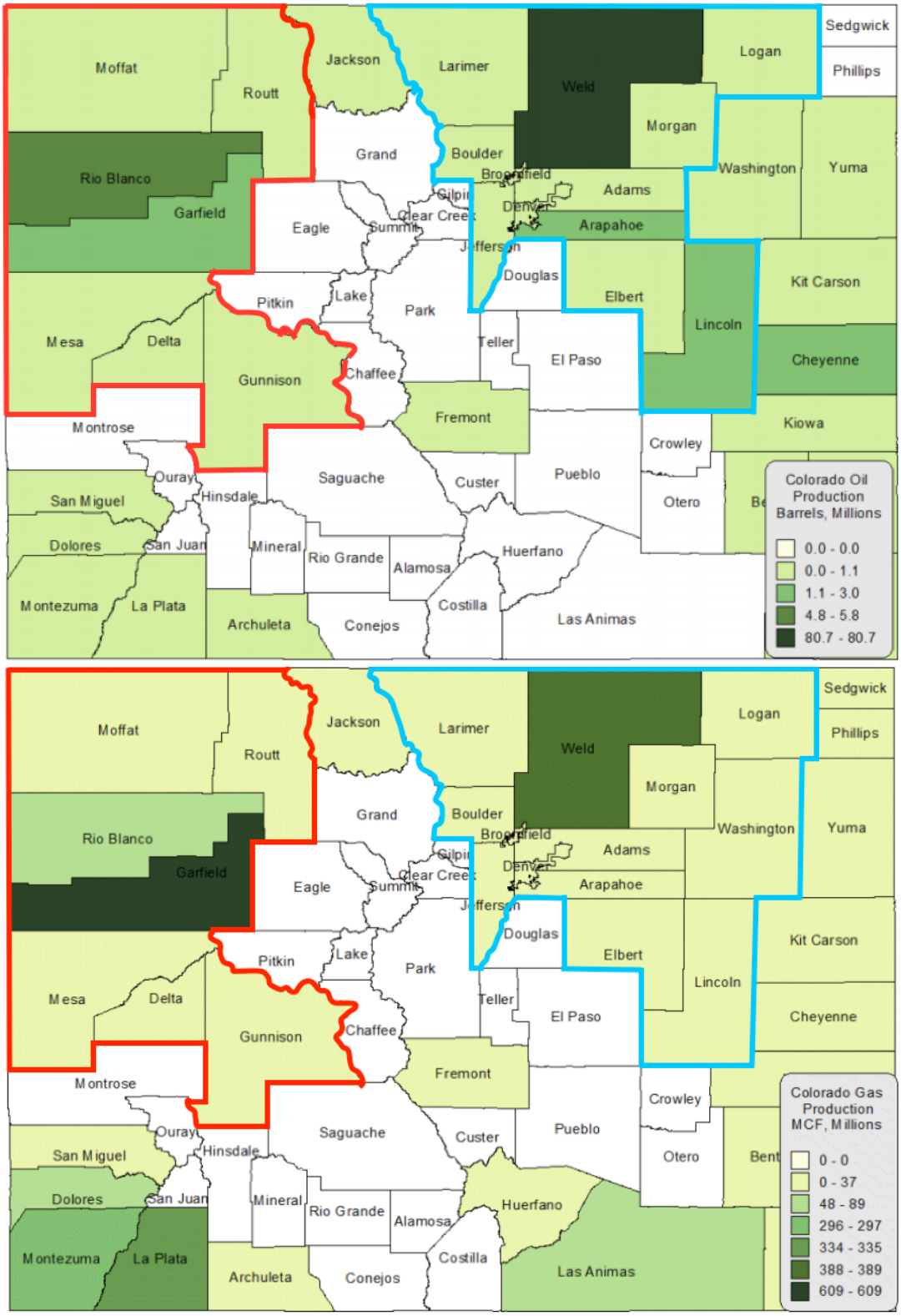

Figure 4.2 Map of Colorado counties colorized by natural gas production (top) and oil production (bottom) in 2014.The Piceance basin is highlighted in red, the DJB basin is highlighted in blue. Images courtesy of COGCC.

pollution from both NFRMA sources and long-range transport contribute to photochemical smog/ozone pollution, visibility degradation, and nitrate deposition in Rocky Mountain National Park and other Wilderness Regions to the West of NFRMA?" (Flocke & Pfister, 2013). The Piceance Basin provides a unique study area due to its remote location and limited agricultural activity in the surrounding area. By developing a trace gas signature of local oil and natural gas activity and the surrounding area, we can compare western and eastern slope emissions from the ONG industry.

4.1 Previous Studies of the Piceance and Surrounding Basins

The Piceance Basin is located on the western slope of the Rocky Mountains in Colorado and is adjacent to the Uintah Basin in Utah and the Green River Basin in Wyoming, Figure 4.3. There have been several studies regarding the ONG fields surrounding the Piceance (Carter & Seinfeld, 2012; Karion et al., 2013; Helmig et al., 2014;Rappengluck et al., 2014; Warneke et al., 2014;). For example, a study of the Green River basin revealed winter time ozone events were directly related to the ONG industry in that area (Rappengluck et al., 2014). Studies over the Uintah Basin have shown it is a major ONG production area and bottom-up inventories of ONG fugitive emissions from this basin are greatly underestimated (Karion et al., 2013).

Figure 4.3 Map of the Denver-Julesburg, Piceance, Uintah, and Green River oil and natural gas basins. Adapted from Jaffe, 2012, courtesy of USGS and NOAA.

Agricultural activity in the Piceance basin is limited to alfalfa, hay, cattle, and sheep, but only contributes a small percentage to the state total agricultural production, e.g., in 2014, 7.7% of Colorado's 2,550,000 cattle resided in the counties that makeup the Piceance basin, five times less than the total number of cattle in the Denver-Julesburg basin area (USDA NASS, 2015). In 2014, these same counties produced 11.2% and 15.2% of the total alfalfa and hay, respectively, in Colorado. Other agricultural activities in this area include apple and peach orchards, but these crops are concentrated in Delta and Mesa counties (USDA NASS, 2015). The sparse agriculture in this region is a result of the mountainous terrain and vast designated federal wilderness areas including those operated by the National Parks Service, Forest Service, and the Bureau of Land Management (courtesy of the U.S. DOI Bureau of Land Management, available at: http://blm-egis.maps.arcgis.com/home/item.html?id=ce8c08ad0ee94a3fb9c9d58375797849). From this information, we conclude that fossil fuel exploration and operations are the dominant hydrocarbon emission source in western Colorado.

Publicly available studies of ONG emissions in the Piceance Basin typically do not separate Piceance emissions from those of other Colorado basins (Bar-Ilan et al., 2007). They also do not provide detailed information of hydrocarbon emissions (Bar-Ilan et al., 2010; Friesen et al., 2009), or they are source specific (WRAP, 2015; Hilliard, 2016). A previous study comparing VOC emissions from the Uintah and Piceance basins found VOCs emissions from these adjacent basis are significantly different. This is presumably a result of emission controls in Colorado put in place by the CDPHE and COGCC. Oil and natural gas emissions from the Uintah basin are not as highly regulated as Colorado basins as the majority of Uintah lies within tribal land, where the Utah Department of Environmental Quality is not authorized to execute emission controls (Bar-Ilan, etal., 2007; Bar-Ilan et al., 2010; Friesen et al., 2009). Here we seek

to define an emission signature of the Piceance basin on a regional scale to assess both local emissions and upwind sources such as the Uintah basin.

4.2 Results

During FRAPPÉ, research flights 8, 13, and 15 surveyed the western slope of the Rocky Mountains on August 6th, 15th, and 17th, respectively. Flights 13 and 15 consisted of two flight segments, with an approximately 1 hour refuel stop (Table 2.1). The second segment of flight 13 and the first segment of flight 15 covered the eastern slope and therefore were excluded from this analysis, while the first segment of flight 13 and the second segment of flight 15 covered the western slope. Figure 4.4 shows a map of research flights 8, 13, and 15 colorized by methane and ethane. Figure 4.5 shows wind rose plots of aircraft wind data collected west of -106 °W and below 4 km. Figure 4.6 is a time series plot of CH_4, C_2H_6 and altitude from flights 8, 13, and 15. Natural gas production in the Piceance basin is concentrated in Garfield County (Figure 4.2), and is highlighted by elevated CH_4 and C_2H_6 concentrations, as shown in Figure 4.4, Elevated CH_4 and C_2H_6 are also found in flight segments over and downwind of the Uintah basin. From the time series plot of CH_4 and C_2H_6 (Figure 4.6) it is apparent that CH_4 and C_2H_6 are well correlated throughout all three flights, and were used to define air masses influenced by the Piceance and Uintah basins. Table 4.1 shows the statistics for 1-Hz measurements of CH_4, C_2H_6, CO, CO_2, NO, NO_2, SO_2 and O_3 in air masses influenced by the Piceance and Uintah basins, compared to background measurements. Table 4.2 shows the statistics for select hydrocarbons measured in AWAS samples. The local background was determined by filtering aircraft data to remove measurements collected over the Uintah and Piceance basins and the eastern slope (-106 °W). Aircraft measurements above 4 km pressure altitude were also removed to better represent surface emissions. Average background values that were below the limit of detection (<LOD), 3

pptv,

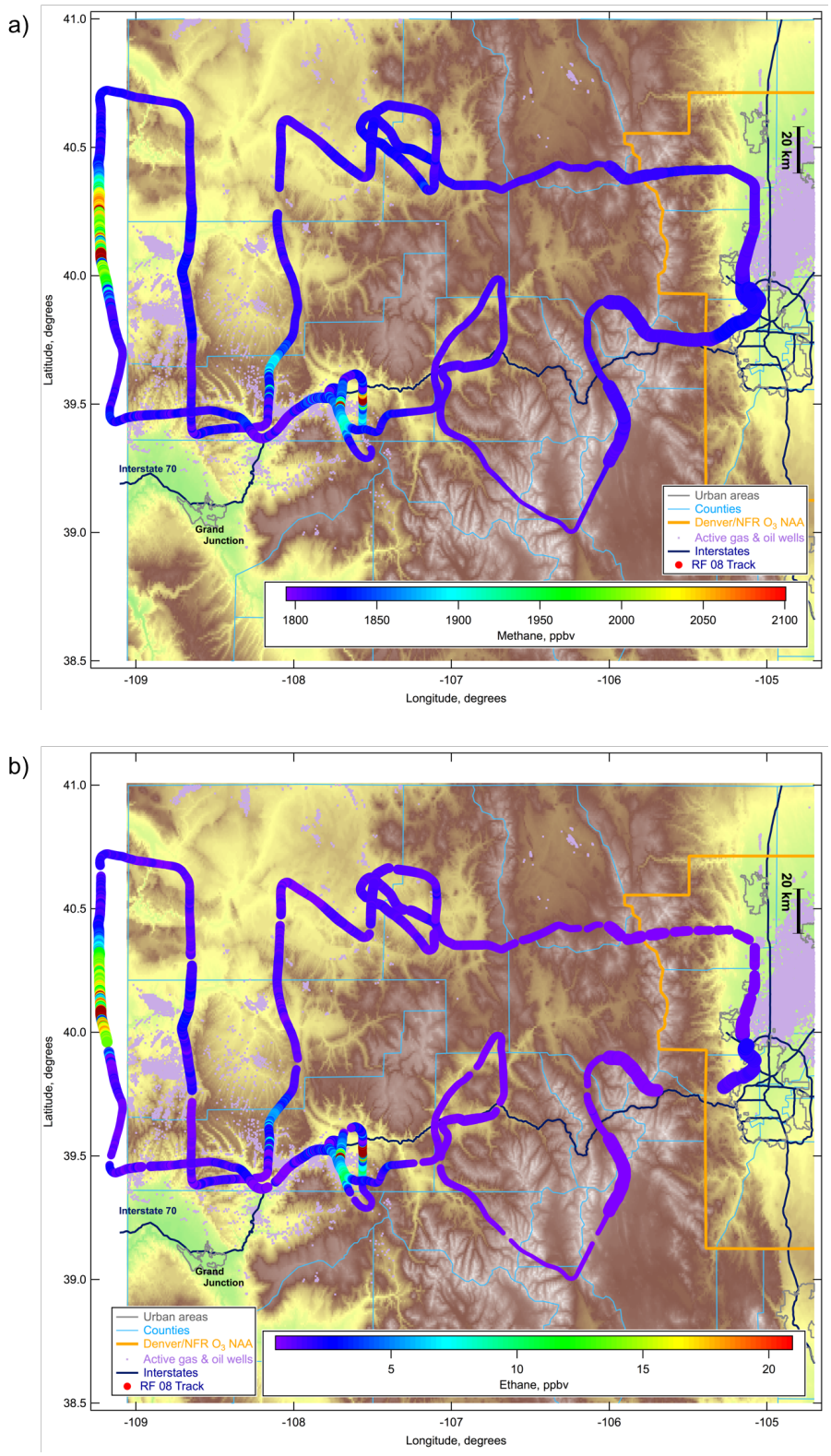

Figure 4.4 Map of research flights 8, 13, and 15 colorized by 1-Hz measurements of methane (a, c, e) and ethane (b, d, f), and AWAS ethane measurements (g). All points are sized by pressure

altitude, with smaller symbols for higher altitudes.

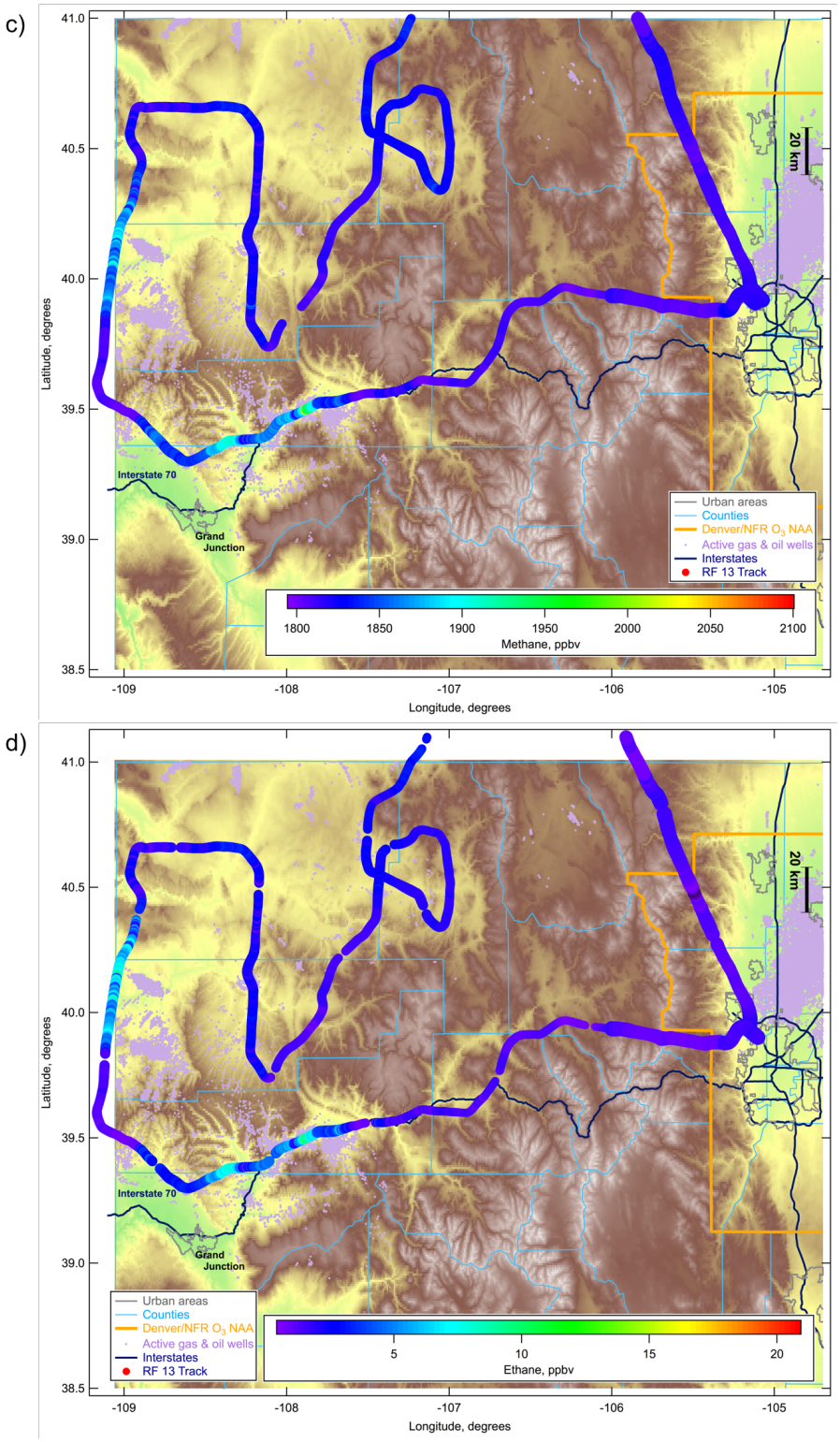

Figure 4.4 (Cont.) Map of research flights 8, 13, and 15 colorized by 1-Hz measurements of methane (a, c, e) and ethane (b, d, f), and AWAS ethane measurements (g). All points are sized by pressure altitude, with smaller symbols for higher altitudes.

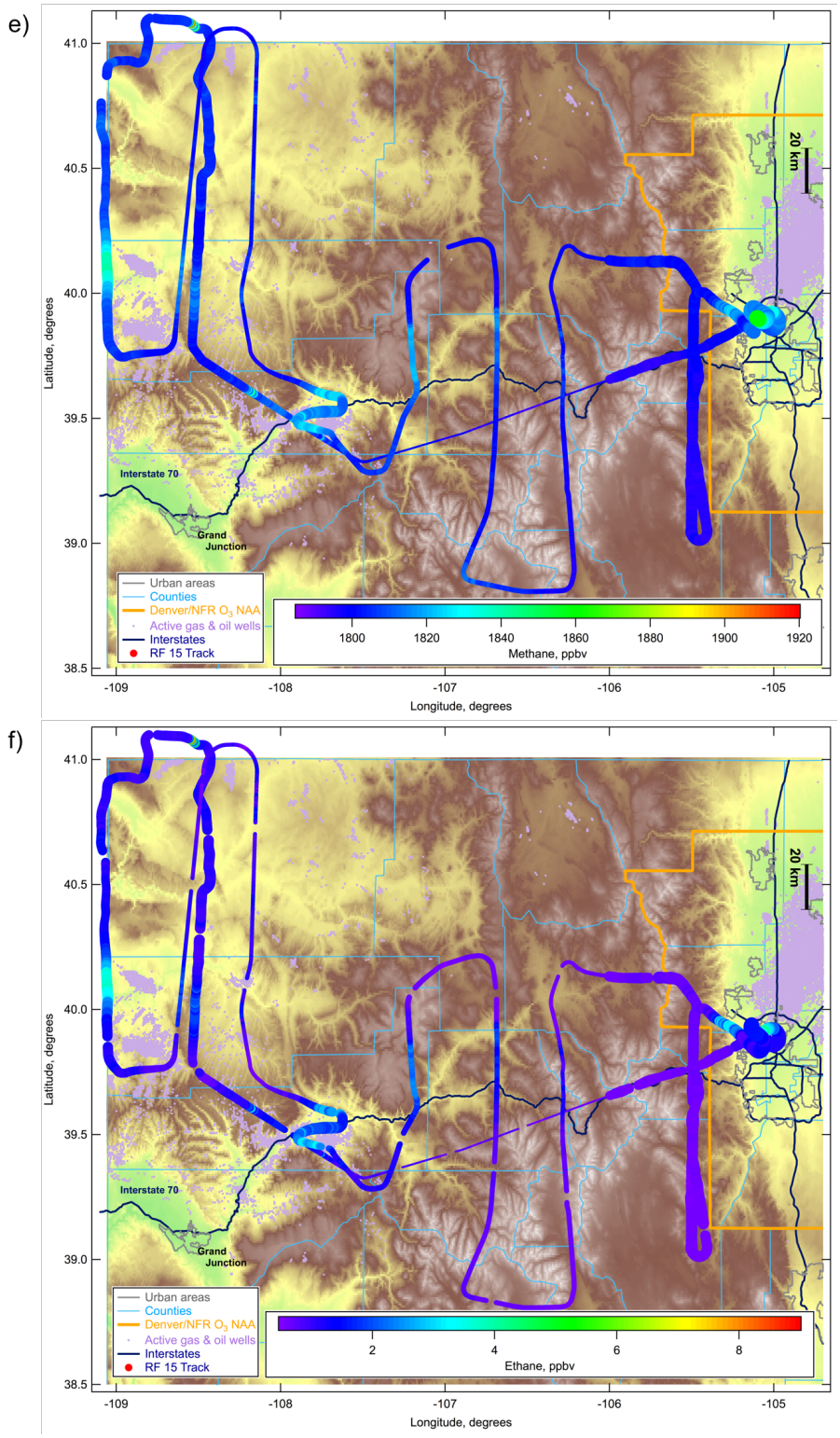

Figure 4.4 (Cont.) Map of research flights 8, 13, and 15 colorized by 1-Hz measurements of methane (a, c, e) and ethane (b, d, f), and AWAS ethane measurements (g). All points are sized by pressure altitude, with smaller symbols for higher altitudes.

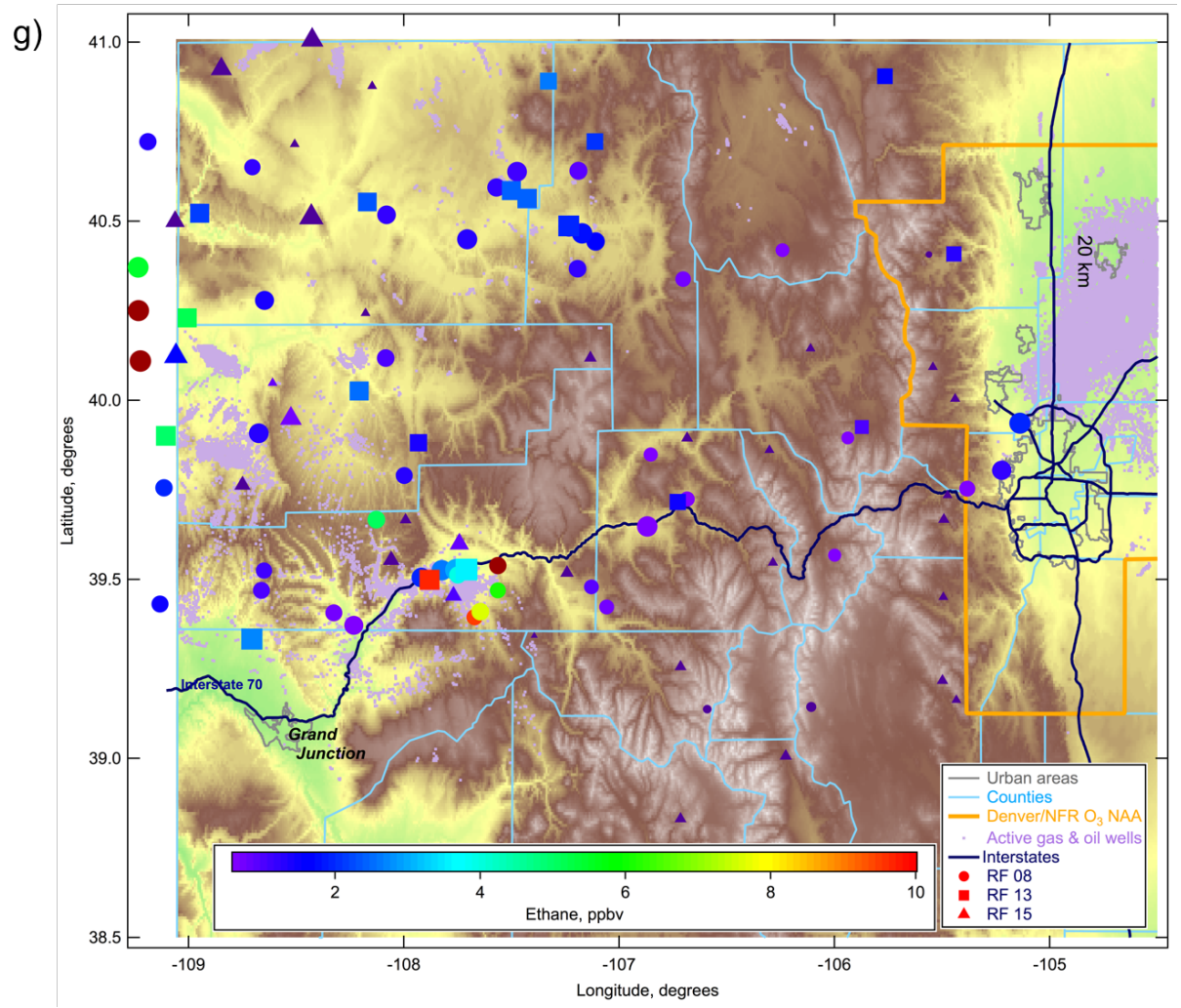

Figure 4.4 (Cont.) Map of research flights 8, 13, and 15 colorized by 1-Hz measurements of methane (a, c, e) and ethane (b, d, f), and AWAS ethane measurements (g). All points are sized by pressure altitude, with smaller symbols for higher altitudes.

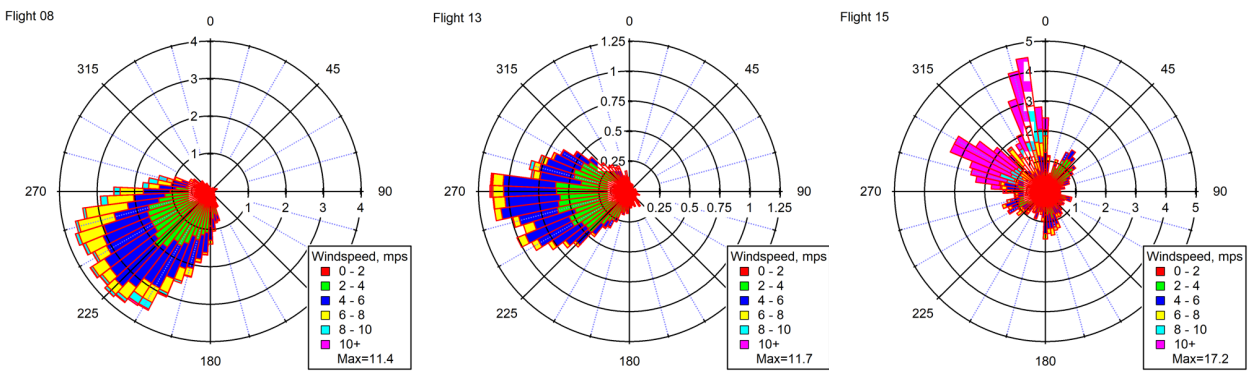

Figure 4.5 Wind rose plots for flight 8 (left), 13 (middle), and 15 (right). Measurements of wind speed and direction were filtered to only include measurements collected west of -106 °W and below a pressure altitude of 4 km.

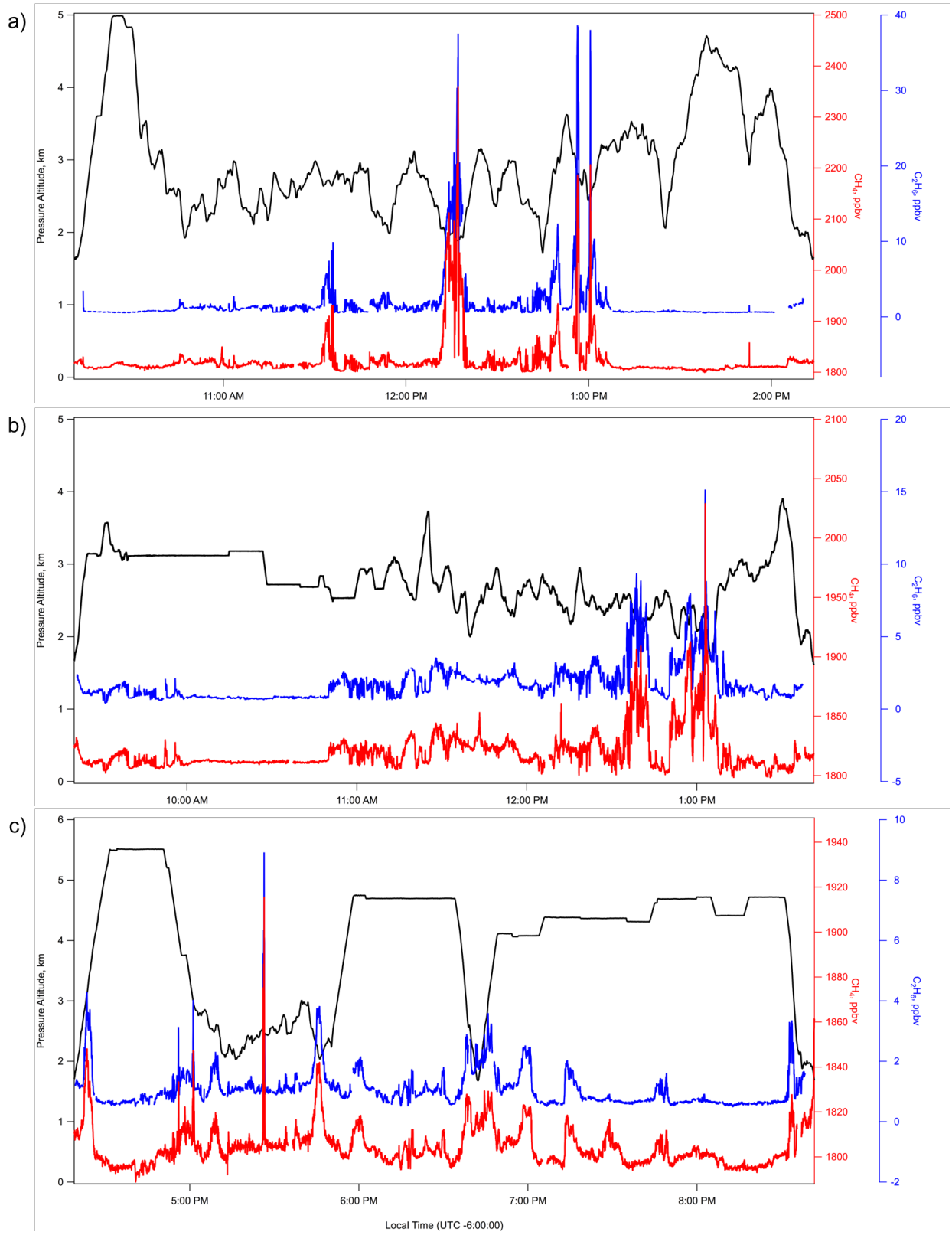

Figure 4.6 Time series plots of pressure altitude (black), methane (red), and ethane (blue) of research flights 08 (a), 13 (b), and 15 (c).

Table 4.1 Minimum (Min), maximum (Max), average (Avg), and standard deviation (StD) of 1-Hz measurements of CH_4, C_2H_6, CO, CO_2, NO, NO_2, SO_2 and O_3 measured over the Piceance (PB) and Uintah (UB) basins. Local background values are also included as well as maximum enhancements (Max Enh.: basin max/BKG) and average enhancements (Avg. Enh.: basin avg./BKG) of measurements collected over basins over background. Units of CH_4, C_6H_6, CO, CO_2, and O_3 are ppbv. Units of NO, NO_2, and SO_2 are pptv. <LOD=below limit of detection. Maximum and average enhancements greater than 10.00 over background averages are highlighted in bold.

		Piceance Basin				**Uintah Basin**				**Background**		**Max Enh.**		**Avg. Enh.**	
RF	Trace Gas	Min	Max	Avg	StD	Min	Max	Avg	StD	Avg	StD	PB	UB	PB	UB
8	CH_4	1800	2207	1841	51	1808	2361	1888	100	1814	7	1.22	1.30	1.01	1.04
	C_2H_6	0.52	38.64	3.70	4.96	0.59	37.53	6.42	7.07	1.07	0.45	**36.00**	**34.97**	3.45	5.98
	CO	79	101	84	2	83	1036	115	112	87	9	1.16	**11.86**	0.96	1.32
	CO_2	394	403	399	1	400	437	403	4	401	4	1.00	1.09	1.00	1.00
	NO	20	936	86	86	30	26826	617	2779	481	1622	1.94	**55.72**	0.18	1.28
	NO_2	37	1997	207	222	86	40368	1157	4408	1099	2783	1.82	**36.71**	0.19	1.05
	SO_2	<LOD	84	28	13	11	7909	269	870	229	759	0.37	**34.54**	0.12	1.17
	O_3	48	62	56	3	27	66	57	4	54	4	1.14	1.21	1.03	1.06
13	CH_4	1801	2029	1848	32	1805	1909	1851	24	1819	9	1.12	1.05	1.02	1.02
	C_2H_6	0.72	15.15	3.79	2.00	0.96	9.37	5.01	1.93	1.91	0.62	7.93	4.90	1.98	2.62
	CO	76	100	90	4	84	353	125	61	89	8	1.13	3.96	1.01	1.41
	CO_2	396	407	401	2	398	411	402	3	400	3	1.02	1.02	1.00	1.00
	NO	23	1603	118	112	43	5286	655	1112	308	709	5.20	**17.15**	0.38	2.12
	NO_2	55	3988	353	344	107	11988	1669	2609	737	1540	5.41	**16.27**	0.48	2.27
	SO_2	<LOD	91	39	18	55	2261	383	486	213	450	0.43	**10.62**	0.16	1.62
	O_3	43	60	54	3	47	64	58	3	52	4	1.15	123	1.04	1.13
15	CH_4	1795	1847	1810	9	1802	1842	1818	11	1805	3	1.02	1.02	1.00	1.01
	C_2H_6	0.50	4.03	1.44	0.64	1.02	3.83	2.08	0.88	1.10	0.16	3.68	3.49	1.31	1.89
	CO	72	102	81	2	79	104	85	6	81	2	1.26	1.28	0.99	1.05
	CO_2	396	400	398	1	398	399	399	1	398	1	1.01	1.00	1.00	1.00
	NO	13	745	50	56	21	219	65	48	38	15	**19.52**	5.74	1.31	1.69
	NO_2	6	4455	171	339	61	875	213	200	107	48	**41.64**	8.18	1.60	1.99
	SO_2	<LOD	154	49	21	20	329	116	69	67	29	2.29	4.90	0.73	1.72
	O_3	48	56	52	2	50	57	53	2	54	2	1.04	1.06	0.96	0.98
Total	**CH_4**	1795	2207	1829	38	1802	2361	1862	77	1815	9	1.22	1.30	1.01	1.03
	C_2H_6	0.50	38.64	2.74	3.33	0.59	37.53	5.05	5.39	1.37	0.63	**28.27**	**27.46**	2.00	3.70
	CO	72	102	84	5	79	1036	111	86	87	9	1.17	**11.89**	0.96	1.28
	CO_2	394	407	399	2	398	437	401	4	400	4	1.02	1.09	1.00	1.00
	NO	13	1603	77	90	21	26826	518	2125	356	1242	4.46	**74.65**	0.21	1.44
	NO_2	6	4455	227	322	61	40368	1107	3531	835	2607	5.34	**48.36**	0.27	1.33
	SO_2	<LOD	154	39	20	11	7909	268	674	210	626	0.73	**37.70**	0.26	1.28
	O_3	43	62	54	3	27	66	57	4	53	4	1.16	1.23	0.73	1.06

Table 4.2 Statistics of AWAS measurements of select NMHCs measured over the Piceance (n=16) and Uintah (n=9) basins compared to local background (n=42) measurements. Units are in pptv, unless otherwise stated. Maximum (basin max/background) and average enhancements (basin avg/background) over background values greater than 10.00 are highlighted in bold.

	Piceance Basin				**Uintah Basin**				**Background**		**Max Enh.**		**Avg. Enh.**	
NMHC	Min	Max	Avg	StD	Min	Max	Avg	StD	Avg	StD	PB	UB	PB	UB
Ethane, *ppbv*	1.26	2.22	6.09	5.56	1.24	13.14	4.69	4.15	1.39	0.62	**15.9**	9.4	3.86	3.37
Ethene	36	177	63	36	25	127	55	34	37	14	4.7	3.4	1.54	1.48
Ethyne	56	94	69	11	42	183	86	45	62	7	1.5	3.0	1.05	1.36
Propane	387	8437	2207	2135	403	7262	2363	2360	573	335	**14.7**	**12.7**	3.38	4.12
Propene	10	24	15	4	7	28	14	6	14	5	1.7	2.0	0.99	1.01
n-Butane	71	2143	576	554	95	2666	844	918	151	106	**14.2**	**17.6**	3.34	5.58
i-Butane	63	2102	532	543	80	1563	497	524	81	49	**25.9**	**19.3**	5.73	6.12
n-Pentane	23	779	221	203	35	1132	343	386	53	36	**14.8**	**21.5**	3.67	6.51
i-Pentane	33	993	290	255	49	1222	357	396	58	35	**17.1**	**21.0**	4.41	6.15
2,2-Dimethylbutane	<LOD	39	13	11	<LOD	37	12	13	<LOD	n/a	**26.0**	**24.7**	9.16	9.64
2,3-Dimethylbutane	<LOD	63	20	18	<LOD	62	16	21	2	3	**35.3**	**34.7**	9.35	9.15
n-Hexane	14	419	121	111	24	534	163	185	21	14	**20.3**	**25.9**	5.14	7.89
2-Methylpentane	9	302	89	78	13	445	117	143	14	10	**22.2**	**32.7**	6.45	8.59
3-Methylpentane	5	169	51	44	7	227	61	70	7	6	**24.1**	**32.3**	5.14	8.63
n-Heptane	9	225	76	67	15	301	89	99	11	8	**20.9**	**27.9**	6.25	8.21
n-Octane	<LOD	108	34	31	<LOD	107	32	36	<LOD	n/a	**72.0**	**71.3**	**20.63**	**21.33**
Cyclopentane	<LOD	42	12	12	<LOD	123	28	38	2	4	**18.6**	**54.4**	4.75	12.3
Cyclohexane	9	203	68	54	<LOD	292	79	93	10	9	**20.7**	**29.8**	6.04	8.06
Methylcylohexane	10	347	111	95	<LOD	422	105	136	6	7	**58.1**	**70.6**	**16.00**	**17.60**
Benzene	33	143	76	38	24	268	84	80	27	9	5.3	**10.0**	2.56	3.14
Toluene	22	162	80	48	11	268	72	81	16	11	9.9	**16.4**	4.28	4.40
Ethylbenzene	<LOD	11	5	4	<LOD	12	3	4	<LOD	n/a	7.3	8.0	2.67	1.78
m+p-Xylene	<LOD	54	30	19	<LOD	49	13	17	<LOD	n/a	**36.0**	**32.7**	**16.75**	8.61
o-Xylene	<LOD	12	5	4	<LOD	8	2	3	<LOD	n/a	8.0	5.3	2.54	1.06
2-Ethyltoluene	<LOD	12	1	3	<LOD	4	1	2	<LOD	n/a	8.0	2.7	0.50	0.44
3-Ethyltoluene	<LOD	13	2	4	<LOD	6	1	1	<LOD	n/a	8.7	2.0	0.83	0.33
4-Ethyltoluene	<LOD	20	2	6	<LOD	3	1	2	<LOD	n/a	**13.3**	4.0	1.00	0.61
1,3,5-Trimethylbenzene	<LOD	12	1	3	<LOD	4	1	2	<LOD	n/a	8.0	2.7	0.63	0.44
1,2,4-Trimethylbenzene	<LOD	17	2	5	<LOD	6	1	2	<LOD	n/a	**11.3**	4.0	1.08	0.61
1,2,3-Trimethylbenzene	<LOD	17	2	5	<LOD	9	1	2	<LOD	n/a	**16.0**	6.0	1.17	0.94
Isoprene	<LOD	220	62	67	<LOD	99	16	29	80	148	2.8	1.2	0.75	0.19
α-Pinene	<LOD	14	6	5	<LOD	9	2	3	4	4	3.9	2.5	0.54	0.51
β-Pinene	<LOD	6	1	2	<LOD	<LOD	n/a	n/a	<LOD	n/a	4.0	n/a	0.25	n/a

were given a value of 1.5 pptv in order to provide estimated maximum and average enhancements. Maximum enhancements are defined as the basin maximum value over the average background. Average enhancements are defined as the basin average value over the average background (Simpson et al., 2010).

Carbon monoxide, NO, NO_2, and SO_2 are produced from the combustion of fossil fuels (Fujita et al., 1992; Benkovitz et al., 1996; Harley et al., 2001; Parrish, 2006; Baker et al., 2008;). From Table 4.1 it is apparent that the Uintah basin is directly influenced by a local combustion source, as shown by maximum enhancement values of CO (11.89x), NO (74.65x), NO_2 (48.36x), and SO_2 (37.70x). During flight 08, we see elevated CO concentrations over the Uintah basin, with a maximum value of 1036 ppbv, that corresponds to the elevated concentrations of NO (26.8 ppbv), NO_2 (40.4 ppbv), and SO_2 (7.9 ppbv) (Figure 4.7). The maximum values of these compounds were measured directly downwind of a coal fired power plant in Bonanza, Utah (40.09 °N, -109.28 °W). During flight 08, the aircraft intersected this plume for 73 seconds, during this time these compounds showed no correlation to methane or ethane ($0.07 \leq R^2 \leq 0.25$) (Figure 4.7). During flight 13, the aircraft intersected this emission source as we also see enhancements of CO (353 ppbv) in the flight segment over the Uintah basin. The aircraft intersected this plume for approximately 3 minutes. During this time, there is also a strong signature of NO, NO_2, and SO_2 (Figure 4.7b), however, these compounds also did not correlate well with CH_4 or C_2H_6 ($0.31 \leq R^2 \leq 0.47$) and intersection of this plume was short lived and therefore did not significantly alter average estimates as average enhancements of these compounds ranged from 0.12 – 2.27. The flight segment over the Uintah basin during flight 15 was further east and winds were much higher and from the north west (Figure 4.5). This flight segment also exhibited slightly enhanced CO, but was statistically similar to background

measurements. We do not see elevated CO, NO, NO_2, or SO_2 further downwind during either of the flights and therefore can eliminate the power plant as a source of CH_4 and C_2H_6 in this region. Further, we conclude that the power plant emissions were localized in this area and did not significantly impact measurements of methane and ethane.

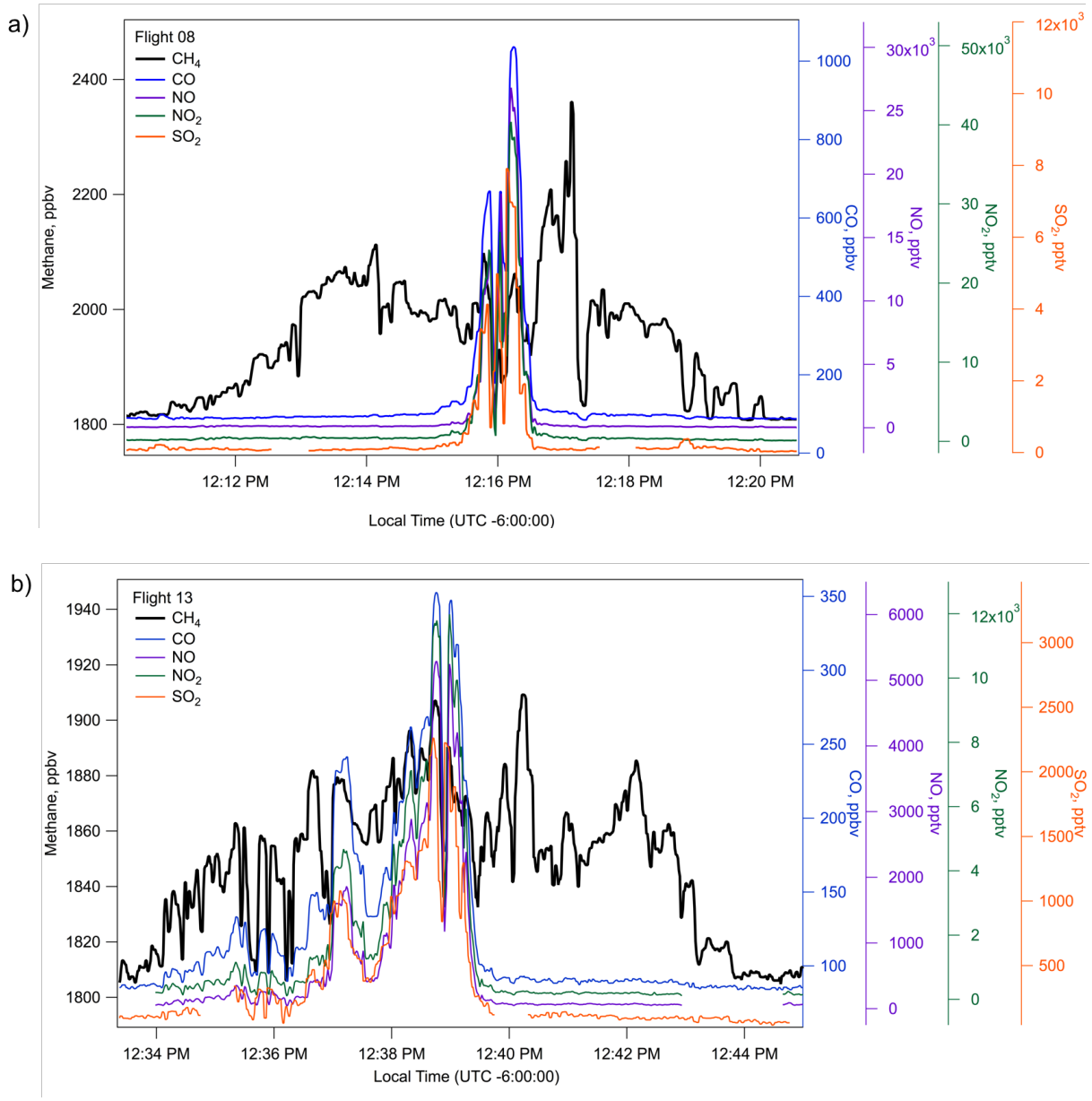

Figure 4.7 Time series plot of CH_4 (black), CO (blue), NO (purple), NO_2 (green), and SO_2 (orange) during flight 8 (a) and flight 13 (b) over the Uintah basin.

Elevated values and large standard deviations of NO, NO_2, and SO_2 in background measurements can be attributed to a second coal fired power plant near Hayden, CO (40.49 °N and -107.18 °W). This area was included in the background as methane and ethane enhancements were indistinguishable from background measurements, even during a missed approach at the Hayden Airport during flight 8. Therefore, we can say that these sources do not contribute to the hydrocarbon signature of the local ONG basins.

The maximum enhancements of NMHCs measured over the Piceance basin ranged from 1.5–72.0x, and 1.2–71.3x over the Uintah basin while average NMHC enhancements ranged from 0.25–20.63x and 0.33–21.33x for each respective basin (Table 4.2) The greatest maximum enhancements over both basins was *n*-octane, followed by methylcyclohexane at 58.1x over the Piceance and 70.6x over the Uintah. Average enhancements of *n*-octane and methylcyclohexane were 20.63x and 16.00 over the Piceance and 21.33x and 17.60 over the Uintah basins, respectively. It is important to note that the average background measurements for *n*-octane were <LOD, and a value of 1.5 pptv was assumed. Biogenic compounds isoprene, α-pinene, and β-pinene were slightly enhanced over the Piceance basin, from 2.8–4.0x, and is likely a result of the absence of vegetation in the Uintah basin. Notably, maximum enhancements for C_3–C_8 alkanes were all greater than 12x (12.7–72.0x over both basins), especially cycloalkanes, ranging from 18.6–70.6x, over both basins. Benzene and toluene were enhanced over both basins, but more significantly over the Uintah basin, with maximum enhancements nearly twice as large as enhancements over the Piceance.

One of the most notable differences between the Piceance and Uintah basins is the magnitude of maximum and average enhancements of several aromatic compounds, the xylenes, ethyltoluenes, and trimethylbenzenes. Maximum and average enhancements over the Piceance

basin ranged from 8.0–36.0x and 0.50–16.75x, respectively, while Uintah maximum enhancements ranged from 2.0–32.7x and 0.33–8.61x, respectively. These enhancements measured over the Piceance basin are the opposite of the trend seen in the alkane enhancements over both basins. Benzene and toluene were, however, most enhanced over the Uintah basin. Average background values of the majority of these compounds were below the limit of detection, therefore the enhancements measured here are a conservative estimate. It is expected average concentrations measured in background levels would be much smaller than the presumed concentration of 1.5 pptv because of their short atmospheric lifetimes of less than 24 hours, as shown in Table 1.8 (Atkinson, 2006).

As described in chapter 3, CH_4 and C_2H_6 are co-emitted from ONG systems and a C_2H_6/CH_4 emission ratio can be used as a strong indicator of oil and natural gas influence. The time series plots of CH_4 and C_2H_6, shown in Figure 4.6, are nearly identical and illustrate the co-emission of these compounds throughout western Colorado. Figure 4.8 shows the C_2H_6/CH_4 emission ratio for all three flights over this region, all of which were strongly correlated, with an average emission ratio of 7.11 ± 0.01% and an overall R^2 value of 0.91. The C_2H_6/CH_4 emission ratio over the Piceance basin was determined to be 8.17 ± 0.03% with an R^2 value of 0.92, compared to Uintah at 6.65 ± 0.03%, (R^2=0.95), and background measurements of 5.85 ± 0.03% (R^2=0.68), Figure 4.9. We compare these emission ratios to previous studies of the area and examine the relationship between higher chained alkanes associated with ONG and their VOC to CH_4 emission ratios, shown in Table 4.3, compared to the natural gas composition/emissions of the Piceance and Uintah basins measured in previous studies, Table 4.4. Previous studies include: the Western Regional Air Partnership (WRAP) 2006 study, which provided an emission inventory of the organic composition of produced natural gas in the Piceance and Uintah basins

from gas wells, oil wells, and flash gas from natural gas condensate and oil tanks (http://www.wrapair.org/forums/ogwg/PhaseIII_Inventory.html), a study from Colorado State University that examined VOC emissions from drilling and fracking operations in the Piceance (Hilliard, 2016), and the 2014 natural gas composition reported from delivery gas measurements taken at Rifle, CO, courtesy of Xcel Energy.

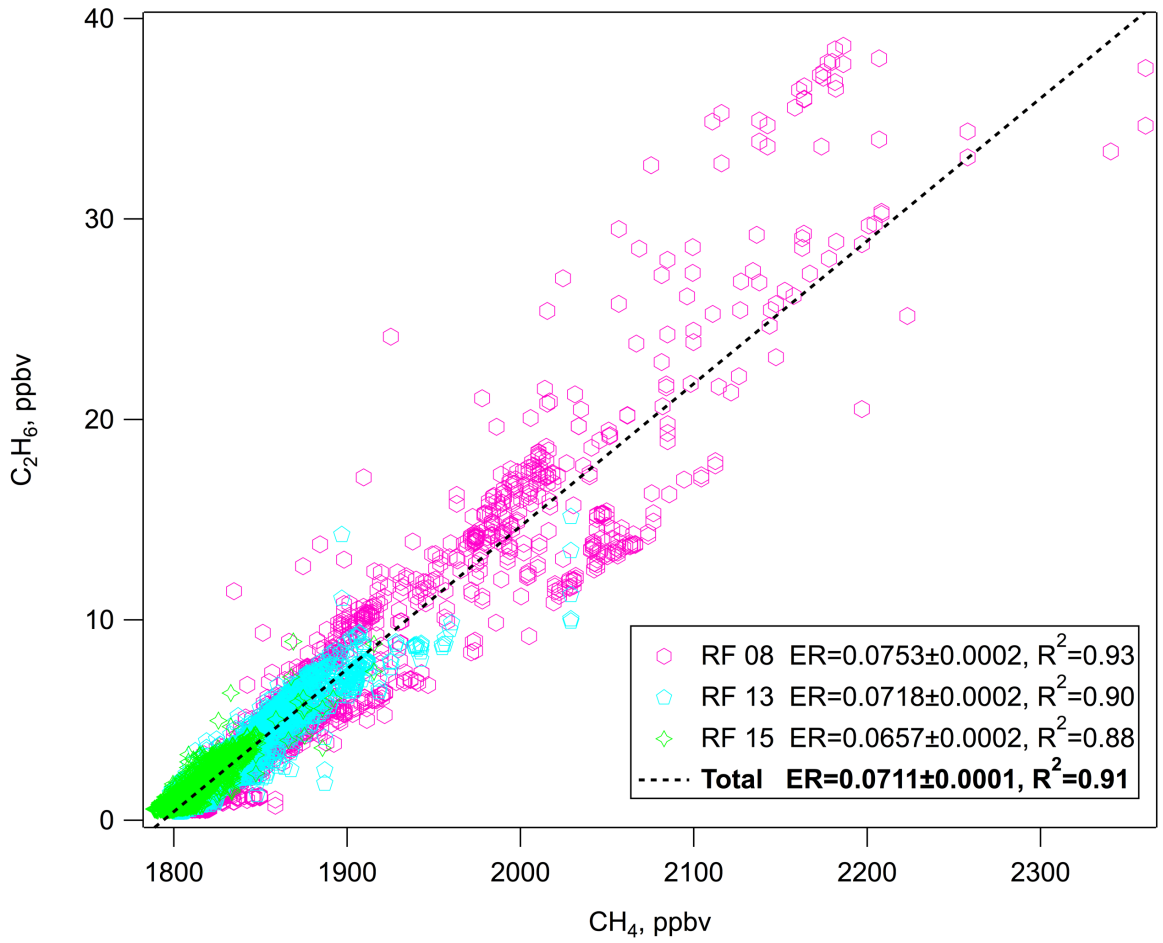

Figure 4.8 Correlation plot of methane to ethane for all measurements during flight 8 (pink), flight 13 (cyan), and flight 15 (green).

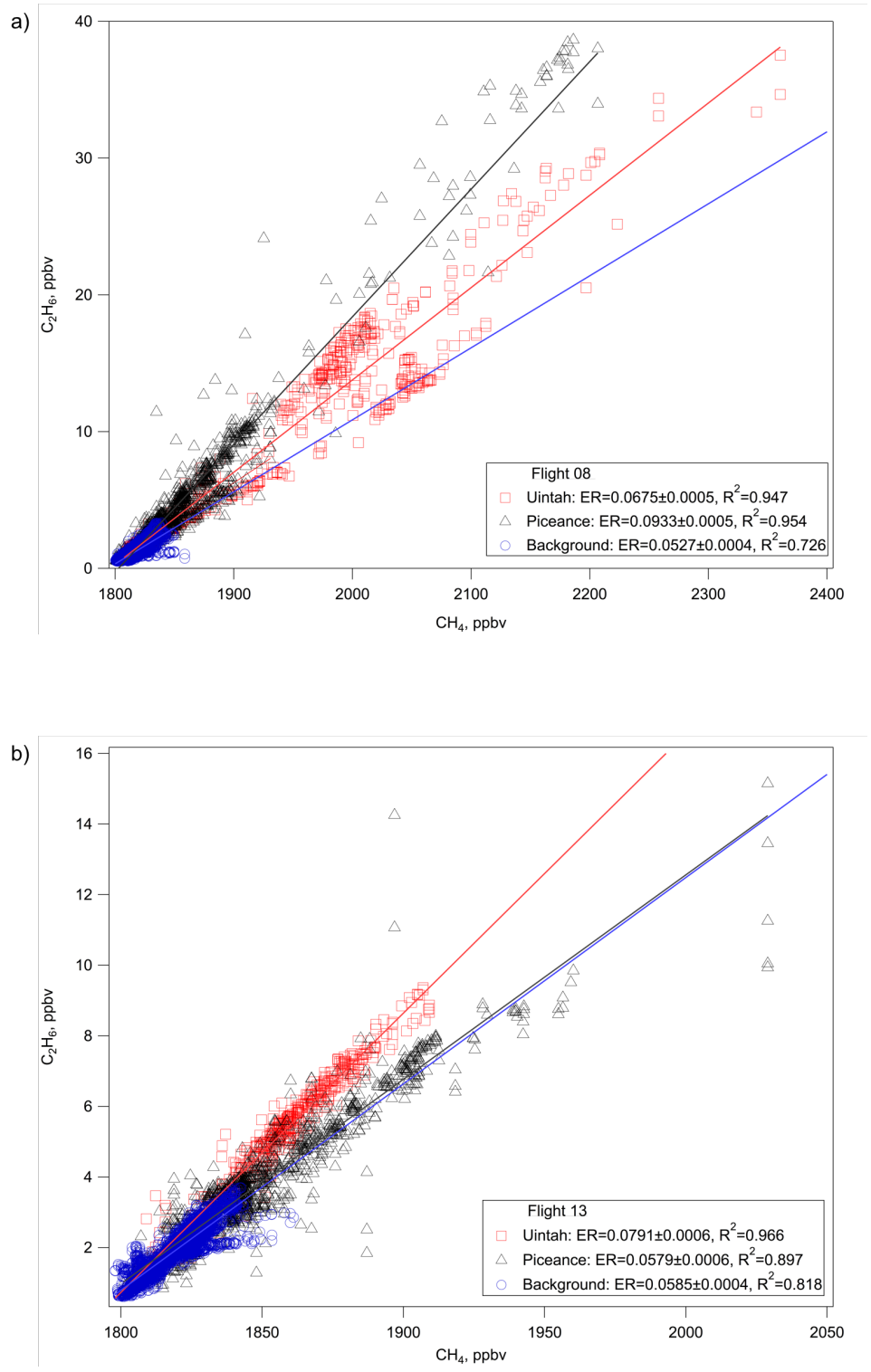

Figure 4.9 Correlation plots of CH_4 and C_2H_6 over the Uintah (red) and Piceance (black) basins and the local background (blue) for research flights 8 (a), 13 (b), and 15 (c), with all data points shown in d.

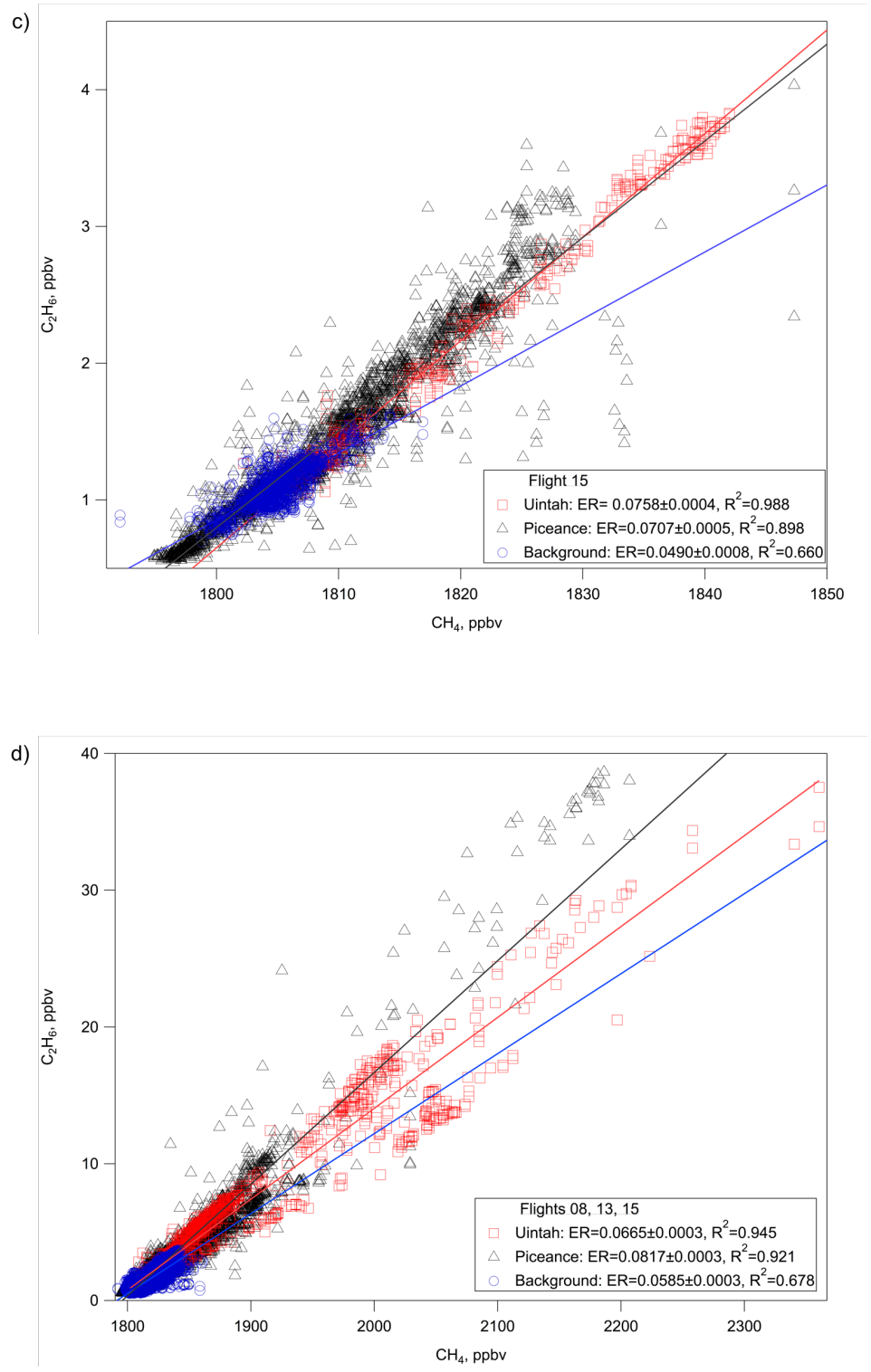

Figure 4.9 (Cont.) Correlation plots of CH_4 and C_2H_6 over the Uintah (red) and Piceance (black) basins and background (blue) for research flights 8 (a), 13 (b), and 15 (c), with all data in plot d.

Table 4.3 Comparison of select VOC to CH_4 emission ratios (ER) in the Piceance and Uintah basins, compared to background. Units are ppbv/ppbv, written as percent.

	Piceance		Uintah		Background	
	ER ×100	R^2	ER ×100	R^2	ER ×100	R^2
C_2H_6/CH_4	8.17 ± 0.03	0.921	6.65 ± 0.03	0.945	5.85 ± 0.03	0.678
C_3H_8/CH_4	2.58 ± 0.29	0.851	2.63 ± 0.20	0.945	3.15 ± 0.31	0.724
nC_4H_{10}/CH_4	0.65 ± 0.08	0.809	1.04 ± 0.06	0.966	0.89 ± 0.12	0.582
iC_4H_{10}/CH_4	0.64 ± 0.08	0.822	0.59 ± 0.03	0.974	0.43 ± 0.05	0.639
nC_5H_{12}/CH_4	0.24 ± 0.03	0.815	0.44 ± 0.02	0.975	0.30 ± 0.04	0.563
iC_5H_{12}/CH_4	0.31 ± 0.04	0.823	0.45 ± 0.01	0.992	0.29 ± 0.04	0.571
C_6H_6/CH_4	0.04 ± 0.01	0.667	0.09 ± 0.01	0.978	0.06 ± 0.01	0.449
nC_7H_{16}/CH_4	0.08 ± 0.01	0.766	0.11± 0.01	0.983	0.07 ± 0.01	0.609

Table 4.4 Comparison of CH_4 emission ratios from the produced natural gas composition (Xcel Energy, WRAP) and VOC emissions measured from various ONG operations (Hilliard, 2016) in the Piceance Basin. Units are mol/mol, written as percent.

	Xcel[a]	Non-CBM[b]	Oil wells[b]	Flash Gas NG[b]	Drilling[c]	Fracking[c]
C_2H_6/CH_4	5.93	12.42	34.24	123.98	6.56	1.94
C_3H_8/CH_4	1.40	4.95	77.9	194.77	5.38	0.17
nC_4H_{10}/CH_4	0.21	1.05	64.40	99.05	2.36	0.02
iC_4H_{10}/CH_4	0.27	1.44	35.79	86.99	1.83	0.04
nC_5H_{12}/CH_4	0.04	0.51	22.56	33.22	1.01	0.03
iC_5H_{12}/CH_4	0.07	0.76	28.87	43.92	1.19	0.03
C_6H_6/CH_4	-	0.06	0.16	3.08	0.73	0.26
nC_7H_{16}/CH_4	0.02	0.40	4.07	23.04	0.18	0.37

[a]Data courtesy of Xcel Energy
[b]https://www.wrapair.org//forums/ogwg/PhaseIII_Inventory.html
[c]Hilliard, 2016

Table 4.5 Comparison of CH_4 emission ratios from the produced natural gas composition (WRAP) and surface VOC measurements (Helmig et al., 2014) in the Uintah Basin. All units are mol/mol, written as percent.

	Surface Measurements[a]	CBM Wells[b]	Non-CBM[b]	Flash Gas Oil[b]	Flash Gas NG[b]
C_2H_6/CH_4	14.0	0.60	11.62	719	90
C_3H_8/CH_4	3.1	0.17	7.13	3.32×10^3	196
nC_4H_{10}/CH_4	0.89	0.02	2.54	$4.25\ 310^5$	209
iC_4H_{10}/CH_4	0.61	0.03	1.87	1.17×10^3	109
nC_5H_{12}/CH_4	0.32	0.01	0.94	8.69×10^3	219
iC_5H_{12}/CH_4	0.42	0.01	1.13	5.05×10^3	205
C_6H_6/CH_4	0.058	0	0.07	4.12×10^3	1
nC_7H_{16}/CH_4	-	0.01	0.66	4.55×10^5	1057

[a]Helmig et al., 2014
[b]https://www.wrapair.org//forums/ogwg/PhaseIII_Inventory.html

Strong correlations of C_2-C_7 alkanes to CH_4 ($0.67 \leq R^2 \leq 0.99$) over the Piceance and Uintah basins shown in Table 4.3 indicate that light alkanes and methane are emitted at equal rates and that CH_4 enhancements over these regions are primarily from co-located sources (Pétron et al., 2012). Tables 4.4 and 4.5, show that emission ratios are strongly source dependent and vary greatly. By comparing Tables 4.3 – 4.5, emissions measured in this study most closely resemble the composition of natural gas from non-coal bed methane natural gas wells reported by the WRAP. This implies that natural gas wells are the dominant emission source of methane and light alkanes in both the Piceance and Uintah areas. As stated in chapter 1, natural gas is mainly comprised of $C_1 – C_5$ alkanes, with C_{6+} alkanes making up <1% of the total organic composition, compared to oil, a dense mix of NMHCs (Berger & Anderson, 1992; Gilman et al., 2013; EPA, 2016). To further define an emission signature of both basins, we examine higher chained alkanes.

Because of the limited number of AWAS samples collected over the Piceance (n=16) and Uintah (n=9) basins and the large number of compounds analyzed, this data set is not appropriate for defining emission estimates or using factor analysis methods (Thurston & Spengler, 1985; Paatero & Tapper, 1994; Ryerson et al., 2001; Choi et al., 2003; Karion et al., 2013). Therefore, to examine the relationship between NMHC emissions over these basins, linear correlations with a least squares fit were used (Simpson et al., 2010), e.g. Figures 4.8 and 4.9. The ethyltoluene and trimethylbenzene compounds were excluded from this analysis as the large number of samples that were below the limit of detection for these compounds would result in skewed correlations. Table 4.6 shows a correlation matrix of trace gases measured over both the Piceance and Uintah basins. Correlations of VOCs, shown in Table 4.6, were made for combustion (SO_2, NO, CO, C_2H_2) and non-combustion (C_3H_8, nC_4H_{12}, and nC_7H_{16}) tracers.

Table 4.6 Correlation matrix of select trace gases measured over the Piceance and Uintah basins. Correlations with $R^2 \geq 0.70$ are in bold. For the VOCs CO, CO_2, NO, NO_2, SO_2, O_3, methane, and ethane, 1 Hz measurements were used. For all other compounds, AWAS measurements were used. (C_2H_2=Ethyne; C_3=Propane; nC_4=*n*-Butane; nC_7=*n*-Heptane).

	Piceance Basin							Uintah Basin						
	SO_2	NO	CO	C_2H_2	C_3	nC_4	nC_7	SO_2	NO	CO	C_2H_2	C_3	nC_4	nC_7
CO	0.00	0.19	**1.00**	0.64	0.00	0.00	0.00	**0.81**	**0.95**	**1.00**	0.26	0.46	0.39	0.35
CO_2	0.00	0.11	0.47	0.44	0.12	0.11	0.13	**0.68**	**0.74**	**0.79**	0.42	0.59	0.50	0.46
NO	0.00	**1.00**	0.19	0.24	0.01	0.00	0.01	**0.76**	**1.00**	**0.95**	0.25	0.44	0.39	0.35
NO_2	0.00	**0.81**	0.13	0.31	0.00	0.00	0.01	**0.80**	**0.97**	**0.98**	0.25	0.45	0.39	0.35
SO_2	**1.00**	0.00	0.00	0.06	0.03	0.03	0.05	**1.00**	**0.76**	**0.81**	0.21	0.43	0.38	0.34
O_3	0.04	0.01	0.04	0.06	0.04	0.05	0.04	0.29	0.37	0.30	0.07	0.18	0.25	0.23
Methane	0.01	0.15	0.27	0.04	**0.85**	**0.81**	**0.77**	0.06	0.06	0.30	**0.93**	**0.95**	**0.97**	**0.98**
Ethane	0.01	0.08	0.16	0.02	**0.99**	**0.97**	**0.84**	0.08	0.08	0.11	**0.87**	**0.99**	**0.99**	**0.99**
Ethene	0.00	**0.86**	0.48	0.36	0.12	0.11	0.15	0.43	0.45	0.47	**0.89**	**0.99**	**0.99**	**0.99**
Ethyne	0.03	0.24	0.64	**1.00**	0.02	0.02	0.02	0.21	0.25	0.26	**1.00**	**0.89**	**0.89**	**0.91**
Propane	0.03	0.01	0.00	0.02	**1.00**	**0.99**	**0.87**	0.43	0.44	0.46	**0.88**	**1.00**	**0.99**	**0.98**
Propene	0.05	0.53	0.44	0.57	0.08	0.08	0.16	0.23	0.25	0.26	**0.80**	**0.86**	**0.90**	**0.92**
n-Butane	0.03	0.00	0.00	0.02	**0.99**	**1.00**	**0.89**	0.38	0.40	0.41	**0.90**	**0.99**	**1.00**	**0.99**
i-Butane	0.04	0.00	0.00	0.02	**0.99**	**0.99**	**0.89**	0.36	0.39	0.40	**0.89**	**0.99**	**0.99**	**0.99**
n-Pentane	0.04	0.00	0.00	0.03	**0.98**	**0.99**	**0.92**	0.36	0.38	0.40	**0.92**	**0.99**	**0.99**	**0.99**
i-Pentane	0.04	0.01	0.00	0.04	**0.98**	**0.99**	**0.92**	0.29	0.32	0.33	**0.92**	**0.97**	**0.99**	**0.99**
2,2-Dimethylbutane	0.05	0.06	0.00	0.09	**0.85**	**0.87**	**0.87**	0.32	0.35	0.36	**0.85**	**0.92**	**0.92**	**0.92**
2,3-Dimethylbutane	0.08	0.00	0.01	0.03	**0.88**	**0.91**	**0.89**	0.31	0.35	0.36	**0.91**	**0.97**	**0.99**	**0.99**
n-Hexane	0.05	0.01	0.00	0.02	**0.97**	**0.98**	**0.95**	0.38	0.40	0.41	**0.90**	**0.99**	**0.99**	**0.99**
2-Methylpentane	0.05	0.01	0.00	0.03	**0.96**	**0.97**	**0.93**	0.23	0.27	0.28	**0.94**	**0.94**	**0.96**	**0.97**
3-Methylpentane	0.05	0.01	0.00	0.03	**0.96**	**0.98**	**0.95**	0.20	0.24	0.25	**0.92**	**0.93**	**0.95**	**0.97**
n-Heptane	0.05	0.01	0.00	0.02	**0.87**	**0.89**	**1.00**	0.34	0.37	0.38	**0.90**	**0.98**	**0.99**	**1.00**
n-Octane	0.20	0.01	0.00	0.01	0.48	0.52	**0.82**	0.36	0.39	0.40	**0.85**	**0.96**	**0.99**	**0.99**
Cyclopentane	0.04	0.00	0.01	0.01	**0.90**	**0.93**	**0.92**	0.12	0.15	0.16	**0.93**	**0.87**	**0.89**	**0.91**
Cyclohexane	0.05	0.02	0.00	0.04	**0.92**	**0.94**	**0.97**	0.23	0.27	0.28	**0.93**	**0.95**	**0.97**	**0.98**
Methylcylohexane	0.06	0.02	0.00	0.03	**0.89**	**0.91**	**0.96**	0.24	0.28	0.29	**0.90**	**0.94**	**0.83**	**0.87**
Benzene	0.04	0.09	0.02	0.06	0.55	0.55	**0.72**	0.21	0.25	0.26	**0.91**	**0.93**	**0.95**	**0.97**
Toluene	0.06	0.09	0.02	0.12	0.62	0.64	**0.84**	0.18	0.22	0.22	**0.92**	**0.90**	**0.93**	**0.96**
Ethylbenzene	0.19	0.05	0.00	0.16	0.17	0.20	0.27	0.22	0.25	0.27	**0.91**	**0.84**	**0.83**	**0.85**
m+*p*-Xylene	0.17	0.04	0.00	0.10	0.38	0.42	0.60	0.42	0.45	0.46	**0.81**	**0.91**	**0.95**	**0.96**
o-Xylene	0.07	0.07	0.00	0.10	0.15	0.18	0.26	0.42	0.43	0.46	**0.75**	**0.88**	**0.87**	**0.86**
Isoprene	0.11	0.03	0.02	0.00	0.02	0.02	0.00	0.12	0.03	0.04	0.19	0.15	0.11	0.12
α-Pinene	0.21	0.07	0.02	0.01	0.05	0.07	0.12	0.07	0.01	0.10	0.00	0.00	0.02	0.03
β-Pinene	0.07	0.00	0.02	0.00	0.02	0.02	0.00	0.00	0.00	0.00	0.00	0.00	0.00	0.00

Ethyne, C_2H_2, was included as a combustion tracer as it is produced from the incomplete combustion of fossil fuels (Sachsse, 1954; Blake et al., 2003; Warneke et al., 2007) and to distinguish combustion emissions from the Uintah basin and those from the local coal power plant, as average and maximum enhancements of C_2H_2 downwind of the Uintah basin were 1.36 and 3.0, respectively. From Table 4.6, we can see that NMHC emissions over the Piceance basin did not correlate significantly with any combustion tracers. The strongest correlations with ethyne were CO (0.64), ethene (0.36), and propene (0.57), which are also common combustion/industrial tracers (Buzcu & Fraser, 2006; de Gouw et al., 2009). Note, these compounds were not strongly enhanced over the Piceance, with maximum enhancements over background for ethyne, ethene, propene, and CO of 1.5x, 4.7x, 1.7x, and 1.2x, respectively (Tables 4.1 and 4.2). There were also no significant correlations between NMHCs and NO or SO_2 in the Piceance area although NO_x and SO_2 were shown in the WRAP campaign to be emitted from compressor engines and drilling rigs in the Piceance basin (WRAP, 2015).

The compounds isoprene, α-pinene, and β-pinene, are emitted by deciduous trees, plants, and shrubs (Guenther et al., 2000). These compounds were slightly enhanced over the Piceance basin, as mentioned above, but did not correlate with any of the trace gases measured. Maximum values of isoprene (220 pptv) over the Piceance occurred as the aircraft began the missed approach into Rifle, CO, over a relatively forested area. Therefore, any enhancements of these species are likely from local natural sources.

Examining VOC correlations to ethyne over the Uintah basin, all NMHCs were strongly correlated, $0.75 \leq R^2 \leq 0.93$. We do not see correlations between ethyne and CO, NO, NO_2, and SO_2 because of the local emissions from the coal power plant. Ethene, R^2=0.89, propene, R^2=0.80, and aromatics, $0.75 \leq R^2 \leq 0.97$, were also strongly correlated with ethyne. This is most

likely attributed to gas and oil flaring activities and compressor engines in the Uintah basin (Friesen et al., 2009).

There are strong correlations between C_3, and C_4 alkanes with C_2-C_7 alkanes and cycloalkanes over the Piceance basin, ($0.81 \leq R^2 \leq 0.99$), and were moderately correlated with *n*-octane, 0.48 and 0.52, respectively. Aromatic compounds showed moderate to no correlation ($0.15 \leq R^2 \leq 0.64$) with C_3 and C_4 alkanes, but benzene and toluene correlated with C_7, 0.72 and 0.84, respectively. The results over the Piceance basin are starkly different from measurements over the Uintah basin, as there were strong correlations between all hydrocarbons ($0.75 \leq R^2 \leq 0.99$). The Piceance basin produces mainly natural gas, while the Uintah basin produces both oil and natural gas (Bar-Ilan et al., 2010). For this reason, we see strong correlations between C_7 and all hydrocarbons over Uintah ($0.85 \leq R^2 \leq 0.99$). For comparison, maximum values of benzene over the Piceance and Uintah basins were 143 pptv and 268 pptv, respectively, compared to an average of 180 ± 101 pptv measured downwind of the GWA, with a maximum value of 367 pptv.

The primary source of butanes in the atmosphere is the evaporation of fossil fuels (Watson et al., 2001; Buzcu & Fraser, 2006). Maximum enhancements over the Piceance and Uintah basins were 14.2x and 17.6x for *n*-butane and 25.9x and 19.3x for *i*-butane, respectively. *N*-butane also strongly correlated with all alkanes over both basins. The emission ratio of *i*-butane to *n*-butane has been historically used to identify the source of butanes in an air mass (Blake & Rowland, 1995; White et al., 2008; Russo et al., 2010). For example, a typical vehicular exhaust ratio ranges from 0.2–0.3 (Fujita, 2001; Russo et al., 2010). A liquefied petroleum gas (LPG) signature is approximately 0.46 (Blake & Rowland, 1995; Chen et al., 2001; Barletta et al., 2002; Russo et al., 2010), while a natural gas signature ranges from 0.6–1.0

(Barletta et al., 2002; Russo et al., 2010; Gilman et al., 2013; Thompson et al., 2014). Figure 4.10 shows the iC_4/nC_4 emission ratio determined for this study. The emission ratio over the Piceance and Uintah basins was 0.978 ± 0.022 pptv/pptv (R^2=0.998) and 0.569 ± 0.012 pptv/pptv (R^2=0.995), respectively, so corresponds to a typical natural gas signature. As combustion is not a known source of butanes, we can assume the iC_4/nC_4 emission ratio measured over these two basins is unique to each respective basin. When compared to the background emission ratio of 0.437 ± 0.022 pptv/pptv (R^2=0.905), it seems the local background is most strongly influenced by local LPG emissions.

As discussed in chapter 3, pentanes have been used historically to define emissions from ONG activities as they are co-emitted and their emission ratio is unaffected by photochemistry and changing boundary layer conditions (Atkinson, 1990; Ryerson et al., 2011; Pétron et al., 2012; Gilman et al., 2013; Pétron et al., 2014). The emission ratios measured in this study over the Piceance and Uintah basins (Figure 4.11) were determined to be 1.26 ± 0.02 pptv/pptv (R^2=0.998) and 1.02 ± 0.03 (R^2=0.992), respectively, and varied greatly from the emission ratio over the GWA, 0.88 ± 0.01 pptv/pptv (R^2=0.99). Compared to previous studies of the Piceance and Uintah basins (Table 4.7), the iC_5/nC_5 ratio measured over the Piceance basin is most similar to the composition of natural gas from oil wells determined by the WRAP (2015), and the iC_5/nC_5 ratio measured over the Uintah basin most closely corresponds to surface emissions of the basin determined by Helmig, et al. (2014), and natural gas flash gas (WRAP, 2015). By comparing this emission signature measured on the Colorado western slope, we can compare them to previous studies of ONG activities that determined an iC_5/nC_5 ratio, discussed in chapter 3. The emission ratio measured over the Piceance (1.26) is most similar to the signature measured in Houston, TX during the Texas Air Quality study in

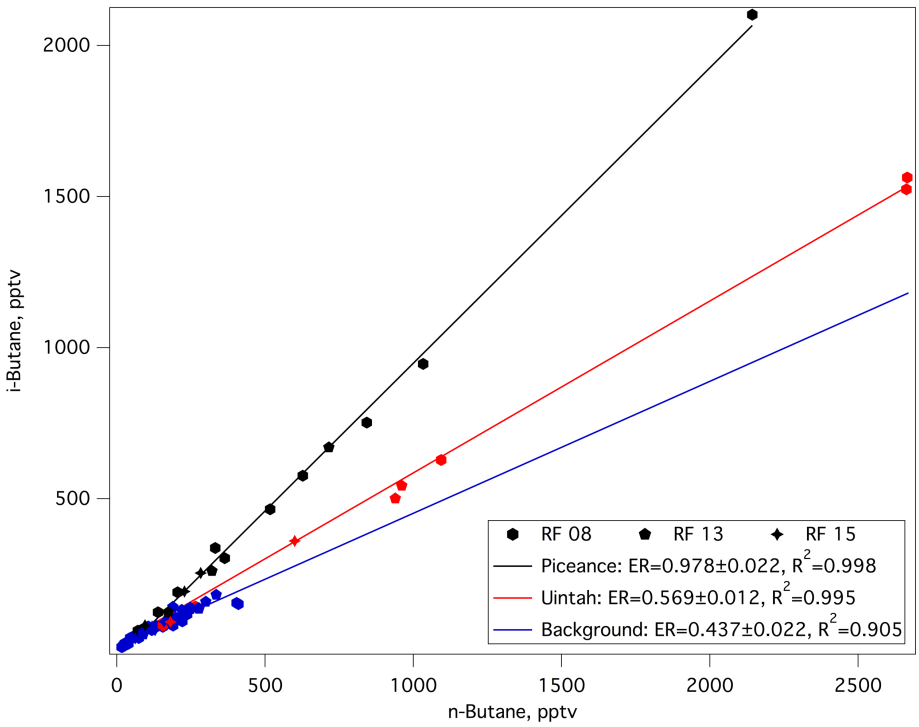

Figure 4.10 Correlation plot of *i*-butane to *n*-butane over the Piceance (black) and Uintah (red) basins. The iC_4/nC_4 ratio of background measurements is shown in blue.

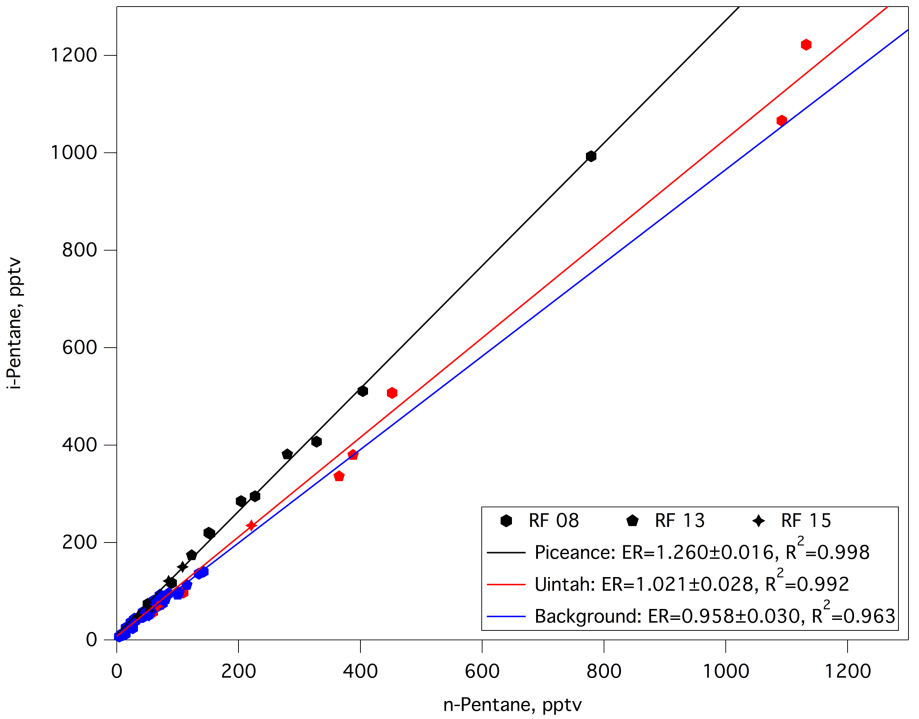

Figure 4.11 Correlation plot of *i*-pentane to *n*-pentane over the Piceance (black) and Uintah (red) basins. The iC_5/nC_5 ratio of background measurements is shown in blue.

Table 4.7 Comparison with previous studies of iC_5/nC_5 emission ratios (ER) measured over the Piceance and Uintah basins.

Piceance	ER	Uintah	ER
This study	1.260 ± 0.016	This study	1.021 ± 0.028
Xcel[a]	1.68	Surface measurements[d]	1.10, 0.91
Non-CBM wells[b]	1.51	Non-CBM wells[b]	1.97
Oil wells[b]	1.28	CBM wells[b]	1.56
Flash Gas NG[b]	1.32	Flash Gas NG[b]	0.93
Drilling[c]	1.19	Flash Gas Oil[b]	0.58
Fracking[c]	0.635		

[a]Xcel
[b]WRAP, 2015
[c]Hilliard, 2016
[d]Helmig et al., 2014 (measurements made in 2012 and 2013, respectively)

2006 of 1.39 (Gilman et al., 2009), while then ratio measured over the Uintah basin is most similar to measurements over ONG fields in Kern county, CA of 0.99 (Hartt, 2013). From the analysis of C_4 and C_5 alkanes and their comparison to previous studies, we can conclude that the air masses sampled over the Piceance and Uintah were directly influenced by ONG emissions. The unique signatures determined here for each basin can be used to investigate the impact of these ONG fugitive emissions in future studies of the Colorado western slope.

4.2.1 Potential Ozone Formation from the Piceance And Uintah Basins

Measurements of O_3 throughout the western slope were fairly constant, with average values of 54 ± 3, 57 ±4, and 53 ±4 ppbv in 1-Hz measurements over the Piceance, Uintah, and local background, respectively (Table 4.1). Ozone also did not correlate significantly with any trace gases shown in Table 4.6 ($0.01 \leq R^2 \leq 0.37$) measured over the two ONG basins in this study. Although correlations are a useful tool in examining source signatures, they do not provide information regarding ozone formation. As discussed in chapter 1, while O_3 is not directly emitted from ONG activities, the ingredients that lead to O_3 formation are.

In the presence of sunlight, the lifetimes of most trace gases in the troposphere are determined by the reaction with OH. The hydroxyl radical readily reacts with hydrocarbons to produce HO_2 and RO_2 radicals. These free radicals oxidize NO to form NO_2 and leads to O_3 production, reactions 1.4 – 1.8 (Atkinson, 1990; Atkinson, 2000)**.** This relationship allows OH reactivity to be used to assess the photochemical activity of VOCs and O_3 formation, and therefore, the rate constant for the reaction between OH and hydrocarbons can be used to reflect overall reactivity and potential O_3 formation. Equation 4.1 shows the calculation used in calculating OH reactivity, R, for each VOC.

$$R_{OH,i} = k_{OH,i}[VOC_i] \quad 4.1$$

Where k_{OH} is the OH rate constant and [VOC_i] is the concentration of the respective VOC. Values for k_{OH} were determined using temperature dependent rate equations described by Atkinson (Atkinson, 2003; Atkinson et al., 2006). Total VOC reactivity was calculated by taking the sum of the reactivities for each individual VOC, equation 4.2.

$$R_{OH,total} = \sum R_{OH,i} \quad 4.2$$

The NO_X cycle (reaction 1.7) is a critical part of ozone formation, however, we exclude CO and NO_X from our OH reactivity estimates because of the emissions from the coal fired power plant which would skew results. In fact, from Figure 4.12, we can see that NO and O_3 were anti-correlated during the flight transect over the Uintah basin due to O_3 titration in the presence of high NO_X. This was not the case over the Piceance basin.

As shown in Figure 4.13, over the Piceance basin, CH_4 accounts for 38% of total OH reactivity, followed by alkanes, biogenics, cycloalkanes, aromatics, and alkenes, 30%, 20%, 5% 4%, and 3%, respectively, with a total reactivity of 0.57 ± 0.37 s^{-1}. Over the Uintah basin, alkanes dominate OH reactivity, accounting for 45% of the total reactivity of 0.59 ± 0.44 s^{-1},

followed by CH_4, cycloalkanes, biogenics, aromatics, and alkenes at 37%, 7%, 4%, 3%, and 3%, respectively. Unsurprisingly, background estimates of OH reactivity were much lower than both basins, 0.42 ± 0.35 s^{-1}, and was primarily from CH_4, 49%, and biogenic compounds, 36%. Methane OH reactivity was relatively constant across both basins and background measurements, ranging from 0.203 – 0.219 s^{-1}. Methane contributes a great deal to OH reactivity because it is relatively homogenous in the troposphere at a higher mixing ratio compared to other hydrocarbons, with average mixing ratios of 1829 ±38, 1862 ± 77, and 1815 ±9 ppbv over the Piceance, Uintah, and local background, respectively. More notable is the variation in alkane reactivity, which ranged from 0.042 s^{-1} in background measurements, to 0.173 s^{-1} over the Piceance, and 0.269 s^{-1} over the Uintah. This is a strong indication of the influence of the ONG industry on air masses over the Piceance and Uintah basins.

Furthermore, these results show the overall importance of VOC distribution on the reactivity of air masses and the impact that it can have on potential O_3 production. From the analysis of VOC contribution to total reactivity, the ONG industry significantly enhances total OH reactivity. Alkane OH reactivity was 6x and 4x enhanced compared to background and cycloalkanes were 14x and 10x enhanced over the Uintah and Piceance basins, respectively. As expected, biogenic trace gases were the only compounds whose OH reactivity did not increase over the ONG basins. If we consider the reactivity of just anthropogenic NMHCs, the reactivity over the Piceance and Uintah basins was found to be 0.240 ± 0.231 s^{-1} and 0.347 ± 0.364 s^{-1}, respectively, compared to background estimates of 0.063 ± 0.042 s^{-1}. This illustrates that hydrocarbon reactivity from ONG basins can lead to substantial O_3 enhancements downwind of these two basins. It is important to note that these results are a low estimate as CO and NO_x were excluded from this calculation.

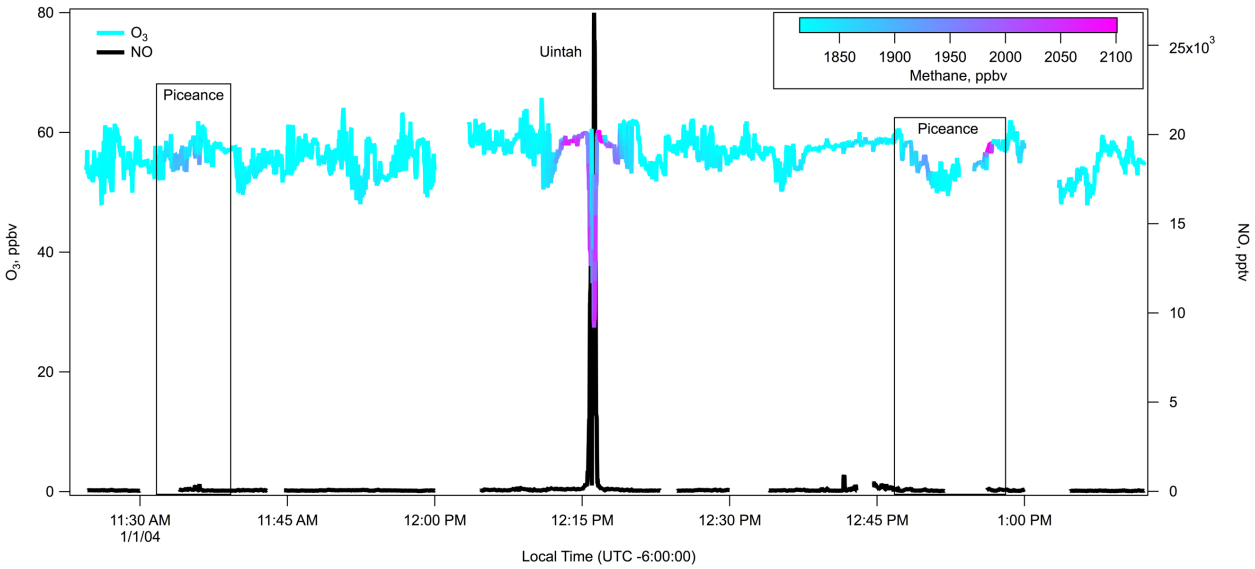

Figure 4.12 Time series plot of NO (black) and O_3 (colorized by CH_4 concentration) during flight 08 over the Piceance and Uintah basins.

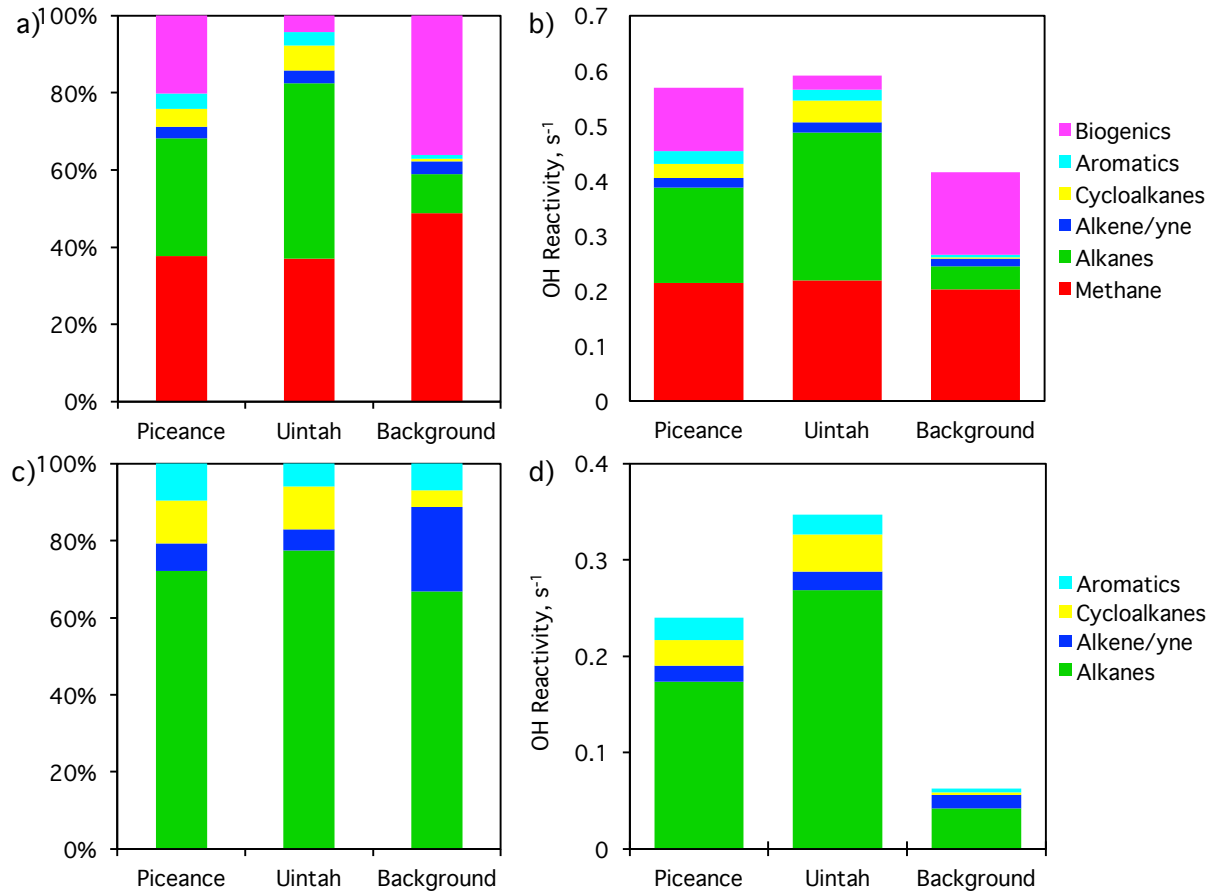

Figure 4.13 Total OH reactivity of NMHCs measured over the Piceance and Uintah basins, compared to local background, shown as percent of total reactivity (a, c) and total reactivity (b, d). Methane and biogenic reactivity is removed in c and d.

4.3 Conclusion

From the analysis of research flights over the Colorado western slope, it is evident that the oil and natural gas industry is a non-trivial source of ozone precursors. The long-range transport of emissions from the Piceance and Uintah basins can potentially influence O_3 levels in the NFRMA. By developing an ONG signature from measurements over the Piceance and Uintah basins, it was determined that iC$_4$/nC$_4$ and iC$_5$/nC$_5$ emission ratios, 0.98 ± 0.02 and 1.26 ±0.02 over the Piceance, and 0.57 ±0.01 and 1.02 ± 0.03 over the Uintah, respectively, are unique to each basin. These signatures can potentially be used to examine the influence of western emissions on the eastern slope of the Rocky Mountains.

Furthermore, these estimates are limited, as we were not able to determine an emission estimate from either basin, and measurements over the Uintah basin included a non-ONG source. To reduce these source errors, a more thorough study of both areas should be performed, and should include continuous measurements both upwind and downwind of each basin on a larger timescale.

4.4 References

Atkinson, R. (1990). Gas phase tropospheric chemistry of organic compounds: A review. *Atmospheric Environment, 24a*, 1-41.

Atkinson, R. (2000). Atmospheric chemistry of VOCs and NOX. *Atmospheric Environment, 34*, 2063-2101.

Atkinson, R. (2003). Kinetics of the gas-phase reactions of OH radicals with alkanes and cycloalkanes, *Atmospheric Chemistry and Physics*. 3, 2233-2307.

Atkinson, R., Baulch, D., Cox, R., Crowley, J., Hampson, R., Hynes, R., Jenkin, M., Rossi, M., Troe, J., IUPAC Subcommittee. (2006). Evaluated kinetic and photochemical data for atmospheric chemistry: Volume II –gas phase re- actions of organic species, *Atmospheric Chemistry and Physics.* 6, 3625-4055.

Baker, A., Beyersdorf, A., Doezema, L., Katzenstein, A., Meinardi, S., Simpson, I., . . . Rowland, F. (2008). Measurement of nonmethane hydrocarbons in 28 United States cities. *Atmospheric Environment, 42*(1), 170-182.

Bar-Ilan, A., Friesen, R., Pollack, A., & Hoats, A. (2007). *WRAP area source emissions inventory projections and control strategy evaluations, WRAP Phase II Report.* Fort Collins, CO: Western Regional Air Partnership. Retrieved from https://www.wrapair.org/forums/ogwg/documents/200710_Phase_II_O&G_Final)Report(v10-07%20rev.s).pdf

Bar-Ilan, A., Grant, J., Parikh, R., Pollack, A., Morris, R., Henderer, D., & Sgamma, K. (2010). *A comprehensive emissions inventory of upstream oil and gas activities in the Rocky Mountain states.* U.S. Environmental Protection Agency. Retrieved from https://www3.epa.gov/ttnchie1/conference/ei19/session8/barilan.pdf

Barletta, B., Meinardi, S., Simpson, I., Khwaja, H., Blake, D., & Rowland, F. (2002). Mixing ratios of volatile organic compounds (VOCs) in the atmosphere of Karachi, Pakistan. *Atmospheric Environment, 36*, 3429-3443.

Benkovitz, C., Scholtz, M., Pacyna, J., Tarrason, L., Dignon, J., Volder, E., . . . Graedel, T. (1996). Global gridded inventories of anthropogenic emissions of sulphur and nitrogen. *Journal of Geophysical Research, 101*(D22), 29239-29253.

Blake, D., & Rowland, F. (1995). Urban leakage of liquefied petroleum gas and its impacts on Mexico City air quality. *Science, 269*(5226), 953-956.

Blake, N., Blake, D., Simpson, I., Meinardi, S., Swanson, A., Lopez, J., . . . Rowland, F. (2003). NMHCs and halocarbons in Asian continental outflow during the Transport and Chemical Evolution over the Pacific (TRACE-P) field campaign: Comparison with PEM-West B. *Journal of Geophysical Research, 108*(D20), 8806.

Buzcu, B., & Fraser, M. (2006). Source identification and apportionment of volatile organic compounds in Houston, TX. *Atmospheric Environment, 40*, 2385-2400.

Carter, W., & Seinfeld, J. (2012). Winter ozone formation and VOC incremental reactivities in the Upper Green River Basin of Wyoming. *Atmospheric Environment, 50*, 255-266.

CDPHE. (2017). *History of Ozone in Colorado*. Retrieved October 17, 2017, from Colorado department of Public Health and Environment: https://www.colorado.gov/pacific/cdphe/ozone-planning-chronology

Chen, T., Simpson, I., Blake, D., & Rowland, F. (2001). Impact of the leakage of liquefied petroleum gas (LPG) on Santiago air quality. *Geophysical Research Letters, 28*, 2193-2196.

Choi, T., Elliott, S., Simpson, I., Blake, D., Colman, J., Dubey, M., . . . Smith, F. (2003). Survey of whole air data from the second airborne biomass burning and lighning experiment using principal componant analysis. *Journal of Geophysical Research, 108*(D5), 4163.

COGCC. (2007). *GREATER WATTENBERG AREA.* Denver, CO: LT ENVIRONMENTAL, INC.

Colorado Oil and Gas Conservation Commission (COGCC). (2014). *COGCC Reports*. Retrieved Jan 02, 2018, from Monthly Production Reports: http://cogcc.state.co.us/COGCCReports/production.aspx?id=MonthlyOilProdByCounty

de Gouw, J., Te Lintel Hekkert, S., Mellqvist, J., Warneke, C., Atlas, E., Fehsenfeld, F., . . . Zhu, X. (2009). Airborne measurements of ethene from industrial sources using Laser Photo-Acoustic Spectroscopy. *Environmental Science Technology, 43*(7), 2437-2442.

EPA. (2016). *Control Techniques Guidelines for the Oil and Natural Gas.* Research Triangle Park, NC: EPA-453/B-16-001.

Flocke, F., & Pfister, G. (2013). *Front Range Air Pollution and Photochemistry Experiment FRAPPÉ: A proposed field experiment in Colorado for summer 2014.* Retrieved from http://www2.acd.ucar.edu/frappe

Friesen, R., Parikh, R., Grant, J., Bar-Ilan, A., Pollack, A., Henderer, D., . . . Schlagel, P. (2009). *Delopment of baseline 2006 emissions from oil and gas activity in the Uinta basin.* Novato, CA: Independent Petroleum Association of Mountain States (IPAMS) and Western Regional Air Parntership (WRAP). Retrieved from https://www.wrapair.org//forums/ogwg/documents/2009-03_06_Baseline_Emissions_Uinta_Basin_Technical_Memo_03-25.pdf

Fujita , E., Croes, B., Bennett, C., Lawson, D., Lurman, F., & Main, H. (1992). Comparison of emission inventory and ambient mixing ratios of CO, NMOG, and NOX in Californias Southcoast Basin. *Journal of Air Waste Management Associeation, 42*(3), 264-276.

Fujita, E. (2001). Hydrocarbon source apportionment for the 1996 Paso del Norte ozone study. *Science of the Total Environment, 276*, 171-184.

Gilman, J., Kuster, W., Goldan, P., Herndon, S., Zahniser, M., Tucker, S., . . . de Gouw, J. (2009). Measurements of volatile organic compounds during the 2006 TexAQS/GoMACCS campaign: Industrial influences, regional characteristics, and diurnal dependencies of the OH reactivity. *Journal of Geophysical Research: Atmospheres, 114*(D7).

Gilman, J., Lerner, B., Kuster, W., & de Gouw, J. (2013). Source signature of volatile organic compounds from oil and natural gas operations in Northeastern Colorado. *Environmental Science and Technology, 47*, 1297-1305.

Guenther, A., Geron, C., Pierce, T., Lamb, B., Harley, P., & Fall, R. (2000). Natural emissions of non-methane volatile organic compounds, carbon monoxide, and oxides of nitrogen from North America. *Atmospheric Environment, 34*, 2205-2230.

Harley, R., McKeen, S., Pearson, J., Rodgers, M., & Lonneman, W. (2001). Analysis of motor vehicle emissions during the Nashville/Middle Tennessee ozone study. *Journal of Geophysical Research, 106*, 3559-3567.

Hartt, G. (2013). *Oil and gas emissions in the Gulf of Mexico and the San Joaquin Valley of Calfornia.* Ph. D. Thesis, University of California - Irvine.

Helmig, D., Thompson, C., Evans, J., Boylan, P., Hueber, J., & Park, J. (2014). Highly elevated atomospheric levels of volatile organic compounds in the Uintah Basin, Utah. *Environmental science and technology, 48*, 4707-4715.

Hilliard, N. (2016). *Volatile organic compound and methane emissions from well development operations in the Piceance basin.* Colorado State University, Atmospheric Science, Fort Collins, CO.

Karion, A., Sweeney, C., Kort, E., Shepson, P., Brewer, A., Cambaliza, M., . . . Tans, P. (2015). Aircraft-based estimate of total methane emissions from the Barnett shale region. *Environmental Science Technology, 49*, 8124-8131.

Karion, A., Sweeney, C., Pétron, G., Frost, G., Hardesty, R., Kofler, J., . . . Conley, S. (2013). Methane emissions estimate from airborne measurements over a western United States natural gas field. *Geophysical Research Letters, 40*, 4393-4397.

Klusman, R., & Jakel, M. (1998). Natural microseepage of methane to the atmosphere from the Denver-Julesburg basin, Colorado. *Journal Geophysical Reserach, 103*(D21), 28041-28045.

LaFranchi, B., Pétron, G., Miller, J., Lehman, S., Andrews, A., Dlugokencky, E., . . . Guilderson, T. (2013). Constraints on emissions of carbon monoxide, methane, and a suite of hydrocarbons in the Colorado Front Range using observations of 14CO2. *Atmospheric Chemistry and Physics, 13*, 11101-11120.

Mays, K., Shepson, P., Stimm, B., Karion, A., Sweeney, C., & Gurney, K. (2009). Aircraft-based measuements of the carbon footprint of Indianapolis. *Environmental Science Technology, 43*(20), 7816-7823.

Paatero, P., & Tapper, U. (1994). Positive matrix factorization: a non-negative factor model with optimal utilization of error estimates of data values. *Environmetrics, 5*, 111-126.

Parrish, D. (2006). Critical evaluatoin of US on-road vehicle emissoin inventories. *Atmospheric Environment, 40*, 2288-2300.

Peischl, J., Ryerson, T., Aiken, K., de Gouw, J., Gilman, J., Holloway, J., . . . Parrish, D. (2015). Quantifying atmospheric methane emissions from the Haynesville, Fayetteville, and northeasern Marcellus shale gas production regions. *Journal of Geophysical Research: Atmospheres, 120*, 2119-2139.

Pétron, G., Grost, G., Miller, B., Hirsch, A., Montzka, S., Karion, A., . . . Tans, P. (2012). Hydrocarbon emissions characterization in the Colorado Front Range: A pilot study. *Journal of Geophysical Research, 117*(D04304).

Pétron, G., Karion, A., Sweeney, C., Miller, B., Montzka, S., Frost, G., . . . Schnell, R. (2014). A new look at methane and nonmethane hydrocarbon emissions from oil and natural gas operations in the Colorado Denver-Julesburg Basin. *Journal of Geophysical Research: Atmospheres, 119*, 6836-6852.

Rappengluck, B., Ackermann, L., Alvarez, S., Golovko, J., Buhr, M., Field, R., . . . Kelsar, C. (2014). Strong wintertime ozone events in the Upper Green River basin, Wyoming. *Atmospheric Chemistry and Physics, 14*, 4909-4934.

Russo, R., Zhou, Y., White, M., Mao, H., Talbot, R., & Sive, B. (2010). Multi-year (2004-2008) record of nonmethane hydrocarbons and halocarbons in New England: seasonal variations and regional sources. *Atmospheric Chemistry and Physics, 10*, 4909-4929.

Ryerson, T., Aikin, K., Angevine, W., Atlas, E., Blake, D., Brock, C., . . . Watts, L. (2011). Atmospheric emissions from the Deepwater Horizon Spill constrain air-water partitioning, hydrocarbon fate, and leak rate. *Geophysical Research Letters, 38*(L07803).

Ryerson, T., Trainer, M., Holloway, J., Parrish, D., Huey, L., Sueper, D., . . . Fehsenfeld, F. (2001). Observations of ozone formation in power plant plumes and implications for ozone control strategies. *Science, 292*(5517), 719-723.

Sachsse, H. (1954). Production of acetylene by incomplete combustion of hydrocarbons with oxygen. *Chemical Engineer Technology, 26*, 245-253.

Simpson, I., Blake, N., Barletta, B., Diskin, G., Fuelberg, H., Gorham, K., . . . Blake, D. (2010). Characterization of trace gases measured over Alberta oil sands mining operations: 76 speciated C2-C10 volatile organic compounds (VOCs), CO, CO2, CH4, CO, NO, NO2, NOy, O3 and SO2. *Atmospheric Chemistry and Physics, 10*, 11931-11954.

Swarthout, R., Russo, R., Zhou, Y., Hart, A., & Sive, B. (2013). Volatile organic compound distribution during the NACHTT campaign at the Boulder Atmospheric Observator: Influence of urban and natural gas source. *Journal of Geophysical Research Atmospheres, 118*, 10614-10637.

Thompson, C., Hueber, J., & Helmig, D. (2014). Influence of oil and gas emissions on ambient non-methane hydrocarbons in residential areas of Northeastern Colorado. *Elementa Science of the Anthropocene, 3*, 35.

Thurston, G., & Spengler, J. (1985). A quantitative assessment of source contributions to inhalale particulate matter pollution in metropolitan Boston. *Atmospheric Environment, 19*(1), 9-25.

Turnbull, J., Karion, A., Fischer, M., Faloona, I., Guilderson, T., Lehman, J., . . . Tans, P. (2011). Assessment of fossl fuel carbon dioxide and other anthropogenic trace gas emissions from airborne measurements over Sacramento, California in spring 2009. *Atmospheric Chemistry and Physics, 11*, 705-721.

U.S. Department of Agriculture National Agricultural Statistics Service (USDA NASS). (2015). *Colorado Agriculturla Statistics.* Lakewood, CO: USDA NASS Mountain Regional Office. Retrieved from https://www.nass.usda.gov/Statistics_by_State/Colorado/Publications/Annual_Statistical_Bulletin/Bulletin2015.pdf

U.S. Energy Information Administration (EIA). (2017, Dec 29). *Natural gas*. Retrieved Jan 02, 2018, from Number of Producing gas wells (1989-2016): https://www.eia.gov/dnav/ng/ng_prod_wells_s1_a.htm

Warneke, C., Geiger, F., Edwards, P., Dube, W., Pétron, G., Kofler, J., . . . Roberts, J. (2014). Volatile organic compound emissions from the oil and nautral gas industry in the Uintah Basin, Utah: oil and gas well pad emissions compared to ambient air composition. *Atmospheric Chemistry and Physics, 14*(10977), e10988.

Warneke, C., McKeen, S., de Gouw, J., Goldan, P., Kuster, W., Holloway, J., . . . Blake, D. (2007). Determination of urban volatile orgainc compound emission ratios and comparison with an emissions database. *Journal of Geophysical Research, 112*(D10S47).

Watson, J., Chow, J., & Fujita, E. (2001). Review of volatile organic compound source apportionment by chemical mass balance. *Atmospheric Environment, 35*, 1567-1584.

Western Regional Air Partnership (WRAP). (2015). *Regional Emissions Data and Analyses*. Retrieved Jan 03, 2018, from https://www.wrapair2.org/emissions.aspx

White, M., Russo, R., Zhou, Y., Mao, H., Varner, R., Ambrose, J., . . . Sive, B. (2008). Volatile organic compounds in nothern New England anmarine continental environments during ICARTT 2004 campaign. *Journal of Geophysical Research, 113*(D08S90).

5. CHARACTERIZATION OF MOUNTAIN-VALLEY CIRCULATION EVENTS

The Rocky Mountains that divide the state of Colorado are the tallest mountain range in the continental United States, peaking at 4400 m above sea level. As discussed in chapter 1, the unique topography of Colorado is a major driver of local wind patterns, such as the recirculation pattern formed from rising thermal gradients up the eastern slope of the mountains, termed the mountain-valley circulation, MVC, effect (Figure 1.5) (Toth & Johnson, 1985; Sullivan et al., 2016). The elevated O_3 concentrations in this area are known to be influenced by these MVC events and long-range transport (Flocke & Pfister, 2012). For example, using ground based LIDAR measurements during the FRAPPÉ campaign, Sullivan et al. (2016) were able to show that MVC events directly lead to enhanced ozone in the NFRMA. However, these LIDAR were at fixed locations in the NFRMA, and did not directly examine the flow pattern up the eastern slope or the distribution of ozone precursors. Here we seek to define these flow patterns, the resulting accumulation of ozone and ozone precursors, and their effect on the air quality of the region to answer the scientific question "*What are the relative contributions of local mountain-valley recirculation patterns and long-range transport to buildup of photochemical oxidants and particulates during smog episodes in the NFRMA in the summer?*" (Flocke & Pfister, 2012).

5.1 Ozone in The NFRMA

5.1.1 Surface Observations

Over the course of the FRAPPÉ campaign (07/26/2014 – 08/17/2014; Julian Day 207 – 229), there were 5 days in the NFRMA that exceeded the current national ambient air quality standard (NAAQS) 8-hour ozone standard of 70 ppb (Figure 5.1). Two research flights on the NSF/NCAR C-130, flights 6 and 7 on August 2nd and 3rd (Julian days 214 and 215) coincided with an 8-hour ozone average that exceeded 70 ppb, with day 215 reaching an 8-hour average of

79 ppbv, above the 2008 NAAQS standard of 75 ppb (EPA, 2016). As shown in Figure 5.1, there were no O_3 exceedances from areas outside of the NFRMA over the span of the FRAPPÉ campaign.

We examine the diurnal trend of O_3 on Julian days 214 and 215, August 2nd and 3rd, using continuous ground based measurements. Figure 5.2 shows 48-hour diurnal measurements of O_3, NO_2, $j(NO_2)$, CH_4, wind speed, and wind direction measured at the NOAA Platteville ground station (40.1828 °N, -104.7261 °W) on August 2nd and 3rd, 2014, during the FRAPPÉ campaign. From Figure 5.2c, the accumulation of NO_2 in the evening is visible, but starting at 6 am, we see a gradual decrease in NO_2 corresponding to the increase in NO_2 photolysis (reaction 1.7b) frequency, $j(NO_2)$. At this time, there is a corresponding increase in O_3 (Figure 5.2a and 5.2b). This coincides with the increase in solar radiation from morning to noon, and implies that the initial peak in O_3 that occurs on both days shortly after 12:00 pm corresponds to photochemically produced O_3. Methane has a lifetime on the order of 10 years (Atkinson et al., 2006) and emissions in the NFRMA are estimated to be relatively unchanged over this time period. Therefore, the trend seen in CH_4 measurements highlights the nocturnal accumulation of surface emissions and diurnal changes in boundary layer conditions.

From Figure 5.2e, we see a transition over the course of the day in wind direction from the southwest to the east beginning at 9:00 am on the 2nd. On the 3rd, a similar transition was observed at 9 am, as winds shifted from the northwest to the east. These observations highlight the formation of upslope events as easterly winds are the dominant wind direction, but there is a great deal of deviation, indicative of turbulent mixing. From 3 pm – 6 pm, we observe a second O_3 enhancement. During this time, NO_2 and CH_4 remained constant at a minimum and solar radiation decreased. This suggests that the second enhancement is not primarily from *in-situ*

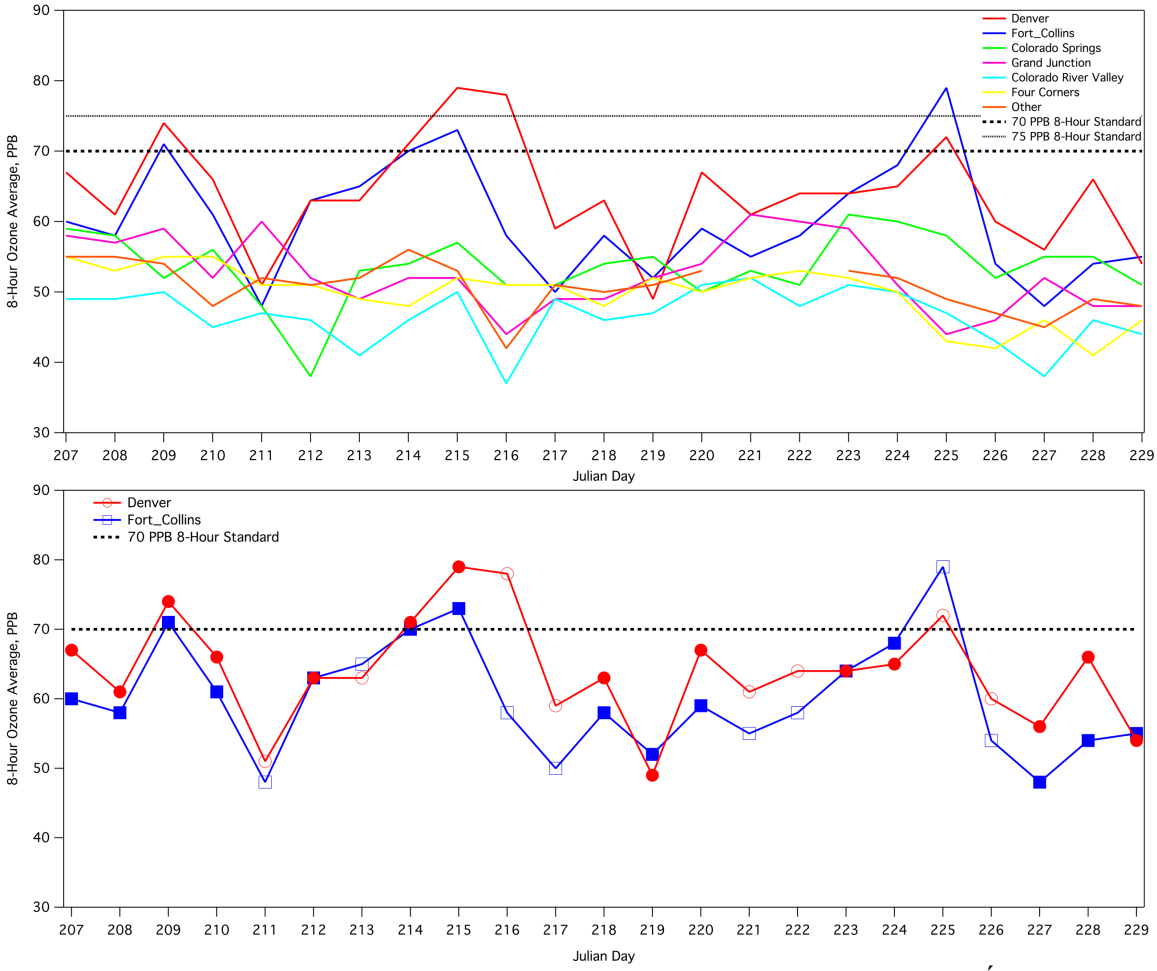

Figure 5.1 Time series plot of daily measured 8-hour ozone during the FRAPPÉ campaign. The top figure shows data from all monitoring areas in Colorado. The bottom figure shows only data collected in the NFRMA (Denver and Fort Collins). Open data points indicate non-flight days. Data courtesy of the CDPHE, available at https://www.colorado.gov/airquality/report.aspx.

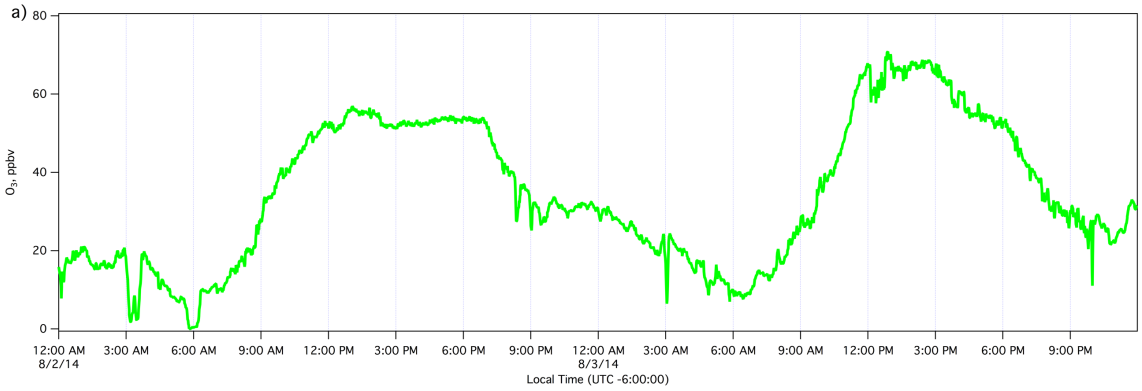

Figure 5.2 48-hour time series plot, starting with Julian Day 214 (08/02/2014), of 1-min O_3 (a), 1-hour averages of O_3 (b), 1-min NO_2 in blue and 1-min $j(NO_2)$ in black (c), 1-min CH_4 (d), and 5-min averages of wind direction colorized by wind speed (e) from the ground site in Platteville, CO.

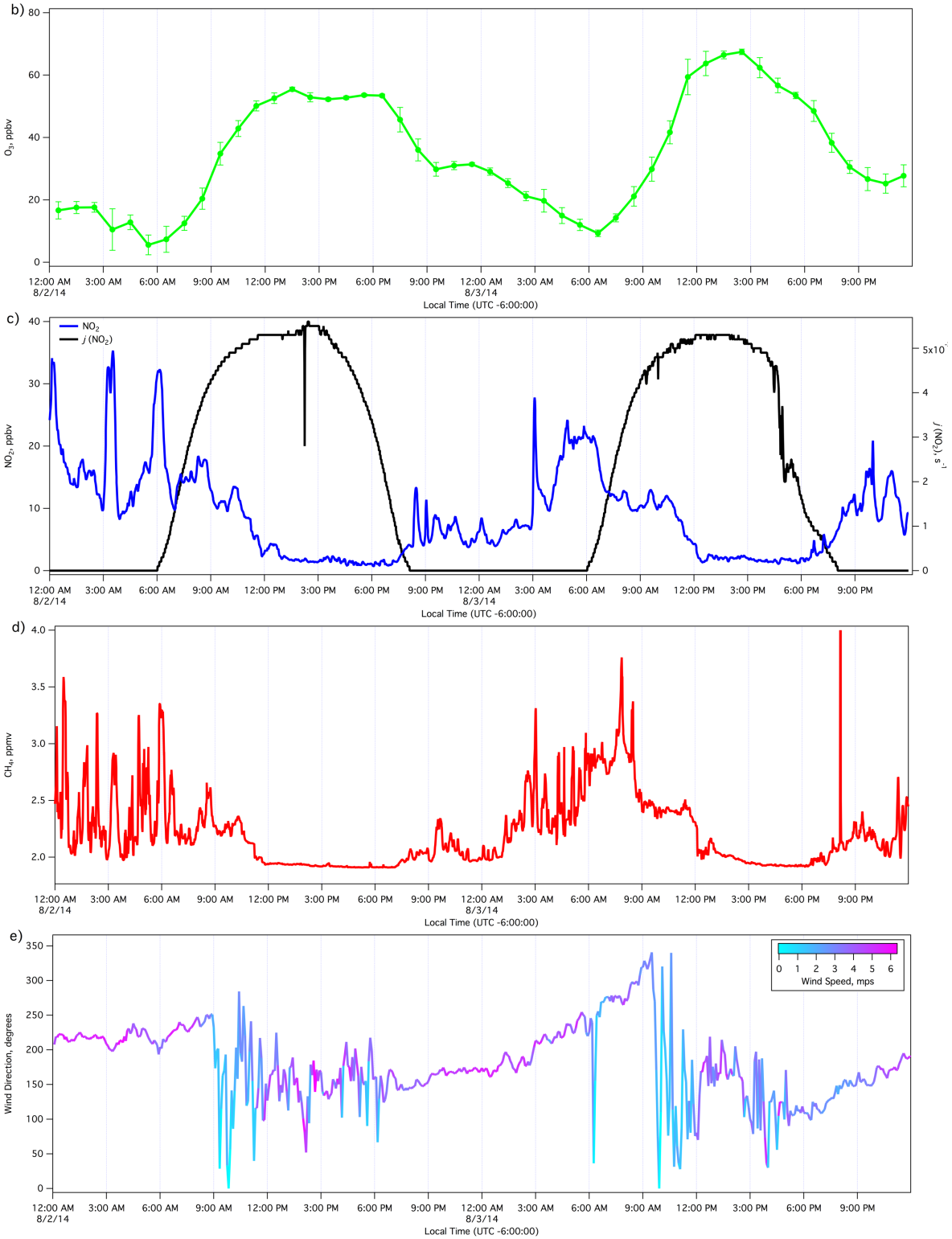

Figure 5.2 (Cont.) 48-hour time series plot, starting with Julian Day 214 (08/02/2014), of 1-min O_3 (a), 1-hour averages of O_3 (b), 1-min NO_2 in blue and 1-min $j(NO_2)$ in black (c), 1-min CH_4 (d), and 5-min averages of wind direction colorized by wind speed (e) from the NOAA Platteville ground site.

photochemical production, and is likely a result of transport. We would expect to see some enhancement in CH_4 corresponding to the second O_3 enhancement as CH_4 has a long atmospheric lifetime (Atkinson et al., 2006), unfortunately, any visible trend is dwarfed by the accumulation of nocturnal CH_4. To describe the processes involved with photochemical evolution, transport, and dilution, analysis of the spatial characterization of meteorological conditions and trace gas distribution is necessary to discern the events that lead to NAAQS O_3 exceedances. By combining *in-situ* measurements and trajectory analysis, we can potentially illuminate a relationship between O_3 events and MVC recirculation.

5.1.2 Aircraft Observations

a. NASA P3-B

On August 2nd and 3rd, the NASA P3-B was also collecting data over the NFRMA. From the 1-Hz measurements collected on board the P3-B, profiles of O_3, NO_2, and CH_4 were constructed to examine the vertical distribution of traces gases during a circulation event. Shown in Figures 5.3 – 5.8 are vertical profiles collected over Fort Collins, CO at three separate times throughout the day on Aug. 2nd and 3rd (vertical profiles collected over Denver, CO, are shown in appendix Figures A.1 and A.2).

From Figures 5.3 – 5.5, the development of the PBL height throughout the day on August 2nd is visible, starting at ~2300 m ASL at 8:00 am and reaching ~3200 m ASL at 1:40 pm. A similar PBL evolution is visible on August 3rd, Figures 5.6 – 5.8, starting at ~2200 m ASL and rising to ~3300 m ASL at 4:30 pm. In the morning on August 2nd, ~8:00 am local, on both research flight days, we do not see a great deal of vertical structure in O_3 in the free troposphere. As the morning progresses, ~10:30 am local, there is some development as the winds begin to shift and a thermal gradient develops. As seen in Figures 5.3c and 5.5c, there is an O_3 and CH_4

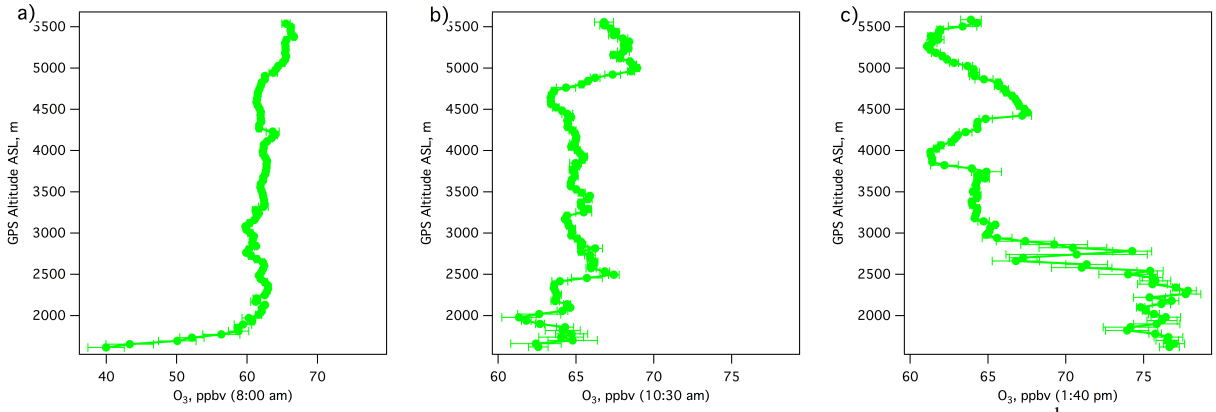

Figure 5.3 Vertical profiles of O_3 measured aboard the NASA P3-B on August 2nd, 2014 with a center bearing over Fort Collins starting at approximately 8:00 am (a), 10:30 am (b), and 1:40 pm (c), local time (UTC -6:00:00).

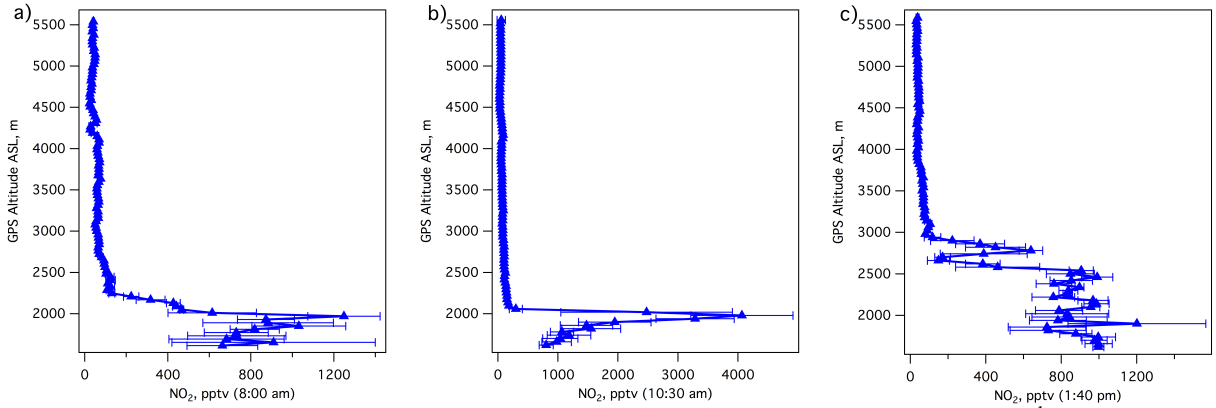

Figure 5.4 Vertical profiles of NO_2 measured aboard the NASA P3-B August 2nd, 2014 with a center bearing over Fort Collins starting at approximately 8:00 am (a), 10:30 am (b), and 1:40 pm (c), local time (UTC -6:00:00).

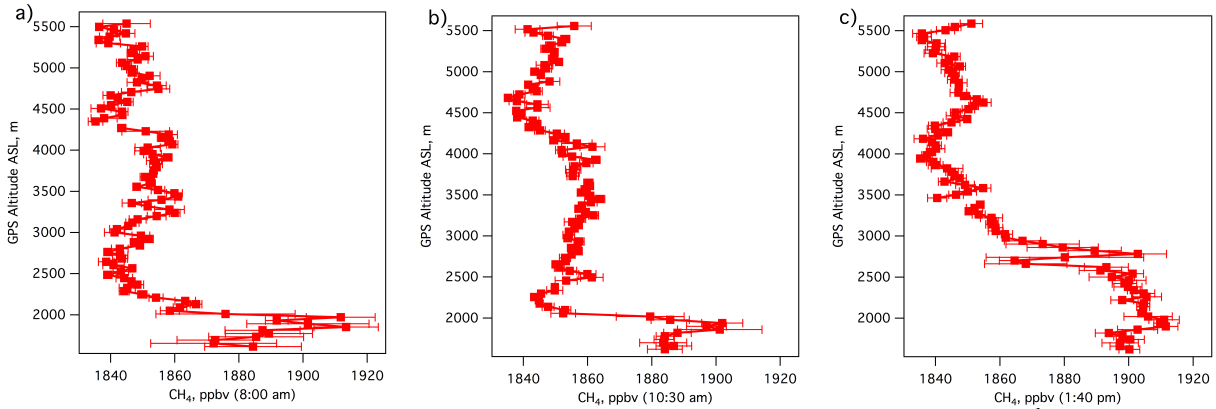

Figure 5.5 Vertical profiles of CH_4 measured aboard the NASA P3-B August 2nd, 2014 with a center bearing over Fort Collins starting at approximately 8:00 am (a), 10:30 am (b), and 1:40 pm (c), local time (UTC -6:00:00).

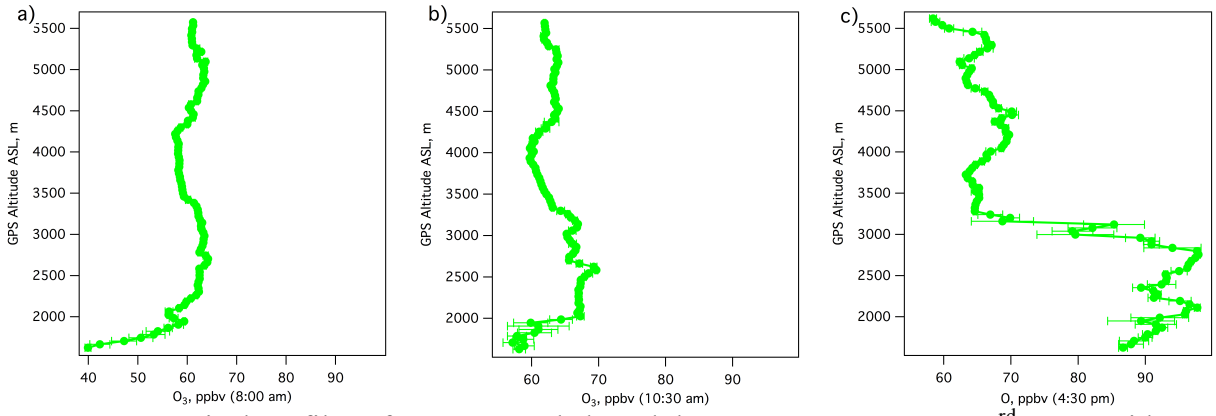

Figure 5.6 Vertical profiles of O_3 measured aboard the NASA P3-B August 3rd, 2014 with a center bearing over Fort Collins starting at approximately 8:00 am (a), 10:30 am (b), and 4:30 pm (c), local time (UTC -6:00:00).

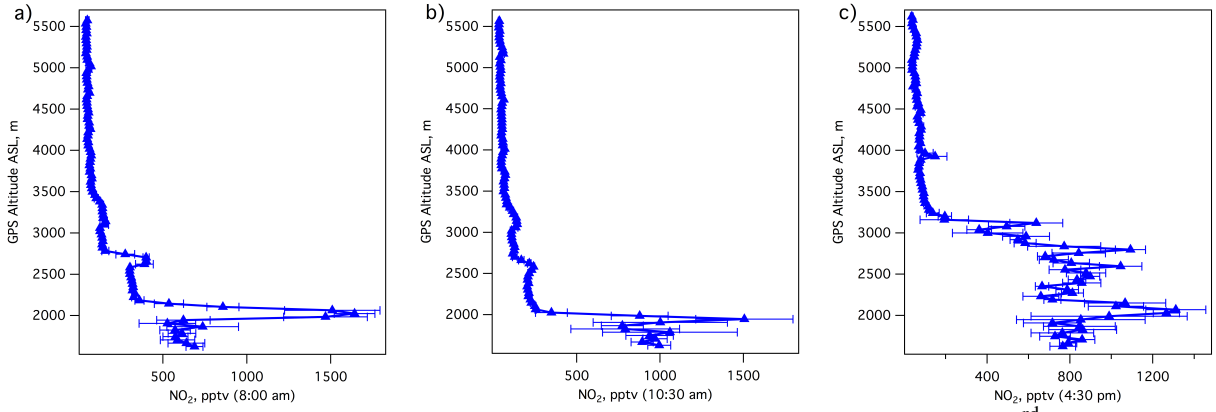

Figure 5.7 Vertical profiles of NO_2 measured aboard the NASA P3-B August 3rd, 2014 with a center bearing over Fort Collins starting at approximately 8:00 am (a), 10:30 am (b), and 4:30 pm (c), local time (UTC -6:00:00).

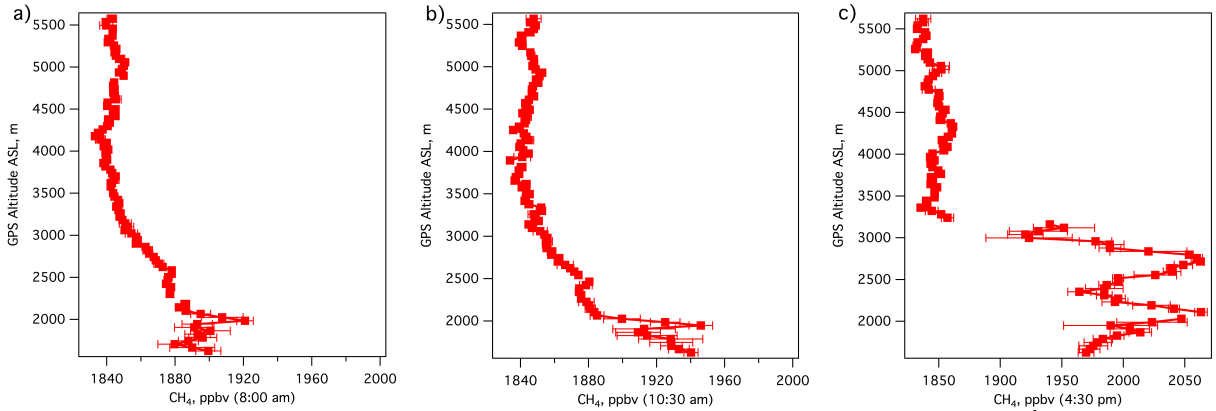

Figure 5.8 Vertical profiles of CH_4 measured aboard the NASA P3-B August 3rd, 2014 with a center bearing over Fort Collins starting at approximately 8:00 am (a), 10:30 am (b), and 4:30 pm (c), local time (UTC -6:00:00).

enhancement from approximately 4000 – 5000 m ASL on Aug. 2nd at 1:40 pm. The vertical structure of O_3 and CH_4 on Aug. 3rd is not as pronounced in the afternoon profile at 4:30 pm. We see a very similar pattern of O_3 and CH_4 in the vertical profiles over Denver (Figures A.1 and A.2). From the examination of NO_2 vertical profiles, there is no visible vertical structure at high altitudes at any point throughout both research flight days. This is to be expected as NO_2 has an atmospheric lifetime of a few hours (Liu, et al., 2016), and it has been shown that throughout the DISCOVER-AQ Colorado campaign, the vertical distribution of NO_2 remained consistently low, with variation constrained to the boundary layer (Flynn et al., 2016).

As shown in Figure 5.2a on Aug. 3rd, the second O_3 enhancement is not as sustained as the one seen on the 2nd, and coincides with a less developed vertical structure of O_3 in the free troposphere, Figure 5.6c. We can assume the observed O_3 enhancements above the PBL, from approximately 4000 – 5000 m ASL are not associated with stratospheric intrusion events as we would not expect to see a similar enhancement from CH_4 measurements. Furthermore, stratospheric intrusion events are characterized as air masses depleted in H_2O and elevated in O_3 (Schroeder et al., 2014; Sullivan et al., 2015). If a stratospheric intrusion event were the source of elevated O_3 between 4000 – 5000 m ASL, we would expect the vertical distribution of H_2O would be at a minimum at the altitudes were O_3 is enhanced. The afternoon profiles of H_2O, shown in Figure 5.9, show that the vertical distribution of H_2O is enhanced in the free troposphere at the same altitudes where we see enhanced O_3 and CH_4. We can conclude the enhanced O_3 observations from 4000 – 5000 m ASL are not a result of stratospheric intrusion events, but rather surface emissions.

Carbon monoxide has been used as a tracer for convection and vertical mixing due to its long lifetime, between 1 and 2 months (Fishman & Seiler, 1983; Parrish et al., 1991;Pan, 2004;

Schroeder et al., 2014), and its prevalence throughout the atmosphere. Because the primary source of CO is anthropogenic (Fujita et al., 1992; Harley et al., 2001; Parrish et al., 2006; Baker et al., 2008), CO concentrations within the free troposphere are not expected to exceed what is considered background mixing ratios in the PBL (Fishman & Seller, 1983; Pan, 2004). From the vertical profiles of CO, Figure 5.10, within the PBL the lowest CO mixing ratio in afternoon profiles collected over Fort Collins were found to be 88 ppbv on August 2nd and 96 ppbv on August 3rd. Within the free troposphere, the maximum value for CO from 4000 – 5300 m ASL was found to be 88 ppbv on August 2nd and 85 ppbv on August 3rd, compared to minimum values of 75 and 80 ppbv, respectively. Though minimal, these enhancements illustrate the influence of surface emissions at higher altitudes, caused by vertical mixing.

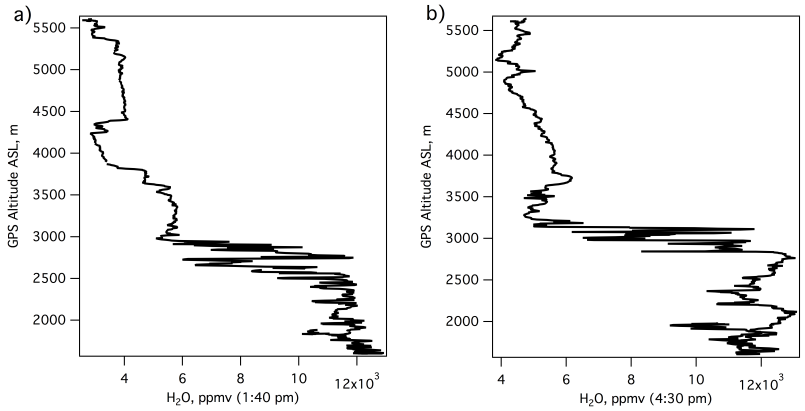

Figure 5.9 Vertical profiles of H_2O measured in the afternoon aboard the NASA P3-B on August 2nd (a), and 3rd (b), 2014 with a center bearing over Fort Collins.

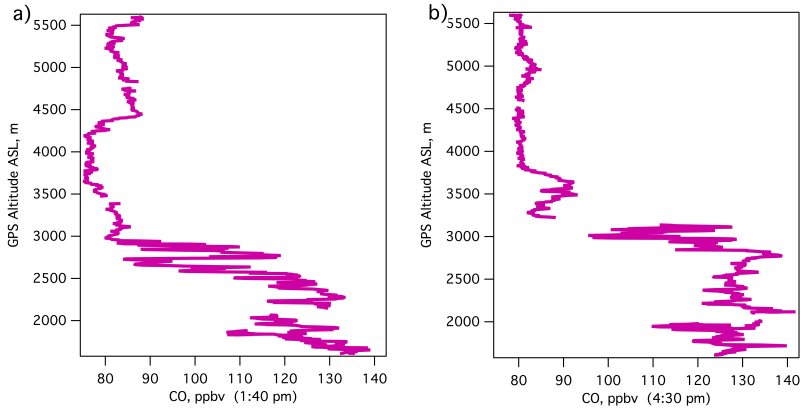

Figure 5.10 Vertical profiles of CO measured in the afternoon aboard the NASA P3-B on August 2nd (a), and 3rd (b), 2014 with a center bearing over Fort Collins.

To examine the origin of trace gases during the vertical profiles, 72-hour 3-dimentional kinematic back trajectories were determined using NOAA ARL's Hybrid Single Particle Lagrangian Integrated Trajectory (HySPLIT) Model (https://www.arl.noaa.gov/hysplit/hysplit/). The 40 km Eta Data Assimilation System (EDAS) meteorological data was used to compute the back trajectories at 7 levels for each profile (500, 1000, 1500, 2000, 2500, 3000, and 3500 m above ground level). Figure 5.11 shows the back trajectory as a function of longitude and altitude for the afternoon profiles at Fort Collins collected on 08/02/2014 at 1:40 pm and 08/03/2014 4:30 pm. For more detailed information regarding all trajectories of profiles collected discussed here, readers are referred to appendix Figures A.3 – A.9. Back trajectories of profiles collected over Denver are shown in appendix Figures A.10 – A.15.

From the morning trajectories (8:00 am) on the 2nd, all altitudes were influenced by long-range transport. In the 500 m and 1000 m AGL trajectories, initially we see a counter-clockwise down-sloping trajectory. This trend continues during the trajectory calculated at 10:30 am. In the morning, the wind direction downshifts as the air masses approach the Rocky Mountains. At 1:40 pm, solar radiation is at a maximum (Figure 5.2c), and upslope events are clearly visible at 500 m AGL, and to a lesser extent at 1000 and 1500 m AGL.

The back trajectories computed starting over Denver exhibited similar flow patterns seen in Fort Collins trajectories at corresponding time points. One of the most notable differences is the defined circulation seen at the 1000 m AGL trajectory at 9:40 am on August 3rd, Figures 5.12 and A.13. This trajectory shows clear upslope and recirculation events from the previous day. As shown in Figure 5.1, the measured 8-hour average O_3 measured in Denver on August 3rd was much higher than the 8-hour average measured over Fort Collins. It is likely that the source of this is the more pronounced circulation shown in the back trajectories. This pattern is also visible

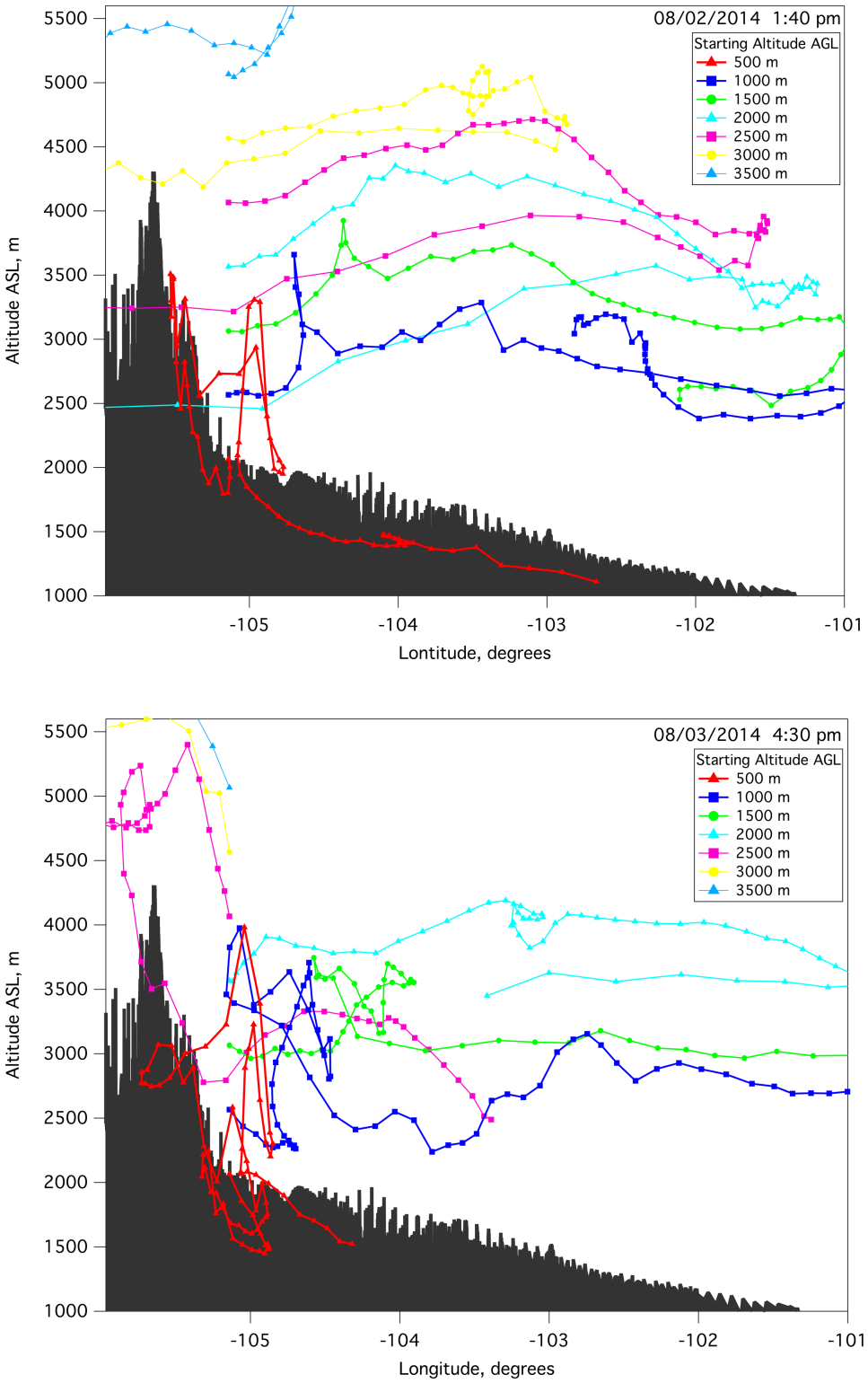

Figure 5.11 72-hour 3-D kinematic back trajectory computed over Fort Collins spiral location starting at 08/02/2014 13:42:05 local time (top) and 08/03/2014 16:26:11 local time (bottom).

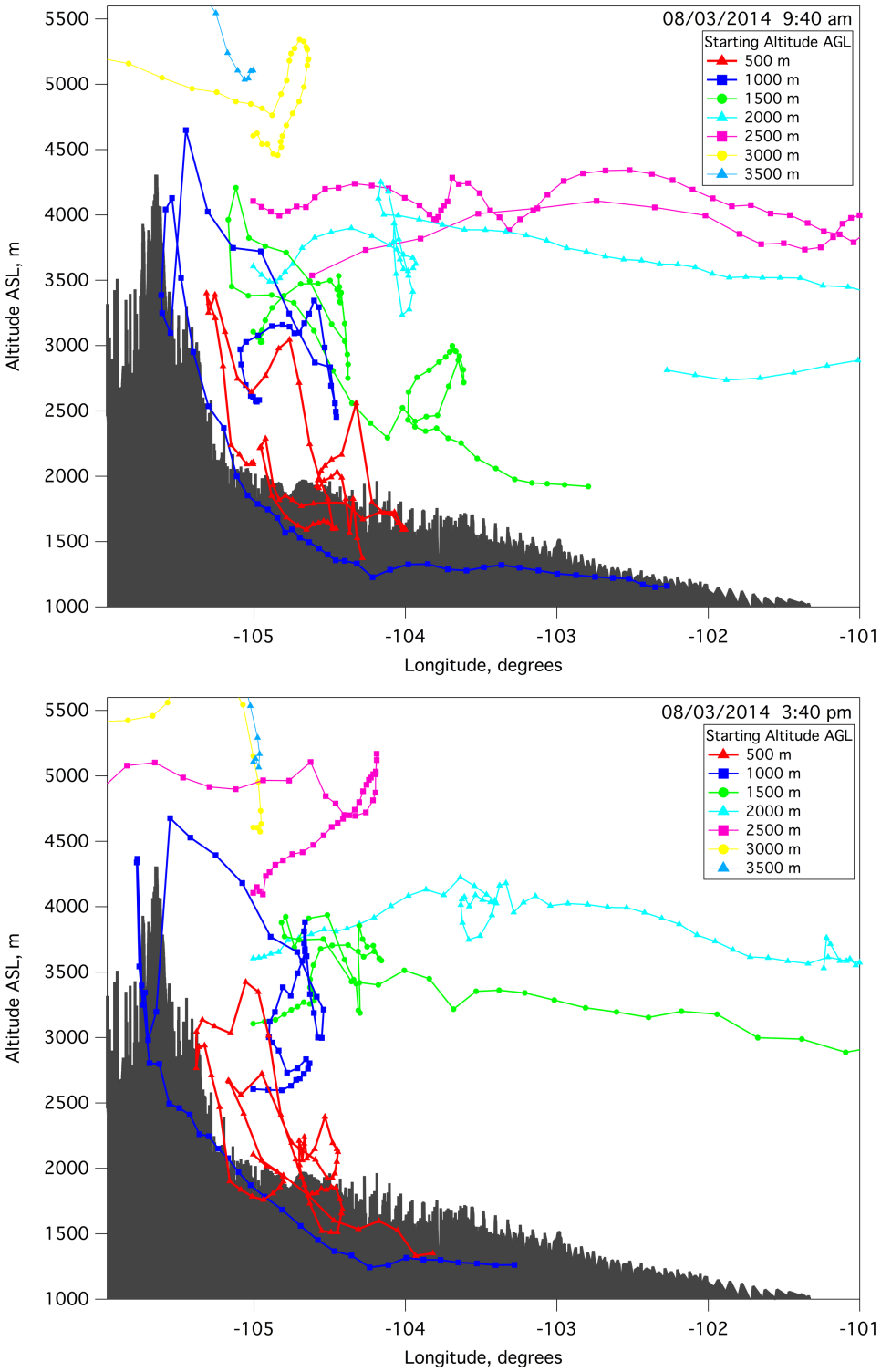

Figure 5.12 72-hour 3-D kinematic back trajectory computed over Denver spiral location starting at 08/03/2014 09:39:47 local time (top) and 08/03/2014 15:38:02 local time (bottom).

at 500 m and 1500 m AGL. This trend continues throughout the day in the trajectories computed over Denver, shown in Figures 5.12 and A.13 – A.15.

At 8:00 am on August 3rd, at lower altitudes (500 – 1500 m AGL), the recirculation event from the previous day and evening are evident and enhancements are visible in the vertical profiles shown in Figures 5.6a, 5.7a, and 5.8a. At 10:30 am, as solar radiation increases, there is evidence of recirculation from 500 – 2500 m AGL. The O_3 enhancements from 4000 – 5000 m corresponds to the 2500 m AGL back trajectory that exhibited strong vertical mixing. Although no data was collected during the vertical profile that was performed at 2:00 pm, the back trajectory at this time highlights recirculation at nearly all trajectories when solar radiation is at a maximum. The latitudinal trajectory (Figure A.8) highlights the extent of circulation and how these events are not localized in the NFRMA, but all along the Rocky Mountains. The last trajectory at 4:30 pm, emphasizes the circulation pattern that occurred throughout the day and the solenoid pattern that leads to afternoon O_3 accumulation at the surface.

Shown in Figure 5.2a and b, there is an accumulation of O_3 the night of August 2nd. On August 3rd, the reported 8-hour O_3 average was higher than the average reported on the 2nd, reaching 79 ppbv. In the morning (8:00 am) on August 3rd, most noticeable in the computed back trajectories is the recirculation seen at 500 m AGL, as the air mass remained in the NFRMA for a minimum of 72-hours. There is also a similar recirculation pattern in the trajectories at 1000 and 1500 m AGL, though not as sustained. This pattern represents the accumulation of O_3 and O_3 precursors that can occur due to recirculation. Throughout the course of the day, from 10:30 am to 4:30 pm, circulation becomes more pronounced.

The vertical profiles of O_3 and CH_4 showed an enhancement from 4000 – 5000 m ASL on August 2nd and from 3700 – 5000m ASL on August 3rd. Based on the back trajectories at

these altitudes during this time, the air mass on the 2nd originated from the north before the easterly approach into the NFRMA while the air mass on the 3rd originated from the northwest. The flow pattern on the 3rd denotes the interaction between upslope movement and synoptic winds that occur during a MVC event. There is clear evidence of enhancements from long range transport at higher altitudes but also entrainment from lower altitudes influenced by thermal gradients.

Vertical profiles and back trajectories provide detailed information about the vertical distribution and air mass flow patterns that occur during recirculation events. To assess the horizontal flow pattern of upslope events and vertical mixing, we examine data collected onboard the NSF/NCAR C-130.

b. NSF/NCAR C-130 1-Hz Measurements

As mentioned in chapter 1, FRAPPÉ flight paths designed to characterize the mountain-valley circulation effect consisted of a north – south pattern, similar to the "lawnmower" pattern used to assess NFRMA emissions discussed in chapter 3. However, this flight pattern included stacked flight legs at approximately 300 m, 1300 m, and 4000 m AGL. This flight pattern was continued up the eastern slope of the Rocky Mountains with passes over the divide and followed by a missed approach into the Granby/Grand County airport, GNB (40.09 °N, -105.90 °W). The two-consecutive ozone/upslope events correspond to research flights 6 and 7 of the FRAPPÉ campaign on Aug. 2nd and 3rd, respectively. The research flights had afternoon take-off times of 3:00 pm and 2:27 pm local, respectively in order to characterize developed upslope events. Research flight paths colorized by O_3 are shown in Figure 5.13 and a 3-D representation is shown in Figure 5.14. Figure 5.15 shows the same research flight paths colorized by CH_4.

Strong O_3 enhancements were observed during the flight legs at approximately -105 °W and -105.4 °W, from the flight legs near the surface (~500 m AGL) and the middle altitude flight legs (~1300 m AGL), shown in Figures 5.13 and 5.14. Minimal enhancements are observed during all flight legs over the ridgeline at -105.7 °W. Similar trends are observed when examining CH_4 distribution on the eastern slope, Figure 5.15. Strong enhancements, up to 2096 ppmv, of CH_4 are observed during the low and middle altitude flight transects through the NFRMA at -105 °W. We also see enhancements along the eastern slope at -105.4 °W with ridgeline measurements at background concentrations, 1824 ± 3 ppmv CH_4.

In Figures 5.13 and 5.15, the most notable difference between research flights 6 and 7 is the high levels of both O_3 and CH_4 seen on August 3rd, especially during the flight legs through the NFRMA at -105 °W. Recalling from above, 8-hour average O_3 was higher on August 3rd compared to August 2nd (Figure 5.1), overnight accumulations of O_3 and CH_4 were visible in continues ground based measurements (Figure 5.2), and the back trajectories at 500 and 1000 m AGL computed in the afternoon on August 3rd exhibited strong recirculation patterns and remained localized to the NFRMA for a minimum of 72-hours. The elevated levels of O_3 and CH_4 measured at the surface and at 1000 m AGL during FRAPPÉ research flight 7 are ostensibly a result of the MVC effect.

As discussed previously, methane and ethane have been used to examine ONG influence. From the comparison of the C_2H_6 to CH_4 emission ratio measured during each flight leg to other areas of ONG influence in Colorado (the NFRMA and western slope), we can examine the distribution of ONG sources during an MVC event. Figure 5.16 shows the correlation of C_2H_6 to CH_4 measured during research flights 6 and 7. Table 5.1 shows the measured emission ratio and correlation for each flight leg.

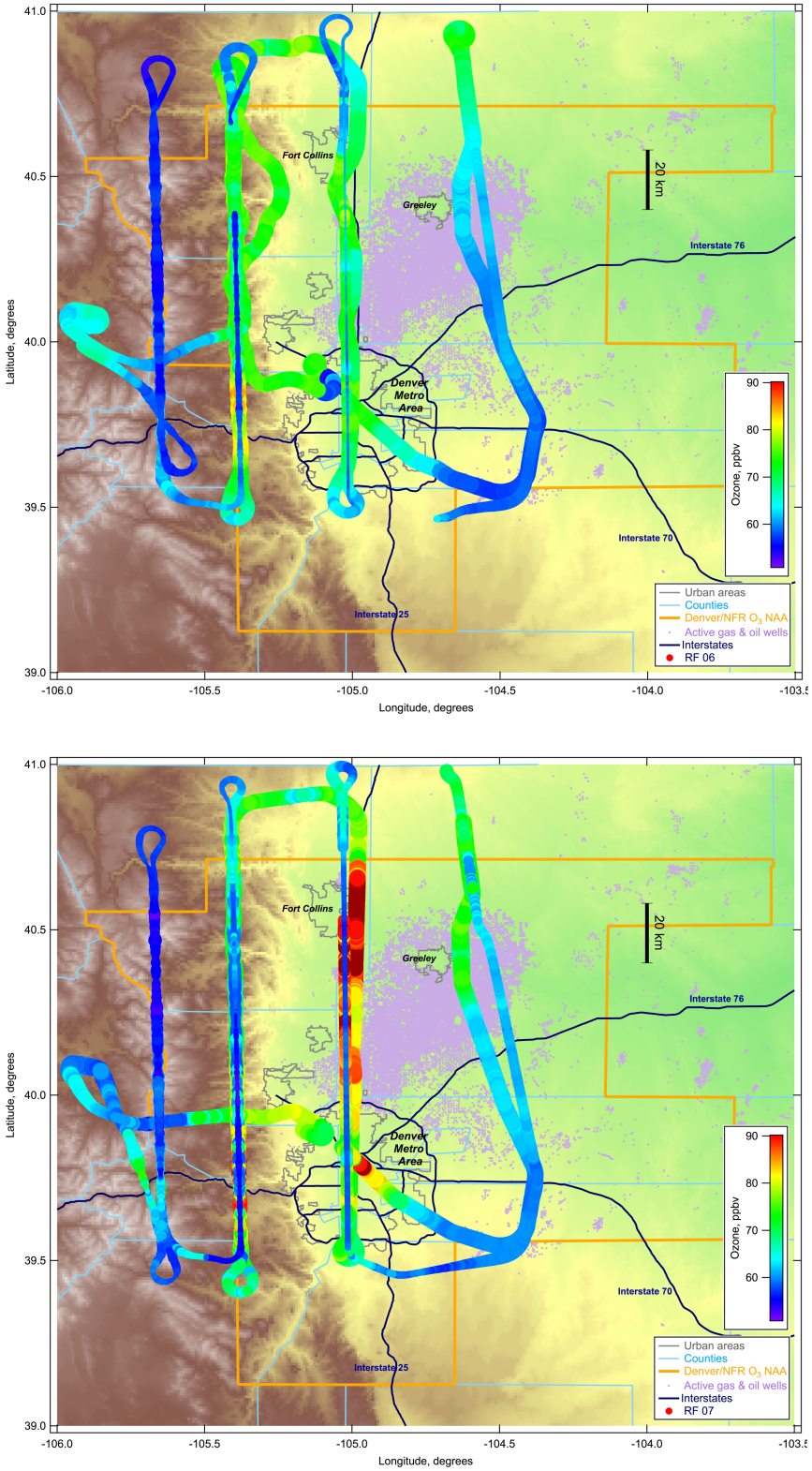

Figure 5.13 Map of research flights 6 (top) and 7 (bottom). Flight tracks are colorized by ozone concentration and sized by altitude above ground level, with smaller markers at higher altitude.

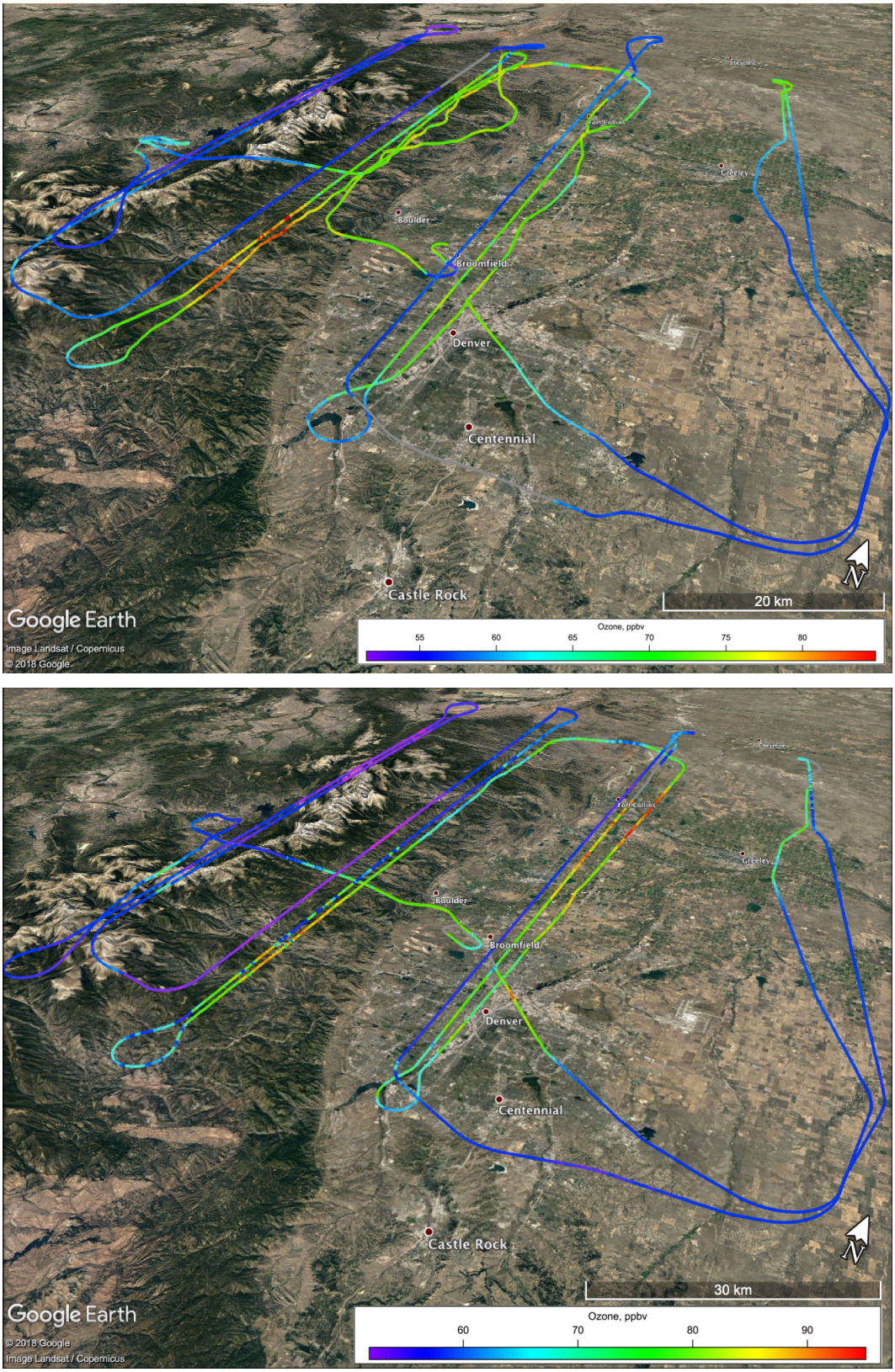

Figure 5.14 Map of research flights 6 (top) and 7 (bottom). Flight tracks are colorized by ozone concentration.

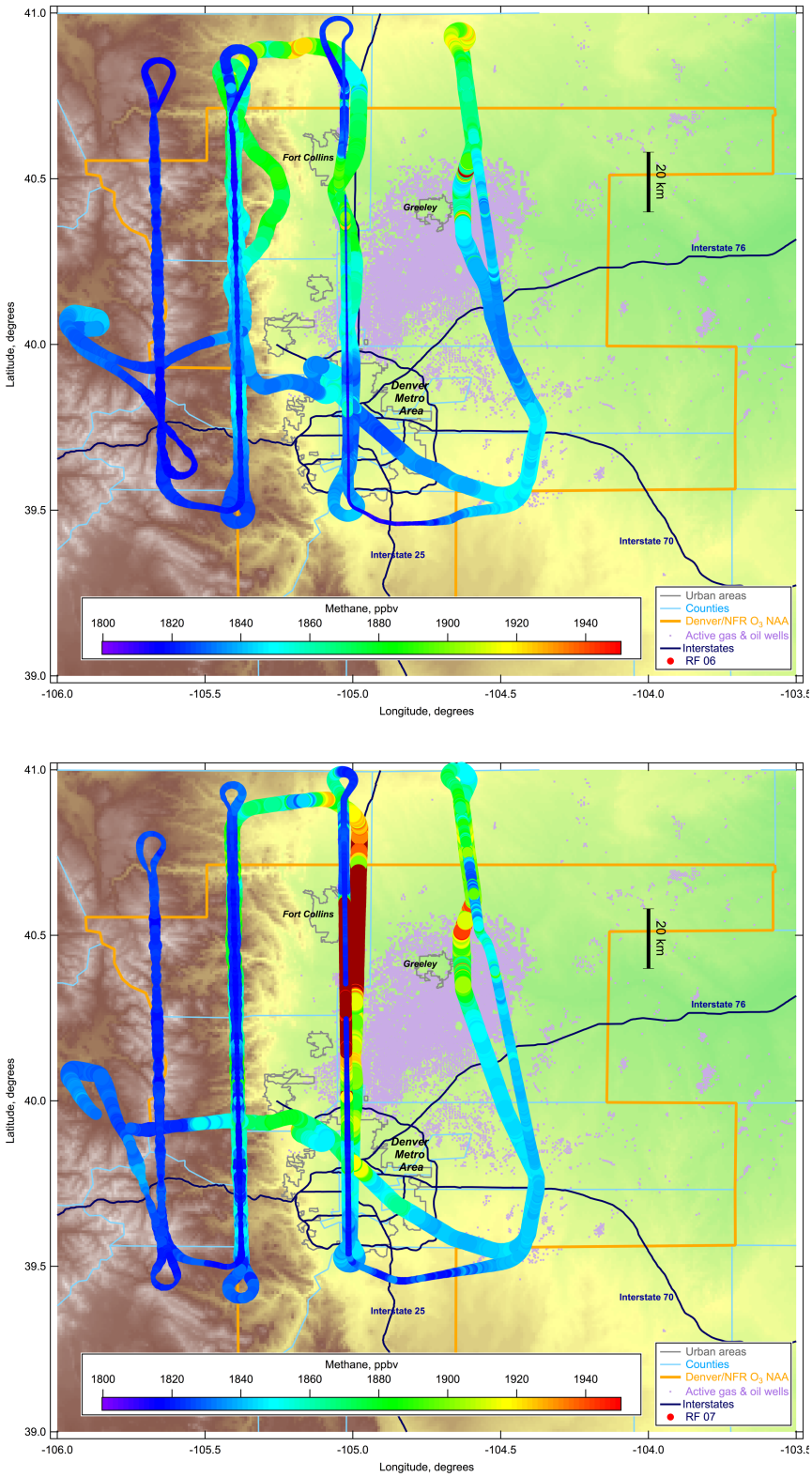

Figure 5.15 Map of research flights 6 (top) and 7 (bottom). Flight tracks are colorized by methane concentration and sized by altitude above ground level with smaller markers at higher altitude.

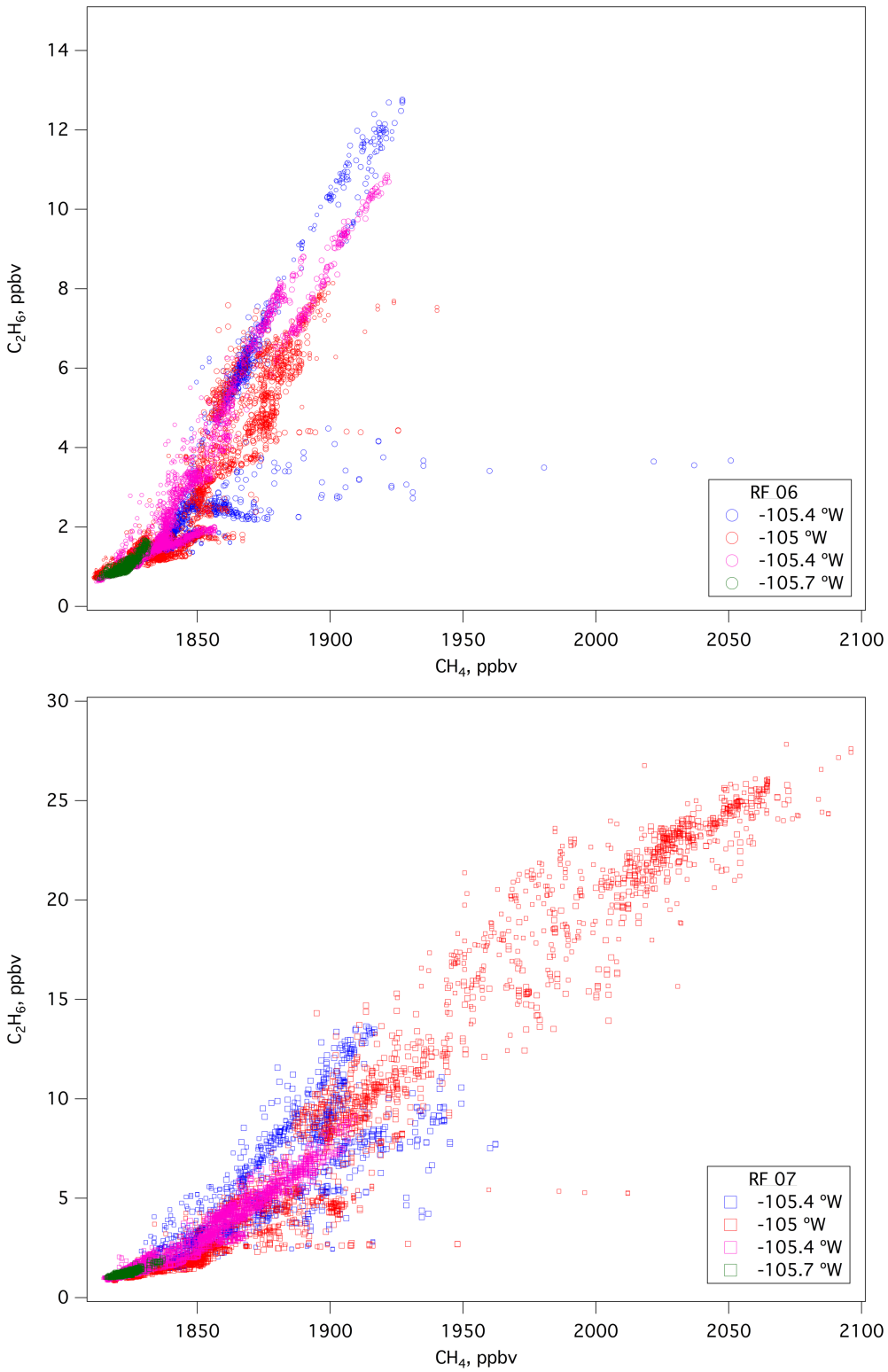

Figure 5.16 Correlation plot of C_2H_6 to CH_4 measured during research flights 6 (top) and 7 (bottom). Points are colorized by longitude and sized by altitude.

Table 5.1 Correlations of C_2H_6 to CH_4 (C_2/C_1), written as percent, measured at each flight leg and compared to NFRMA and western slope emission ratios. Emission ratios statistically similar to NFRMA downwind ratios are highlighted in bold; R^2 values less than 0.70 are highlighted in italics.

	RF 06		**RF 07**	
	C_2/C_1	R^2	C_2/C_1	R^2
-104.5 °W				
350 m	8.21 ± 0.22	*0.548*	**10.20 ± 0.16**	0.764
1450 m	13.38 ± 0.10	0.935	12.29 ± 0.18	0.795
-105 °W				
400 m	8.57 ± 0.13	0.790	11.25 ± 0.07	0.953
1200 m	**9.24 ± 0.10**	0.884	11.04 0.07	0.948
3000 m	4.51 ± 0.41	0.934	5.88 ±0.12	*0.696*
-105.4 °W				
600 m	11.42 ± 0.08	0.952	8.92 ± 0.07	0.921
1250 m	10.64 ± 0.20	0.758	5.67 ±0.07	0.857
2500 m	3.62 ± 0.05	0.872	6.06 ± 0.06	0.910
-105.7 °W				
1650 m	4.66 ± 0.09	0.747	3.84 ±0.07	0.794
2000 m	3.40 ± 0.06	0.727	4.02 ± 0.07	0.790
Downwind[a]	9.87 ± 0.19	0.61		
Upwind[a]	0.55 ± 0.09	0.01		
Piceance[b]	5.79 ± 0.06	0.90		
Uintah[b]	7.91 ±0.06	0.97		

[a]Chapter 3: NFRMA emissions
[b]Chapter 4: western slope emissions

From Figure 5.16, there is a clear bimodal distribution in measurements to the far east at -104.5 °W, and to a lesser extent at -105 °W in flight 6. During flight 7, there is a slight bimodal character in measurements collected at -105 °W. The accumulation in CH_4 from August 2nd is also visible as the CH_4 maximum has nearly doubled on August 3rd (research flight 7). As shown in Table 5.1, C_2H_6 and CH_4 correlated well throughout both research flights at all altitudes, excluding the low-level leg at -104.5 °W during flight 6 and the high-altitude leg at -105°W during flight 7.

There was a great deal of variation in the C_2H_6 to CH_4 emission ratios measured across both research flights, ranging from 3.40 – 13.38. The middle altitude flight leg at -105 °W during

flight 6 and the low altitude flight leg at -104.5 °W during flight 7 were the only flight legs whose emission ratio was statistically similar to the emission ratio measured downwind of the NFRMA of 9.87 ± 0.19, discussed in chapter 3. The ratio measured downwind of the NFRMA was only moderately correlated, R^2=0.61, and as mentioned previously, is indicative of the abundance of CH_4 emission sources in the NFRMA. The variation in the C_2H_6 to CH_4 ratios measured at each flight leg emphasizes the influence of dynamic local emission sources, the contribution from long-range transport, and turbulent mixing on the distribution of trace gases. From ONG systems, CH_4 and C_2H_6 are emitted at consistent mol/mol rates (Pétron et al., 2012; Franco et al., 2016), however, CH_4 has an atmospheric lifetime of ~9 years, compared to C_2H_6, ~50 days (Khalil & Rasmussen, 1983; Rudolph, 1995). As shown in Table 5.1, it is likely that the primary source of CH_4 measured throughout the eastern slope during MVC events is from long-range transport. From the computed back trajectories discussed above (Figures 5.11, 5.12, and A.3 – A.15), this is a reasonable assumption. To further investigate the distribution and sources of trace gases we examine wind speed and direction during all flight legs, as follows.

To investigate the transport of NFRMA emissions during MVC events, we examine the change in wind direction with respect to altitude. Figure 5.17 shows the average wind direction with respect to altitude and longitude of each flight leg (for more detailed information regarding wind direction and speed for each flight leg, readers are referred to Figures A.16 and A.17). By examining the average wind speed and direction per altitude flight leg, there is an evident trend with easterly winds dominating during surface level flight legs and predominately westerly winds at higher altitudes, while the middle altitude flight legs show a transition between east and west. This is most evident during research flight 6, at the middle altitude flight legs at -105 °W and -105.4 °W, where there is a great deal of variation in wind direction which coincides with an

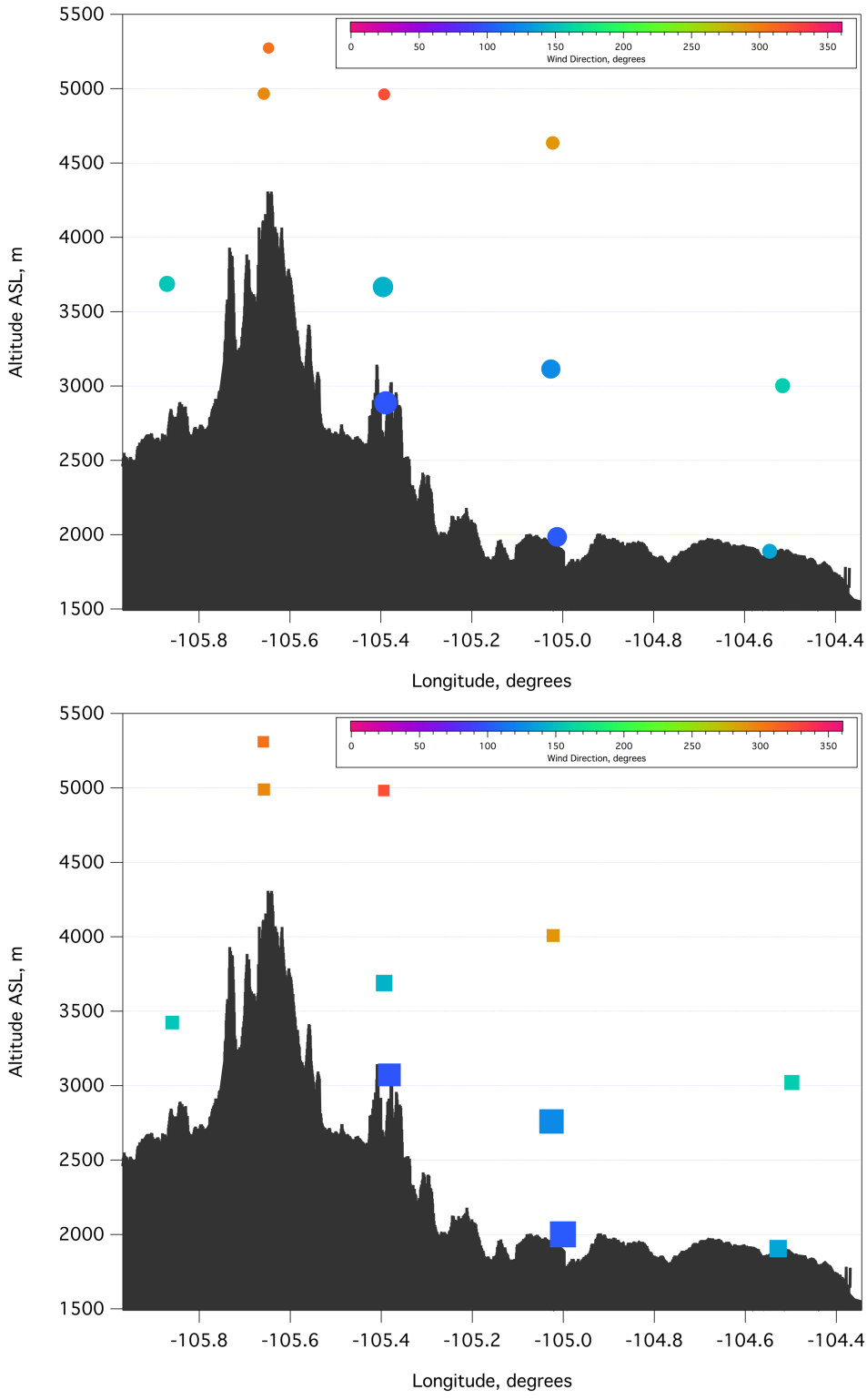

Figure 5.17 Averaged longitudinal and altitudinal flight legs from research flights 6 (top) and 7 (bottom) colorized by average wind direction and sized by average O_3 concentration. Overlaid is the latitudinal cross-section of the Rocky Mountains and eastern slope.

average decrease in wind speed. This is indicative of the convergence of air masses within the circulation event, and corresponds to the recirculation pattern shown in Figure 5.11 from the 500 m AGL back trajectory. This mixing is also visible in the morning back trajectory shown in Figure 5.12.

During flight 7, the wind direction over the ridgeline during the lower altitude leg showed a great deal of variance, with winds from both the east and west, and highlights the convergence of air masses shown in Figure 5.12. At middle altitudes, there is a slight shift in wind direction towards a north – south orientation, which corresponds to the turbulent mixing at these altitudes (Figures 5.12 and A.15). At the lowest level flight leg at -105.4 °W, there is a bimodal distribution in the average wind direction (Figure A.17), and emphasizes the convergence of two air masses and resulting turbulence, with the south easterly winds corresponding to surface winds, and the north easterly winds corresponding to the wind direction at higher altitudes.

c. NSF/NCAR C-130 AWAS Measurements

During FRAPPÉ research flights 6 and 7, a total of 96 AWAS samples were collected (n=48 samples per flight), with approximately 4 samples collected per respective flight leg. To examine the vertical distribution of upslope events, an average value of the hydrocarbons and other VOCs measured per flight leg was determined from 1-Hz and AWAS measurements during flights 6 and 7, shown in Table 5.2 and 5.3, respectively (the Figure ID refers to Figures A.17 and A.18). A map of the distribution of the AWAS measurements collected during research flights 6 and 7 is shown in Figures 5.18 and are colorized by averaged 1-Hz O_3 measurements.

From the analysis of research flight 6, shown in Table 5.2, it is apparent that hydrocarbons were the most concentrated during the lowest altitude flight leg at -105 °W. This flight leg bisects the NFRMA and is closest to emission sources. This trend was consistent when

comparing short-lived and long-lived hydrocarbons. Interestingly, aromatic compounds were concentrated at the middle altitude leg at -105 °W, with toluene reaching a maximum value of 181 pptv. The mixing ratios of VOCs during the flight legs to the far east, -104.5 °W, were considerably lower than measurements over the NFRMA and the foothills, -105.4 °W. Strong easterly winds dominated these flight legs and were upwind of the majority of emission sources in the NFRMA, and are representative of local background trace gas concentrations.

Beginning at -105 °W, there is a visible decreasing east to west trend in hydrocarbon concentrations. We see the reverse of this trend when examining biogenic compounds, particularly isoprene. Maximum isoprene was seen at the highest altitude leg over the ridgeline, with a maximum value of 71 pptv. Isoprene has an atmospheric lifetime of only a few hours (Atkinson & Carter, 1984) and it is unexpected to see such high concentrations at the highest altitude leg, so is likely indicative of the turbulent mixing of surface emissions during upslope events. At the low altitude flight leg over the foothills, there is less isoprene than measured over the NFRMA. We attribute this enhancement to emissions from the western slope. The wind direction during this flight leg is strongly from the west, and as mentioned in chapter 4, the western slope is distinct from the eastern slope with vast designated wilderness areas where isoprene emissions would dominate. We do not see this same trend during flight 7, as biogenic emissions are concentrated at the low altitude foothills flight leg at -105.4 W.

From Table 5.2, there is a decreasing trend in the concentration of the pentanes from east to west, starting at -105 °W during flight 6. There is also a decreasing trend from low to high altitudes. In Table 5.3, at the low altitude legs at -105 °W, *n*-pentane and *i*-pentane concentrations are more than double what was measured during the previous flight. This was also true for the flight leg to the far east at -104.5 °W. The overall east to west and low to high

Table 5.2 Average concentration of select trace gases measured during research flight 6 for each respective flight leg, arranged by longitude and altitude. Maximum values for each compound are highlighted in bold. Units are pptv unless otherwise specified.

Longitude:	-105.7 °W		-105.4 °W			-105 °W			-104.5 °W	
Altitude AGL, *m*:	2015 ±322	1628 ±341	2514 ±201	1236 ±213	503 ±143	3042 ±81	1538 ±173	403 ±138	1441 ±136	340 ±88
Fig A.17 ID:	j	i	h	g	f	e	d	c	b	a
n:	4	4	4	4	4	3	4	4	3	6
CO, *ppbv*	86 ±2	89 ±4	85 ±3	109 ±14	115 ±10	81 ±5	107 ±16	111 ±10	95 ±4	101 ±3
CO_2, *ppmv*	394 ±1	393 ±1	394 ±2	394 ±1	394 ±1	396 ±1	393 ±3	390 ±3	390 ±1	389 ±2
NO	35 ±7	42 ±9	29 ±6	138 ±136	161 ±119	27 ±36	256 ±359	227 ±246	79 ±24	77 ±32
NO_2	52 ±19	68 ±29	39 ±19	384 ±398	553 ±437	30 ± 36	677 ±902	860 ±942	200 ±66	270 ±79
SO_2	33 ±17	57 ±39	32 ±25	260 ±312	331 ±339	29 ±20	250 ±518	251 ±298	108 ±61	117 ±59
O_3, *ppbv*	57 ±1	58 ±3	58 ±2	71 ±6	76 ±3	60 ±1	70 ±5	70 ±3	63 ±4	62 ±4
Methane, *ppbv*	1820 ±2	1824 ±3	1819 ±3	1841 ±11	1856 ±24	1819 ±6	1849 ±23	1857 ±19	1849 ±18	1855 ±23
Ethane, *ppbv*	0.79±0.16	0.93±0.04	0.79±0.11	2.15±0.82	3.15±2.68	1.06±0.22	4.23±2.03	4.53±2.09	1.76±0.72	2.52±1.63
Ethene	39 ±11	38 ±7	29 ±7	66 ±30	83 ±18	20±1	95 ±53	115 ±50	31 ±10	69 ±39
Ethyne	60 ±12	70 ±12	63 ±2	132 ±59	149 ±38	57±5	141 ±66	150 ±66	64 ±4	70 ±4
Propane	305 ±74	362 ±29	271 ±73	1177±682	1904±1958	492±171	2562±1550	2850±1513	908 ±776	1396±1330
Propene	19 ±5	13 ±5	14 ±3	20 ±5	24 ±3	11±5	21 ±5	28 ±9	15 ±4	32±25
n-Butane	61 ±17	75 ±7	52 ±14	434 ±263	757 ±828	117±50	1142±681	1274±577	322 ±394	522 ±601
i-Butane	26 ±6	33 ±3	24 ±5	170 ±97	302 ±323	48±19	445 ±267	495 ±234	105 ±118	180 ±190
n-Pentane	18 ±5	24 ±5	16 ±6	146 ±62	250 ±234	24±11	409 ±199	462 ±118	93 ±122	159 ±182
i-Pentane	24 ±8	32 ±12	19 ±8	192 ±81	290 ±193	23±10	452 ±133	513 ±65	75 ±92	135 ±144
2,2-Dimethylbutane	<LOD	<LOD	<LOD	5 ±4	10 ±4	<LOD	14 ±7	14 ±6	<LOD	2 ±2
2,3-Dimethylbutane	<LOD	<LOD	<LOD	6 ±2	8 ±4	<LOD	15 ±6	17 ±5	<LOD	3 ±4
n-Hexane	4 ±2	7 ±1	<LOD	50 ±19	71 ±69	7±1	130 ±55	144 ±33	22 ±30	43 ±46
2-Methylpentane	<LOD	<LOD	<LOD	40 ±14	72 ±59	<LOD	124 ±34	148 ±26	<LOD	22 ±54
3-Methylpentane	<LOD	<LOD	<LOD	23 ±8	33 ±24	<LOD	57 ±16	63 ±9	6 ±10	19 ±16
n-Heptane	<LOD	<LOD	<LOD	15 ±5	21 ±22	<LOD	35 ±10	44 ±7	5 ±9	13 ±13
n-Octane	<LOD	<LOD	<LOD	<LOD	<LOD	<LOD	15 ±7	17 ±6	<LOD	3 ±6
Cyclopentane	<LOD	<LOD	<LOD	6 ±1	15 ±11	<LOD	22 ±11	26 ±5	6 ±10	8 ±13
Cyclohexane	<LOD	<LOD	<LOD	15 ±4	23 ±19	<LOD	40 ±15	46 ±12	8 ±14	11 ±16
Methylcylohexane	<LOD	<LOD	<LOD	<LOD	7 ±15	<LOD	31 ±15	30 ±16	<LOD	<LOD
Benzene	18 ±4	19 ±6	17 ±3	42 ±16	64 ±50	19 ±3	66 ±25	75 ±12	24 ±3	25 ±9
Toluene	9 ±4	13 ±12	7 ±5	43 ±29	50 ±19	5 ±6	138 ±161	92 ±61	6 ±7	12 ±9
Ethylbenzene	<LOD	<LOD	<LOD	4 ±3	5 ±1	<LOD	9 ±6	7 ±5	<LOD	<LOD
m+p-Xylene	<LOD	<LOD	<LOD	4 ±3	7 ±1	<LOD	16 ±10	15 ±10	<LOD	<LOD
o-Xylene	<LOD	<LOD	<LOD	<LOD	<LOD	<LOD	5 ±4	5 ±4	<LOD	<LOD
Isoprene	48 ±26	45 ±16	9 ±11	16 ±6	21 ±8	<LOD	11 ±3	32 ±26	<LOD	10±12
α-Pinene	5 ±3	7 ±3	<LOD	7 ±3	8 ±2	<LOD	<LOD	<LOD	<LOD	<LOD
β-Pinene	6 ±4	8 ±3	<LOD	6 ±4	7 ±2	<LOD	<LOD	<LOD	<LOD	<LOD
Methyl Nitrate	4 ±1	4 ±1	4 ±1	5 ±1	5 ±1	4 ±1	5 ±1	5 ±1	5 ±1	6 ±1
Ethyl Nitrate	3 ±1	3 ±1	3 ±1	6 ±1	6 ±1	3 ±1	7 ±2	7 ±2	5 ±1	5 ±1
i-Propyl Nitrate	6 ±1	6 ±1	4 ±1	13 ±2	16 ±7	6 ±1	18 ±7	19 ±8	9 ±1	11 ±2
n-Propyl Nitrate	1 ±1	1 ±1	1 ±1	3 ±1	4 ±2	1 ±1	4 ±2	4 ±2	2 ±2	3 ±1
2-Butyl Nitrate	1 ±1	7 ±1	5 ±2	22 ±8	33 ±29	9 ±3	37 ±22	40 ±24	13 ±4	15 ±5
3-Methyl-2-Butyl Nitrate	1 ±1	1 ±1	1 ±1	6 ±2	9 ±4	1 ±1	9 ±4	9 ±4	2 ±1	2 ±1
3-Pentyl Nitrate	1 ±1	1 ±1	1 ±1	5 ±1	8 ±5	2 ±1	8 ±5	9 ±5	2 ±1	3 ±1
2-Pentyl Nitrate	2 ±1	2 ±1	1 ±1	8 ±2	12 ±9	2 ±1	13 ±8	14 ±8	3 ±1	4 ±2

Table 5.3 Average concentration of select trace gases measured during research flight 7 for each respective flight leg, arranged by longitude and altitude. Maximum values for each compound are highlighted in bold. Units are pptv unless otherwise specified.

Longitude:	-105.7 °W		-105.4 °W			-105 °W			-104.5 °W	
Altitude AGL, *m*:	1953 ±302	1641 ±343	2576 ±206	1286 ±219	703 ±227	2420 ±77	1155 ±133	399 ±92	1462 ±110	340 ±81
Fig A.18 ID:	j	i	h	g	f	e	d	c	b	a
n:	4	3	4	4	4	5	5	4	4	5
CO, *ppbv*	96 ±5	96 ±5	86 ±2	97 ±16	121 ±10	91 ±5	119 ±16	124 ±10	99 ±5	106 ±7
CO_2, *ppmv*	394 ±1	394 ±1	396 ±1	396 ±1	394 ±2	396 ±1	396 ±3	396 ±3	391 ±2	392 ±3
NO	19 ±6	25 ±9	21 ±5	54 ±57	98 ±98	26 ±25	231 ±463	142 ±120	90 ±47	109 ±124
NO_2	62 ±27	58 ±40	20 ±38	202 ±215	511 ±393	58 ±45	934±1355	903 ±578	214 ±104	388 ±312
SO_2	46 ±29	71 ±57	25 ±22	164 ±182	312 ±309	57 ±104	316 ±589	278 ±154	87 ±73	206 ±180
O_3, *ppbv*	57 ±3	58 ±3	57 ±3	65 ±8	75 ±7	59 ±3	78 ±9	80 ±7	63 ±4	67 ±6
Methane, *ppbv*	1823 ±2	1824 ±3	1819 ±3	1828 ±10	1865 ±19	1821 ±2	1903 ±75	1921 ±68	1849 ±16	1870 ±29
Ethane, *ppbv*	1.21±0.15	1.24±0.04	0.99±0.05	1.39±0.38	4.09±1.06	0.96±0.08	9.64±8.05	11.86±8.13	1.94±0.39	4.48±2.73
Ethene	52 ±19	73 ±15	21 ±3	26 ±16	76 ±8	25 ±12	131 ±60	147 ±64	30 ±4	57 ±26
Ethyne	90 ±15	91 ±14	68 ±4	84 ±36	155 ±30	77 ±15	164 ±50	186 ±49	68 ±3	105 ±30
Propane	507 ±69	521 ±21	326 ±51	551 ±294	2657±806	292 ±41	6612±5979	8439±6179	1002±446	2654±2097
Propene	20 ±8	38 ±7	2 ±2	4 ±5	18 ±1	10 ±9	28 ±11	30 ±11	11 ±3	12 ±7
n-Butane	140 ±11	143±5	66 ±26	147 ±140	1068±290	53 ±7	2964±2765	3798±2830	315 ±220	1025±953
i-Butane	62 ±5	62 ±2	35 ±9	69 ±52	404 ±105	28 ±6	1189±1089	1470±1106	111 ±70	362 ±315
n-Pentane	47 ±4	45 ±4	17 ±10	45 ±55	326 ±62	11 ±1	1012±911	1268±903	90 ±71	343 ±324
i-Pentane	63 14	63 ±14	21 ±14	64 ±90	375 ±56	12 ±2	1025±757	1231±756	82 ±57	306 ±264
2,2-Dimethylbutane	<LOD	<LOD	<LOD	<LOD	7 ±6	<LOD	22 ±13	25 ±13	<LOD	6 ±7
2,3-Dimethylbutane	<LOD	<LOD	<LOD	<LOD	12 ±2	<LOD	31 ±25	40 ±22	<LOD	8 ±8
n-Hexane	12 ±3	10 ±2	<LOD	<LOD	81 ±17	<LOD	301 ±258	357 ±258	21 ±21	102 ±99
2-Methylpentane	12 ±3	12 ±3	<LOD	11 ±18	80 ±21	<LOD	243 ±186	290 ±186	<LOD	88 ±84
3-Methylpentane	6 ±4	<LOD	<LOD	<LOD	41 ±7	<LOD	124 ±96	146 ±94	<LOD	37 ±36
n-Heptane	3 ±2	5 ±2	<LOD	<LOD	24 ±5	<LOD	85 ±75	100 ±76	<LOD	34 ±34
n-Octane	<LOD	<LOD	<LOD	<LOD	7 ±1	<LOD	26 ±26	32 ±22	<LOD	10 ±9
Cyclopentane	<LOD	<LOD	<LOD	<LOD	20 ±4	<LOD	53 ±43	72 ±45	<LOD	21 ±25
Cyclohexane	<LOD	<LOD	<LOD	<LOD	25 ±17	<LOD	85 ±73	105 ±71	<LOD	35 ±33
Methylcylohexane	<LOD	<LOD	<LOD	<LOD	8 ±9	<LOD	61 ±59	70 ±55	<LOD	22 ±26
Benzene	25 ±1	31 ±5	21 ±4	32 ±21	74 ±16	26 ±5	129 ±91	159 ±107	21 ±1	55 ±33
Toluene	15 ±5	17 ±7	7 ±3	17 ±21	56 ±13	6 ±4	119 ±68	119 ±64	9 ±4	37 ±27
Ethylbenzene	<LOD	<LOD	<LOD	<LOD	4 ±3	<LOD	8 ±6	9 ±3	<LOD	3 ±3
m+p-Xylene	<LOD	<LOD	<LOD	<LOD	5 ±1	<LOD	20 ±15	22 ±10	<LOD	9 ±10
o-Xylene	<LOD	<LOD	<LOD	<LOD	<LOD	<LOD	5 ±4	6 ±2	<LOD	<LOD
Isoprene	35 ±11	22 ±7	<LOD	<LOD	49 ±25	<LOD	17 ±12	21 ±17	<LOD	33 ±47
α-Pinene	3 ±2	<LOD	<LOD	<LOD	12 ±5	<LOD	<LOD	<LOD	<LOD	<LOD
β-Pinene	3 ±3	<LOD	<LOD	<LOD	12 ±5	<LOD	<LOD	<LOD	<LOD	<LOD
Methyl Nitrate	5 ±1	5 ±1	5 ±1	5 ±1	5 ±1	4 ±1	6 ±1	6 ±1	5 ±1	5 ±1
Ethyl Nitrate	4 ±1	4 ±1	3 ±1	4 ±1	9 ±1	3 ±1	10 ±5	13 ±5	5 ±1	7 ±2
i-Propyl Nitrate	8 ±1	8 ±1	5 ±1	9 ±4	24 ±4	5 ±1	32 ±19	42 ±21	11 ±1	18 ±7
n-Propyl Nitrate	2 ±1	2 ±1	1 ±1	2 ±1	5 ±1	1 ±1	7 ±4	8 ±4	2 ±1	4 ±2
2-Butyl Nitrate	11 ±1	11 ±1	6 ±1	13 ±9	49 ±10	6 ±1	86 ±65	112 ±72	15 ±2	32 ±17
3-Methyl-2-Butyl Nitrate	3 ±1	3 ±1	1 ±1	3 ±3	11 ±3	1 ±1	18 ±12	22 ±13	2 ±1	6 ±4
3-Pentyl Nitrate	2 ±1	2 ±1	1 ±1	3±2	11 ±2	1 ±1	18 ±13	23 ±15	3 ±1	6 ±4
2-Pentyl Nitrate	3 ±1	4 ±1	2 ±1	4 ±4	17 ±3	2 ±1	30 ±23	38 ±26	4 ±1	10 ±6

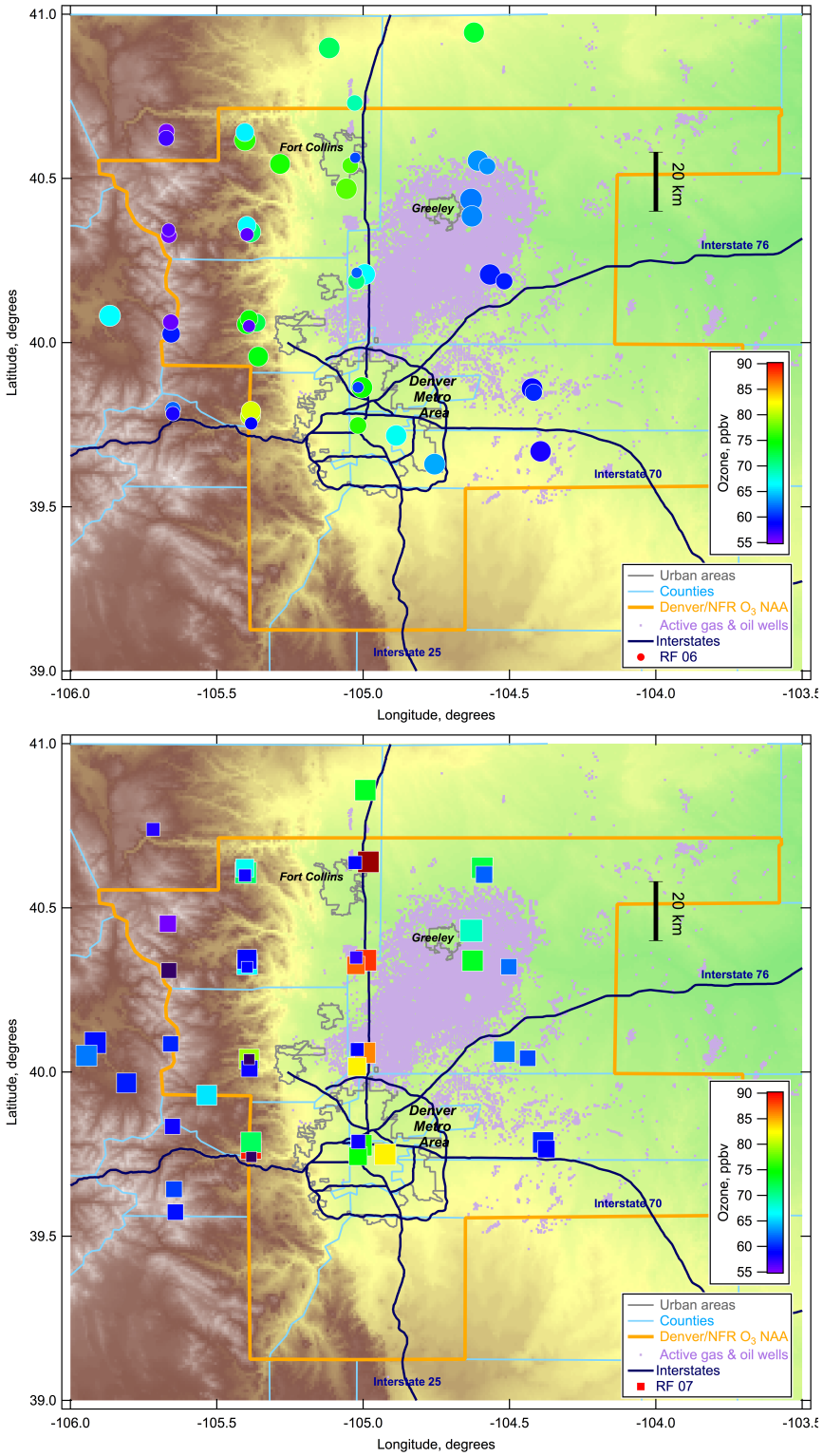

Figure 5.18 A map of AWAS measurement locations during research flights 6 (top) and 7 (bottom), colorized by averaged 1-Hz O_3 measurements and sized by altitude, with smaller markers at higher altitude.

altitude trends followed the same trend as the previous day.

In chapters 3 and 4, we discussed the use of the *i*-pentane to *n*-pentane enhancement ratio to establish an emission signature as the emission ratio is unaffected by photochemistry, dilution, and changing boundary layer conditions (Atkinson, 1990; Ryerson, et al., 2011; Pétron, et al., 2012; Gilman, et al., 2013; Pétron, et al., 2014). Here, we apply this method to examine the extent of mixing from the MVC effect and the distribution of sources throughout the circulation. Figure 5.19 and Table 5.4 shows the iC_5/nC_5 emission ratio measured during each respective flight leg during research flights 6 and 7.

As mentioned previously, values of iC_5/nC_5 vary by source and location. Studies of urban iC_5/nC_5 emission signatures range are generally much greater than 1, with previous studies of urban areas and gasoline vapors ranging from 2.30 to 3.80 (Fraser, et al., 1998; Gentner, et al., 2009) iC_5/nC_5 emission signatures ranging from 0.82 to 0.99 (Ryerson, et al., 2011; Hartt, 2013). From Figure 5.19, there is a great deal of variance in this emission signature measured throughout both research flights as there are many data points greater than as well as less than the 1:1 emission ratio line. This is indicates, as expected, that emissions from the ONG industry and urban emissions mix during a circulation event of this type.

The flight legs to the far east at -104.5 °W during flight 6, the iC_5/nC_5 emission ratio was found to be 0.79 and 0.75 at low and high altitudes, respectively. This ratio slightly increases during flight 7 to 0.81. This value most closely corresponds to the emission ratio measured during flight legs upwind of the NFRMA of 0.81, discussed in chapter 3. From this analysis, we can conclude that the flight legs at -104.5 °W are not so much influenced by local emissions, but rather indicate a signature associated with long-range transport. At -105 °W, during research flight 6, the iC_5/nC_5 ratio at low and middle altitude flight legs were not highly correlated. These

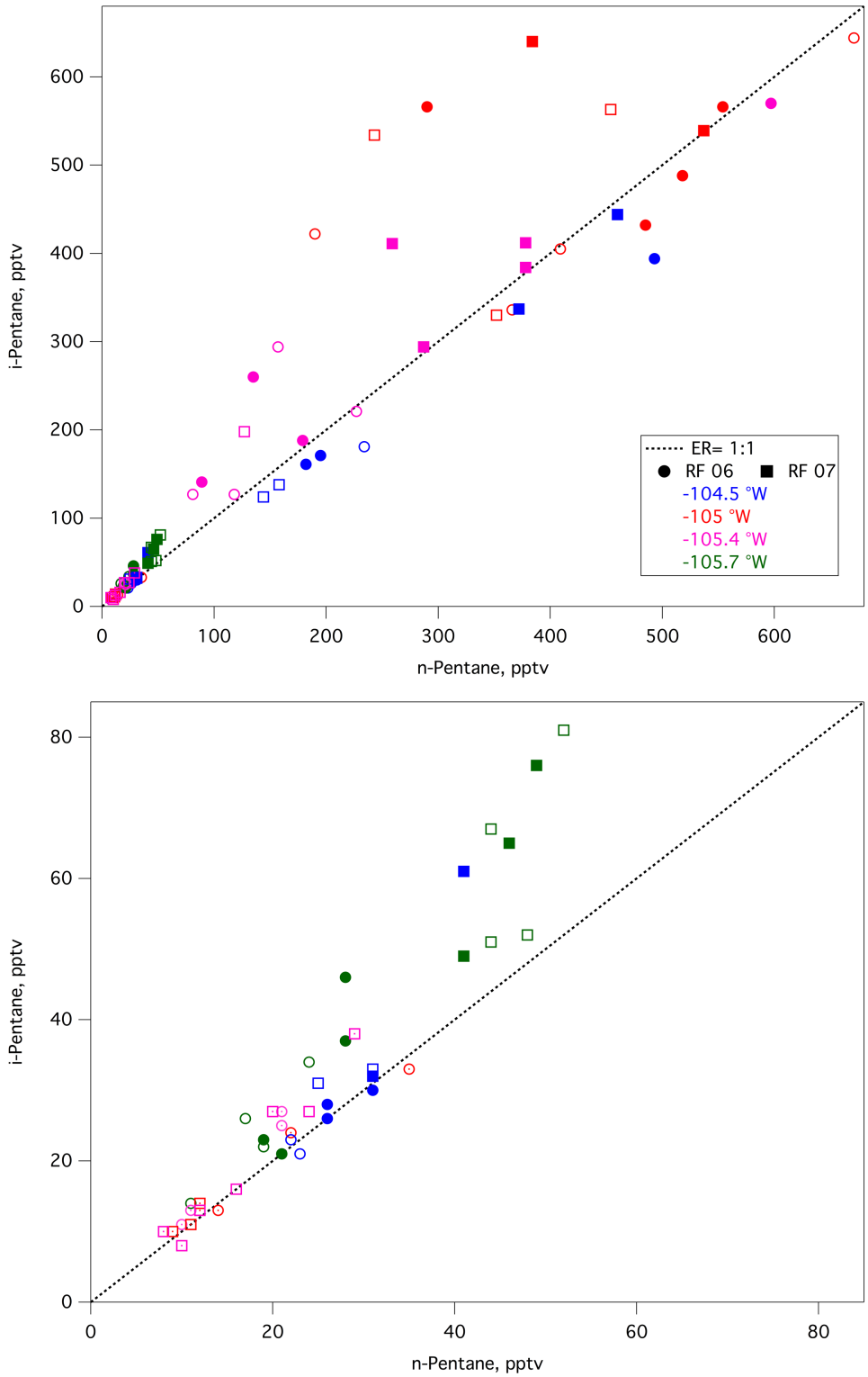

Figure 5.19 Correlation plot of *i*-pentane to *n*-pentane showing all data points (top) and low concentration points (bottom). Solid data points are low altitude measurements, open data points indicate middle altitude measurements, and open data points with a dot indicate highest altitude measurements. The black dotted line is the 1:1 ratio line.

Table 5.4 Correlations of *i*-pentane to *n*-pentane measured at each flight leg and compared to NFRMA and western slope emission ratios. Emission ratios statistically similar to NFRMA downwind ratios are highlighted in bold; R^2 values less than 0.70 are highlighted in italics.

	RF 06		**RF 07**	
	iC_5/nC_5	R^2	iC_5/nC_5	R^2
-104.5 °W				
350 m	0.791 ± 0.016	0.998	0.809 ± 0.049	0.989
1450 m	0.752 ± 0.011	0.999	0.806 ± 0.016	0.999
-105 °W				
400 m	-0.180 ±0.371	*0.105*	**0.830 ± 0.063**	0.983
1200 m	0.522 ± 0.290	*0.605*	**0.823 ± 0.068**	0.980
3000 m	**0.927 ± 0.182**	0.963	**1.168 ± 0.391**	0.817
-105.4 °W				
600 m	**0.801 ± 0.138**	0.944	0.275 ± 0.608	*0.093*
1250 m	**0.814 ± 0.715**	*0.393*	1.632 ± 0.030	0.999
2500 m	1.336 ± 0.100	0.989	1.456 ± 0.164	0.975
-105.7 °W				
1650 m	2.333 ± 0.693	0.850	3.357 ± 0.124	0.999
2000 m	1.452 ± 0.380	0.880	2.341 ± 2.03	*0.399*
Downwind[a]	0.881 ± 0.012	0.998		
Upwind[a]	0.810 ± 0.015	0.996		
Piceance[b]	1.260 ± 0.016	0.998		
Uintah[b]	1.021 ± 0.028	0.992		

[a]Chapter 3: NFRMA emissions
[b]Chapter 4: western slope emissions

flight legs each contained an outlier, which, when removed produced high correlations, $R^2 \geq 0.99$, with a change in emission ratio to 0.98 ± 0.08 and 1.95 ± 0.14 for the low and middle altitude flight legs, respectively, highlighting the vertical mixing that can occur. During research flight 7, all three flight legs at -105 °W were highly correlated, with low altitude iC_5/nC_5 emission ratios corresponding to ONG emissions, and the high altitude legs more closely corresponding to an urban signature.

During research flight 6, over the foothills, at 105.4 °W, the lowest altitude flight legs iC_5/nC_5 emission ratio closely matched emisison ratios measured during the far east flight legs. The middle altitude leg was only somewhat what correlated, R^2=0.39, with no obvious outliers.

During research flight 7, the lowest altitude flight leg showed no correlation, but with the removal of an outlier, the correlation increased from 0.09 to 0.95, resulting in an emission ratio of 1.14 ± 0.27.

From Figure 5.19 and Table 5.4, most flight legs are strongly influenced by urban emissions. From Tables 5.2 and 5.3, concentrations of C_2H_2 and C_3H_8 are greatest at the surface and follow the same east to west trend of other hydrocarbons measured. As discussed previously, C_2H_2 is a good tracer for urban vehicular combustion (Fraser, Cass & Simoneit, 1998; Guo et al., 2007; Warneke et al., 2007). Raw and unprocessed natural gas contains little to no C_2H_2, but is a major source of propane (COGCC, 2007; Gilman et al., 2013). Therefore, a large C_3H_8/C_2H_2 emission ratio would be indicative of ONG emissions, and a small ratio would indicate urban emissions.

From the correlation plot of C_3H_8/C_2H_2, shown in Figure 5.20, there are two clear lobes with one indicating ONG emissions and the other urban emission sources. This correlation showed little to moderate correlation throughout most flight legs, $0.03 \leq R^2 \leq 0.76$, as most flight legs exhibited a bimodal distribution. As shown in Figure 5.20, there is a great deal of mixing occurring between ONG and urban emissions at all flight legs, as indicated by what could be a third lobe. The strongest ONG signatures are seen in the flight legs at -105 °W during flight 6. The strongest urban signature is also seen at -105 °W during flight 6, demonstrating the impact of both urban and ONG emissions. The "mixing" lobe is mostly comprised of samples collected over the NFRMA, at -105 °W, and over the foothills, at -105.4 °W, for both research flights, and correspond with the back trajectories that indicate a great deal of vertical mixing in this area. The high concentrations of C_3H_8 during research flight 7 are indicative of the accumulation of emissions from ONG sources.

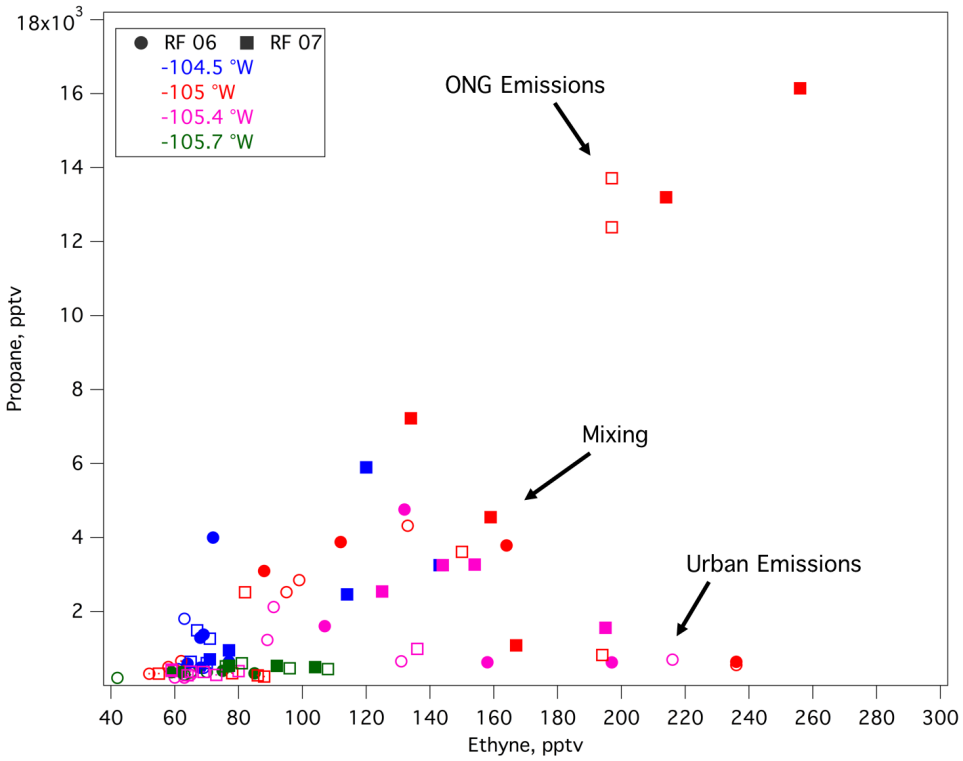

Figure 5.20 Correlation plot of ethyne to propane. Solid data points are low altitude measurements, open data points indicate middle altitude measurements, and open data points with a dot indicate highest altitude measurements.

From Tables 5.2 and 5.3, there is a near three-fold increase from August 2nd to August 3rd in propane, *i*/*n*-butanes, and *i*/*n*-pentanes. There is also approximately a two-fold increase in most alkyl nitrates, and a nearly three-fold increase in 2-butyl nitrate. Alkyl nitrates are formed when the parent hydrocarbon reacts with a hydroxyl radical, reaction 1.22. the alkyl peroxy radical can then react with NO via two pathways, reactions 1.23a and 1.23b. The fraction of alkyl peroxy radical that follows the reaction pathway and produces alkyl nitrates is denoted as α, shown in Figure 5.21.

A common method in calculating photochemical age of an air mass is through the relationship of *n*-butane and 2-butyl nitrate. The reaction rates from the formation of alkyl nitrates can be used to estimate photochemical air mass age using equation 5.1 (Bertman, et al., 1995).

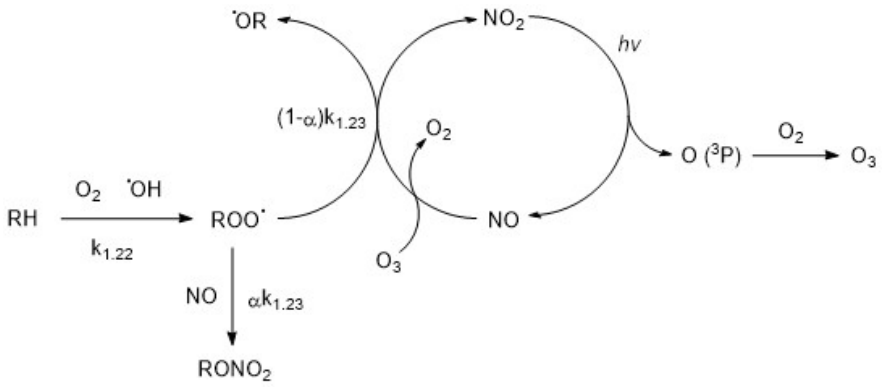

Figure 5.21 Reaction pathway denoting the formation of alky nitrates, $RONO_2$.

$$t = \frac{\ln\left(1-\frac{[2-butyl\ nitrate]}{[n-butane]}\frac{(k_{1.23}-k_{1,22})}{\alpha k_{1.22}}\right)}{k_{1.22}-k_{1.23}} \qquad \text{Equation 5.1}$$

Where $k_{1.22}$ is the rate constant of reaction 1.22 (≈2.54 x 10^{-12} cm^3 $molecules^{-1}$ s^{-1}) and $k_{1.23}$ is the rate constant of reaction 1.23 (≈9.2x 10^{-13} cm^3 $molecules^{-1}$ s^{-1}) (Atkinson, 2003; Atkinson, et al., 2006), and α (0.077) is the branching ratio, or percent reaction that forms the alkyl nitrate (Bertman, et al., 1995).

Shown in Tables 5.5 and 5.6 is the calculated average air mass age of each flight leg measured during research flights 6 and 7, respectively. There is a visible trend from east to west in terms of air mass age. The flight legs at the -104.5 °W are approximately 24 hours old, with the "youngest" flight leg at low altitudes at -105 °W, followed by the pass over the foothills at -105.4 °W, with the air masses measured over the ridgeline at -105.7 °W as the "oldest." There is also a vertical trend, as air mass age increases with altitude.

From the analysis of the air mass age, the youngest average air mass ages of a flight leg corresponds to the low altitude flight legs at -105 °W, at 12.79 ± 2.35 and 12.35 ± 3.07 hours for flights 6 and 7. Although these air masses were the youngest measured, the range varied from 8 to 16 hours. This flight location is directly above local emission sources and bisects the GWA. At this altitude and location, an air mass age of a few hours is expected. For example, isoprene

Table 5.5 Average, minimum, and maximum air mass age calculated in hours for each flight leg during research flight 6. Flight leg ID corresponds to Figure A.17.

Longitude:	-105.7 °W		-105.4 °W			-105 °W			-104.5 °W	
Altitude AGL, *m*:	2015 ±322	1628 ±341	2514 ±201	1236 ±213	503 ±143	3042 ±81	1538 ±173	403 ±138	1441 ±136	340 ±88
Fig A.2 ID:	j	i	h	g	f	e	d	c	b	a
Average	25.55	25.20	29.88	30.81	17.61	33.33	13.98	12.79	22.88	17.95
Std. Deviation	2.02	1.34	6.79	6.62	3.81	2.26	4.12	2.35	11.56	9.79
Minimum	23.81	23.96	23.72	24.12	14.07	30.71	10.21	10.93	12.71	9.10
Maximum	27.87	26.63	37.69	39.73	22.89	35.63	18.67	16.19	34.87	33.15

Table 5.6 Average, minimum, and maximum air mass age calculated in hours for each flight leg during research flight 7. Flight leg ID corresponds to Figure A.18.

Longitude:	-105.7 °W		-105.4 °W			-105 °W			-104.5 °W	
Altitude AGL, *m*:	1953 ±302	1641 ±343	2576 ±206	1286 ±219	703 ±227	2420 ±77	1155 ±133	399 ±92	1462 ±110	340 ±81
Fig A.2 ID:	j	i	h	g	f	e	d	c	b	a
Average	30.63	29.06	27.66	20.20	19.63	25.18	13.34	12.35	25.31	20.69
Std. Deviation	9.21	2.82	1.78	3.77	4.68	2.48	2.42	3.07	14.05	12.57
Minimum	25.49	25.90	25.15	15.75	14.71	22.68	10.61	7.84	9.15	6.23
Maximum	44.42	32.60	29.29	24.23	24.28	27.64	16.50	14.50	34.53	35.12

concentrations measured during these flight legs were higher compared to other flight legs. With a lifetime of ~2 hours, we would expect the calculated air mass to mimic the trend seen in isoprene. The calculated air mass age as a "photochemical clock" requires photolysis. With a takeoff time of ~3 pm and an air mass age of ~12 hours, the clock would have begun around 3 am, in the absence of sunlight. As the air mass remained within the NFRMA, Figure 5.11, we can attribute this aged air mass to accumulation in hydrocarbon emissions that can occur as a result of recirculation.

5.2 Conclusion

Observations from the DISCOVER-AQ and FRAPPÉ campaigns during an NAAQS O_3 exceedance event in the NFRMA from 2 August – 3 August, 2014 were used to investigate the cause of the O_3 event. The analysis of surface emissions show the diurnal accumulation of O_3 at the ground level. Vertical profiles highlight abnormal behavior in the free troposphere of O_3 from 4000 – 5000 m ASL. Back trajectories of these vertical profiles indicate the source of O_3 enhancements to be a combination of vertical mixing from the NFRMA and long-range transport. Emission signatures measured along the eastern slope of the Rocky Mountains show that upslope events lead to a mixing of ONG and urban emissions. The analysis of air mass age throughout the eastern slope highlights mixing between local emission sources and long range transport. Therefore, we can conclude that emission sources in the NFRMA that led to ozone exceedances are a result of both local emissions and long-range transport. In the absence of upslope events, the accumulation of hydrocarbons in the NFRMA would not have occurred and the ozone limits would not have been exceeded. These results are not inconsistent with the findings from Sullivan et al., (2016). This study further elucidates the relationship between local meteorology and air quality.

5.3 References

Atkinson, R. & Carter, W. (1984). Kinetics and mechanism of the gas-phase reactions of ozone and organic compounds under atmospheric conditions. *Chemical Reviews*. 84(5), 437-470.

Atkinson, R. (2003). Kinetics of the gas-phase reactions of OH radicals with alkanes and cycloalkanes, *Atmospheric Chemistry and Physics*. 3, 2233-2307

Atkinson, R., Baulch, D., Cox, R., Crowley, J., Hampson, R., Hynes, R., Jenkin, M., Rossi, M., Troe, J., IUPAC Subcommittee. (2006). Evaluated kinetic and photochemical data for atmospheric chemistry: Volume II –gas phase re- actions of organic species, *Atmospheric Chemistry and Physics.* 6, 3625-4055.

Baker, A., Beyersdorf, A., Doezema, L., Katzenstein, A., Meinardi, S., Simpson, I., . . . Rowland, F. (2008). Measurement of nonmethane hydrocarbons in 28 United States cities. *Atmospheric Environment, 42*(1), 170-182.

Bertman, S., Roberts, J., Parrish, D., Buhr, M., Goldan, P., Kuster, W., Fehsenfeld, F. (1995). Evolution of alkyl nitrates with air mass age. *Journal of Geophysical Research*. 100(D11), 22805-22313.

COGCC. (2007). *GREATER WATTENBERG AREA.* Denver, CO: LT ENVIRONMENTAL, INC.

Fishman, J., & Seiler, W. (1983). Correlative nature of ozone and carbon monoxide in the troposphere: Implications for the tropospheric ozonebudget. *Journal of Geophysical Research: Oceans*, 88(C6), 3662-3670.

Flocke, F., & Pfister, G. (2013). Front Range Air Pollution and Photochemistry Experiment FRAPPÉ: A proposed field experiment in Colorado for summer 2014. Retrieved from http://www2.acd.ucar.edu/frappe

Flynn, C., Pickering, K., Crawford, J., Weinheimer, A., Diskin, G., Thornhill, L., Loughner, C., Lee, P., Strode, S. (2016). Variability of O3 and NO2 profile shapes during DISCOVER-AQ: Implications for satellite observations and comparisons to model-simulated profiles. *Atmospheric Environment*. 147, 133-156.

Franco, B., Mahieu, E., Emmons, L., Tzompa-Sosa, Z., Fischer, E., Sudo, K., Bovy, B., Conway, S., Griffin, D., Hannigan, J., Strong, K., Walker, K. (2016). Evaluating ethane and methane emissions associated with the development of oil and natural gas extraction in North America. *Environmental Research Letters.* 11(4), 044010.

Fraser, M., Cass, G., Simoneit, B. (1998). Gas-phase and particle-phase organic compounds emitted from motor vehicle traffic in a Los Angeles roadway tunnel. *Environmental Science and Technology.* 32(14), 2051-2060.

Fujita , E., Croes, B., Bennett, C., Lawson, D., Lurman, F., & Main, H. (1992). Comparison of emission inventory and ambient mixing ratios of CO, NMOG, and NOX in Californias Southcoast Basin. *Journal of Air Waste Management Associeation, 42*(3), 264-276.

Gentner, D., Harley, R., Miller, A., & Goldstein, A. (2009). Diurnal and seasonal variability of gasoline-related volatile orgainc compound emissions in Riverside, California. *Environmental Science Technology, 43*(12), 4247-4252.

Gilman, J., Lerner, B., Kuster, W., & de Gouw, J. (2013). Source signature of volatile organic compounds from oil and natural gas operations in Northeastern Colorado. *Environmental Science and Technology, 47*, 1297-1305.

Guo, H., So, K., Simpson, I., Barletta, B., Meinardi, S., & Blake, D. (2007). C1-C8 volatile organic compounds in the atmosphere of Hong Kong: Overview of atmospheric processing ans source apportionment. *Atmospheric Environment, 41*(7), 1456-1472.

Harley, R., McKeen, S., Pearson, J., Rodgers, M., & Lonneman, W. (2001). Analysis of motor vehicle emissions during the Nashville/Middle Tennessee ozone study. *Journal of Geophysical Research, 106*, 3559-3567.

Hartt, G. (2013). *Oil and gas emissions in the Gulf of Mexico and the San Joaquin Valley of Calfornia.* Ph. D. Thesis, University of California - Irvine.

Khalil, M. & Rasmussin, R. (1983). Sources, sinks, and seasonal cycles of atmospheric methane. *Journal of Geophysical Research*. 88(C9), 5131-5144.

Pan, L. (2004). Definitions and sharpness of the extratropical tropopause: A trace gas perspective. *Journal of Geophysical Research*. 109, D23103,

Parrish, D., Trainer, M., Buhr, B., Watkins, A., Fehsenfield, J. 1991. Carbon monoxide concentrations and their relation to concentrations of total reactive oxidized nitrogen at two rural us sites. *Journal of Geophysical Research*. 96, 9309-9320.

Parrish D., Stohl, A., Forster C., Atlas, E., Blake, D., Goldan, P., Kuster, W., de Gouw, J. (2007). Effects of mixing on evolution of hydrocarbon ratios in the troposphere. *Journal of Geophysical Research Atmospheres.* 112, D10S34.

Pétron, G., Grost, G., Miller, B., Hirsch, A., Montzka, S., Karion, A., . . . Tans, P. (2012). Hydrocarbon emissions characterization in the Colorado Front Range: A pilot study. *Journal of Geophysical Research, 117*(D04304).

Rudolph J 1995 The tropospheric distribution and budget of ethane. *Journal of Geophysical Research*. 100 11369–81

Ryerson, T., Aikin, K., Angevine, W., Atlas, E., Blake, D., Brock, C., . . . Watts, L. (2011). Atmospheric emissions from the Deepwater Horizon Spill constrain air-water partitioning, hydrocarbon fate, and leak rate. *Geophysical Research Letters, 38*(L07803).

Schroeder, J., Pan, L., Ryerson, T., Diskin, G., Hair, J., Meinardi, S., Simpson, I., Barletta, B., Blake, N., Blake,R. 2014. Evidence of mixing between polluted convective outflow and stratospheric air in the upper troposphere during DC3. *Journal of Geophysical Research: Atmospheres*, 119, 11477-11491.

Sullivan, J., McGee, T., Langford, A., Alvarez II, R., Senff, C., Reddy, P., . . . Hoff, R. (2016). Quantifying the contribution of thermally driven recircultion to a high-ozone event along the Colorado Front Range using lidar. *Journal of Geophysical Research: Atmospheres*, 121, 10377-10390.

Toth, J., & Johnson, R. (1985). Summer surface flow characteristics over northeast Colorodo. *Monthly Weather Review*, 113(9), 1458-1469.

Warneke, C., McKeen, S., de Gouw, J., Goldan, P., Kuster, W., Holloway, J., . . . Blake, D. (2007). Determination of urban volatile orgainc compound emission ratios and comparison with an emissions database. *Journal of Geophysical Research, 112*(D10S47).

APPENDIX

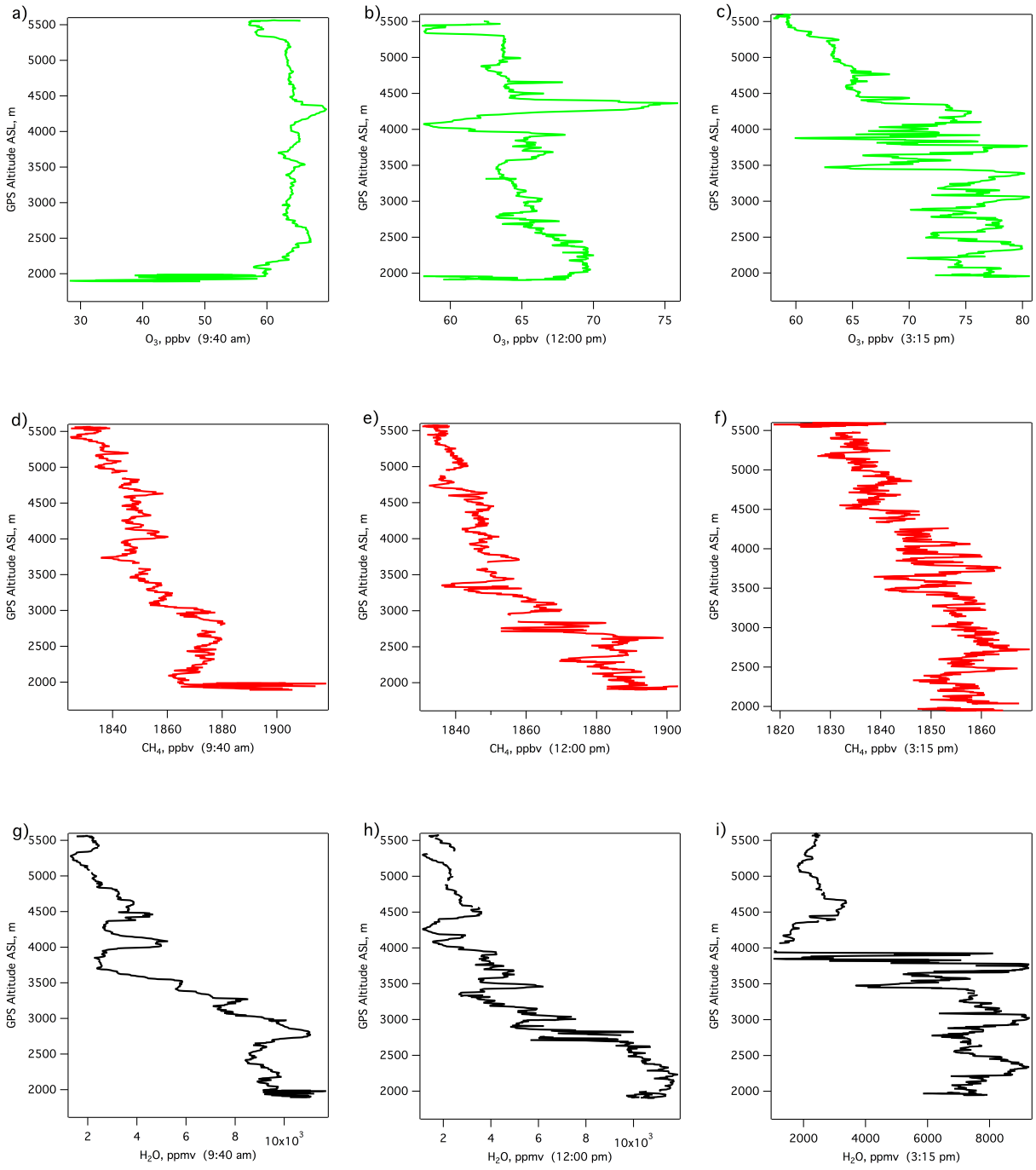

Figure A.1 Vertical profiles of O_3 (a, b, c), CH_4 (d, e, f), and H_2O (g, h, i) measured aboard the NASA P3-B August 2nd, 2014 with a center bearing over Denver starting at 9:40 am (a, d, g), 12:00 pm (b, e, h), and 3:15 pm (c, f, i), local time (UTC -6:00:00).

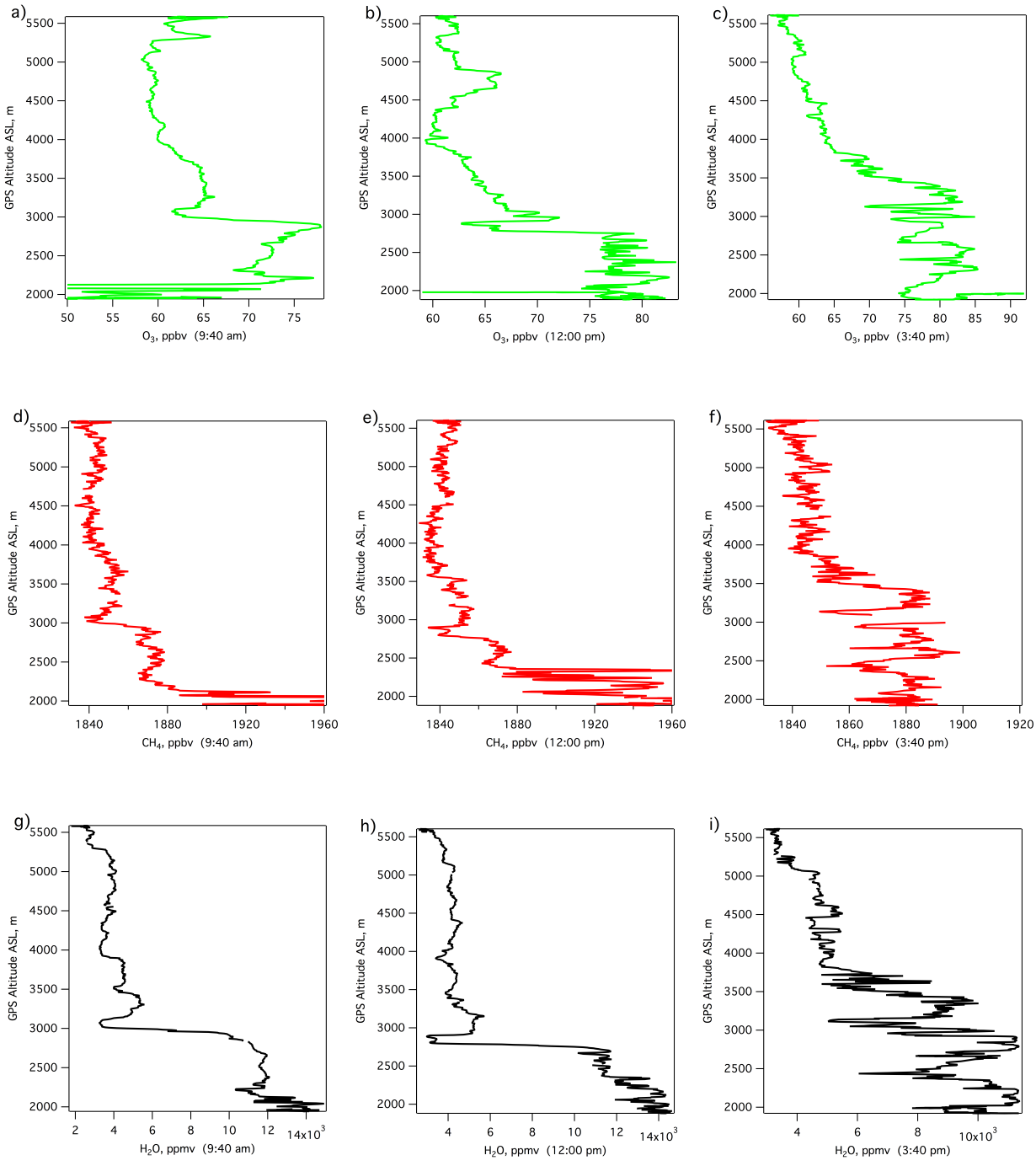

Figure A.2 Vertical profiles of O_3 (a, b, c), CH_4 (d, e, f), and H_2O (g, h, i) measured aboard the NASA P3-B August 3rd, 2014 with a center bearing over Denver starting at 9:40 am (a, d, g), 12:00 pm (b, e, h), and 3:40 pm (c, f, i), local time (UTC -6:00:00).

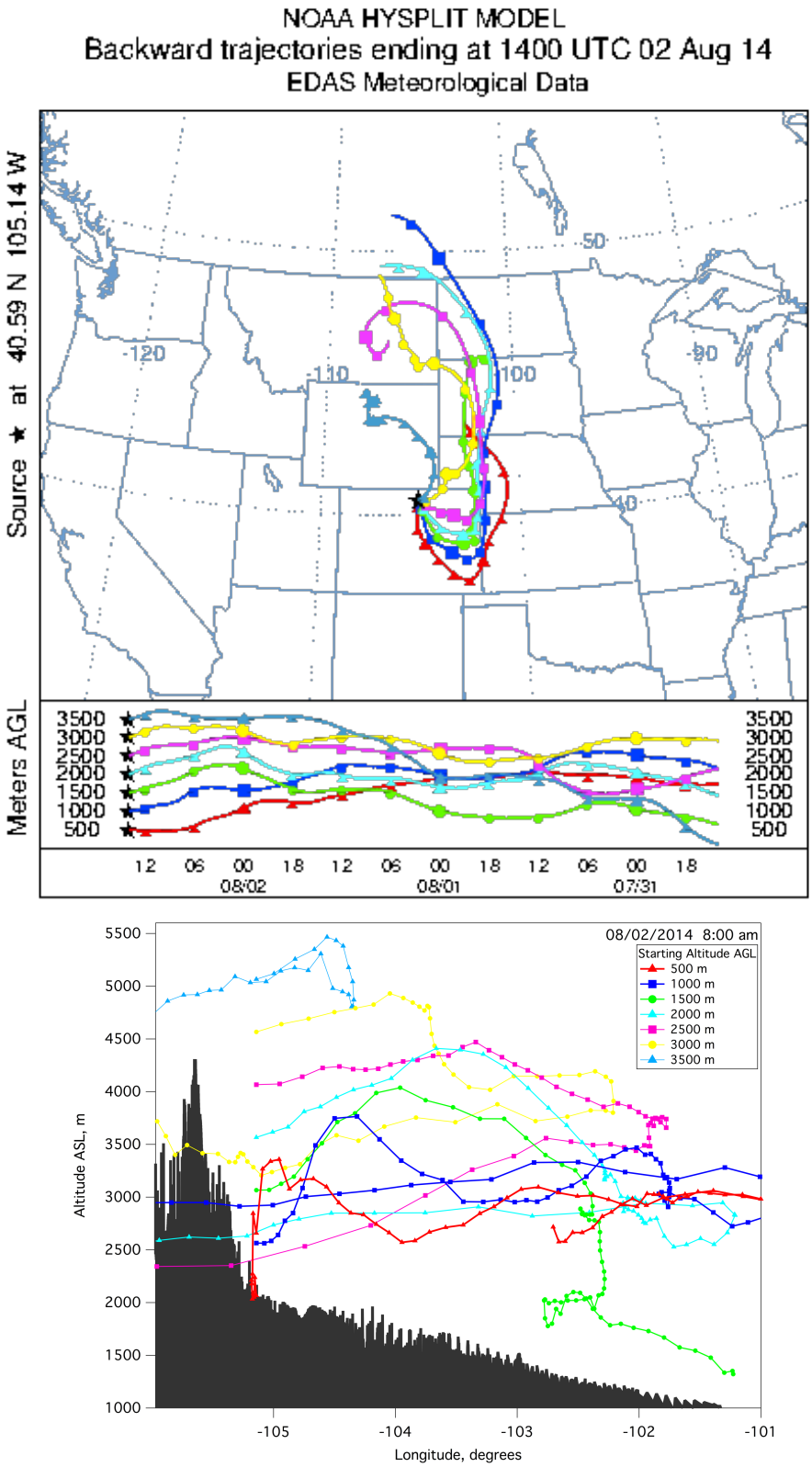

Figure A.3 72-hour 3-D kinematic back trajectory computed over Fort Collins spiral location starting at 08/02/2014 08:03:44 local time as a function of latitude and longitude (top), and altitude and longitude (bottom).

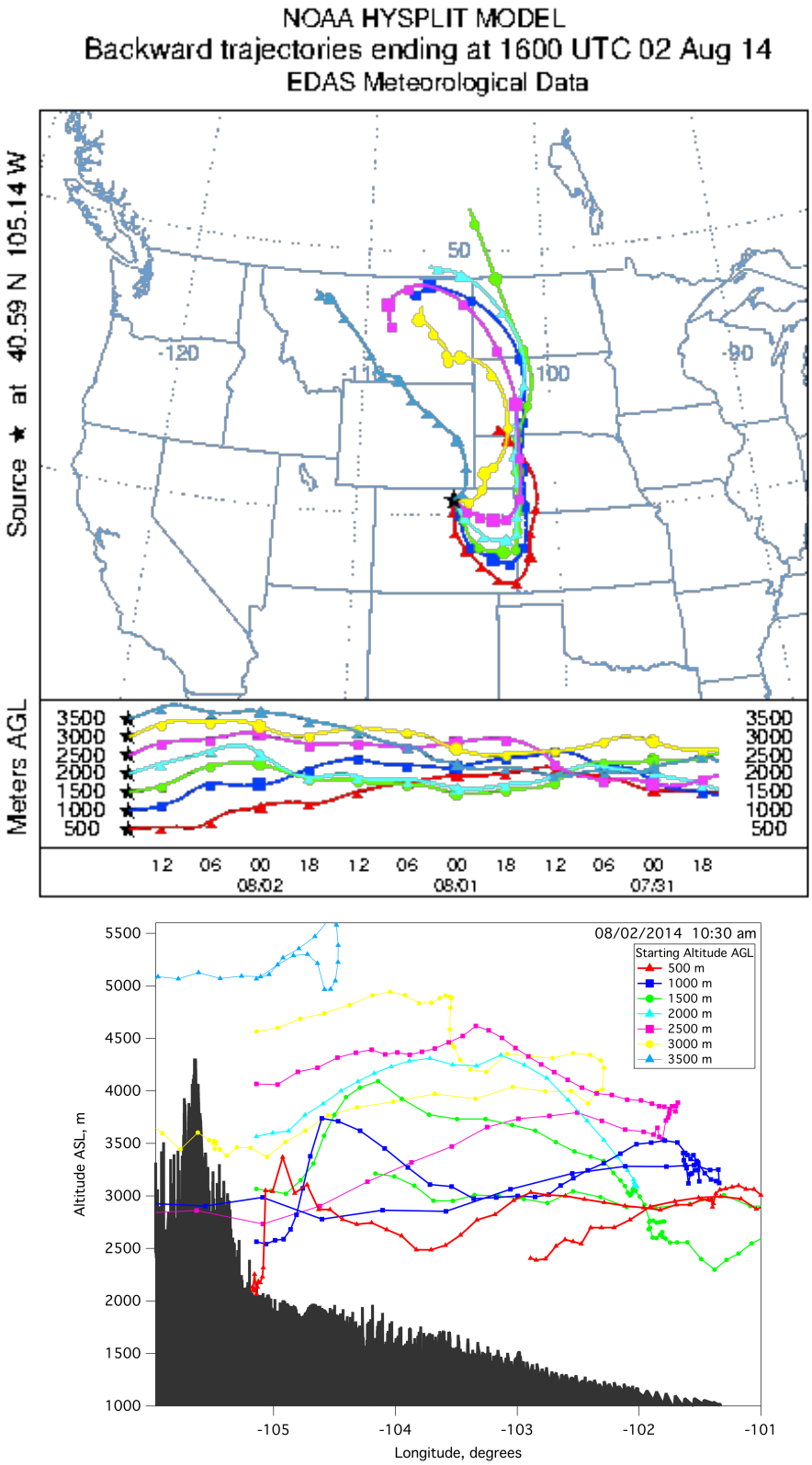

Figure A.4 72-hour 3-D kinematic back trajectory computed over Fort Collins spiral location starting at 08/02/2014 10:30:01 local time as a function of latitude and longitude (top), and altitude and longitude (bottom).

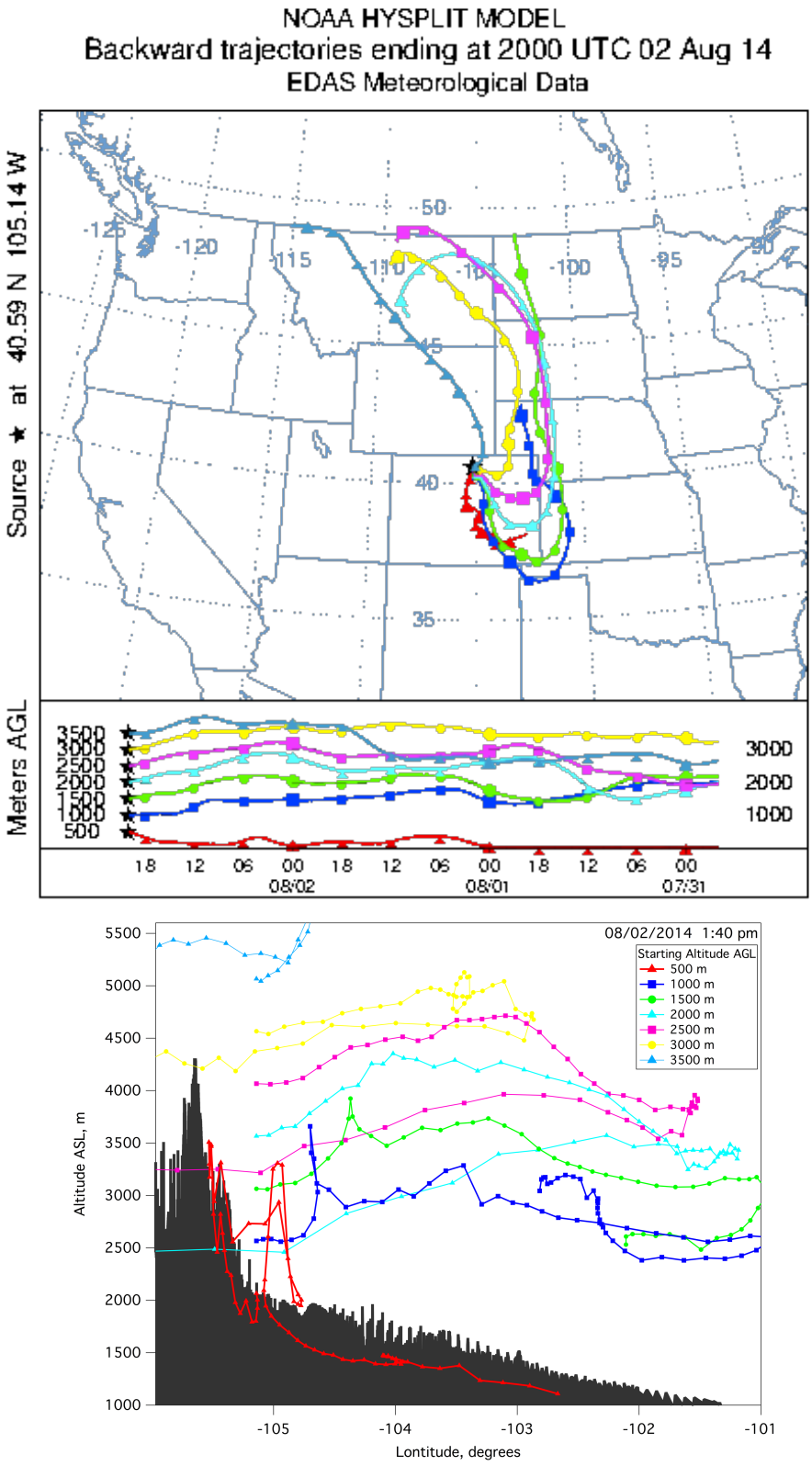

Figure A.5 72-hour 3-D kinematic back trajectory computed over Fort Collins spiral location starting at 08/02/2014 13:42:05 local time as a function of latitude and longitude (top), and altitude and longitude (bottom).

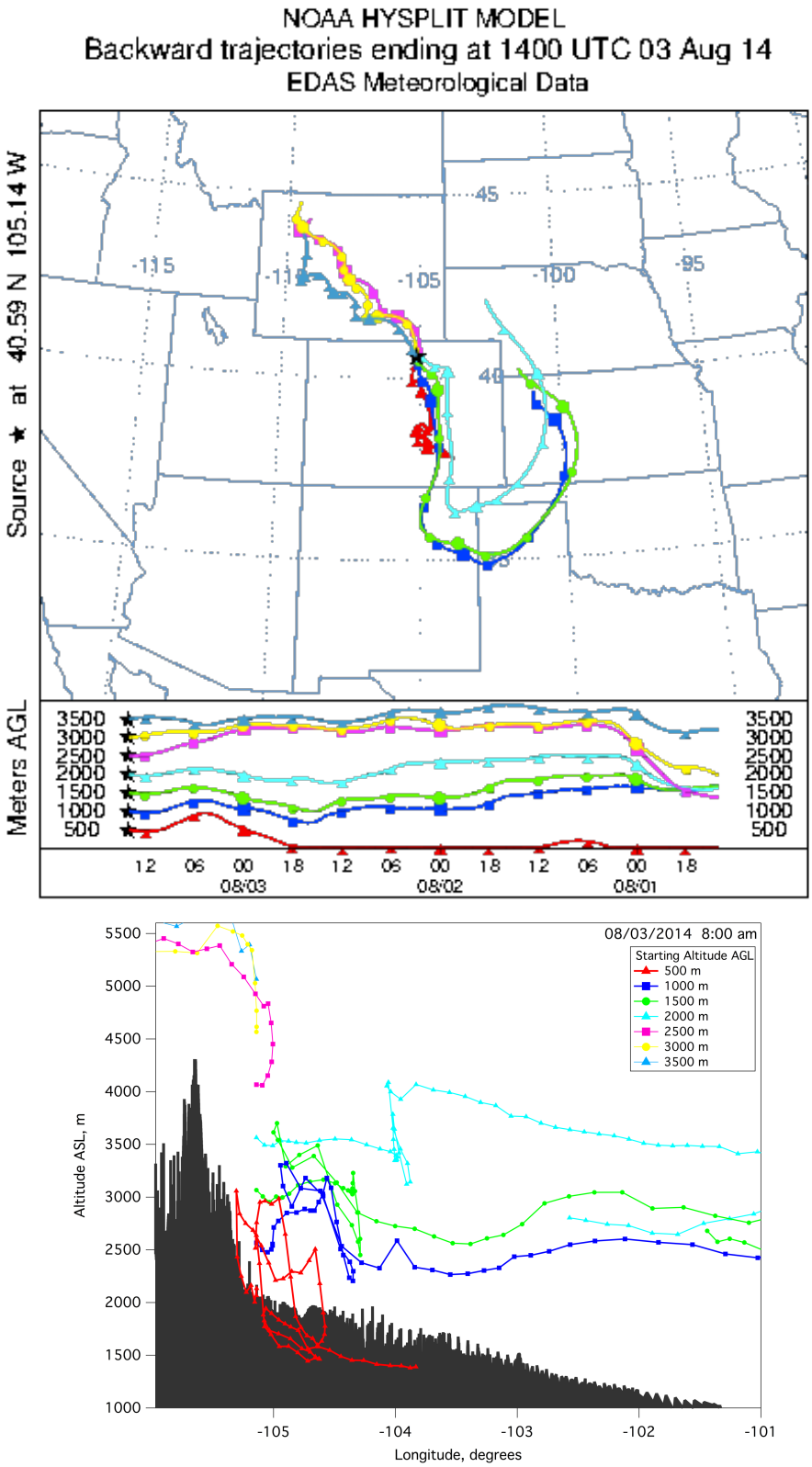

Figure A.6 72-hour 3-D kinematic back trajectory computed over Fort Collins spiral location starting at 08/03/2014 08:07:35 local time as a function of latitude and longitude (top), and altitude and longitude (bottom).

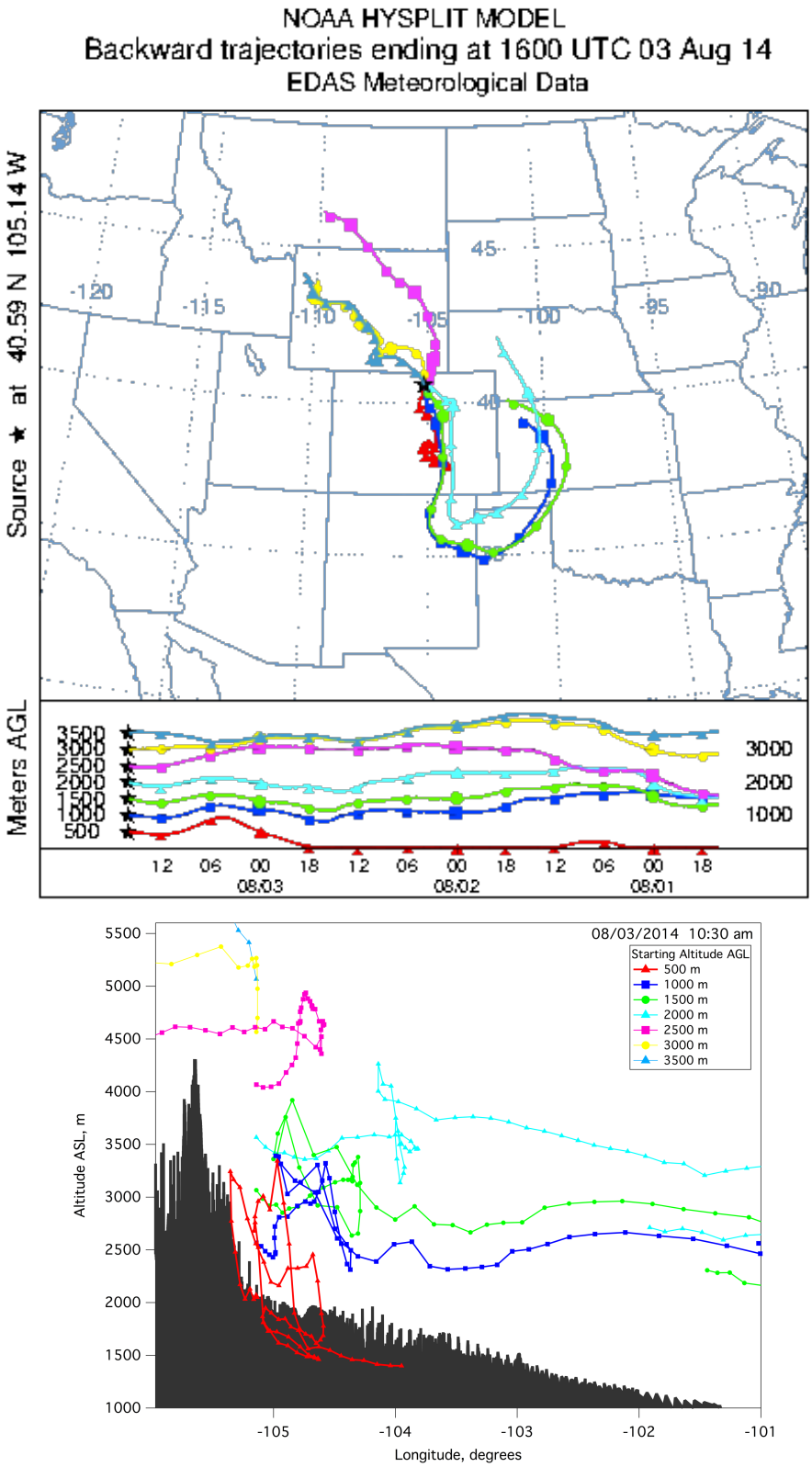

Figure A.7 72-hour 3-D kinematic back trajectory computed over Fort Collins spiral location starting at 08/03/2014 10:25:16 local time as a function of latitude and longitude (top), and altitude and longitude (bottom).

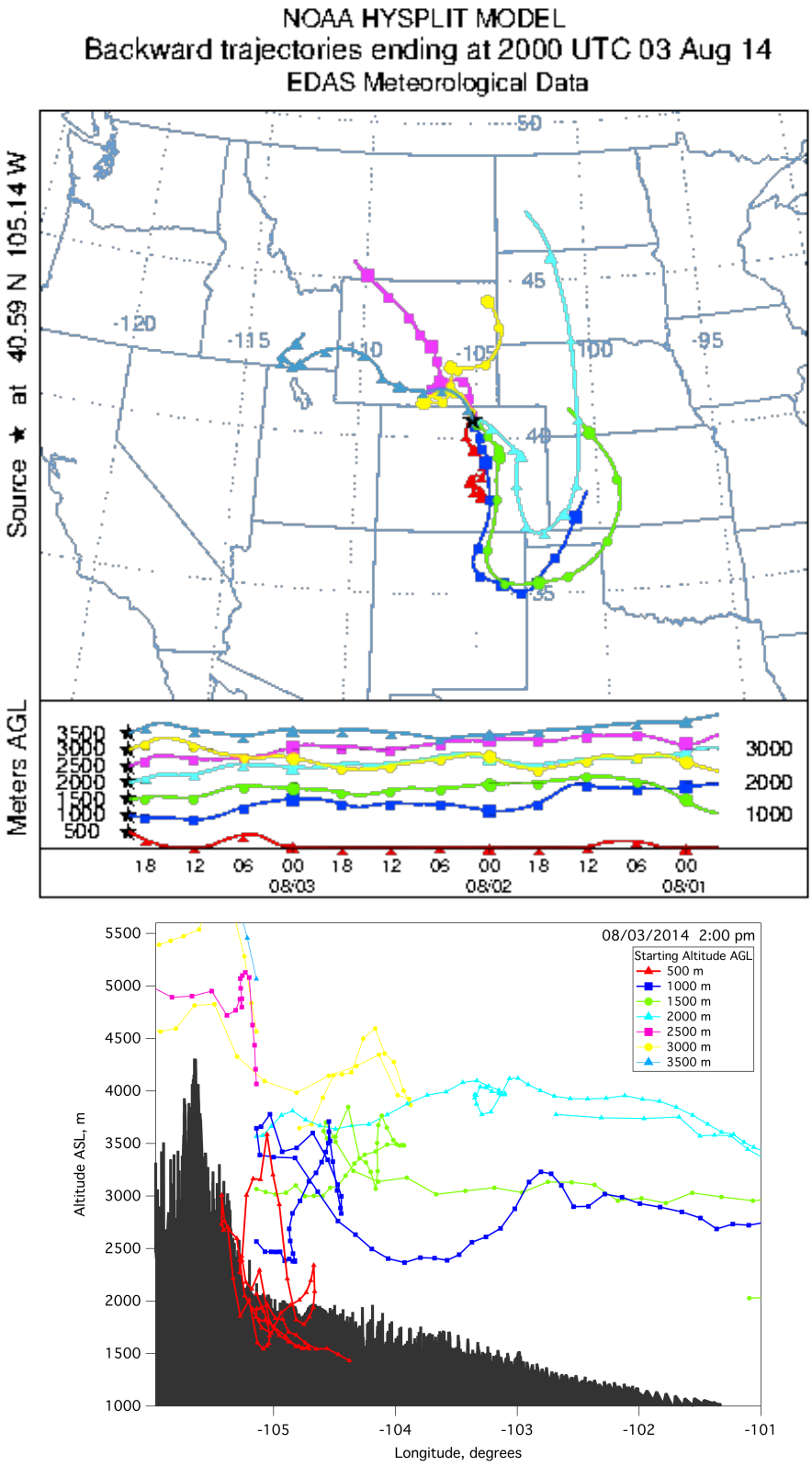

Figure A.8 72-hour 3-D kinematic back trajectory computed over Fort Collins spiral location starting at 08/03/2014 14:05:39 local time as a function of latitude and longitude (top), and altitude and longitude (bottom).

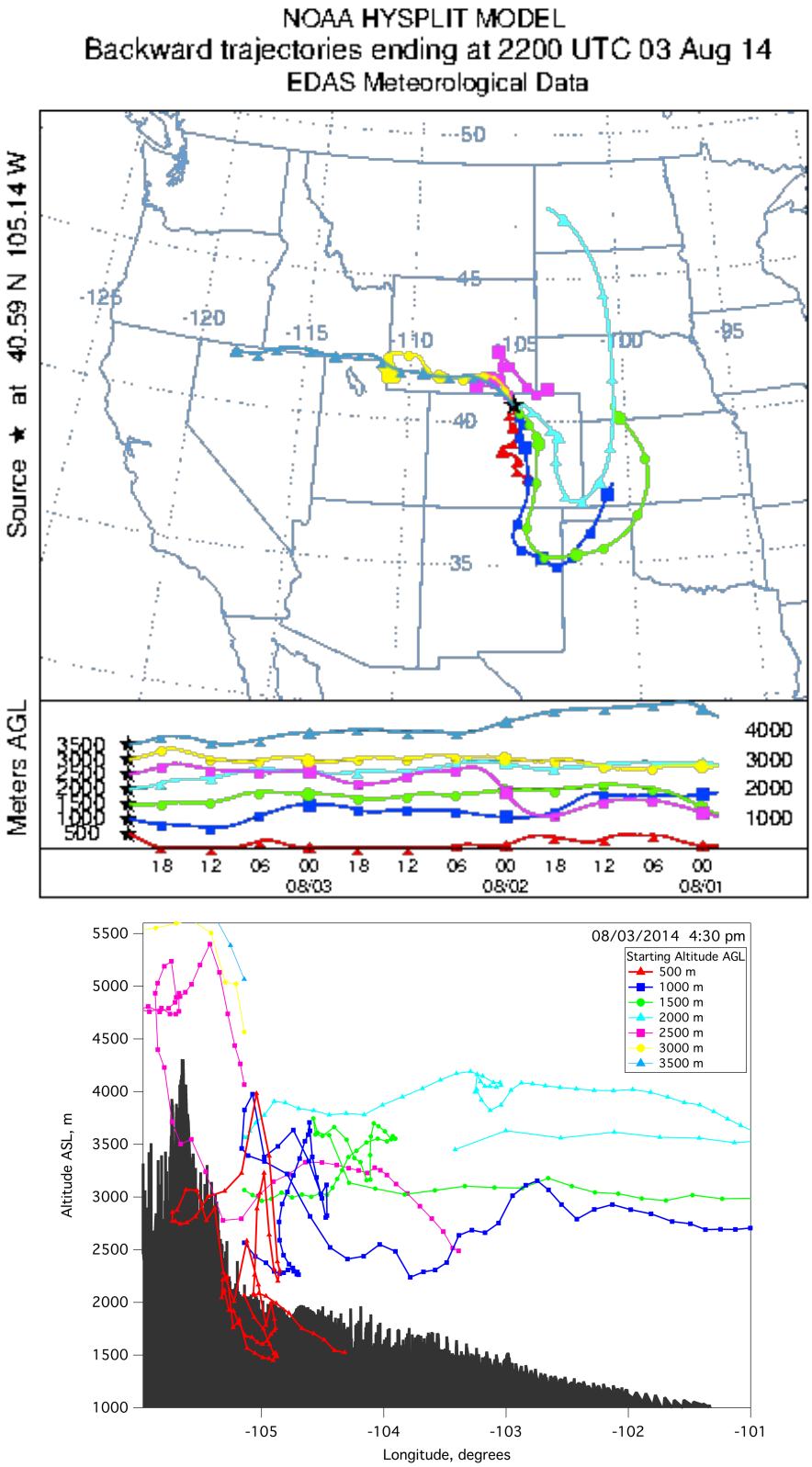

Figure A.9 72-hour 3-D kinematic back trajectory computed over Fort Collins spiral location starting at 08/03/2014 16:26:11 local time as a function of latitude and longitude (top), and altitude and longitude (bottom).

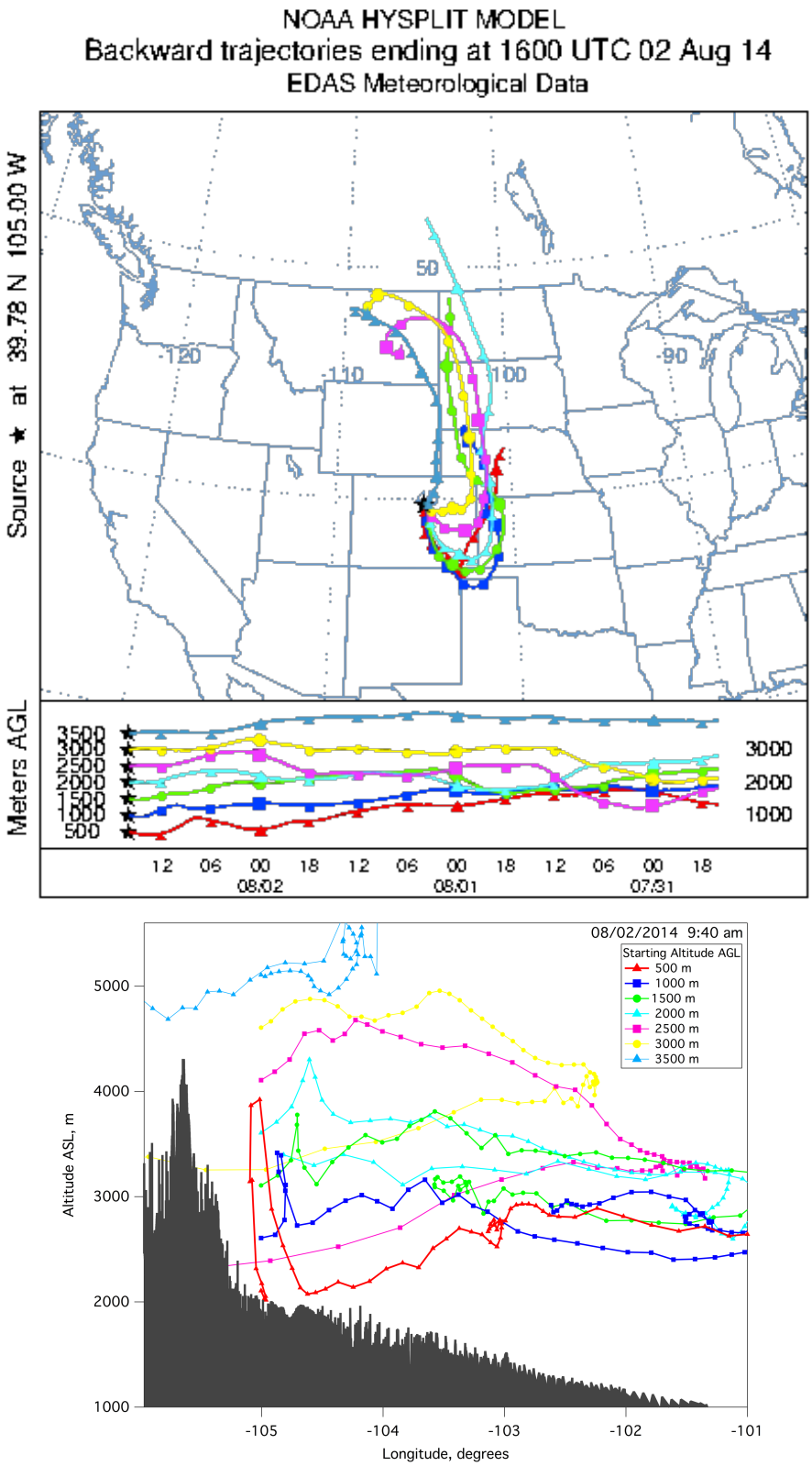

Figure A.10 72-hour 3-D kinematic back trajectory computed over Denver spiral location starting at 08/02/2014 9:39:2 local time as a function of latitude and longitude (top), and altitude and longitude (bottom).

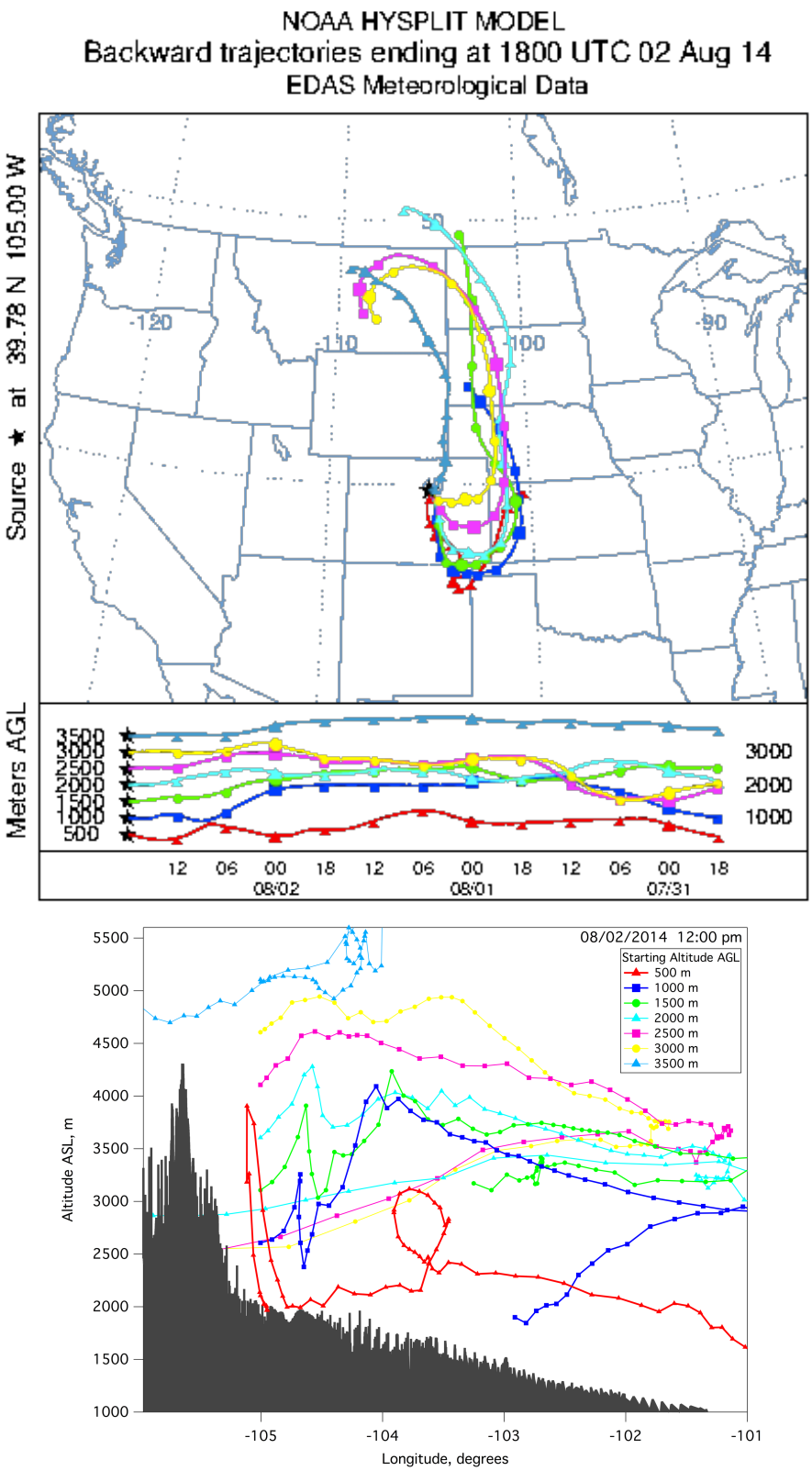

Figure A.11 72-hour 3-D kinematic back trajectory computed over Fort Collins spiral location starting at 08/02/2014 12:05:07 local time as a function of latitude and longitude (top), and altitude and longitude (bottom).

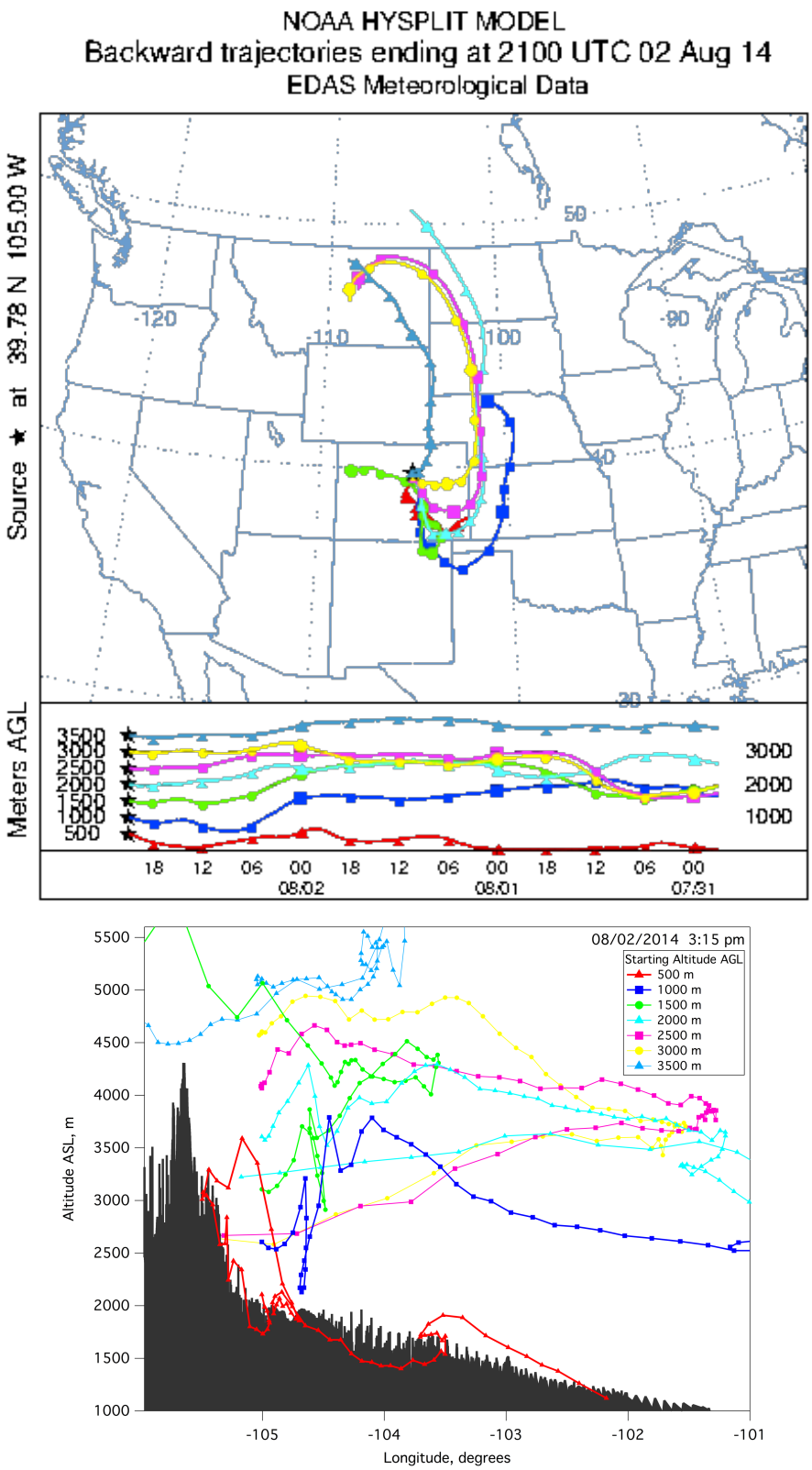

Figure A.12 72-hour 3-D kinematic back trajectory computed over Denver spiral location starting at 08/02/2014 15:15:10 local time as a function of latitude and longitude (top), and altitude and longitude (bottom).

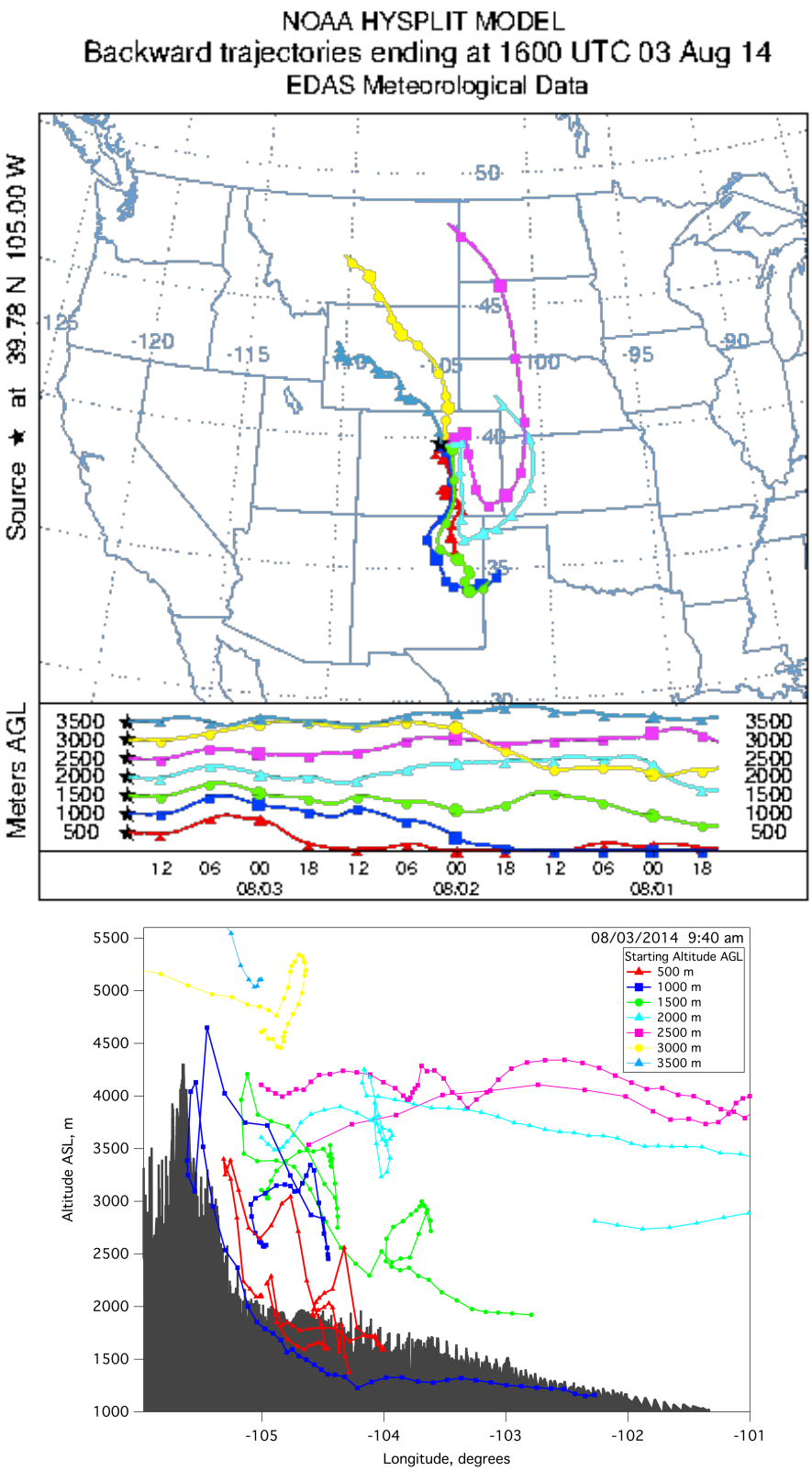

Figure A.13 72-hour 3-D kinematic back trajectory computed over Denver spiral location starting at 08/03/2014 09:39:47 local time as a function of latitude and longitude (top), and altitude and longitude (bottom).

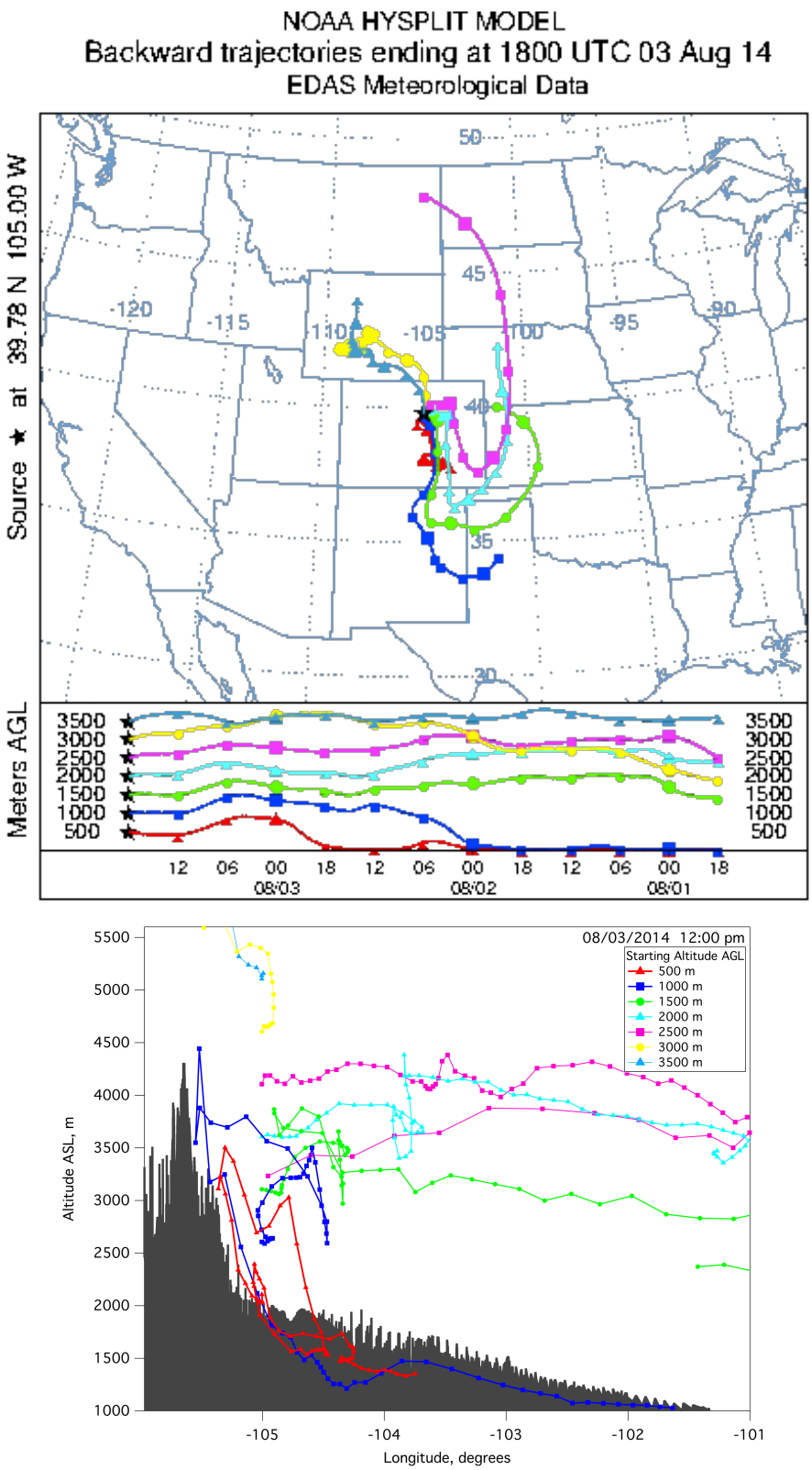

Figure A.14 72-hour 3-D kinematic back trajectory computed over Denver spiral location starting at 08/03/2014 11:58:13 local time as a function of latitude and longitude (top), and altitude and longitude (bottom).

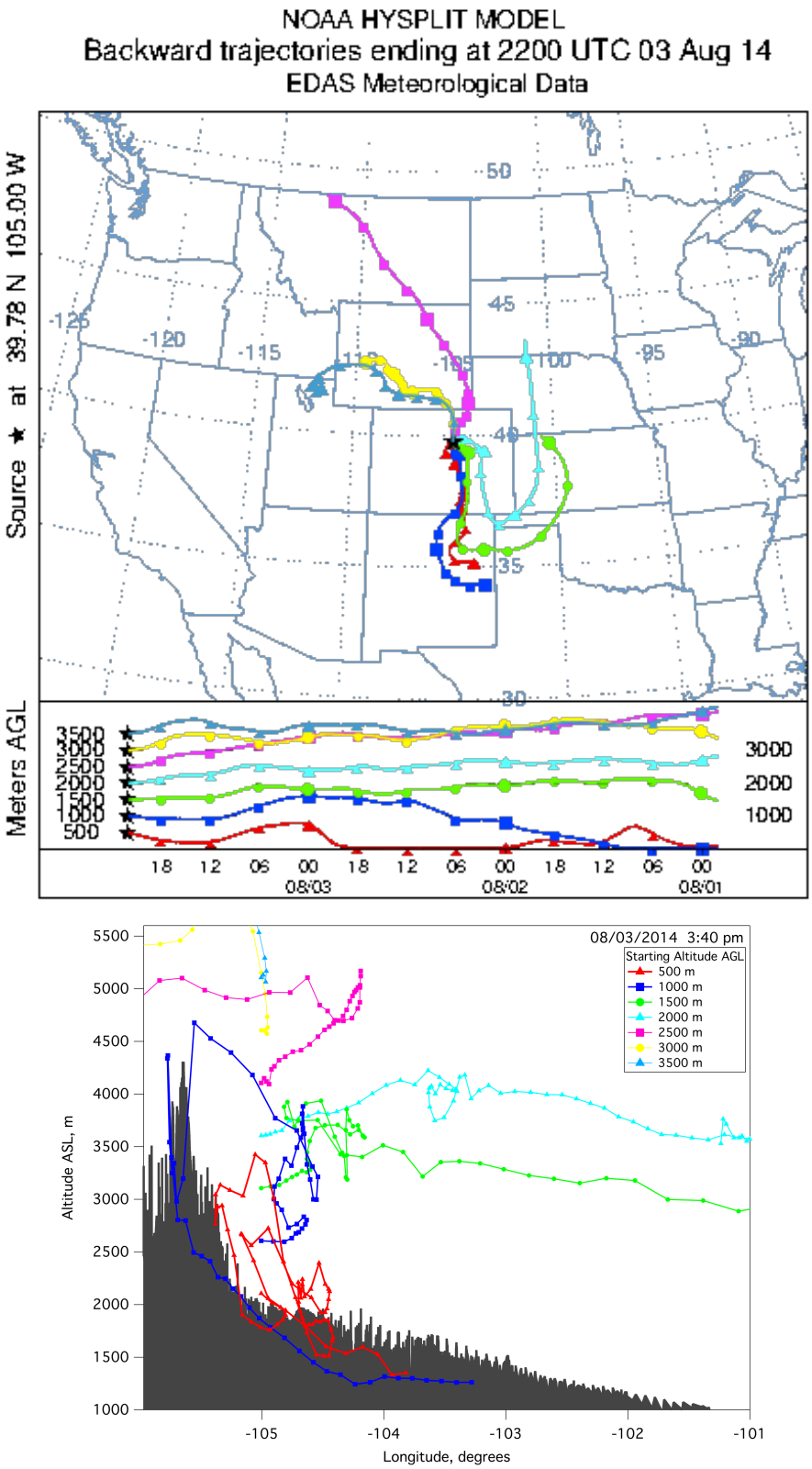

Figure A.15 72-hour 3-D kinematic back trajectory computed over Denver spiral location starting at 08/03/2014 15:38:02 local time as a function of latitude and longitude (top), and altitude and longitude (bottom).

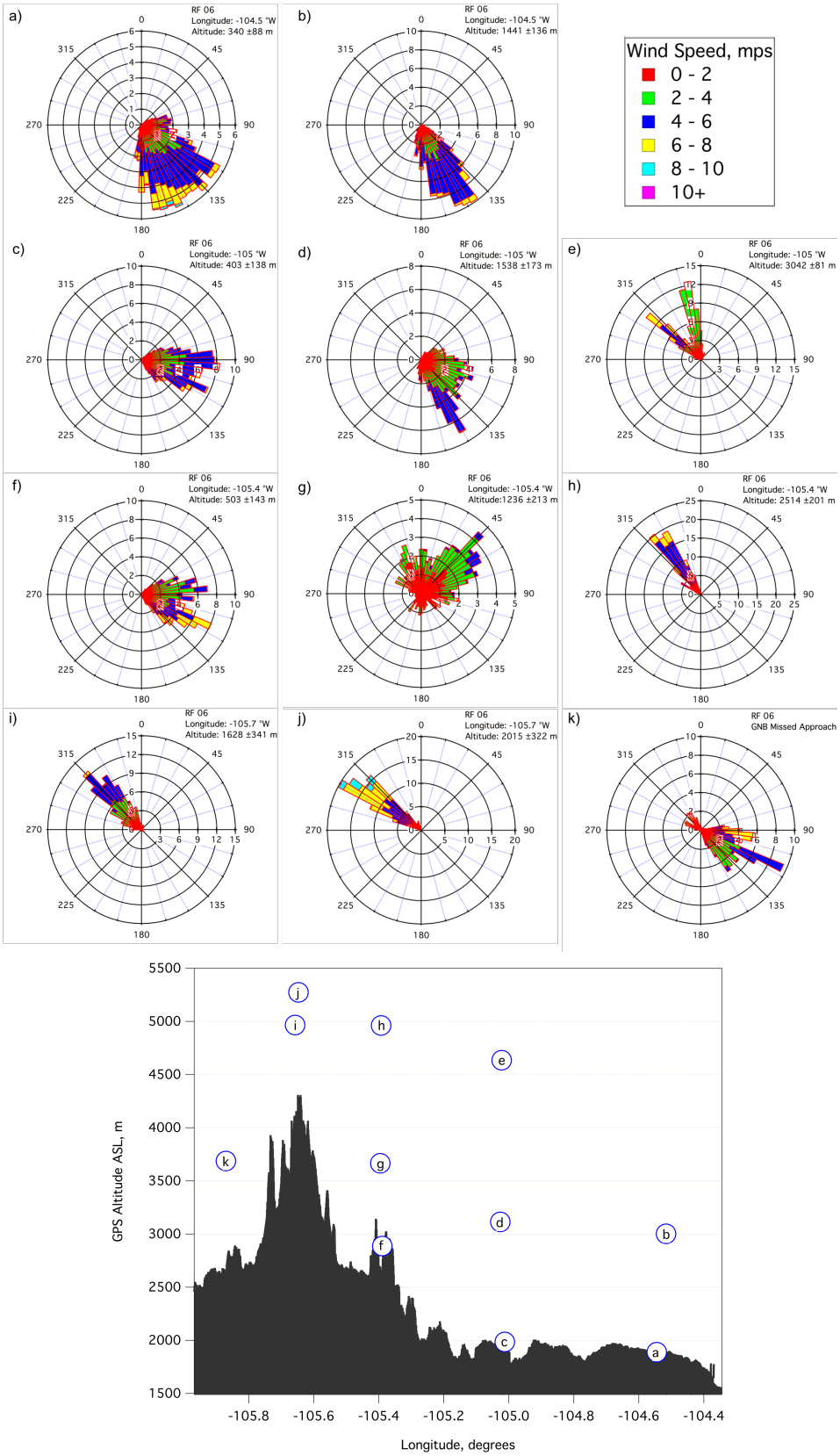

Figure A.16 Wind data (top panel) for each respective flight leg from research flight 6 and corresponding flight leg location (bottom panel).

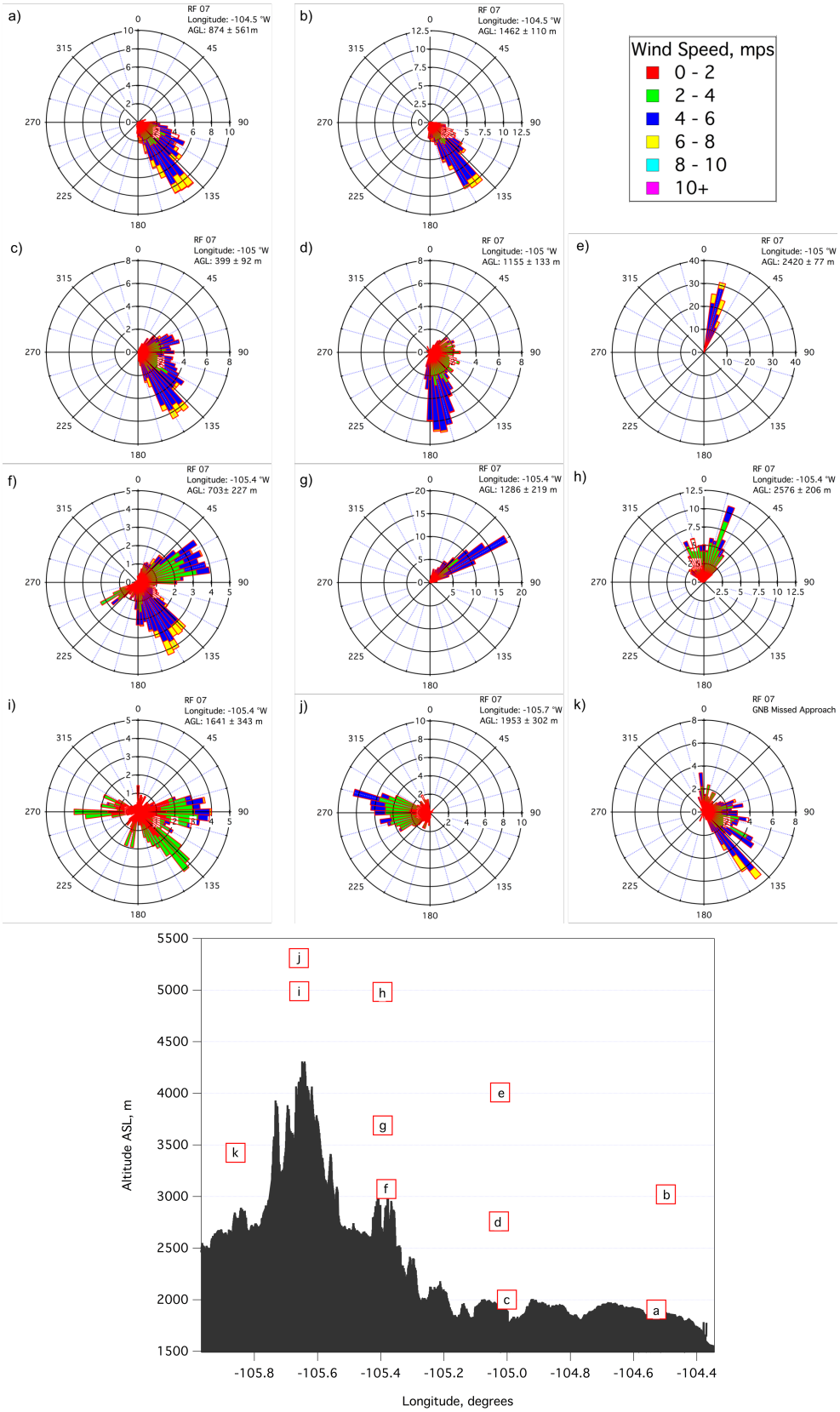

Figure A.17 Wind data (top panel) for each respective flight leg from research flight 7 and corresponding flight leg location (bottom panel).